Platinum-lanthanide metallodrugs for imaging and therapy

A thesis submitted for the degree of

Doctor of Philosophy

in Inorganic Chemistry

Kezi Yao

Keble College

University of Oxford

Trinity Term 2021

Abstract

This work describes the development of several Lanthanide-Platinum complexes and outlines the application of the products as theranostic agents. The luminescence and relaxivity properties of the complexes is investigated for imaging purposes and the cytotoxicity of the complexes is exploited for therapeutic use.

Chapter 1 discusses the fundamental properties of lanthanides and platinum. For lanthanides, the discuss focuses on their luminescence, magnetism and stability. As for platinum, the discussion focuses on the properties that relates to its cytotoxicity, such as cellular uptake. A brief literature review on Ln-Pt theronostic complexes is given.

Using the CuAAC reaction to conjugate Ln and Pt building blocks is described in Chapter 2. Another type of click reaction-SPAAC is utilised in Chapter 3. The photochemical properties of the clicked Pt complexes are studied thoroughly. The purification and characterisation of Ln-Pt complexes are also investigated.

Chapter 4 describes a series of cell-permeable Ln-Pt complexes, of which the relaxivity and cell diffusion NMR of the Gd complexes were studied and the photophysical properties of the switch-on Eu complexes was also investigated.

Chapter 5 delineates the conclusion and chapter 6 provides experimental procedures.

Publications

1 K. Yao, A. Bertran, J. Morgan, S. M. Hare, N. H. Rees, A. M. Kenwright, K. Edkins, A. M. Bowen and N. J. Farrer, *Dalton. Trans.*, 2019, **48**, 6416–6420.

2 K. Yao, A. Bertran, J. Morgan, C. Greenhalgh, K. Edkins, A. M. Bowen and N. J. Farrer, *Eur. J. Inorg. Chem.*, 2021, 1397-1404.

3 K. Yao, A. Bertran, A. Howarth, J. M. Goicoechea, S. M. Hare, N. H. Rees, M. Foroozandeh, A. M. Bowen and N. J. Farrer, *Chem. Commun.*, 2019, **55**, 11287–11290.

4 K. Yao, G. Karunanithy, A. Howarth, P. Holdship, A. L. Thompson, K. E. Christensen, A. J. Baldwin, S. Faulkner and N. J. Farrer, *Dalton. Trans.*, 2021, **50**, 8761–8767.

5 L. R. Tear, M. L. Maguire, M. Tropiano, K. Yao, N. J. Farrer, S. Faulkner and J. E. Schneider, *Dalton. Trans.*, 2020, **49**, 2989–2993.

Contents

Acknowledgements

This doctoral thesis has been completed through the support of many adorable people that I would like to thank. First and foremost, I would like to express my deep gratitude to my supervisors Dr. Nicola Farrer and Prof. Stephen Faulkner for their greatest support and guidance during my D.Phil. study. Thank you for having me in your group where I enjoyed working in and learned a lot, especially from your persistent spirit in exploring and discovering scientific challenges. I sincerely wish you and your families great happiness and health from the bottom of my heart.

I would like to express my special thanks to all the members of staff in the CRL who provide the facilities and support in the department. In particular, Dr. Nick Rees for teaching me paramagnetic NMR and the mass spectrometry service for accurate mass spec. Thanks go to Dr. Gogulan Karunanithy and Prof. Andrew Baldwin for collaboration in cell diffusion NMR, to Arnau Bertran and Dr. Alice Bowen for their help in EPR experiments.

I would also like to express my deep gratitude to Dr. Louise Tear for teaching me HPLC, Dr Xuejian Zhang for introducing me to the chemistry of lanthanide, Dr. Alison Howarth for teaching me cell culture, Dr. Daniel Kovacs and Dr. Deborah Sneddon for sharing scientific advice. Thanks to everyone else in the group, including but not limited to Agnes, Carlson, Grace, Qidian, Marie, Laura, Tom, Shitong and Xiaofan, thank you for making the lab an enjoyable and friendly place.

Also, specially thanks to the Great Britain-China Educational Trust for their financial support. I am also grateful to be a member of Keble college and Department of Chemistry at University of Oxford.

Last but not the least, I would like to thank my family, especially my parents for their

unconditional support and love during my abroad study. I would also like to express my thanks to my love, Haonan Le, for his sincere love and accompany. You supported me in every aspects of my life. What a pleasure to be Dr. together with you!

Abbreviations

a.u.	arbitrary units
br	broad
CuAAC	copper azide-alkyne cycloaddition
Cyclen	1,4,7,10-tetraazacyclododecane
d	days
DCM	dichloromethane
DI	deionised
DMF	dimethylformamide
DMSO	dimethylsulfoxide
DO3A	1,4,7,10-tetraazacyclododecane-1,4,7-triacetic acid
DOTA	1,4,7,10-tetraazacyclododecane-1,4,7,10-tetraacetic acid
DOTAM	1,4,7,10-tetraazacyclododecane-1,4,7,10-tetraacetamide
DTPA	diethylene triamine pentaacetic acid
DTPA-BMA	diethylenetriaminepentaacetic acid bis(methylamide)
ESI-MS	electrospray ionization mass spectrometry
eT	electron transfer
ET	energy transfer
EtOAC	ethyl acetate
5'-GMP	Guanosine monophosphate
h	hours
HPLC	high-performance liquid chromatography
HRMS	high-resolution mass spectrometry
IC	internal conversion
ICP-MS	inductively coupled plasma mass spectrometry
ILCT	intra-ligand charge transfer
IR	infrared
ISC	inter-system crossing
LMCT	ligand to metal charge transfer Ln lanthanide
MeCN	acetonitrile

MeOH	methanol
MLCT	metal to ligand charge transfer
MRI	magnetic resonance imaging MsCl methanesulfonyl chloride
MWCO	molecular weight cut-off NMR nuclear magnetic resonance
OAc	acetate
NSF	nephrogenic systemic fibrosis
PBS	phosphate buffered saline
PPh_3	triphenylphosphine
r_1	T_1 relaxivity
r_2	T_2 relaxivity
R_1	T_1 relaxation rate
R_1	T_1 relaxation rate
RP-HPLC	reverse-phase high-performance liquid chromatography
RT	room temperature
SAP	square anti-prism
T_1	longitudinal relaxation time
T_2	transverse relaxation time
^{t}Bu	tert-butyl
TFA	trifluoroacetic acid
TLC	thin layer chromatography
TSAP	twisted square anti-prism
t_R	retention time
UV-Vis	ultraviolet-visible

Chapter 1: Introduction

Molecular imaging agents have made a significant impact on the field of biomedical imaging, allowing biochemical detail and specificity in images beyond the capabilities of the imaging hardware alone. The lanthanides have a broad spectrum of properties that have facilitated the application of these elements as probes in magnetic resonance imaging (MRI), optical imaging and positron-emission topography (PET).

One of the major causes of human deaths throughout the world is cancer. According to the World Health Organization (WHO), cancer-related deaths are expected to rise to 22 million by 2030.[1] The discovery of cisplatin by Rosenberg and colleagues in 1965 provided the first indication of the anti-proliferative properties of platinum complexes. Since then, cisplatin and its analogous have achieved great success in treating cancer despite the disadvantages of these drugs, which include side-effects and drug resistance. Thus, new and more advanced platinum-based cancer treatments are needed, and could be highly beneficial in enhancing cancer patient survival.

In this thesis, the development of lanthanide-platinum complexes for theranostic purpose of cancer is discussed and explored. The lanthanide (Ln) part of the complexes discussed can be utilised in multimodal imaging methods including MRI and luminescent imaging. On the other hand, the platinum (Pt) moiety can be used for therapeutic purposes. A number of different features of platinum complexes were studied in this thesis such as oxidation state (Pt(II), Pt(IV)) and photoresponsiveness. To achieve a combination of imaging and therapeutic abilities, which can be called the theranostic properties, success in synthesis of the Ln-Pt complexes is needed involving effective coupling strategies between the lanthanide and platinum moieties, requiring the understanding of the chemical and spectroscopic nature of Ln and the chemical and

cytotoxic studies of Pt. Therefore, in this chapter, the properties of Ln and Pt are first presented before the introduction of Ln-Pt complexes.

1.1 General Lanthanide Chemistry

In this section, the general chemical properties of lanthanides are presented. The general electronic configuration of Ln is [Xe]$4f^n6s^2$, except for lanthanum, cerium, gadolinium and lutetium possessing [Xe]$4f^{n-1}5d^16s^2$ configurations. The electronic configurations of Ln elements become uniformly [Xe]$4f^{n-1}$, once they are ionised to the most common +3 oxidation state. It is worth noting that, upon ionisation, La(III) does not possess any *f* electrons while Lu(III) possesses a filled 4*f* orbital. The trivalent lanthanide ions are the most stable form for the lanthanides and dominate the lanthanide chemistry. Lanthanide complexes exhibit similar chemical properties because of their electronic properties stated above. 4*f* orbitals are valence orbitals, which are shielded by the more spatially dispersed filled 5*s* and 5*p* orbitals from the coordination environment. Thus, the electrostatic interactions between the Lewis acidic lanthanide metal ion and ligand play a major role in bond formation in lanthanide complexes, and the ligand field perturbation upon 4*f* orbitals is minimal. In an aqueous environment, the coordination number of the Ln complexes varies from 8 to 10. Substantially, the lanthanide ion with the most common +3 oxidation state contributes to the coordination geometry, leading to the fact that it is more favourable for hard donors like N and O atoms to be bound to hard Ln metal ions.

1.2 Lanthanide Luminescence

Beyond their general chemical properties, the luminescence properties of many of the

Ln has been studied extensively for several decades; their unique emission spectra are being exploited for application as imaging probes as a consequence of their unique photo-physical properties, such as long luminescent lifetime, large pseudo-Stokes shift and sharp emission. The electronic configurations introduced in the last section lead to the fact that the emission properties of different Ln metals are largely different throughout the Ln series. All of the open shell lanthanide ions demonstrate luminescent properties, as shown in Figure 1.1 and Table 1.1, and their characteristic emission spectra are distributed from the ultra-violet (UV) region (Gd(III)), green (Tb(III)), yellow (Dy(III)), red (Eu(III)) to near-infrared (NIR) (Nd(III), Yb(III), Er(III)) (Figure X).[2]

Table 1.1. *Most common emissive f-f transitions of Ln(III)* [2,4]

Ln	Transition	λ [nm]
Pr	$^1D_2 \rightarrow {}^3F_4$	1000
	$^1D_2 \rightarrow {}^1G_4$	1440
	$^1D_2 \rightarrow {}^3H_J (J = 4,5)$	600, 690
	$^3P_0 \rightarrow {}^3H_J (J = 4-6)$	490, 545, 615, 640,
	$^3P_0 \rightarrow {}^3F_J (J = 2-4)$	700, 725
Nd	$^4F_{3/2} \rightarrow {}^4I_J (J = 9/2-13/2)$	900, 1060, 1350
Sm	$^4G_{5/2} \rightarrow {}^6H_J (J = 5/2-13/2)$	560, 595, 640, 700, 775
	$^4G_{5/2} \rightarrow {}^6F_J (J = 1/2-9/2)$	870, 887, 926, 1010, 1150
Eu	$^5D_0 \rightarrow {}^7F_J (J = 0-6)$	580, 590, 615, 650, 720, 750, 820
Gd	$^6P_{7/2} \rightarrow {}^8S_{7/2}$	315
Tb	$^5D_4 \rightarrow {}^7F_J (J = 6-0)$	490, 540, 580, 620, 650, 660, 675
Dy	$^4F_{9/2} \rightarrow {}^6H_J (J = 15/2-9/2)$	475, 570, 660, 750
	$^4I_{15/2} \rightarrow {}^6H_J (J = 15/2-9/2)$	455, 540, 615, 695
Ho	$^5S_2 \rightarrow {}^5I_J (J = 8,7)$	545, 750
	$^5F_5 \rightarrow {}^5I_J (J = 8,7)$	650, 965
Er	$^4S_{3/2} \rightarrow {}^4I_J (J = 15/2, 13/2)$	545, 850
	$^4F_{9/2} \rightarrow {}^4I_{15/2}$	660
	$^4I_J (J = 9/2, 13/2) \rightarrow {}^4I_{15/2}$	810, 1540
Tm	$^1D_2 \rightarrow {}^3F_4, {}^3H_4, {}^3F_J (J = 3,2)$	450, 650, 740, 775
	$^1G_4 \rightarrow {}^3H_6, {}^3F_4, {}^3H_5$	470, 650, 770
	$^3H_4 \rightarrow {}^3H_6$	800
Yb	$^2F_{5/2} \rightarrow {}^2F_{7/2}$	980

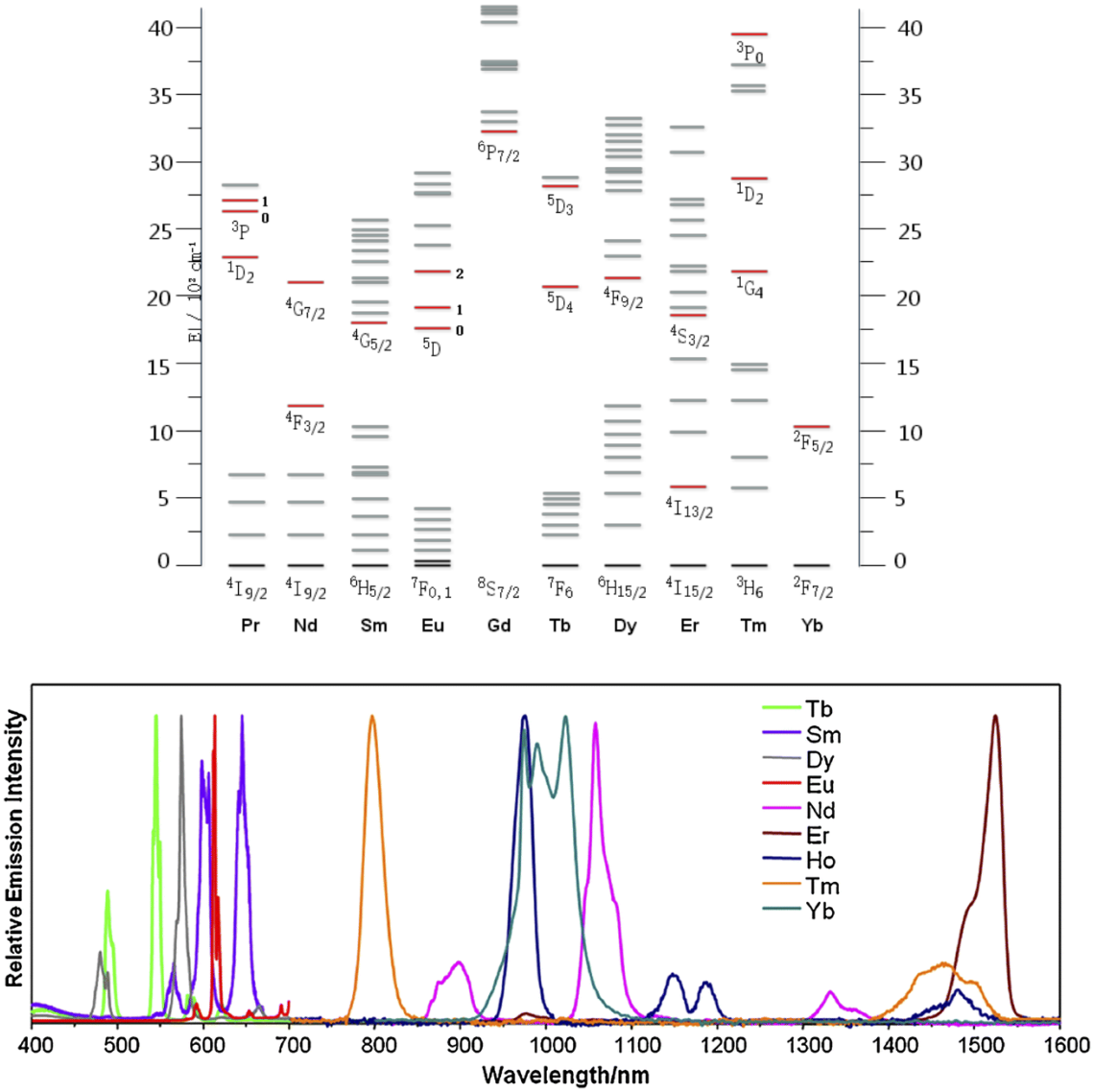

Figure 1.1: *Top: partial energy diagram for Ln(III) ions. The main excited states are marked in red, while the fundamental ground state is indicated in black.*[2] *Bottom: illustration of Ln(III) emission from reference.*[3]

Lanthanide ions possessing partially filled 4*f* orbitals show sharp line-shape emission spectra. The *f-f* transitions contain electric dipole and magnetic dipole characters. As suggested by the Laporte rule (electric dipole selection rule), although magnetic dipole transitions are allowed, *f-f* transitions are weak due to no changes in parity on transition. There a number of mechanisms to partially relax the selection rules (*e.g.* vibronic coupling). The symmetry of metal ions is affected by molecular vibration, the vibronic

coupling of excited states takes place and leads to very narrow transitions.

The small extinction coefficients, usually in the range of 0.5 – 3.0 $dm^3mol^{-1}cm^{-1}$, of trivalent lanthanide ions results in extremely inefficient direct excitation, which is only feasible with laser pulses. Therefore, direct excitation of a lanthanide ion will only result in weak emission.[2]

1.3 Sensitised Lanthanide Luminescence

High-intensity sources are required in many applications of Ln complexes to directly excite the lanthanide ions, which limits their utilisation in various aspects. By populating the emissive excited state of a lanthanide ion, the weak *f-f* emission can be mitigated through the excitation of a nearby chromophore which acts as a sensitising group, also known as an antenna group, and populates the emissive excited states of Ln through energy transfer.

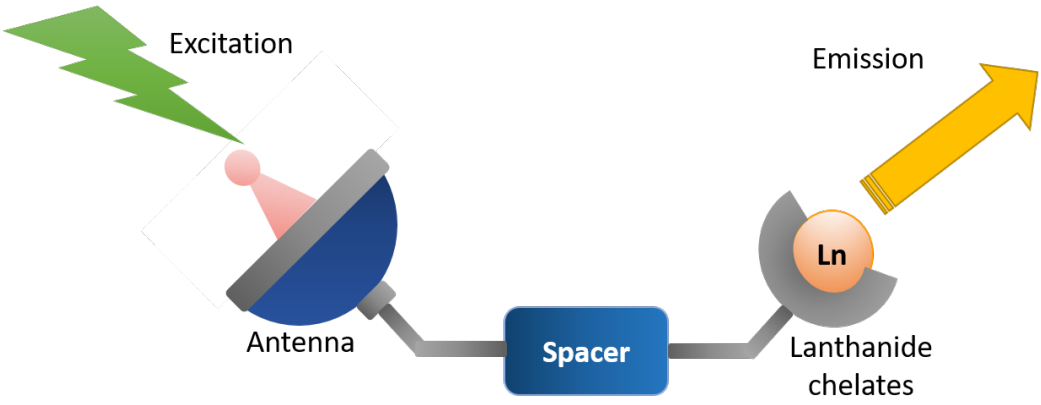

Figure 1.2: *Schematic representation of sensitised lanthanide luminescence with energy transfer.*

Introducing the antenna groups can be achieved by covalently incorporating them into the ligand manifold or other methods (*e.g.* co-ligand). Radiative processes can take place for these *f*-centred excited states to produce lanthanide emission with large Stokes

shift, microsecond (or longer) lifetime and well-defined characteristics, resulted from the forbidden *f-f* transitions and antenna effect. Moreover, high energy oscillators, such as X-H, C-H, and N-H, can quench the luminescence of the lanthanide.

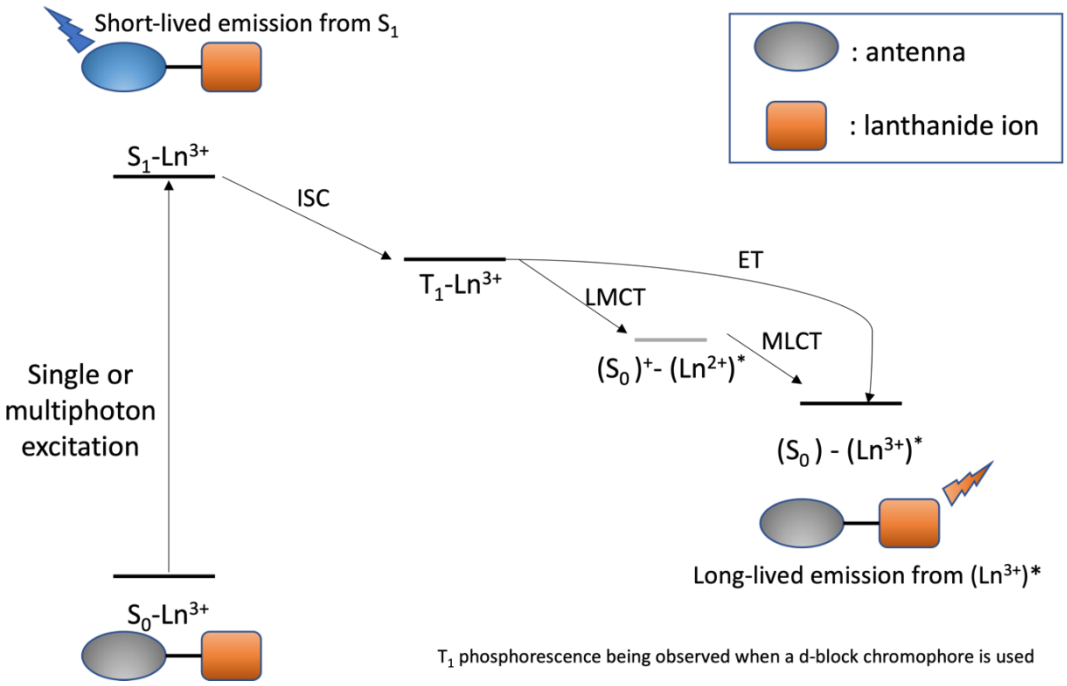

Figure 1.3: *Simplified Jablonski diagram for the main energy transfer processes leading to the lanthanide emission.*

Figure 1.2 shows the demonstration of the sensitisation process for lanthanide luminescence while Figure 1.3 presents the Jablonski diagram of the energy transfer pathways. The excitation of an organic chromophore begins with single- or multi-photon absorption for a typical sensitisation process. After internal conversion (IC), the excitation results in the singlet excited states (S_1) of the organic chromophore, which can be relaxed down to ground state via non-radiative decay or radiative decay with fluorescence. Alternatively, intersystem crossing (ISC) can take place from S_1 leading to the population of the triplet excited states (T_1), which can be followed by the events of non-radiative decay - phosphorescence of the organic chromophore, or energy

transfer (ET) to the lanthanide excited state. The ISC between S_1 and T_1 can take place by either a Dexter or Förster mechanism (shown in Figure 1.4), depending on the donor-acceptor energy overlap and chemical structure.[5] Dexter transfer involves the two parts of the molecule directly exchanging electrons via orbital overlap, so it requires facile electron exchange or superexchange (i.e. through the bridging ligand orbitals). Förster transfer is a resonant process and is a dipolar, longer-range interaction.

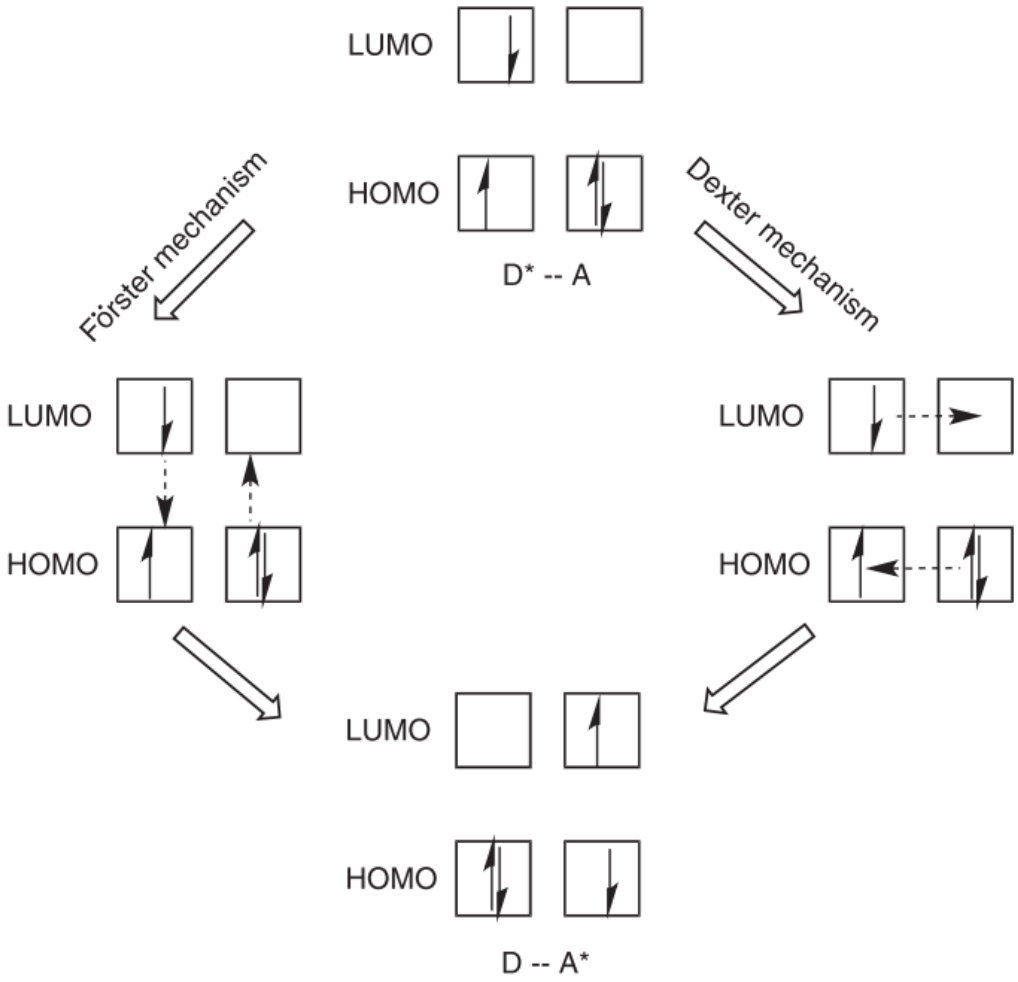

Figure 1.4: *Pictorial representation of energy transfer between donor D and acceptor A through the Förster and Dexter mechanisms.*[5]

The energy-transfer effectiveness is dependent on the properties of the Ln (III)

acceptor state and donor triplet state. The back energy transfer can depopulate the Ln (III) emissive states when the gap is less than 2000 cm^{-1}, which means the energy transfer mediated by the triplet state usually plays the major role in the sensitisation.[6] The short-life S_1 states of the antenna can also result in the sensitisation of the Ln luminescence which can be a leading factor in the sensitisation of emissive state of the lanthanide with the intra-ligand charge transfer (ILCT).[6] It is worth noting that Figure 1.3 shows a simplified presentation of the sensitisation process while the practical situation can be more complicated.

Complexes containing Yb are particularly attractive because charge transfer plays an important role in such systems, since the emissive excited states $^2F_{5/2}$ of Yb(III) is much lower than triplet excited states of the common organic chromophore. Horrocks *et al.* assumed that the $^2F_{5/2}$ emissive states can be excited via a reversible ligand-to-metal electron transfer.[7] Yb^{3+} is reduced to Yb^{2+} by the excited organic chromophores and forms ligand-to-metal charge transfer (LMCT) states in the process followed by the oxidisation of Yb^{2+} generating the (Yb^{3+})* excited states by the radical chromophore, which leads to the ytterbium emission. Other than Yb complexes, LMCT can also be found in the energy transfer processes of other Ln systems. Nevertheless, LMCT states can possess lower energy than those of the emissive states of Ln in these systems. Subsequently, it results in the quenching in Ln luminescence.

While organic chromophores are widely exploited for the sensitisation of high energy emitting lanthanides such as terbium and europium,[8] chromophores containing transition metals have been increasingly studied for more than 20 years.[9,10] Transition metal containing chromophores can be employed as antennae for the sensitisation of near IR emitting lanthanides, as they offer higher photostability when compared to organic counterparts and a wide range of absorptions: from visible to near IR

wavelengths. The triplet metal-to-ligand charge-transfer (^{3}MLCT) state in such systems ensures an efficient energy transfer process. The long emission lifetime of some complexes enable them to be used for the study of the energy transfer mechanism of this type of complexes.[11,12] The result showed that the energy transfer in this type of d-f complexes is mainly mediated by a Dexter-type mechanism where the donor is directly linked to the lanthanide, or where the through-space superexchange can govern a Dexter-type process, with efficient lanthanide emission at distance up to 20 Å for conjugated systems.[13]

Sensitising near-IR lanthanide luminescence

Due to the limited choices of chromophores that could be used to sensitise the emission from lanthanides that emit light at longer wavelengths, d-block metal complexes have been intensively studied as sensitizers for NIR luminescence from Er^{3+}, Nd^{3+}, Pr^{3+} and Yb^{3+} since the beginning of this century.[14] Among the transition metal chromophores, Pt complexes were found to be quite effective. Ward and Faulkner reported a covalently-attached Pt (II)-Ln (III) heteromatallic complex, whose structure is shown in Figure 1.5, where the Ln(1,3-diketone)$_3$ and the Pt (II) fragment were bound together via 5,6-dihydroxy-1,10-phenanthroline.[15] Subsequently, other polynuclear Ln_n-Pt complexes have also been investigated to study their potential application in biological imaging and telecommunication.[16–19]

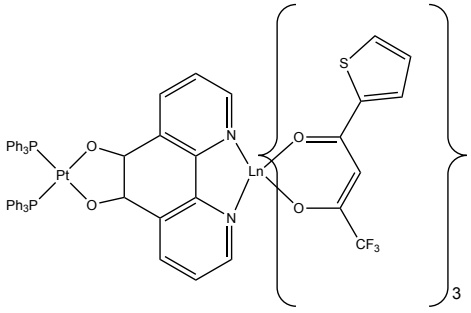

Figure 1.5: *Ln-Pt complexes in which the Pt fragment acts as an antenna to excite the NIR emission of* Ln^{3+}

1.4 Lanthanide Luminescence quenching

The quenching of the lanthanide luminescence is a very important concept in the Ln complexes. As mentioned above (Section 1.3), oscillators such as NH and OH can quench the emissive states of Ln(III) ions because of their vibrational energy which is close to the *f-f* transition energy.[20] It is a non-radiative quenching process, which subsequently results in reduced Ln(III)-centred emission intensity. The smaller the gap is between the lowest-lying lanthanide excited state and the ground level, the more efficient quenching by vibrational modes will be. O-H oscillators are found to be the most efficient at quenching lanthanide emission, resulting from the closer overlap of the vibrational states with the metal centred energy levels. Nevertheless, the luminescence of Ln complexes cannot be efficiently quenched by deuterated oscillators such as ND, OD and CH because the deuterated molecules have lower vibrational frequencies, which reduces the extent of quenching in deuterated solvents and results in longer emissive lifetimes than for their protonated equivalents. The depopulation rate of emissive states in H_2O is much faster than that in D_2O (~200 times). Ln(III) centres such as Eu(III) and Tb(III) are less likely to be quenched by the bound H_2O molecule since the energy gaps between excited and ground states are larger because their Franck-Condon overlap with higher vibrational harmonics is reduced. As a consequence of the increased rate of non-radiative relaxation, the oscillators can also significantly lengthen the luminescent lifetime of the systems.

The Ln(III) ion in aqueous solution is bound by H_2O molecules in completion of the coordination of lanthanide complexes. X-ray crystallography can be used to determine the hydration states of Ln complexes. However, it is limited by the difficulty of crystal growth and structural inconsistency between solution state and solid state. Typically,

the modified Horrocks' equation, as shown in Equation 1.1, can also be used to calculate the number of bound H_2O molecules for the Ln complexes.[21] This means that one could use the decay constant of the emissive states in time-resolved luminescence measurements for both H_2O (k_H) and D_2O (k_D) to calculate the number of inner-sphere solvent molecules, q.[21]

$$\boldsymbol{q} = A_{Ln} (k_H - k_D - B_{Ln}) \qquad 1.1$$

Constant A indicates how likely it is that lanthanide radiation will be quenched by OH oscillators, and is parameterised for each lanthanide ion. Moreover, the lanthanide emission can be quenched by the donors bound to it and solvent molecules in the outer sphere. Therefore, the constant *B*, as an empirical correction factor in the equation, was introduced representing the quenching effect from all outer-sphere solvent oscillators. Values of A and B for Eu(III) and Tb(III) are tabulated in Table 1.2.[22]

Table 1.2: *Factors of A and B used in the Horrocks' equation in aqueous solution*

	A	B
Eu	1.2 ms	0.25 ms^{-1}
Tb	5 ms	0.06 ms^{-1}

1.5 Lanthanide as luminescent probes

In this section, the application of lanthanides as luminescent probes is introduced and discussed. Ln-containing compounds have been studied extensively over the years focusing on their luminescence properties. Time-resolved luminescence techniques can be used to remove all short-lived fluorescence signal from the system background, leaving the long-lived signal displayed by the lanthanide probe. Upon adopting this

technique, the signal-to-noise ratio of the signals obtained can be reduced to the extent that analyte concentrations can be detected to the femtomolar level. A graphical presentation is shown in Figure 1.6 about applying a delay time in a complex biological matrix which enables the detection of lanthanide luminescence.[23]

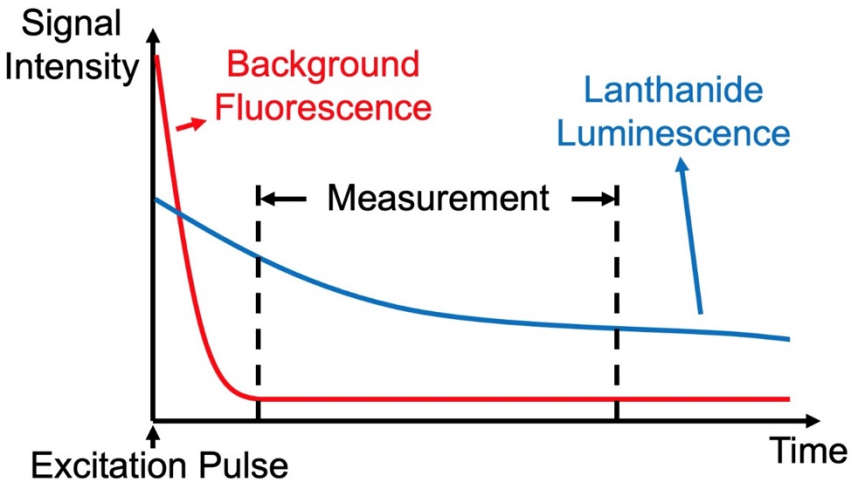

***Figure 1.6**: Time-resolved detection of Lanthanide luminescent signal modified from reference 23*[23] *. The measurement take place after a delay of the excitation pulse. This allows the decay of all short-lived processes and the detection of only long-lived luminescence during the acquisition time.*

Lanthanide luminescence, as introduced in previous sections, involves a series of complex energy-transfer processes. Therefore, changes in each step of those processes can lead to the modulation of the luminescence signals. Different strategies are employed to develop responsive luminescent lanthanide complexes, the principle behind the design is the modulation of sensitisation pathways of Ln(III) centred emission via external analytes. In the first mechanism, analytes can directly interact with the Ln(III) ion, modulating the luminescent intensity or lifetime. The second method involves perturbation in the excited states of the sensitising chromophore, which then affects the energy transfer between the chromophore and Ln(III). In the third mechanism, the analytes can act as sensitizer for the Ln(III) luminescence, thus

the presence of the analytes populates the Ln(III) emissive states.

Responsive Ln(III) complexes have been developed to detect changes in pH[22,24,25] or presence of other anions (F^-, PO_4^{3-}, CO_3^{2-}),[26–28] cations (Zn^{2+}, K^+, Na^+),[29–31] and even macromolecular biological substrates (proteins, DNA). There are a range of important properties that the Ln(III) probes need to possess to achieve the sensing process, such as good aqueous solubilities, long excitation wavelength (visible range), and, most importantly, thermodynamic stabilities and high kinetic rates.

1.6 Paramagnetic NMR / Lanthanide as MRI contrast agent

1.6.1 Introduction of MRI imaging

Magnetic resonance imaging (MRI) has revolutionised medicine and soft tissue imaging over the past few decades. This technique probes the local magnetic field around a nucleus, by applying a constant magnetic field (B_0) to the sample, which aligns the nuclear spin populations, then a radio-frequency (RF) pulse is applied perpendicular to B_0. The RF pulse transfers the magnetization away from equilibrium. The realignment to B_0 results in emission of a radio-frequency signal which is recorded. The frequency of this signal is dependent on the effective magnetic field at the nucleus, which is used to indicate the chemical environment. MR-active nuclei must have non-zero spin to possess a nuclear magnetic moment, these include ^1H, ^{13}C, ^{19}F and ^{31}P (spin, I = ½). In the case of biological samples, the vast majority of the MR- active nuclei present belong to protons in water. Thus, MRI utilises proton relaxation times to probe biological environments, as the relaxation of the water molecules from the aligned state

is highly dependent on their environment. There are two kinds of relaxation time:[32]

(a) The spin-lattice, or longitudinal, relaxation time, T_1: a measure of the time taken for the nucleus to return to equilibrium after the applied RF pulse. Essentially T_1 determines how often an experiment can be repeated.

(b) The spin-spin relaxation time, or transverse time T_2: describe the time taken for the nuclear spins to diphase. T_2 determines the rate at which the signal dies away.

Relaxation times enable differentiation of biological tissue in images. Various relaxation-based pulse sequences in MRI can be used to generate contrast and highlight specific biological features. MRI contrast agents – such as lanthanide-based complexes can be used to shorten the relaxation time which enhances the contrast.

For example, contrast agents like gadolinium complexes are widely used in acquisition and interpretation of MRI.[33] Gd(III) process seven unpaired electrons, isotropic electronic distribution which confers relatively slow electronic relaxation rates and no paramagnetically induced chemical shift. Rapid exchange of bound solvent with bulk solvent gives rise to a single peak for which the weighted average chemical shift is indistinguishable from bulk water under the conditions of an MRI experiment. These properties, combined with the chemical stability of gadolinium(III), make gadolinium contrast agents ideal for the purposes of imaging – provided that issues of toxicity of the free metal can be dealt with by encapsulation into stable complexes (a topic that we will discuss in detail later in this chapter)

1.6.2 Relaxivity

It is necessary to introduce the concept and details of relaxivity when it comes to the effectiveness of complexes as contrast agents. Because of the isotropic ground state of

seven unpaired f-electrons of gadolinium, it is mainly used as a T_1 contrast agent. The relaxivity (r_1) of a contrast agent is defined as the relaxation rate ($R_1 = 1/T_1$) per mmol of Gd. Therefore, the relaxivity is independent with respect to concentration, and it is used to compare between different contrast agents. The larger relaxivities per mmol of Gd indicate the complexes to be better contrast agents, which also means one can obtain decent images with lower concentrations of contrast agent.

T_1 can be influenced by both diamagnetic and paramagnetic contributions, as shown in Equation 1.2. T_1^{dia} is equivalent to relaxation time of the molecule with no contrast agent, while the paramagnetic relaxation can be divided up into inner-sphere and outer-sphere components (Equation 1.3).[34] Outer sphere molecules are more numerous than inner sphere molecules and they tend to exchange more rapidly with bulk solvent, thus complexes with q = 0 give rise to a significant enhancement in contrast as the solvation of the molecule is considered as a whole.[35] The first approximation adopted here is that the outer-sphere contribution is likely to be similar for all complexes in current use, considering the similarity in their structures. However, there is expected to be a much greater contribution for the inner-sphere solvent molecules such as H_2O directly bound to the Gd centre in the rapid exchanging environment on the NMR timescale. The following equations gives the relationship between T_1^{IS} and the number of inner-sphere H_2O molecules, q is shown in Equation 1.4.

$$(1/T_i)_{obs} = (1/T_i)_{dia} + (1/T_i)_{para} \qquad i=1,2 \tag{1.2}$$

$$(1/T_i)_{para} = (1/T_1^{IS}) + (1/T_1^{OS}) \tag{1.3}$$

$$\frac{1}{T_1^{IS}} = \frac{qP_m}{T_{1m} + \tau_m} \tag{1.4}$$

In Equation 1.4 P_m is the molar fraction of coordinated solvent molecules with respect to the total solvent molecules which relates to the concentration of the complex, T_{1m} is the enhancement in relaxation rate for a bound solvent molecule, and τ_m is the

residence lifetime of a coordinated solvent molecule which is the reciprocal of the exchange rate of the bound solvent molecules.[34,36,37] Therefore, it is worth noting that the number of inner-sphere solvent molecules bound to an individual Gd complex is related to the magnitude of the relaxivity (though equation 1.4 may oversimplify the situation, as it assumes that all bound water molecules have the same residence time). Moreover, T_{1m} plays the major role in the observed relaxivity in the case when $T_{1m} >> \tau_m$.

1.6.3 Safety

The toxicity of contrast agent is an important factor for the use *in vivo*.[38,39] Therefore, Gd(III) must be complexed in such a way as to maintain the enhancement of MRI but minimise toxicity. If the gadolinium contrast agents have poor blood stream clearance and poor kinetic stability, this will result in free Gd(III) ions being released from chelated complexes. As free Gd(III) ions are of a similar size to calcium(II) ions this can disturb Ca(II) - mediated signalling processes. Free Gd(III) ions can also induce colloidal precipitate formation and accretion in membranes.[40] In 2006, several studies demonstrated a link between gadolinium contrast agents and nephrogenic systemic fibrosis (NSF) in patients.[41,42]

Approval for the three least kinetically stable commercial contrast agents (Gd.DTPA, Gd.DTPA-BMA, Gd.DTPA-BMEA, in which the ligands are all linear) were withdrawn by the FDA in 2010, as the highest number of NSF cases was associated with these linear contrast agents.[43–45] The FDA also introduced a box safety warning on all contrast agents, advising against over dosing and repeat dosing. Since the introduction of the warning, patient with reduced kidney function need to be assessed before the use of Gd contrast agents, and this action has helped to reduce cases of NSF

significantly.[46]

Increasing evidence since 2013 also shows that Gd(III) contrast agents can be irreversibly retained in the central nervous system (CNS).[47–49] This finding was observed with all Gd contrast agents, while there are significantly higher incidents of Gd(III) deposition from linear contrast agents.[50] As a result, in 2017, the European Medical Agency (EMA) reviewed the Gd contrast agents, leading to the suspension of two contrast agents Omniscan® and Optimark®; and restriction of two agents: Multihance® to liver imaging, and Magnevist® to low concentration intra-articular imaging.[51] The FDA also required new warnings regarding the accumulation of Gd in the brain.[52]

Due to the safety concern of the Gd contrast agents, the Gd agents need to have both high thermodynamic stability and kinetic inertness and remain intact for the duration of their residence within the patient. The stability of chelated lanthanide complexes will be discussed in Section 1.8.

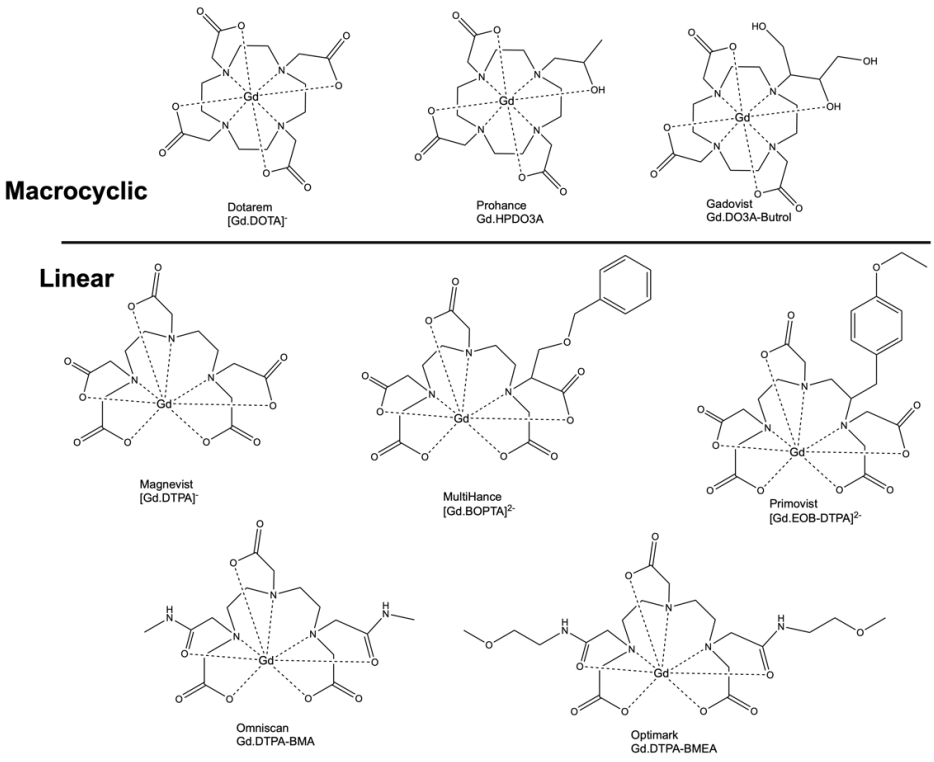

Figure 1.7: Structure of commercially available Gd contrast agents for MRI.

1.7 Magnetic properties and NMR/Paramagnetic NMR

The NMR spectra of most of the Ln-containing systems are influenced by their paramagnetic properties. The Ln-induced shift (LIS, $\Delta\omega$) is given by the sum of the diamagnetic shift (Δd) and the hyperfine shift. The hyperfine shift is defined as the difference in chemical shift of the nucleus between the paramagnetic and the corresponding diamagnetic system. It consists of contact shift (Δc) and pseudo-contact shift (Δp). The contact shift originates from interactions through chemical bonds. Generally, it is a relatively small contribution in Ln complexes since the f-orbitals influence the overlap between the Ln centre and the corresponding nucleus.[53] On the other hand, the pseudo-contact shift resulting from the dipole-dipole interactions through space usually is the dominating contribution due to the local magnetic field created by the magnetic anisotropy of the paramagnetic centre.

$$\Delta\omega = \Delta_d + \Delta_c + \Delta_p \qquad 1.5$$

where the diamagnetic shift Δ_d is the variation in chemical shift of the ligand proton in the process of complexation between the Ln(III) ion and free ligand. It is worth noting that Δ_d only contributes to a small share in the shift difference since the structural changes of complexes are relatively more influential than the diamagnetic parts such as for Lu(III) complexes. The contact shift Δ_c, also known as the *Fermi contact shift*, originates from the charge density of unpaired electrons via spin polarisation at the given nucleus. Δ_c results from the through-bond spin coupling between the unpaired electron orbitals and the nucleus. The paramagnetic metal centre can be several chemical bonds away, or longer if the chemical bonds contain π character. Therefore,

Δ_c can reflect information about the bonding structure.[54] Moreover, in the complexes, Δ_c from the paramagnetic Ln(III) ion can be calculated by:

$$\Delta_c = \frac{-A \cdot \langle S_2 \rangle_j}{h \cdot \gamma_l \cdot B_o} \quad 1.6$$

The pseudo-contact shift Δ_p differs from another contributions and derives from the same unpaired electron, though via a different mechanism. It usually relates to the paramagnetic shift in the NMR spectra of Ln complexes, and it is caused by the coupling between nuclear dipole moment and electron dipole moment. Bleaney in 1972 first proposed the equation to estimate Δ_p in a paramagnetic Ln-containing system,[55] and it is based on the assumption of larger magnitude of J states split by the ligand field in comparison to kT. The expression can be written as following:

$$\Delta_p = \frac{2\beta^2 D}{60k^2T^2}\left(\frac{\langle r^2 \rangle A_2^0(3cos^2\theta - 1) + (r^2)A_2^2(sin^2\theta cos2\varphi)}{r^3}\right) \quad 1.7$$

where β is the Bohr magneton, k is the Boltzmann constant, ϕ, θ are the angles involving the nucleus being observed, the lanthanide ion and the external magnetic field, as shown Figure 1.8, $\langle r^2 \rangle A_2^0$ and $\langle r^2 \rangle A_2^2$ parameters are crystal field terms originated from the polarisability of ligand donor and the symmetry features of the system. The coefficient C_j determines the sign of hyperfine shift, and it relates to the magnetic susceptibility. Equation 1.7 can be simplified as following for a system featuring axial symmetry characters.

$$\Delta_p = \frac{2\beta^2 C_j}{60k^2T^2}\left(\frac{\langle r^2 \rangle A_2^0(3cos^2\theta - 1)}{r^3}\right) \quad 1.8$$

It is worth noting that the relative angle and position of the nucleus to the Ln ion are only adopted in the determination of Δ_p. Moreover, the magnitude of Δ_p depends primarily on the distance between nucleus of interest and the Ln ion.

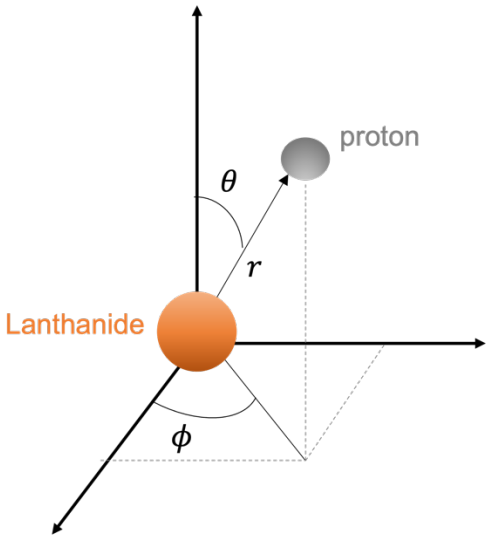

Figure 1.8: *Lanthanide induced shift as a function of angle (θ, ϕ) and distance (r) of the nucleus. The paramagnetic centre is located at the origin of the axes. The direction of the external magnetic is parallel to the z axis.*

However, as reported by Aime *et al.*,[56] the pseudo-contact part of the paramagnetic shifts of Ln complexes can be recognised as the dominating contributor of paramagnetic effect despite the fact that the previously introduced two factors are both present in the paramagnetic effect.

Blackburn *et al.*[57,58] demonstrated that the Bleaney analysis is a useful method when analysing the behaviours of solution composed of the Yb(III) complex with DTMA ligand, (where DTMA = DOTA tetrakis-methylamide). Nevertheless, Parker *et al.*[6] showed the limits of the Bleaney's theory in describing the magnetic anisotropy of a number of Ln complexes with low symmetry. Furthermore, they noted three assumptions for this theory to be applied to Ln complexes containing DO3A. First, in systems with low symmetry, terms for higher-ordered crystal field are important and influential. Thus, upon performing a Bleaney analysis, one is advised to include the contribution of higher-ordered crystal field terms.[59] Second, considering the electron

distribution of Ln(III) ion as a point charge is an over-simplification. It is more appropriate to regard the electron distribution to be in prolate or oblate shape depending on the coordination environment of each Ln atom.[60] Last, this theory uses the total angular momentum quantum number J, derived from the spin-orbit coupling, to determine the Bleaney coefficient C_j. In certain cases, using the J-mixing instead of J is more appropriate in the case where the spin-orbit coupling energy is of similar magnitude to that of the ligand field.

1.7.1 Structural aspects derived from NMR spectroscopy

Since the activation energy barrier to the interconversion is relatively high, the octadentate isomer structures, *e.g.* DOTA, are mostly in slow exchange (as shown in Figure1.9). The SAP isomer is generally the major component. However, the overall composition will depend on conditions such as the temperature, solvent, and structural changes of the complex.[61] For heptadentate DO3A complexes, due to a lower activation energy barrier to the interconversion, the SAP and TSAP isomers are more likely to be in fast exchange on the NMR timescale, leading to broader NMR peaks.[62] The asymmetry of DO3A complexes also leads to NMR spectra being more difficult to assign in comparison to C4 symmetric systems such as DOTA. For axial symmetric complexes, the largest Ln-induced shift of TSAP axial protons is generally recognised to be smaller than that of the equivalent counterpart for the SAP isomer.[63,64] This is because the TSAP isomer has a larger angle (θ) at the z axis, which also leads to a larger Δ_p. Furthermore, structures of the complexes also result in faster water exchange rate for TSAP isomers in comparison with SAP isomers at the Gd centre, which can make purification of the TSAP isomer beneficial to enhancing relaxivity.[65]

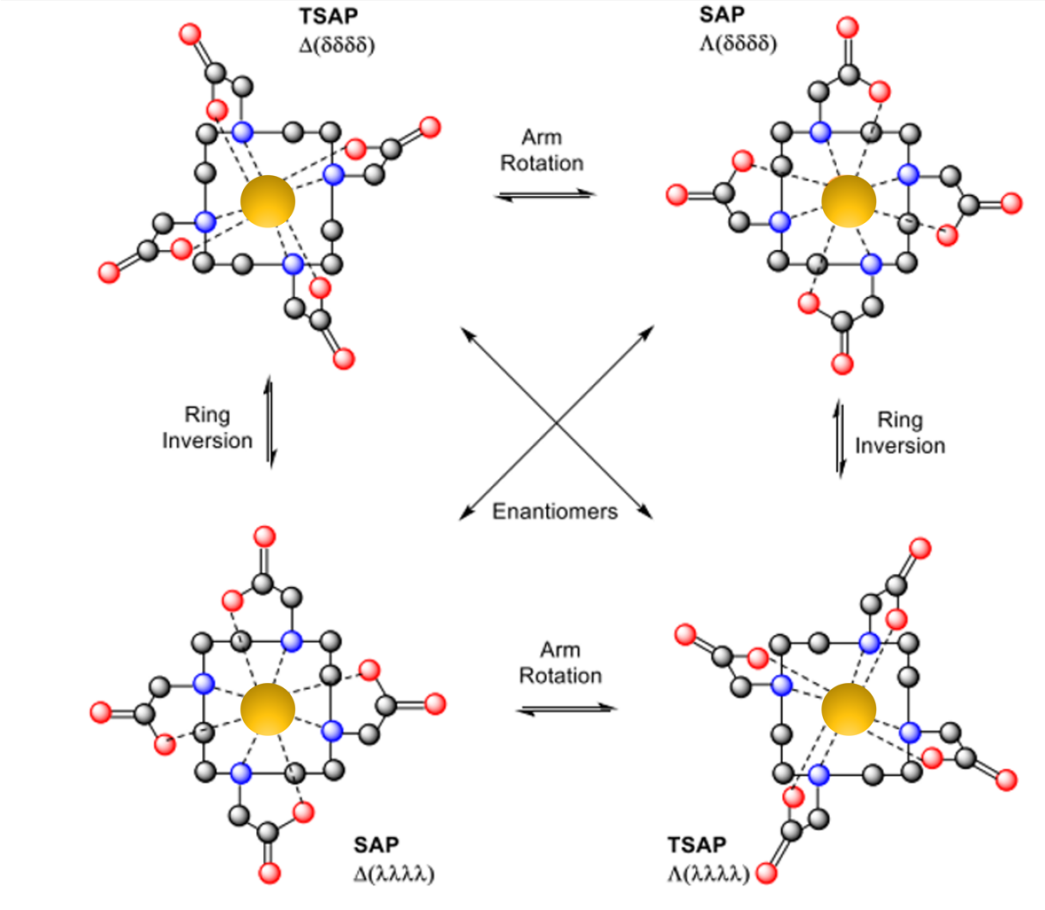

Figure 1.9: *Representation of possible diastereoisomers of [Ln.DOTA]⁻ complexes and the mechanism of interconversion. Image adapted from literature.*[35]

1.8 Stability of Ln complexes

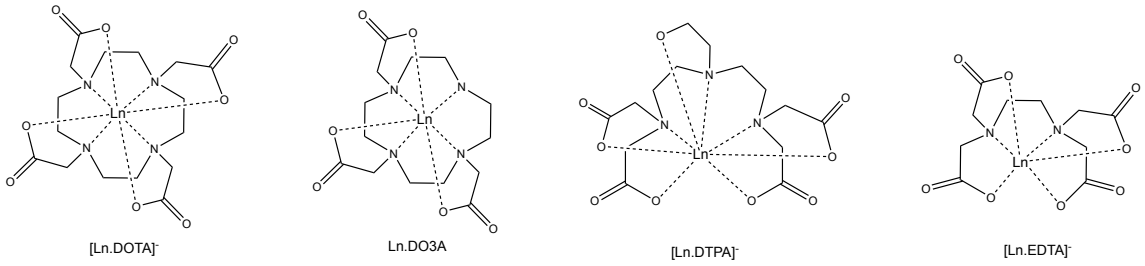

Figure 1.10: *Representation of 4 common lanthanide complexes which will be discussed in this section.*

In this section, the stability of the lanthanide complexes is introduced, which is regarded as primary importance especially when it comes to the design of Ln complexes for *in vivo* use. The range of the coordination numbers of Ln ion is from 2 to 12, in which the most common ones are 8 and 9. In the preparation process, to avoid demetallation, the Ln ion needs to be tightly coordinated in the corresponding chelate ligand. The non-bonding 4f orbitals and high oxidation state contribute to the special properties of Ln ions, and the bonding of Ln ions is predominantly ionic in character, which means the hard donor atoms such as O and N are more favourable as the bonding atoms of the ligands. Furthermore, the exchange between ligand and metal is extremely fast due to the ionic nature of 4*f*-elements.[39,66] Using ligands with chelating arms arranged around the Ln(III) ion can significantly overcome the intrinsic lability of the Ln(III) ions. Adopting hard donor atoms in the macrocyclic chelating ligand can further enhance the thermodynamic stability of the Ln complexes and minimise the possibility of demetallation due to the strong ionic interaction between the metal and ligand. Whilst linear (acyclic) ligands can dissociate from the Ln ion by removing one donor atom at a time, dissociation of macrocyclic ligands requires all donor atoms to be removed at the same time, requiring a much higher activation energy.

1.8.1 Thermodynamic Stability

The thermodynamic stability can be represented by the stability constant which is defined as the equilibrium constant of the complexation reaction. The thermodynamic stability constant can be calculated based on the concentration values of all species in solution, as shown in Equation 1.9:

$$K_{therm} = \frac{[LnL]}{[Ln^{3+}][L]} \quad 1.9$$

However, an important assumption for applying the thermodynamic stability constant is that the ligand is fully protonated in the solution. Therefore, in the case of a physiological environment, the thermodynamic stability constant is not applicable. Hence, under physiological conditions another indicator, the conditional thermodynamic stability constant, is introduced to predict the thermodynamic stability of Ln complexes. For the use of Ln complexes at physiological pH 7.4, by considering which level the ligand will be protonated at this pH, the relationship can be demonstrated as Equation 1.10:

$$K_{therm} = \frac{[LnL][H^+]^n}{[Ln^{3+}][H_nL]} \quad 1.10$$

In Table 1.3, the thermodynamic properties of several common Ln(III) ions and representative chelators are presented. Complexes of the aminopolycarboxylate ligands (EDTA, DPTA and DOTA) show good thermodynamic stability since the ligands are hard donors. Moreover, less steric hindrance while encapsulating the Ln ion also plays an important role in the nature of thermodynamic stability, despite the decresse in entropy which originates from the flexible arms of ligands which are constrained by complexation.

Table 1.3*: Thermodynamic stability constants for examples of linear and macrocyclic ligands with Ln(III) ions.*

	EDTA[67]	DPTA[67]	DOTA[68]
La(III)	15.5	19.5	22.9
Eu(III)	17.3	22.5	23.5
Gd(III)	17.4	22.5	24.7
Tb(III)	17.9	22.7	24.2
Lu(III)	19.9	22.4	25.4

As shown in the first column of Table 1.3, the stability of EDTA-based Ln complexes depends on the charge density of the corresponding Ln centre. This can be contributed to the increase in electrostatic interaction between the Ln(III) and the ligand, resulting from the changes in charge density across the Ln series. When it comes to the DTPA-based complexes, the same trend of increased thermodynamic stability persists until the stability reaches a maximum value at around Tb(III).

The DOTA-based Ln complexes generally possesses better thermodynamic stability among the three ligands shown in Table 1.3. This can be rationalised by the fact that the overall increase in thermodynamic stability of $[Ln.DOTA]^-$ complexes results from the pre-organised macrocyclic nature of DOTA ligands, which means less energy is required to rearrange the ligand to forming the chelate for the Ln(III) ions.

1.8.2 Kinetic Stability

Kinetic stability is an important factor in evaluating the stability of complexes in solution. Ln(III) ions are generally kinetically unstable, with exchange rates with water around the order of 10^9 s^{-1}.[69] Ln complexes with aminopolycarboxylate ligands have been extensively studied, especially for Gd complexes, since they are used as MRI contrast agents. The kinetic stability of Ln complexes depends on several factors such the rigidity of ligand, pH in water and the temperature. The formation of Ln(III) complexes with a flexible chain ligand such as EDTA is much faster than for macrocyclic ligands like DOTA (structure of Ln.EDTA and Ln.DOTA is shown in Figure 1.10). The formation of [Ln.EDTA] complexes consists of a rapid forming step of an intermediate and a slow rearrangement step of the total structure.[39] On contrary, the complexation of DOTA-based (macrocyclic) Ln complexes involves a mechanism

with three steps outlined below, which has been elucidated by potentiometry, luminescence spectrometry and EXAFS. The first step is the fast formation of the intermediate $LnH_2DOTA(H_2O)_5$ by coordinating to the acetate arms outside the cavity. Coordination to two nitrogen atoms and concerted proton transfer to two carboxylate arms follow in the first slow rate determining step forming $LnH_2DOTA(H_2O)_3$. In the third step, the Ln(III) ion moves into the ligand cavity and coordinates to the four nitrogen atoms after a concerted rearrangement. Simultaneously, the last H atom is removed, which is the second rate-determining step, to yield the final product $[Ln.DOTA]^-$. In this step, the four nitrogen atoms and four oxygen atoms are finally bound to the Ln(III) ion.[70,71] It is worth noting that the local pH has an impact on the formation rate of the complex. The pH of the mixture drops dramatically after the Ln salt is added and continues to slowly decrease for 48 hours. After stirring for three to four days, the pH of the mixture decreases gradually, remaining constant after 7 weeks. Therefore, the complexation rate can be optimised for pH lower than 7 since it enables the deprotonation of intermediate and avoids the formation of the Ln hydroxide precipitates.

While investigating the kinetics of the formation of Ln complexes, it is also importance to consider and study the dissociation of Ln complexes, which is influenced by several competing factors: including precipitation of Ln hydroxide salt and competition from other cations such as Zn(II), Cu(II). Transmetallation of linear chelates with Zn(II) or Cu(II) in phosphate buffer has been found to be the most significant for Gd.DTPA-BMA, followed by Gd.DTPA and then Gd.BOPTA.[72,73] Moreover, the transmetallation rate of acyclic complexes such as $[Gd.DTPA]^{2-}$ correlates with the concentration of Zn(II) ion, which confirms the direct attack of the complex by another cation.[74] The structure of complexes was demonstrated in Figure

1.7 and 1.10. On the other hand, for EDTA-based Ln complexes, the proton-involved mechanism primarily dominates the dissociation process instead of being attacked directly by competitive cations since all acetate arms are hindered resulting in the inaccessibility to the cavity.[74]

***Table 1.4**: Kinetic stability constants (K_{obs}) and percentage release of Gd(III) in human serum at pH 7.4 after 15 days.*[38,39,75,76]

Contrast Agent	k_{obs} (s^{-1})	% Release in human serum
Gd.DTPA (Magnevist®)	1.2×10^{-3}	1.9
Gd.DTPA-BMA (Omniscan®)	2.0×10^{-2}	20
Gd.DO3A (Not clinically approved)	2.3×10^{-3}	-
Gd.HP-DO3A (ProHance®)	6.3×10^{-5}	<0.1
Gd.DOTA (Dotarem®)	2.1×10^{-5}	<0.1

It is shown in Table 1.4 that the Gd complexes of a macrocyclic ligand (DO3A/DOTA) exhibit enhanced kinetic stability in comparison to those of an acyclic ligand (DTPA). Brücher *et al.* reported the dominance of the transmetallation of Gd(III) complexes under physiological conditions and the accelerated exchange rate of $[Gd.DTPA]^{2-}$ with Cu(II) while endogenous anions are present such as citrate, carbonate and phosphate.[26,77] The transmetallation rate of $[Gd.DOTA]^{-}$ is not affected by the acid-catalysed dissociation at the level of physiological pH.[71] The DOTA-based complexes benefit from extra contribution of kinetic stability originating from the macrocyclic effect of DOTA compared to acyclic chelates such as DTPA.

The kinetic stability of Gd-DO3A complexes has been thoroughly reviewed by Long *et al.* They also reported that the kinetic stability of Gd(III) chelates depends

substantially on the their appended arms, and the coordination number of the ligand does not obviously affect the total kinetic stability.[78] The reduction in kinetic inertness of Gd(III) complexes is prevented by the strong coordination of pendant arm to the Gd(III) centre due to the decrease in the number of coordination. It is worth noting that the ligand backbone could be less strong by the alkylation of fourth position on the cyclen nitrogen with a bulky group. This would hold the Gd(III) ion in a tighter cavity position and increase the kinetic inertness of the chelates. The hydration state reduction upon N-alkylation leads to enhanced steric hindrance in the ligand cavity.

1.9 General Platinum Properties

In this section, the general properties of platinum are introduced based on its physical and chemical nature. There are six natural isotopes for platinum: ^{190}Pt, ^{192}Pt, ^{194}Pt, ^{195}Pt, ^{196}Pt, and ^{198}Pt with the most abundant one being ^{195}Pt, which makes up 33.83% of total Pt abundance as shown in Table 1.5.

Table 1.5*: Natural platinum isotopes and nuclear spin quantum number*

Isotopes	Natural Abundance	Nuclear Spin Quantum Number (I)
^{190}Pt	0.01%	I = 0
^{192}Pt	0.078%	I = 0
^{194}Pt	32.9%	I = 0
^{195}Pt	33.8%	I = 1/2
^{196}Pt	25.3%	I = 0
^{198}Pt	7.21%	I = 0

Furthermore, ^{195}Pt is the only Pt isotope with NMR activity as shown in Table 1.2 due to its nuclear spin quantum number I = ½. Since all other isotopes of Platinum have

zero nuclear spin quantum number, the NMR spectroscopy of ^{195}Pt is of wide and effective use both in direct observation of ^{195}Pt resonance and of the "satellites" of ^{195}Pt. It is worth noting that the term of "Pt satellites" is defined to describe the NMR resonance of a nucleus coupled to ^{195}Pt which splits into a symmetrical doublet around the central resonance which results from species with all the other Pt isotopes. Relatively, the ratio of intensities of the NMR resonances is roughly 1:4:1 as shown in Figure 1.11.[79,80]

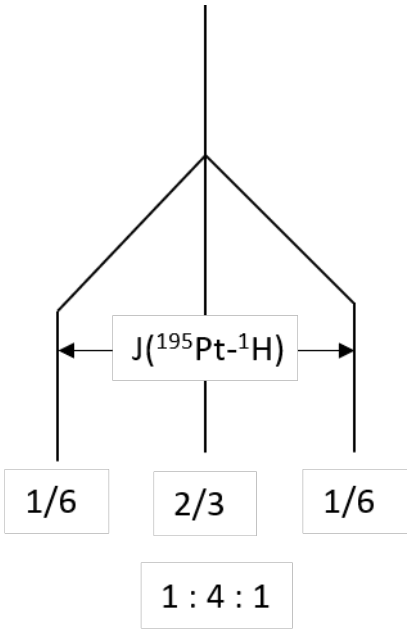

Figure 1.11: *A demonstration of ^{195}Pt – ^{1}H satellites.*

1.10 Coordination chemistry of platinum complexes

The coordination-related properties of platinum complexes based on the oxidation states of Pt are introduced in this section. The most common oxidation states for Pt are +2 and +4, though platinum can exhibit in oxidation states from 0 to +6.[79,81] It is worth noting that the +1 and +3 oxidation states of Pt generally exist in molecules with M–M bonds. The +2 oxidation state strongly favours square-planar geometry, with a

coordination number of four. The +4 oxidation state of Pt typically is found in octahedral systems with a coordination number of six. Figure 1.12 shows the splitting of the d-orbitals for Pt(II) and Pt(IV) together with their electronic configurations with strong field ligands.

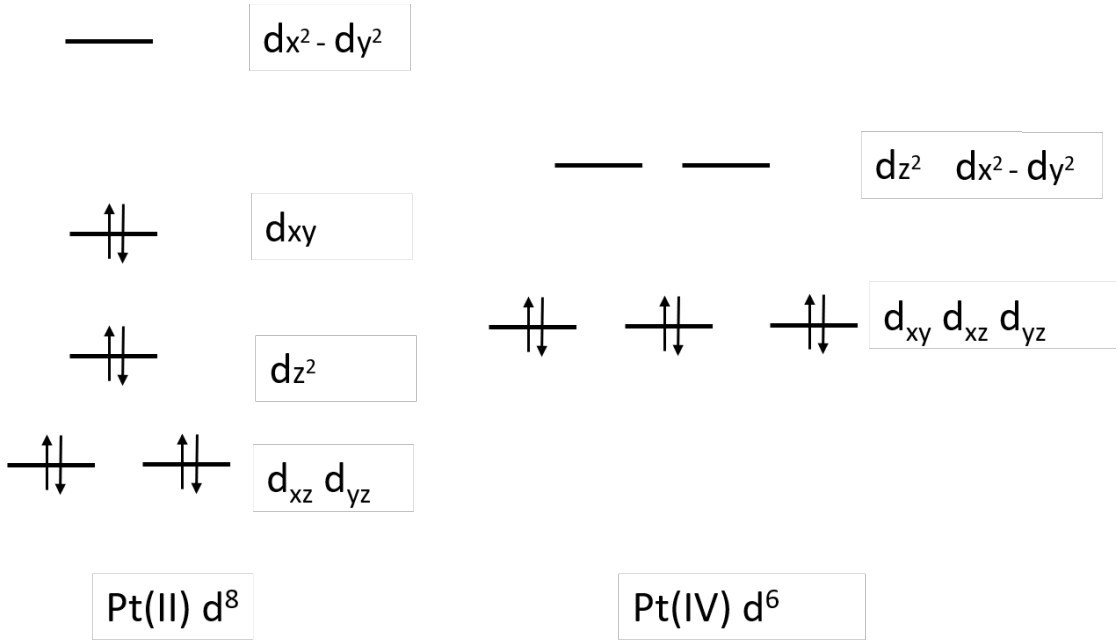

***Figure 1.12**: Splitting of the d-orbitals in crystal fields of square-planner (Pt(II), d^8) and octahedral (Pt(IV), d^6) symmetries. The electrons are configured in a strong ligand field.*

Pt(II) is recognised as a "soft" acid, according to the Pearson's "soft/hard" acid/base theory, which means it is easy to be polarized and prone to form complexes with "soft" bases.[82,83] Stable Pt(II) complexes are usually formed with "soft" ligands with S or P donors and ligands which enables π-bonding such as alkynes, alkenes, NO^{2-} and CN^-. The stability of halide complexes with Pt(II) rank in the or Pt(II) also shows high affinity for some O-donor ligands such as acetates, phenoxides diketonates and carboxylates while it generally shows low affinity for "hard" (F and O) ligands.[84] Platinum(IV) with +4 oxidation state possesses a d^6 electronic configuration, and the coordination number of Pt(IV) is 6 with octahedral geometry.[84] Pt(IV) complexes are

low-spin because the splitting of d-orbitals is large thus with a large stabilisation energy of the crystal field. Based on previously introduced "hard/soft" acid/base theory, Pt(IV) is also regarded as a "soft" acid. However, it is much "harder" compared to Pt(II). Moreover, Pt(IV) complexes are generally more kinetically inert and more thermally stable than Pt(II) complexes.[79]

1.11 *Trans* effect

In this section, the concept of *trans* effect is introduced, which is important for the discussion of Pt complexes. The *trans* effect is a kinetic effect which is first systematically discussed by Chernyaev in the 1920s in the discussion of the coordination chemistry of metals, especially for Pt(II) and Pt(IV). It can be defined as the effect of which, in a metal complex, a ligand influences the rate of substitution reaction of a leaving group at the opposite position.[85] It is worth noting that this influence to the *trans* groups is larger than to the adjacent groups, or *cis* groups. The *trans* effect is a kinetic effect defined only in the substitution reaction, which is regarded as related to the corresponding transition state and the ground state. Substitution reactions of platinum complexes with square-planar geometry do not always produce the thermodynamically preferred isomer. As follows, the empirical series comparing the *trans* effect are presented based on the kinetics of substitution reactions for a range of ligands [84–86]:

$$CO,\ CN^-,\ C_2H_4 > PR_3,\ H^- > CH_3^- > R_2S > C_6H_5^-,\ NO_2^-,\ I^- > SCN^- > Br^- > Cl^- >$$
$$pyridine > NH_3 > OH^- > H_2O$$

The *trans effect* can be attributed to the combination of σ-bonding and π-bonding effects.[86] For ligand with strong σ-donor effect, such as PR_3 and H^-, they are capable to contribute a high electron density to the metal centre and thus weaken the chemical

bond for the *trans* group. On the other hand, ligands such as CO and CN^- can provide empty orbitals which has strong π-acceptor effect and draws the electron density from the metal ion to them, which makes the *trans* ligand electron-deficient and allows nucleophiles to attack the *trans* group.

The *trans-influence* can be investigated through the measurements of coupling constants by NMR spectroscopy, vibrational strength by IR spectroscopy and lengthening of bonds determined by X- ray diffraction.[85,86]

1.12 Cisplatin and its mechanism of action

In 1968, Dr B. Rosenberg accidently discovered the anticancer activity of cisplatin (*cis*-$[PtCl_2(NH_3)_2]$, also known as CDDP).[87,88] Clinical trials quickly showed its anticancer effectiveness towards solid tumours. In 1978, cisplatin was approved by the FDA for clinical use in metastatic testicular cancer and ovarian cancer.[89] Later, it was approved for other cancers such as transitional bladder cancer, lung cancer, lymphomas, myelomas and melanoma. Nowadays, it is widely and routinely applied worldwide, together with a series of additional drugs.[90,91]

Since the hydrolysis of the Cl is suppressed by the high concentration of Cl^- in the blood stream, the cisplatin stays as the neutral form after it is administered in a saline solution via blood perfusion. The cellular uptake of cisplatin takes place via passive and active transport (partly via copper transporters).[92] After the cisplatin enters a cell, where the concentration of Cl^- is significantly lower, the aquation of cisplatin takes place which leads to the DNA binding as shown in Figure 1.13.

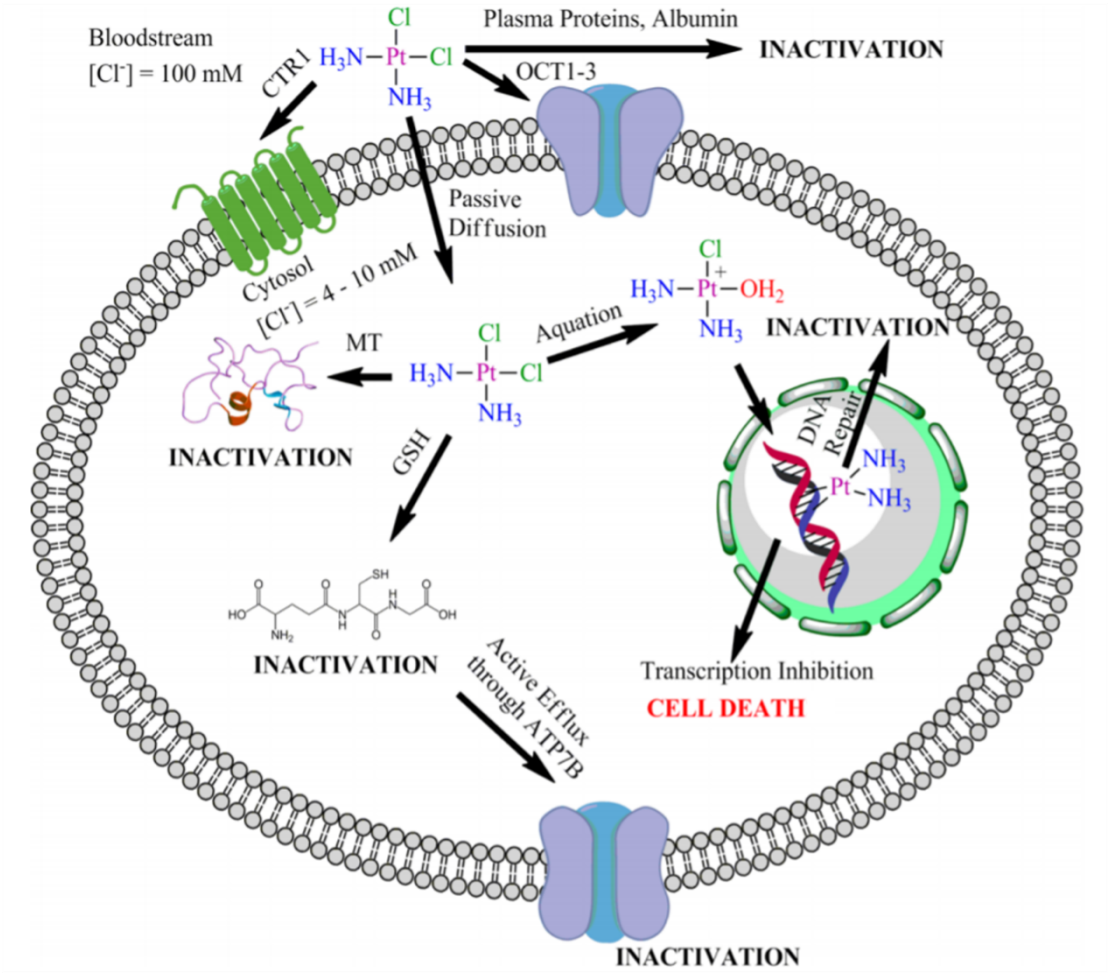

Figure 1.13: *Cellular uptake, aquation and inactivation pathways of cisplatin. Image adopted from that in reference 86.*

Nuclear DNA is the main target of cisplatin, and cisplatin can bind to two adjacent nucleobases on DNA and form intra- and inter-strand crosslinks. The majorities of crosslinks are 1,2-GpG intra-strand which accounts for 60-65% of the total amount and 1,2-ApG intrastrand takes up another 20-25%. The rest of crosslinks are the 1,3-GpXpG intrastrand which features another base between the two platinated guanines, the G-G interstrand and monofunctional adducts.[83,87] The structure of the DNA is damaged by the formation of the 1,2-intrastrand crosslinks, which disables the replication and transcription of the DNA. Furthermore, several nuclear proteins such as High Mobility Group-domain (HMG) proteins can recognise the platinum-DNA lesions. Upon binding

with those proteins, nucleotide excision repair is hindered, and subsequently this leads to cell death.[92] The structure of the DNA-cisplatin adducts are illustrated in Figure 1.14.

There are also other pathways that lead to the cytotoxicity of cisplatin. For example, cisplatin can increase the levels of reactive oxygen species (ROS), which originate from the reaction of cisplatin with -SH (thiol) containing molecules. This maintains the redox homeostasis within the cell.[94] Moreover, cisplatin can block the Thioredoxin Reductase (TrxR) enzyme, which is responsible for the reduction of disulfide bonds. TrxR is also able to alter the mitochondrial functioning and cause NADPH depletion, which thus increases in the levels of $OH\cdot$ and $O_2\cdot^-$ species.[95]

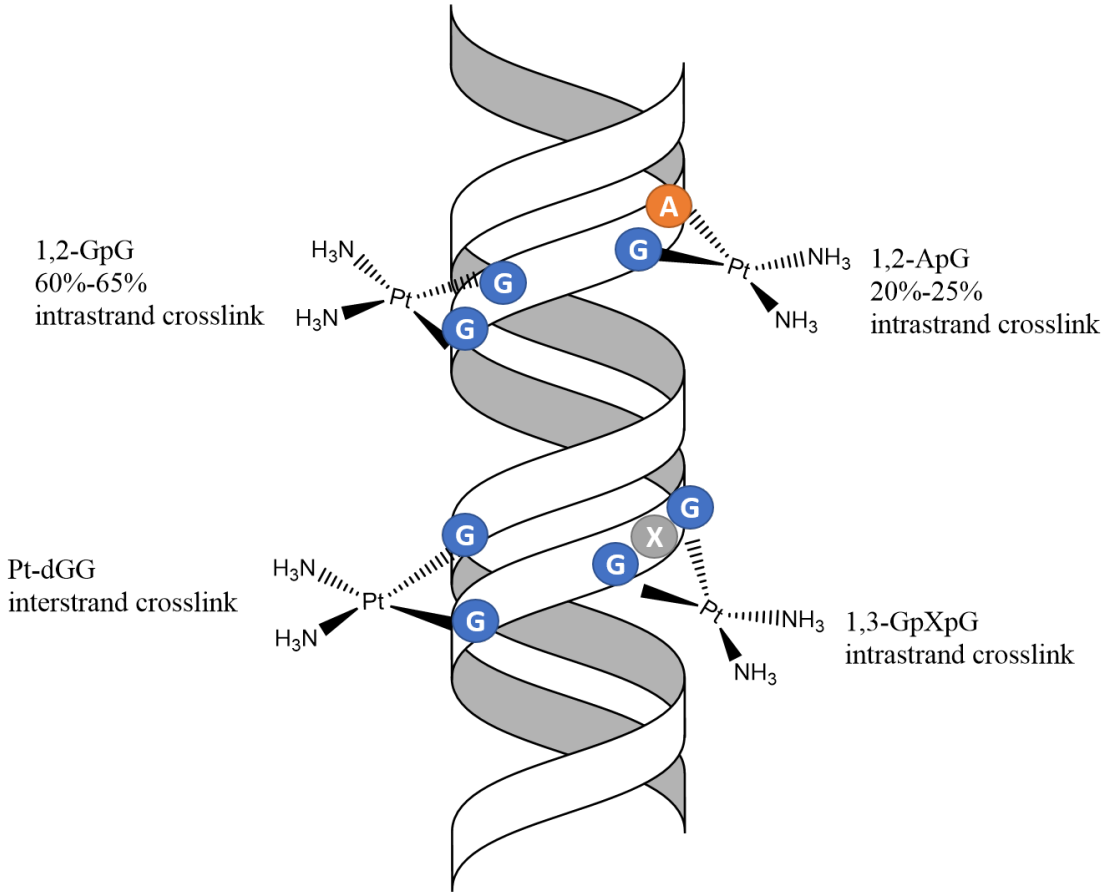

***Figure 1.14**: The common Cisplatin-DNA adducts formed.*

1.13 The limitations of cisplatin and the development of second and third generation Pt(II) anticancer drugs

In this section, the further discussion of cisplatin is presented with its drawbacks and the improvements made to develop later generations of Pt(II)-based anticancer drugs. First, despite the clinical success of cisplatin, it possesses several flaws. The first and main one is the development of resistance, which can be either inherent or acquired. The inherent resistance of cisplatin results from the intrinsic genetic instability, specifically, the spontaneous mutations during cell division. The acquired resistance of cisplatin can originate from the exposure to the chemotherapeutic agent.[95]

Moreover, some serious side-effects can be produced by using cisplatin such as nausea, nephrotoxicity, vomiting, renal toxicity, asthenia and hair loss.[95] Furthermore, cisplatin is relatively inconvenient to be administered: it is given intravenously instead of orally.[96] Essentially, the therapeutic effect of cisplatin is therefore limited which makes it necessary for the study of alternative drugs.

Alternative strategies for the development of new generation of Pt drugs have also been extensively researched from which the second and the third generation of Pt anticancer drugs were developed, by modifying the leaving group (Cl) and changing the ammines, respectively. Among the newer generations of Pt complexes, as shown in Figure 1.15, oxaliplatin, carboplatin, lobaplatin, nedaplatin, and heptaplatin have been approved clinically. The former two have been used worldwide, and the latter three have been used in Asia.[97] Carboplatin can be used for similar cancers as cisplatin with fewer side-effects, while oxaliplatin has been applied on different series of cancers with the major focus on colorectal cancer.[89] However, there are still some disadvantages for these Pt-based drugs, in which the majority are serious dose-limiting side-effects and

the development of resistance.[98] There are several other approaches to overcome the drawbacks of Pt(II)-related drugs such as targeting delivery to increase drugs that reach cancer cells, improving combination therapy and developing new drugs without cross-resistance.[89]

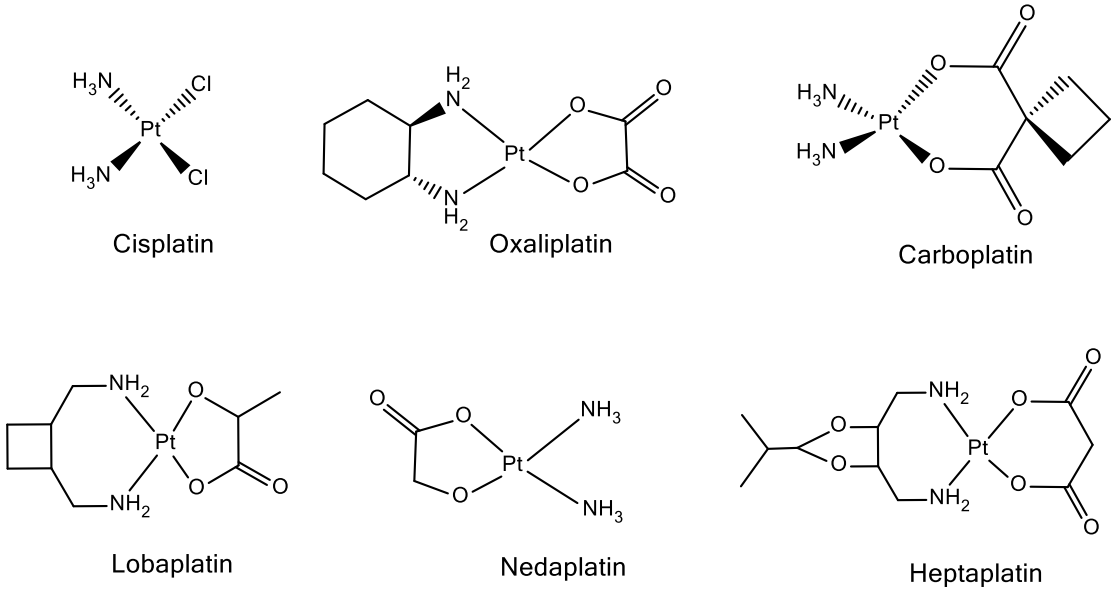

***Figure 1.15**: Pt(II)-anticancer drugs approved for clinical use.*

1.14 Pt(IV) Prodrugs

The concept of prodrugs is important in the development of drugs, especially cancer-related drugs, it is a "derivative of a drug that is metabolized or activated in the body to release or generate the active drug, ideally at the target site of specific position".[99] Prodrugs can be introduced to overcome several potential limitations of Pt(II) anticancer drugs: low permeability or lipophilicity, weak aqueous solubility, chemical instability, requirement for intravenous administration, limited membrane absorption, lack of site-specificity and over-rapid excretion.[100] There are two main pathways for developing prodrugs for cancer chemotherapy. The first aspect is cancer targeting which can result in increased permeability and accumulation of drugs. For example, the drugs can be targeted through conjugation of drugs with antibodies,[101] or polymeric

cancer cell targeting peptide carriers.[102–104] The second one is that the release of drug molecules is controlled towards the tumour site, such as the hypoxia-mediated release/immunotoxins, enzymatic cleavage and acid-promoted liberation.[99]

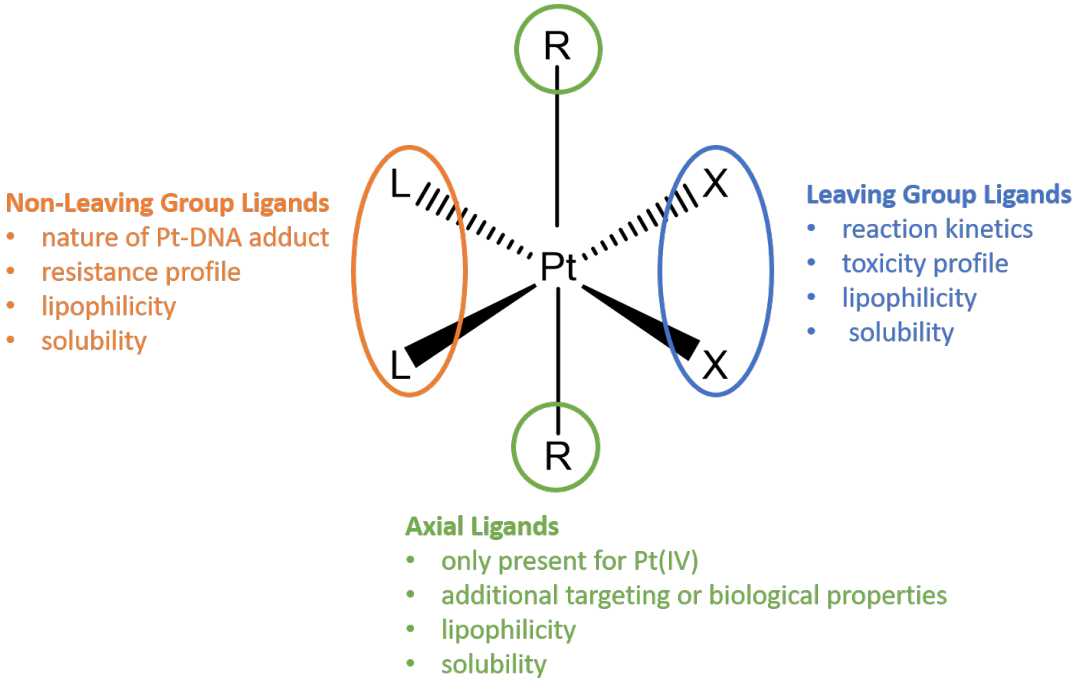

***Figure 1.16**: The generalised structure of platinum (IV) prodrugs adapted from reference104.*[105]

Pt(IV)-based drugs are recognised as an important type of prodrugs, which are a useful alternative to Pt(II) drugs to reduce treatment side-effects. The Pt(IV) prodrugs feature these advantages since they can enter the cells as Pt(IV) complexes before they are reduced to Pt(II) complexes where substitution reactions can then take place.[106,107]

Pt(IV) complexes are relatively kinetically inert compared to Pt(II) ones. Therefore, they are excellent prodrugs for Pt(II) complexes as they could avoid undergoing reactions on the way to the target area and feature a higher therapeutic index.[106] Two additional ligands of Pt(IV) complexes compared to Pt(II) counterparts enables the modification of a range of important chemical properties of Pt(II) drugs such as the aqueous solubility, lipophilicity, and reduction potential. Additionally, it can be used in

combination with other approaches such as nanoparticles and peptides to incorporate additional desirable properties. Moreover, biologically active axial ligands can be released in the target cell upon reduction.[92]

There have been four Pt(IV) drugs entering clinical trials: iproplatin, tetraplatin, satraplatin and LA-12 as shown in Figure 1.17. Iproplatin and tetraplatin have been abandoned due to the weak cytotoxicity compared to cisplatin of the former and the over-toxicity of the latter. Satraplatin is currently under clinical trials for the purpose of combination therapy,[108] and LA-12 is now in phase I of clinical trials.[109]

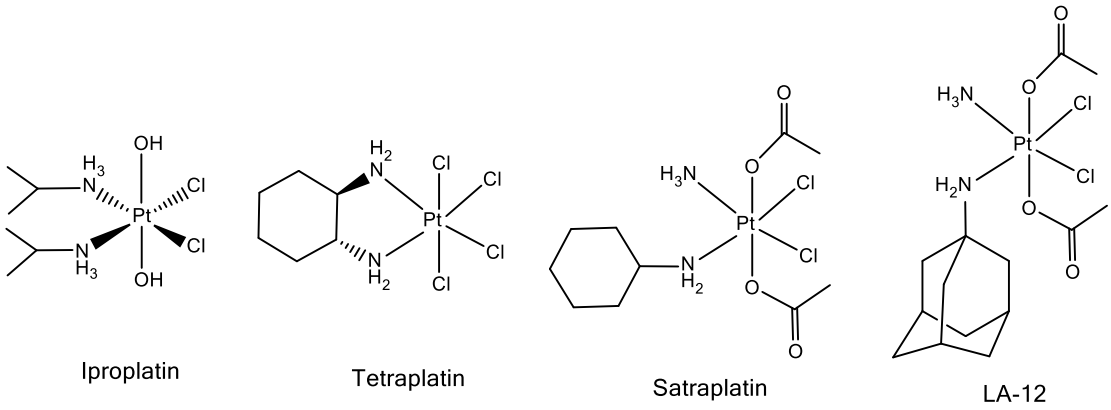

***Figure 1.17**: Pt(IV) complexes that have entered clinical trials.*

1.15 Ln-Pt Theranostic Complexes

Theranostic agents combine diagnostic and therapeutic properties within the same unit (particle or molecule) and allow direct monitoring of drugs in the body, yielding information on drug location, safety and efficiency. The development of theranostic agents and their application in drug delivery is a rapidly emerging field and is an important step toward more personalized medicine.

In this thesis, I mainly focus on Pt-Ln molecular theranostic agents. There are already several example in literature exploiting Pt-Ln theranostic agents. In 2003, Z. Pikramenou reported a hairpin-shaped Ln-Pt_2 luminescent complex which binds to

DNA.[110] The structure of the complex is shown in Figure 1.18, where the Ln(III) ion is bound to a DTPA-type ligand with two thiol arms. The Pt(II) terpyridyl moieties that are established as DNA intercalators are linked to the Ln-DTPA via the aromatic thiolates. The synthetic approach of the Ln-Pt_2 is a one-pot reaction between the DTPA ligand, $LnCl_3$ and Pt terpyridine in a 1: 1: 2 ratio. The Eu emission of the Eu-Pt_2 was quenched due to the overlap of the charge transfer absorption and its spectral region, while the Nd-Pt_2 complex shows characteristic NIR emission of Nd(III). The DNA recognition is detected by linear dichroism. In 2009, L.M. Rendina presented that the Gd version of the hairpin molecule that Pikramenou reported can effectively target the nuclei of tumour cell.[111] The cellular uptake study showed that the Gd-Pt_2 complex can accumulate in tumour cells by one order of magnitude higher than that of human endothelial cells. Intracellularly, the Gd-Pt_2 complex is found to accumulate in nuclei as a result of its propensity to bind to DNA.

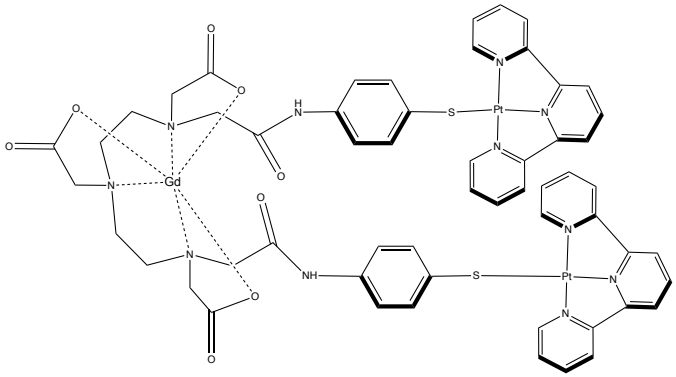

Figure 1.18: *Structure of hairpin-shaped Ln_2-Pt complex.*

There have been increasing examples of Pt-Ln theranostic agents during the past decade. For example, both Z. Guo and A.K.Patra reported modified hairpin-shaped Ln-Pt_2 complexes in 2014 and 2017 respectively.[112,113] In both of their molecules the Ln(III) ions stay in the DTPA-type cage, and the Pt fragments are linked to the Ln part via pyridine or quinoline. Guo found the Gd-Pt_2 has comparable cytotoxicity with cisplatin at high concentration ($\geq$ 0.1 mM) and its proton relaxivity is higher than that of the

commercial MRI contrast agent Gd-DTPA. Therefore, he defined the Gd-Pt_2 complexes as promising theranostic agents. The Eu-Pt_2 and Tb-Pt_2 complexes that Patra reported were found to be stable in aqueous media by ESI-MS and time-dependent UV-vis traces. Cell uptake studies using confocal microscopy showed that the complexes ultimately localise in nuclei.

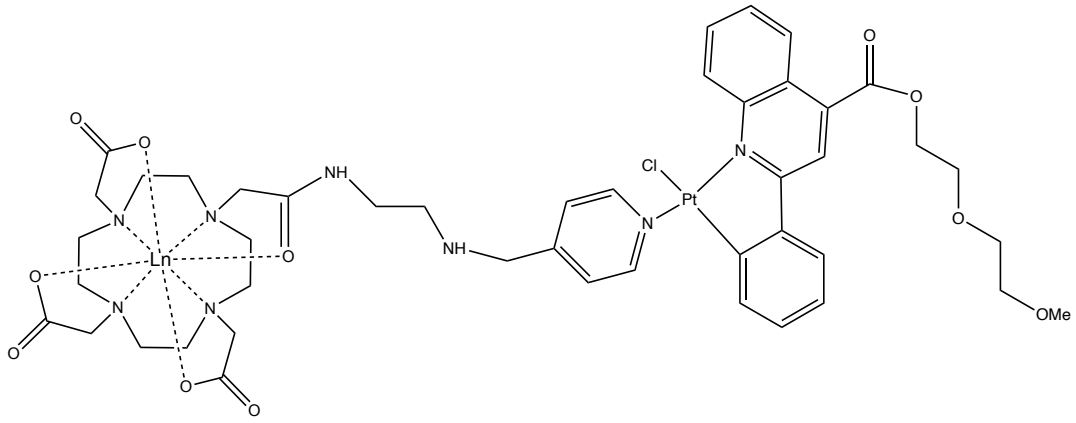

Figure 1.19*: Structure of water soluble cyclometalated Ln-Pt conjugates.*

In 2015, Pope reported a water soluble cyclometalated Ln-Pt conjugate, whose structure is shown in Figure 1.19, which shows visible luminescence and enhanced water relaxivity.[114] The confocal fluorescence microscopy reveals that the complex is poorly taken up by MCF7 cancer cells. In the same year, Wong reported a water-soluble light-responsive antitumor agent as shown in Figure 1.20. The Pt (II) moiety is found to quench the Ln emission. The excitation energy absorbed by the antenna chromophore is channelled mostly *via* intersystem charge transfer to the dissociative states of Pt and no Eu emission is detected. The dissociation of the Pt fragment can be further understood by a paper presented by P. Sadler in which the two-photon induced dissociative Pt complex has similar structure.[115] The change of Eu emission enables a real-time monitoring of cisplatin release in an off-on manner. The Gd version of this compound was reported later in 2017, which therefore has MRI or fluorescence imaging

properties depending on the choice of lanthanide. [116]

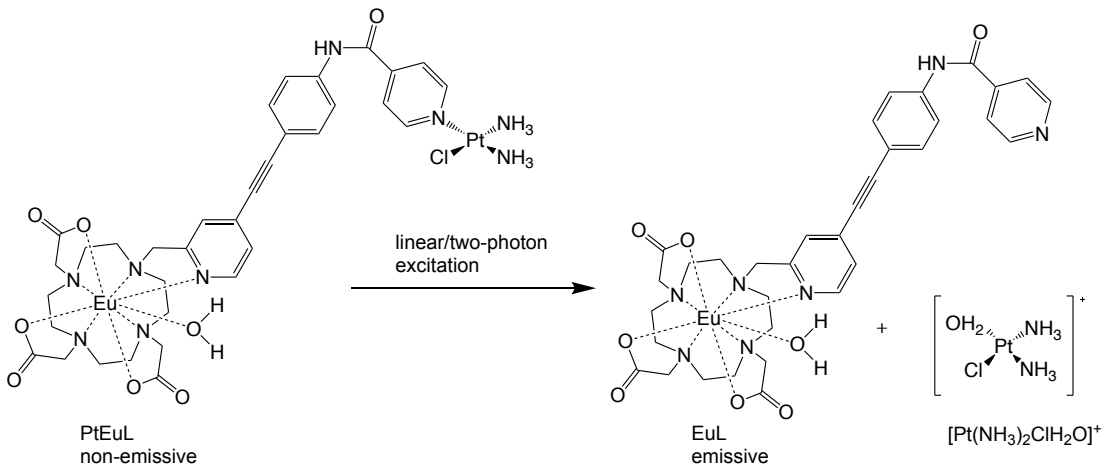

***Figure 1.20**: Schematic illustration of the photo-induced cleavage of the Eu-Pt complexes.*

1.16 Project aims

This work explores the preparation of kinetically stable Ln-Pt complexes in which the lanthanide moiety is based on the DO3A structure and is employed as an emissive/MR-active probe. The platinum moiety is a therapeutic building block with potential anti-cancer activity, with access to different oxidation states. The following chapters discuss the synthesis of the Ln-Pt conjugates, including photoactivatable complexes and "switch-on" luminescent Ln-Pt(IV) complexes. The characterisation of the properties of these compounds, and the relaxivity behavior and cellular penetration properties of the Gd complexes are discussed in detail.

Reference

1 https://www.who.int/news-room/fact-sheets/detail/c.

2 J. C. G. Bünzli and C. Piguet, *Chem. Soc. Rev.*, 2005, **34**, 1048–1077.

3 T. Terai, K. Kikuchi, S. Y. Iwasawa, T. Kawabe, Y. Hirata, Y. Urano and T. Nagano, *J. Am. Chem. Soc.*, 2006, **128**, 8699–8700.

4 W. T. Carnall, P. R. Fields, and K. Rajnak, *J. Chem. Phys.*, 1968, **3797**, 18–21.

5 J. C. G. Bünzli and C. Piguet, *Chem. Soc. Rev.*, 2005, **34**, 1048–1077.

6 A. Beeby, I. M. Clarkson, R. S. Dickins, S. Faulkner, D. Parker, L. Royle, A. S. De Sousa, J. A. G. Williams and M. Woods, *J. Chem. Soc. Perkin Trans. 2*, 1999, **2**, 493–503.

7 C. Duan, Y. Zhang, C. Ma, G. Xie and L. Hu, *J. Rare Earths*, 2010, **28**, 258–261.

8 S. J. Butler, M. Delbianco, L. Lamarque, B. K. Mcmahon, E. R. Neil, R. Pal, D. Parker, J. W. Walton and J. M. Zwier, *Dalt. Trans.*, 2015, **44**, 4791–4803.

9 O. Reany, T. Gunnlaugsson and D. Parker, *Chem. Commun.*, 2000, 473–474.

10 F. C. J. M. Van Veggel, *Angew. Chem. Int. Ed.*, 2000, **39**, 4319–4321.

11 S. Faulkner, L. S. Natrajan, W. S. Perry and D. Sykes, *Dalt. Trans.*, 2009, 3890–3899.

12 W. S. Perry, S. J. A. Pope, C. Allain, B. J. Coe, A. M. Kenwright and S. Faulkner, *Dalt. Trans.*, 2010, **39**, 10974–10983.

13 T. Lazarides, D. Sykes, S. Faulkner, A. Barbieri and M. D. Ward, *Chem. - A Eur. J.*, 2008, **14**, 9389–9399.

14 F. C. J. M. Veggel, S. I. Klink and H. Keizer, *Angew. Chem. Int. Ed. Engl.*, 2000, **39**, 4319–4321.

15 N. M. Shavaleev, L. P. Moorcraft, S. J. A. Pope, Z. R. Bell, S. Faulkner and M. D. Ward, *Chem. Commun.*, 2003, 1134–1135.

16 N. M. Shavaleev, G. Accorsi, D. Virgili, Z. R. Bell, T. Lazarides, G. Calogero, N. Armaroli and M. D. Ward, *Inorg. Chem.*, 2005, **44**, 61–72.

17 T. K. Ronson, T. Lazarides, H. Adams, S. J. A. Pope, D. Sykes, S. Faulkner, S. J. Coles, M. B. Hursthouse, W. Clegg, R. W. Harrington and M. D. Ward, *Chem. - A Eur. J.*, 2006, **12**, 9299–9313.

18 H. B. Xu, L. Y. Zhang, Z. H. Chen, L. X. Shi and Z. N. Chen, *Dalt. Trans.*, 2008, **2**, 4664–4670.

19 X. L. Li, L. X. Shi, L. Y. Zhang, H. M. Wen and Z. N. Chen, *Inorg. Chem.*, 2007, **46**, 10892–10900.

20 T. Sagami, Y. O. Tahara, M. Miyata, H. Miyake and S. Shinoda, *Chem. Commun.*, 2017, **53**, 3967–3970.

21 A. Beeby, I. M. Clarkson, R. S. Dickins, S. Faulkner, D. Parker, L. Royle, A. S. de Sousa, J. A. G. Williams and M. Woods, *J. Chem. Soc. Perkin Trans. 2*, 1999, **2**, 493–504.

22 D. Parker, *Coord. Chem. Rev.*, 2000, **205**, 109–130.

23 A. De Bettencourt-Dias, *Luminescence of Lanthanide Ions in Coordination Compounds and Nanomaterials*, John Wiley & Sons, Inc, Hoboken, NJ, 2014.

24 T. Gunnlaugsson, D. A. Mac Dónaill and D. Parker, *J. Am. Chem. Soc.*, 2001, **123**, 12866–12876.

25 S. Faulkner and B. P. Burton-Pye, *Chem. Commun.*, 2005, 259–261.

26 L. Sarka, L. Burai and E. Brücher, *Chem. - A Eur. J.*, 2000, **6**, 719–724.

27 O. Kotova, S. Comby and T. Gunnlaugsson, *Chem. Commun.*, 2011, **47**, 6810–6812.

28 S. E. Plush and T. Gunnlaugsson, *Org. Lett.*, 2007, **9**, 1919–1922.

29 S. J. A. Pope and R. H. Laye, *Dalt. Trans.*, 2006, **44**, 3108–3113.

30 K. Hanaoka, K. Kikuchi, H. Kojima, Y. Urano and T. Nagano, *J. Am. Chem. Soc.*, 2004, **126**, 12470–12476.

31 T. Gunnlaugsson, J. P. Leonard, K. Sénéchal and A. J. Harte, *Chem. Commun.*, 2004, **4**, 782–783.

32 G. P. Yan, L. Robinson and P. Hogg, *Radiography*, 2007, **13**, e5-e19.

33 V. M. Runge, T. Ai, D. Hao and X. Hu, *Invest. Radiol.*, 2011, **46**, 807–816.

34 N. J. Long and W.-T. Wong, The Chemistry of Molecular Imaging, John Wiley & Sons, Inc, Hoboken, NJ, 2014, p185.

35 N. J. Long and W.-T. Wong, The Chemistry of Molecular Imaging, John Wiley & Sons, Inc, Hoboken, NJ, 2014, p186-p187.

36 B. R. Mcgarvey, A. Pople, Y. Kurita, K. Ito and H. F. Hameka, *J. Chem. Phys.*, 1960, **394**, 842–850.

37 I. Soromont, *Phys. Rev.*, 1955, **99**, 559–565.

38 J. M. Idée, M. Port, I. Raynal, M. Schaefer, S. Le Greneur and C. Corot, *Fundam. Clin. Pharmacol.*, 2006, **20**, 563–576.

39 A. D. Sherry, P. Caravan and R. E. Lenkinski, *J. Magn. Reson. Imaging*, 2009, **30**, 1240–1248.

40 M. Rogosnitzky and S. Branch, *BioMetals*, 2016, **29**, 365–376.

41 P. Marckmann, L. Skov, K. Rossen, A. Dupont, M. B. Damholt, J. G. Heaf and H. S. Thomsen, *J. Am. Soc. Nephrol.*, 2006, **17**, 2359–2362.

42 T. Grobner, *Nephrol. Dial. Transplant.*, 2006, **21**, 1104–1108.

43 C. Rydahl, H. S. Thomsen and P. Marckmann, *Invest. Radiol.*, 2008, **43**, 141–144.

44 J. G. Penfield and R. F. Reilly, *Nat. Clin. Pract. Nephrol.*, 2007, **3**, 654–668.

45 J. Wahsner, E. M. Gale, A. Rodríguez-Rodríguez and P. Caravan, *Chem. Rev.*, 2019, **119**, 957–1057.

46 http://wayback.archive-it.org/7993/20161022205103/.

47 T. Kanda, M. Matsuda, H. Oba, K. Toyoda and S. Furui, *Radiology*, 2015, **277**, 924–925.

48 T. Kanda, K. Ishii, H. Kawaguchi, K. Kitajima and D. Takenaka, *Radiology*, 2014, **270**, 834–841.

49 Y. Zhang, Y. Cao, G. L. Shih, E. M. Hecht and M. R. Prince, *Radiology*, 2017, **282**, 516–525.

50 V. Gulani, F. Calamante, F. G. Shellock, E. Kanal and S. B. Reeder, *Lancet Neurol.*, 2017, **16**, 564–570.

51 https://www.ema.europa.eu/en/news/emas-final-opini.

52 https://www.fda.gov/Drugs/DrugSafety/ucm589213.htm.

53 J. A. Peters, J. Huskens and D. J. Raber, *Prog. Nucl. Magn. Reson. Spectrosc.*, 1996, **28**, 283–350.

54 H. Singh, M. Shukla, B. J. Rao and K. V. R. Chary, *Chem. Commun.*, 2013, **49**, 11403–11405.

55 B. Bleaney, *J. Magn. Reson.*, 1972, **8**, 91–100.

56 S. Aime, M. Botta and G. Ermondi, *Inorg. Chem.*, 1992, **31**, 4291–4299.

57 O. A. Blackburn, A. M. Kenwright, P. D. Beer and S. Faulkner, *Dalt. Trans.*, 2015, **44**, 19509–19517.

58 O. A. Blackburn, N. F. Chilton, K. Keller, C. E. Tait, W. K. Myers, E. J. L. McInnes, A. M. Kenwright, P. D. Beer, C. R. Timmel and S. Faulkner, *Angew. Chemie - Int. Ed.*, 2015, **54**, 10783–10786.

59 M. E. Boulon, G. Cucinotta, J. Luzon, C. Degl'Innocenti, M. Perfetti, K. Bernot, G. Calvez, A. Caneschi and R. Sessoli, *Angew. Chemie - Int. Ed.*, 2013, **52**, 350–354.

60 J. D. Rinehart and J. R. Long, *Chem. Sci.*, 2011, **2**, 2078–2085.

61 K. J. Miller, A. A. Saherwala, B. C. Webber, Y. Wu, A. D. Sherry and M. Woods, *Inorg. Chem.*, 2010, **49**, 8662–8664.

62 M. P. Placidi, L. S. Natrajan, D. Sykes, A. M. Kenwright and S. Faulkner, *Helv. Chim. Acta*, 2009, **92**, 2427–2438.

63 S. Aime, A. Barge, J. I. Bruce, M. Botta, J. A. K. Howard, J. M. Moloney, D. Parker, A. S. De Sousa and M. Woods, *J. Am. Chem. Soc.*, 1999, **121**, 5762–5771.

64 L. S. Natrajan, N. M. Khoabane, B. L. Dadds, C. A. Muryn, R. G. Pritchard, S. L. Heath, A. M. Kenwright, I. Kuprov and S. Faulkner, *Inorg. Chem.*, 2010, **49**, 7700–7709.

65 M. Woods, S. Aime, M. Botta, J. A. K. Howard, J. M. Moloney, M. Navet, D. Parker, M. Port and O. Rousseaux, *J. Am. Chem. Soc.*, 2000, **122**, 9781–9792.

66 K. Micskei, D. H. Powell, L. Helm, E. Brücher and A. E. Merbach, *Magn. Reson. Chem.*, 1993, **31**, 1011–1020.

67 R. M. Smith and A. E. Martell, *Sci. Total Environ.*, 1987, **64**, 125–147.

68 W. P. Cacheris, S. K. Nickle, and A. D. Sherry, *Inorg. Chem.*, 1987, **26**, 958–960.

69 P. Hermann, J. Kotek, V. Kubíček and I. Lukeš, *Dalt. Trans.*, 2008, **9226**, 3027–3047.

70 V. Comblin, D. Gilsoul, M. Hermann, V. Humblet, V. Jacques, M. Mesbahi, C. Sauvage and J. F. Desreux, *Coord. Chem. Rev.*, 1999, **185**–**186**, 451–470.

71 E. Brücher, I. Lázár and I. Tóth, *Inorg. Chem.*, 1994, **33**, 4070–4076.

72 M. F. Tweedle, J. J. Hagan, K. Kumar, S. Mantha and C. A. Chang, *Magn. Reson. Imaging*, 1991, **9**, 409–415.

73 S. Laurent, L. Vander Elst, F. Copoix and R. N. Muller, *Invest. Radiol.*, 2001, **36**, 115–122.

74 E. Brücher and P. Szarvas, *Inorganica Chim. Acta*, 1970, **4**, 632–636.

75 T. Frenzel, P. Lengsfeld, H. Schirmer, J. Hütter and H. J. Weinmann, *Invest. Radiol.*, 2008, **43**, 817–828.

76 É. Tóth, R. Király, J. Platzek, B. Radüchel and E. Brücher, *Inorganica Chim. Acta*, 1996, **249**, 191–199.

77 L. Sarka, L. Burai, R. Király, L. Zékány and E. Brücher, *J. Inorg. Biochem.*, 2002, **91**, 320–326.

78 T. J. Clough, L. Jiang, K. L. Wong and N. J. Long, *Nat. Commun.*, 2019, **10**, 1–14.

79 N. N. G. and A. Earnshaw, *Chemistry of the Elements*, Oxford, UK, 2nd Editio., 1997.

80 I. M. Ismail, S. J. S. Kerrison and P. J. Sadler, *Polyhedron*, 1982, **1**, 57–59.

81 N. Turova, *Inorganic Chemistry in Table*, Springer, 2011.

82 G. L. M. and D. A. Tarr, *Inorganic Chemistry*, 3rd Edn., 2004.

83 R. G. Pearson, *J. Chem. Educ.*, 1968, **45**, 581–587.

84 C. A. M. and M. B. F. A. Cotton, G. Wilkinson, *Advanced Inorganic Chemistry*, John Wiley and Sons, Inc., New York, 6th Edn., 1999.

85 S. A. Cotton, *Chemistry of precious metals*, Blackie Academic & Professional, London, 1997.

86 B. F. R. Hartley, *Chem. Soc. Rev.*, 1973, **2**, 163-179.

87 B. Rosenberg, L. Van Camp and T. Krigas, *Nature*, 1965, **205**, 698–699.

88 B. Rosenberg, L. Van Camp, J. E. Trosko and V. H. Mansour, *Nature*, 1969, **222**, 385–386.

89 L. Kelland, *Nat. Rev. Cancer*, 2007, **7**, 573–584.

90 S. C. Sweetman, *The complete drug reference*, Pharmaceutical Press, London, 35th Edn., 2007.

91 N. J. Wheate, S. Walker, G. E. Craig and R. Oun, *Dalt. Trans.*, 2010, **39**, 8113–8127.

92 T. C. Johnstone, J. J. Wilson and S. J. Lippard, *Inorg. Chem.*, 2013, **52**, 12234–12249.

93 J. M. Malinge, M. J. Giraud-Panis and M. Leng, *J. Inorg. Biochem.*, 1999, **77**, 23–29.

94 A. M. Florea and D. Büsselberg, *Cancers (Basel).*, 2011, **3**, 1351–1371.

95 I. Romero-Canelón and P. J. Sadler, *Inorg. Chem.*, 2013, **52**, 12276–12291.

96 S. P. Fricker, *Dalt. Trans.*, 2007, 4903–4917.

97 J. Reedijk, *Eur. J. Inorg. Chem.*, 2009, 1303–1312.

98 E. Shaili, *Photoactivatable Platinum (IV) Anticancer Complexes*, DPhil Thesis, 2013.

99 F. Kratz, I. A. Müller, C. Ryppa and A. Warnecke, *ChemMedChem*, 2008, **3**, 20–53.

100 J. Rautio, H. Kumpulainen, T. Heimbach, R. Oliyai, D. Oh, T. Järvinen and J. Savolainen, *Nat. Rev. Drug Discov.*, 2008, **7**, 255–270.

101 M. Mitsunaga, M. Ogawa, N. Kosaka, L. T. Rosenblum, P. L. Choyke and H. Kobayashi, *Nat. Med.*, 2011, **17**, 1685–1691.

102 S. Mukhopadhyay, C. M. Barnés, A. Haskel, S. M. Short, K. R. Barnes and S. J. Lippard, *Bioconjug. Chem.*, 2008, **19**, 39–49.

103 M. W. Ndinguri, R. Solipuram, R. P. Gambrell, S. Aggarwal and R. P. Hammer, *Bioconjug. Chem.*, 2009, **20**, 1869–1878.

104 S. Hatakeyama, K. Sugihara, T. K. Shibata, J. Nakayama, T. O. Akama, N. Tamura, S. M. Wong, A. A. Bobkov, Y. Takano, C. Ohyama, M. Fukuda and M. N. Fukuda, *Proc. Natl. Acad. Sci. U. S. A.*, 2011, **108**, 19587–19592.

105 J. J. Wilson and S. J. Lippard, *Chem. Rev.*, 2014, **114**, 4470–4495.

106 M. D. Hall and T. W. Hambley, *Coord. Chem. Rev.*, 2002, **232**, 49–67.

107 P. D. Bonnitcha, M. D. Hall, C. K. Underwood, G. J. Foran, M. Zhang, P. J. Beale and T. W. Hambley, *J. Inorg. Biochem.*, 2006, **100**, 963–971.

108 Q. Mi, S. Shu, C. Yang, C. Gao, X. Zhang, X. Luo, C. Bao, X. Zhang and J. Niu, *Int. J. Med. Physics, Clin. Eng. Radiat. Oncol.*, 2018, **07**, 231–247.

109 A. M. Pizarro and P. J. Sadler, *Biochimie*, 2009, **91**, 1198–1211.

110 P. B. Glover, P. R. Ashton, L. J. Childs, A. Rodger, M. Kercher, R. M. Williams, L. De Cola and Z. Pikramenou, *J. Am. Chem. Soc.*, 2003, **125**, 9918–9919.

111 E. L. Crossley, J. B. Aitken, S. Vogt, H. H. Harris and L. M. Rendina, *Angew. Chemie - Int. Ed.*, 2010, **49**, 1231–1233.

112 Z. Zhu, X. Wang, T. Li, S. Aime, P. J. Sadler and Z. Guo, *Angew. Chemie - Int. Ed.*, 2014, **53**, 13225.

113 K. Singh, S. Singh, P. Srivastava, S. Sivakumar and A. K. Patra, *Chem. Commun.*, 2017, **53**, 6144–6147.

114 O. J. Stacey, A. J. Amoroso, J. A. Platts, P. N. Horton, S. J. Coles, D. Lloyd, C. F. Williams, A. J. Hayes, J. J. Dunsford and S. J. A. Pope, *Chem. Commun.*, 2015, **51**, 12305–12308.

115 Y. Zhao, G. M. Roberts, S. E. Greenough, N. J. Farrer, M. J. Paterson, W. H. Powell, V. G. Stavros and P. J. Sadler, *Angew. Chemie - Int. Ed.*, 2012, **51**, 11263–11266.

116 H. Li, B. I. Harriss, A. Phinikaridou, S. Lacerda, G. Ramniceanu, B.-T. Doan, K.-L. Ho, C.-F. Chan, W.-S. Lo, R. M. Botnar, R. Lan, C. Richard, G.-L. Law, N. J. Long and K.-L. Wong, *Nanotheranostics*, 2017, **1**, 186–195.

Chapter 2: Copper(I) Catalysed Click Reaction of Ln-Pt Complexes

2.1 Introduction

2.1.1 Click chemistry

In 2001, the concept of "click chemistry" was first introduced by Kolb, Finn and Sharpless.[1] This term was expected to include all those synthetic approaches that could be used in both small- and large scale reactions in which the starting substrates are selective for each other. Thus, the synthesis of compound can be simplified, and the drug discovery process could be accelerated. The authors also outlined a number of criteria that the click chemistry should meet including high yields, modularity, regiospecificity and stereospecificity, wide scope, inoffensive by-product, simplicity of performing and ease of removing solvents.

2.1.2 Copper-catalysed alkyne azide click reaction

There are several chemical reactions that are identified as click reactions: nucleophilic ring opening reactions, Diels-Alder reactions, the addition to carbon-carbon multiple bonds and cycloaddition reactions. Among these click reactions, the cycloaddition of alkynes with azides is the most widespread example. The syntheses of compounds containing alkyne and azide groups are relatively easy to perform and stable towards a range of different chemical conditions. Moreover, most common organic groups do not interact with azide or alkyne functional groups in mild conditions. In particular, the

alkyne and azide cycloaddition catalysed by a copper(I) catalyst which forms1,2,3-triazoles is the most heavily explored click reaction. Since its report by Sharpless, Folkin and Meldal, it has been successfully applied in bioconjugation, materials science and drug discovery.[2–4] The Cu(I) catalysed alkyne-azide cycloaddition (CuAAC) reaction has demonstrated several advantages as there is no protecting group required, the reaction yield is excellent, and the reaction is compatible with water and a lot of organic solvents used in organic chemistry. An extra advantage of using Cu(I) catalyst is that it forms stereospecific products compared to the uncatalysed reaction.

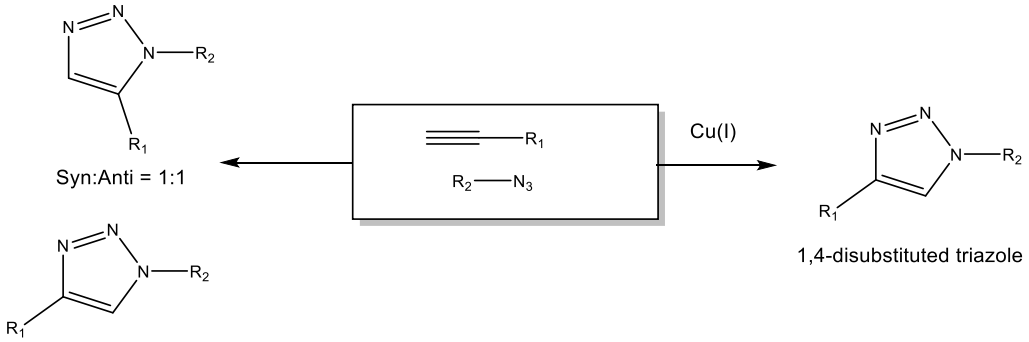

Figure 2.1: *The copper(I) catalysed cycloaddition of alkynes and azides (Right); Non-catalysed alkyne-azide cycloaddition with non-stereoselectivity (Left).*

2.1.3 Lanthanide complexes undergoing CuAAC reactions

a. Lanthanide complexes with appended alkyne groups

The first example that used lanthanide complexes in a CuAAc reaction was published by Hulme in 2006. The coupling between the Eu(III) DOTA-derived complex and the azide containing antenna group was conducted in presence of micromolar amount of Cu(I), which resulted in a dramatic enhancement of Eu(III) luminescence.[5]

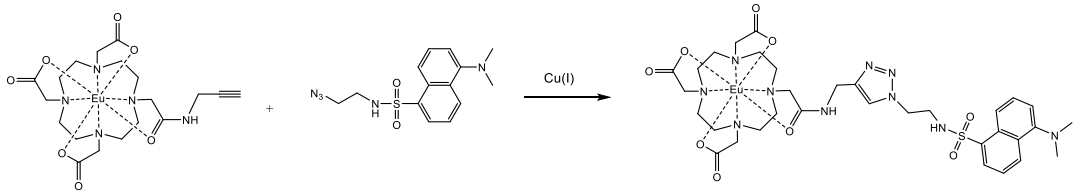

Figure 2.2: *Illustration of the first alkyne-appended lanthanide complex that underwent CuAAC reaction.*

In 2009, Lowe and Faulkner exploited the use of a heptadentate DO3A ligand containing a propargyl arm in CuAAC reactions. The propargyl-appended lanthanide complexes were used as synthetic substrates to couple with the azide-containing molecules via the CuAAC reaction. Upon the click reaction, the coordination environment of the lanthanide ions can be dramatically changed as the resulting triazole group was able to coordinate to the lanthanide centre. These changes can be observed by ^{1}H NMR and luminescence spectra.[6,7] A later example of a click reaction between propargyl-appended lanthanide complexes and azide appended ferrocene resulted in a redox-active d-f dyad whose luminescence can be reversibly switched by changing the oxidation state of the ferrocene chromophore.[8]

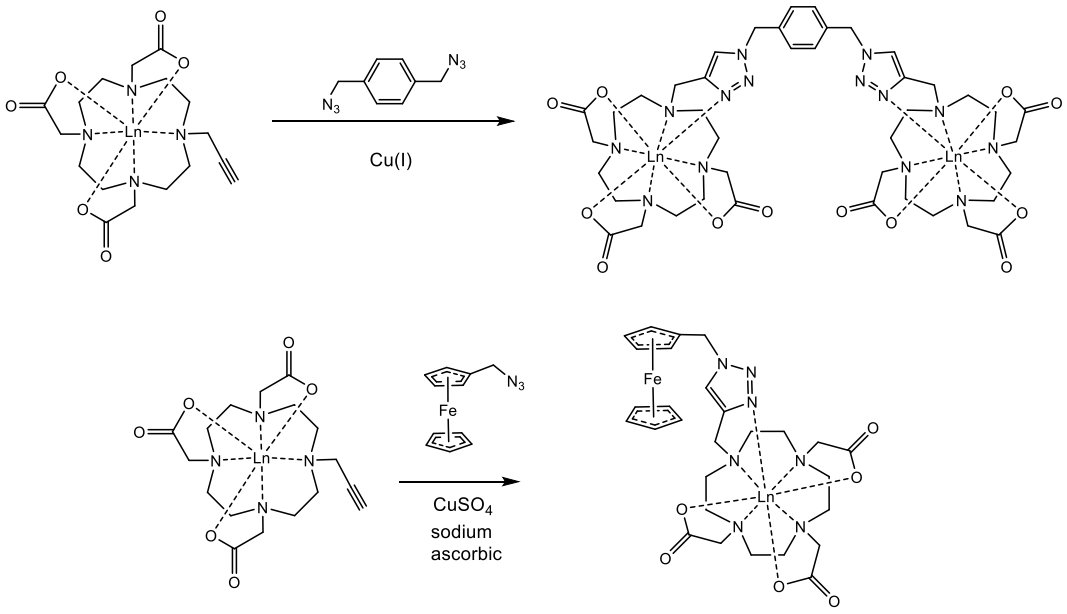

Figure 2.3: *Illustration of examples of alkyne appended lanthanide DO3A complex that underwent CuAAC reactions.*

b. Lanthanide complexes containing azide groups

While CuAAC reactions have been widely exploited with alkyne-appended DO3A-like complexes for the formation of multimetallic, bioconjugates and multimodal imaging agents[9–13], there are fewer examples of using the azide-containing lanthanide complexes as the Cu(I) click-reaction precursors. Faulkner and co-workers have

presented an example where the azidophenacyl DO3A lanthanide complexes and the propargyl DO3A lanthanide complex act as effective substrates for Cu(I) click reaction resulting in aryl-triazole-appended bimetallic complexes, in which the carbonyl oxygen allows the phenacyl moiety to directly coordinate to the metal centre, which reduces the quenching effect from the surrounding water molecules. The coordination of the carbonyl oxygen also facilitates the efficiency of energy transfer from chromophore to the metal centre, which results in a better sensitising effect of the lanthanide emission. The resulting aryl triazole acts as the sensitising chromophore which mediates lanthanide luminescence.[14].

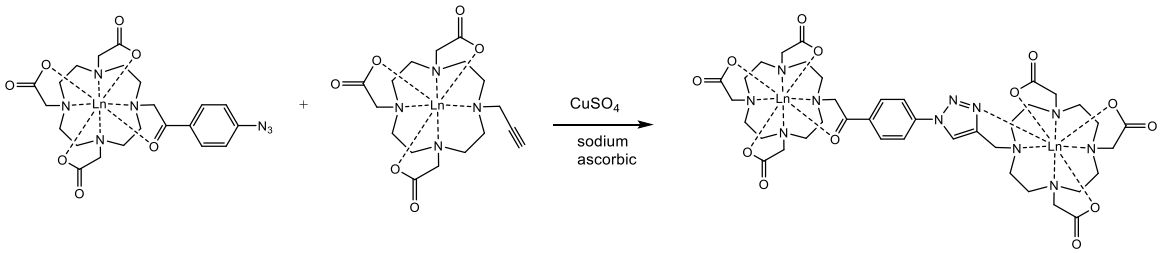

Figure 2.4: *Illustration of CuAAC click chemistry reaction applied to azide-appended lanthanide DO3A complex.*

2.2 The Design of the Ln-Pt complex

In this work, novel lanthanide-platinum complexes were designed based on two main building blocks: azidophenacyl-DO3A and alkyne-appended malonate. The azidophenacyl-DO3A moiety provides an octadentate binding site for the lanthanide ion and an antenna for sensitising the emission of lanthanide, while the malonic acid group can act as a ligand to the platinum. After coordination to the malonate ligand, the platinum(II) centre can be oxidised by H_2O_2 to platinum(IV). Figure 2.5 shows the structure of the designed Ln-Pt complexes, the azidophenacyl-DO3A lanthanide and the alkyne appended malonate were linked by Cu(I) catalysed azide-alkyne

cycloaddition reaction.

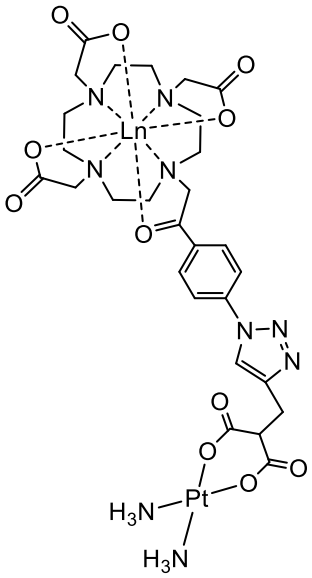

Figure 2.5: *Chemical structure of the designed Ln-Pt complex, where the lanthanide is coordinated to the phenacyl-DO3A ligand and the platinum is bound to the malonate ligand.*

2.2.1 Malonate platinum complexes

Malonate platinum complexes and their derivatives have a similar structure to carboplatin. Carboplatin is recognised as the next generation of platinum anticancer drug after cisplatin.[15] It was designed to overcome the drawbacks of cisplatin, especially toxicity. The lower toxicity of carboplatin can be attributed to the inclusion of the 1,1-cyclobutyldicaboxylate moiety as a leaving ligand which promotes both the stability and aqueous solubility of carboplatin in comparison with cisplatin.

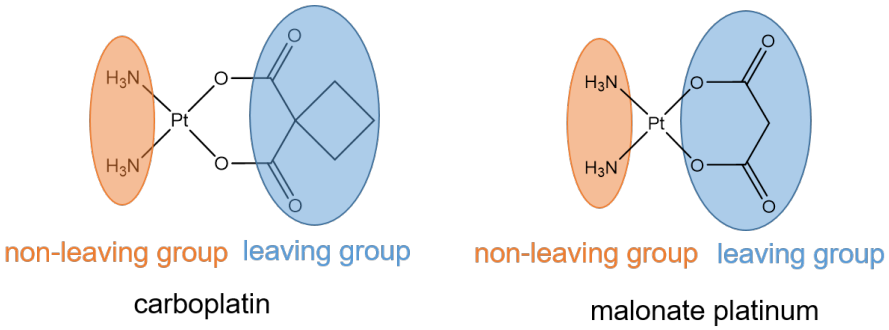

Figure 2.7: *Illustration of the structure of carboplatin and malonate platinum complexes indicating leaving and non-leaving groups.*

Similar to carboplatin, the malonate group coordinates to the platinum atom through a six-membered ring and acts as a leaving group when the platinum centre binds to DNA, while the amine groups act as non-leaving groups and remain attached following DNA binding. It is well-recognised that the nature of the leaving ligand plays an important role in determining the toxicity and side-effects of a platinum drug, because the leaving capability of different leaving ligands from the binding platinum atom can remarkably influence the biodistribution of the drugs *in vivo*. The bidentate anionic leaving groups like the malonate group hydrolyse slower than labile anionic leaving groups such as chloride from cisplatin, leading to increased stability of the platinum complexes in blood. Additionally, dicarboxylate platinum complexes are typically more water-soluble. Thus, they are less toxic because they can be excreted via kidney efficiently. However, their anti-tumour abilities can be reduced as their cytotoxicity and tissue penetration ability are weaker.[16]

There are some examples of previous malonate platinum complexes and their derivatives as anticancer drugs that have been reported. The modifications on the malonate ligand will be discussed in Section 2.2.1.1, while modifications focused on altering the axial position of the platinum will be discussed in Section 2.2.1.2.

2.2.1.1. Examples of modification on the malonate ligand

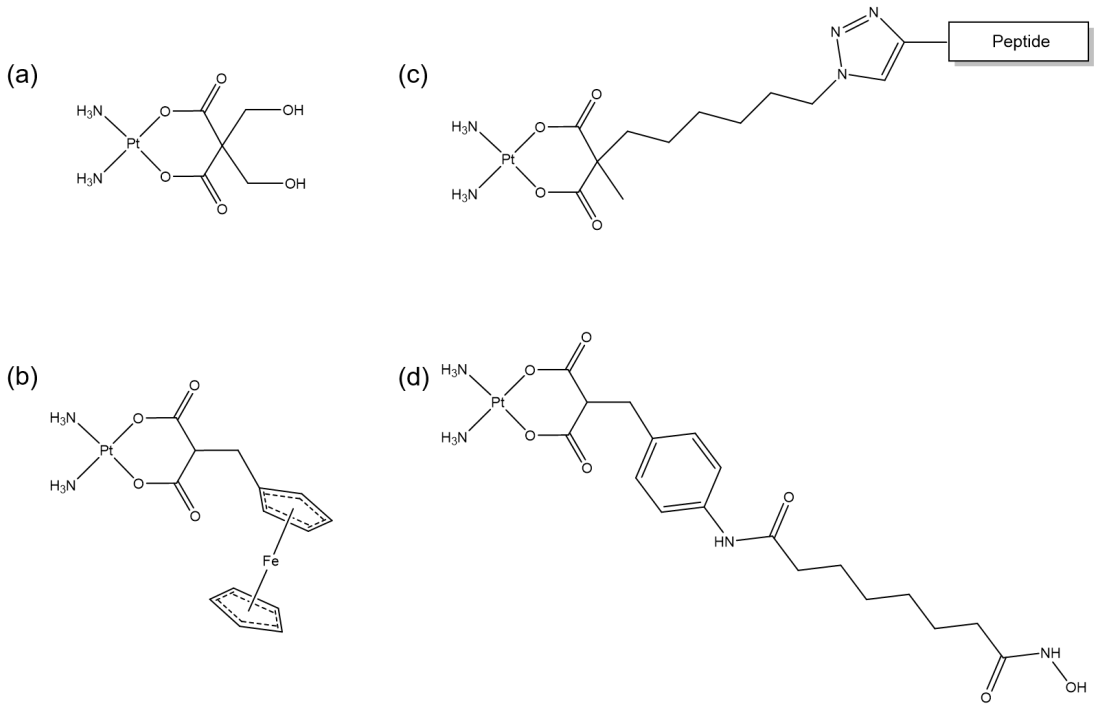

Figure 2.8: *Illustration of some examples of malonate platinum derivatives: (a) alternation of the lipophilic properties by adding two hydroxymethyl groups; (b) attaching ferrocene group to form the Pt-Fe bimetallic complexes; (c) peptide functionalisation of the complex via CuAAC reaction; (d) conjugation with other drug molecule to achieve higher selectivity.*

As shown in Figure 2.8 (a), two hydroxymethyl groups were adding to the malonate ligand which changed the kinetic reactivity and DNA-binding rate of the complex, ultimately leading to higher anti-cancer efficacy.[17,18] In 1992 D. Gibson and co-workers attached ferrocene to the malonate complexes which result in a series of Pt-Fe bimetallic complexes, structure was demonstrated in Figure 2.8 (b). The metallocene was shown to navigate the drug almost entirely to the liver and the spleen, but had only negligible antitumor activity.[19] As shown in Figure 2.8 (c), A.J. Mieszawaska and co-workers reported an alkyne-appended malonate platinum complexes in which the alkyne had undergone a CuAAC reaction with a nuclear localization sequence peptide to improve the drug localisation into the cell's nucleus.[20] C.J. Marmion *etc.* tethered the first FDA-approved histone deacetylases inhibitors: suberoylanilide hydroxamic

acid(SAHA) with the malonate platinum which enhance the selectivity of the drug to cancer cells, the structure of the complex is shown in Figure 2.8 (d).[21]

2.2.1.2. Modification on axial position of the platinum

B.K. Keppler and co-workers synthesised a series of malonate platinum(IV) complexes by replacing the axial hydroxide groups with carboxylate groups including both symmetric and asymmetric axial ligands. They also evaluated their antiproliferative potency in various human cancer cell lines, the malonate platinum(IV) complexes investigated are shown in Figure2.9.[22–24]

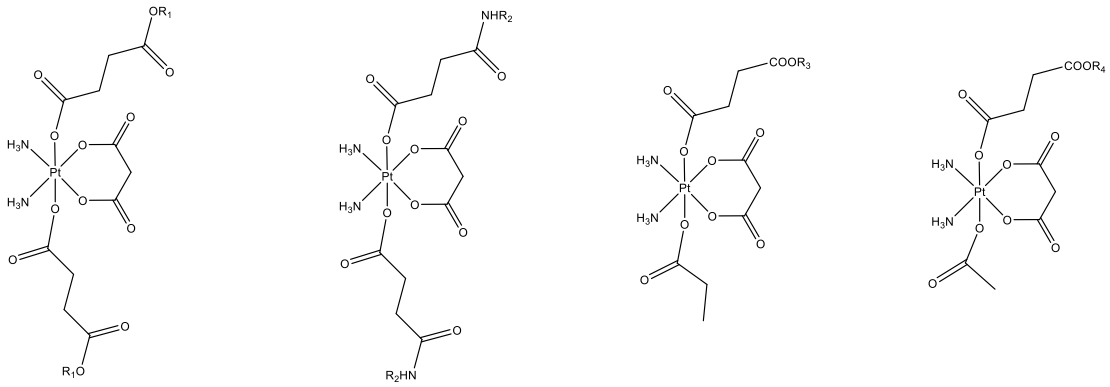

Figure 2.9: *Examples of axial modifications of malonate platinum(IV) complexes from B.K. Keppler's work. R_1= Me, Et, Pr, Bu, ^{i}Pr, MeO$(CH_2)_2$; R_2= Pr, Cyclopentyl; R_3= Pr, Bu, Pentyl, Hexyl; R_4= Me, Et, Pr, Bu, Pentyl, Hexyl, Octyl, ^{i}Pr.*

2.3 Synthesis and Characterisation

The Cu(I)-catalysed click reaction between azidophenacyl DO3A Ln complexes and propargyl-appended diethyl malonate yielded the triazolophenacylDO3A Ln complexes with the malonate bidentate ligand which can bind to the Pt, the reaction scheme is shown in Figure 2.16.

2.3.1 Synthesis of azidophenacylDO3A Ln complexes

Figure 2.10 depicts the general synthetic pathway for the formation of azidophenacylbromide (compound **2.1**). It was synthesised from 4'-aminoacetophenone, the primary aromatic amine underwent nitrosation with nitrous acid which was generated *in situ* from sodium nitrite and hydrochloric acid. The diazotization reaction occurred through reaction with sodium azide. The crude product was extracted with ethyl acetate. The reaction went to completion with a high yield, as a result of the electron-withdrawing acetyl substituent. The product, azido-acetophenone, was obtained after washing with cold hexane. The brominated compound **2.1** was obtained by using 2 equivalents of p-toluenesulfonic acid and N-bromosuccinimide in acetonitrile with heating to reflux. This method was adopted from a bromination procedure reported by Chang in 2002.[25] The crude product was purified by using flash column chromatography on silica gel with hexane and ethyl acetate. The final product was kept in the dark at low temperature in case of photodecomposition.

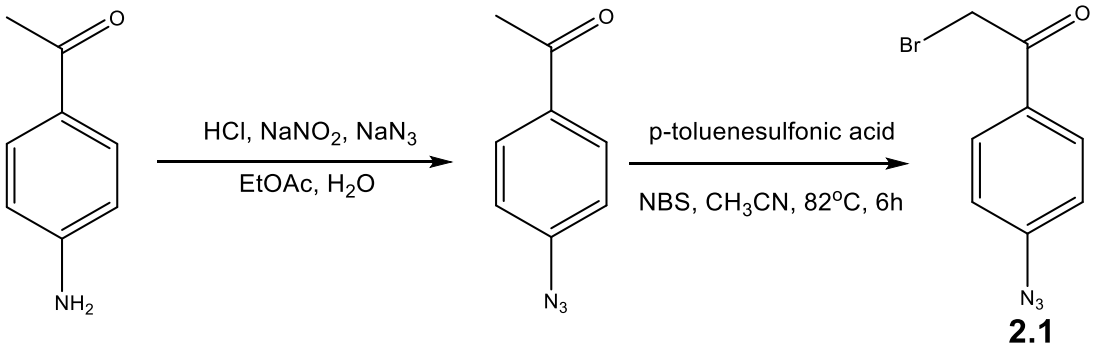

Figure 2.10: *Synthetic pathway for formation of Azidophenacylbromide*

The reaction between compound **2.1** and tert-butyl protected triester (compound **2.2**) was carried out in the presence of potassium carbonate and a nucleophilic catalyst (KI) in acetonitrile at room temperature. After 16 hours the solid was removed by filtration, and the solvent was removed by rotary evaporation, which resulted in crude protected

ligand. The purification was achieved by the flash column chromatography on silica gel. The deprotection of the tert-butyl protection group was carried out in dichloromethane by treatment of trifluoroacetic acid at room temperature. The deprotected ligand was dissolved in methanol with corresponding lanthanide triflate salts with heating to 60 °C for 48 hours at pH 6. The methanol was removed, and the product was dissolved in water. Sodium hydroxide solution was added dropwise to remove excess of lanthanide ions, which were precipitated as $Ln(OH)_3$ and removed by centrifuging. The resulting complexes were characterised by ^{1}H-NMR spectroscopy, UV-Vis spectroscopy, and mass spectrometry.

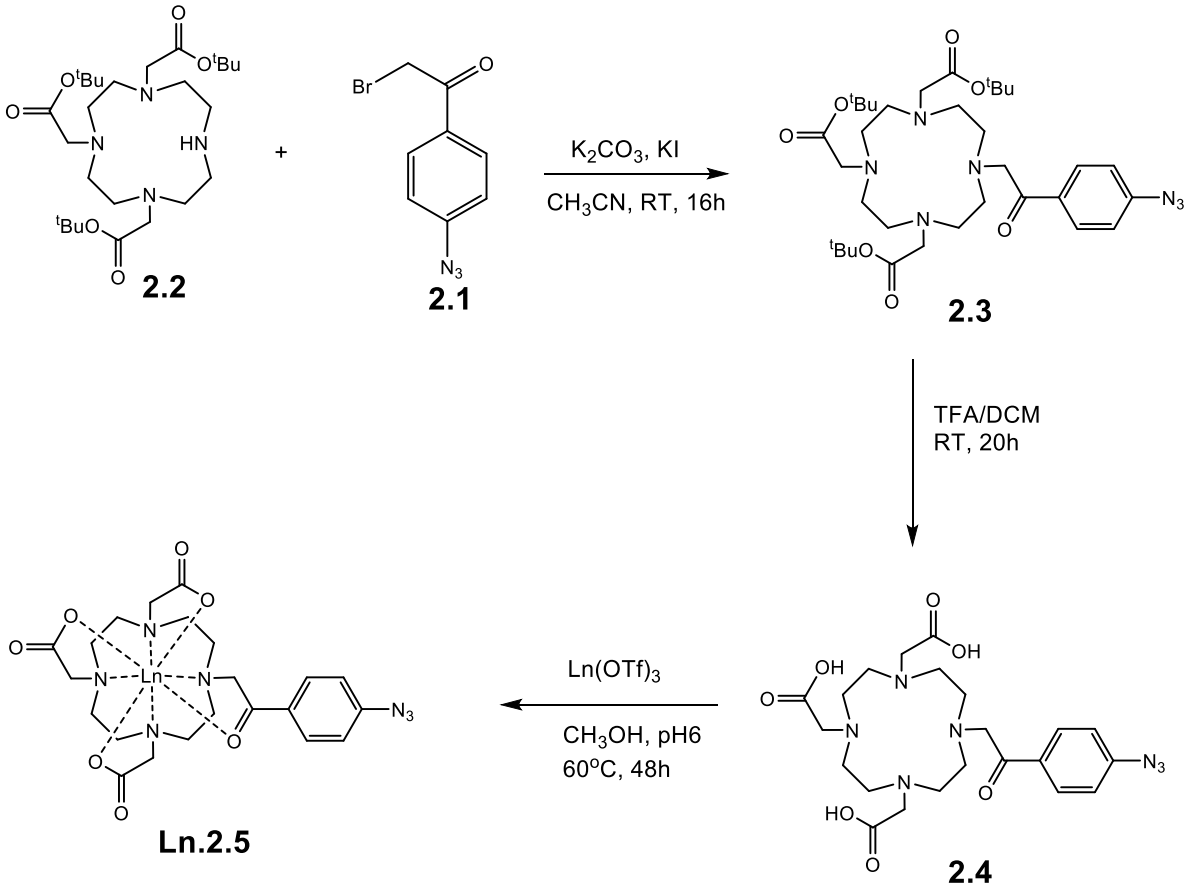

Figure 2.11: *synthetic pathway for formation of AzidophenacylDO3A lanthanide complexes.*

2.3.2 Characterisation of azidophenacylDO3A Ln complexes

Figure 2.12 illustrates the ^{1}H NMR spectra of **Yb.2.5** and **Eu.2.5**. The exchange of SAP

and TSAP isomers is slow enough in both complexes so that the isomers can be clearly distinguished. For **Yb.2.5** complex, peaks between 80 - 140 ppm are assigned to typical axial protons of SAP isomers while resonances around 50-14 ppm are assigned to axial protons of TSAP isomer. In the case of **Eu.2.5**, the highly shifted resonances in the region around 35-25 ppm are assigned to the axial protons of the SAP isomer. Signals that indicate the presence of the TSAP isomer are also observed in the spectrum around 8-12 ppm.

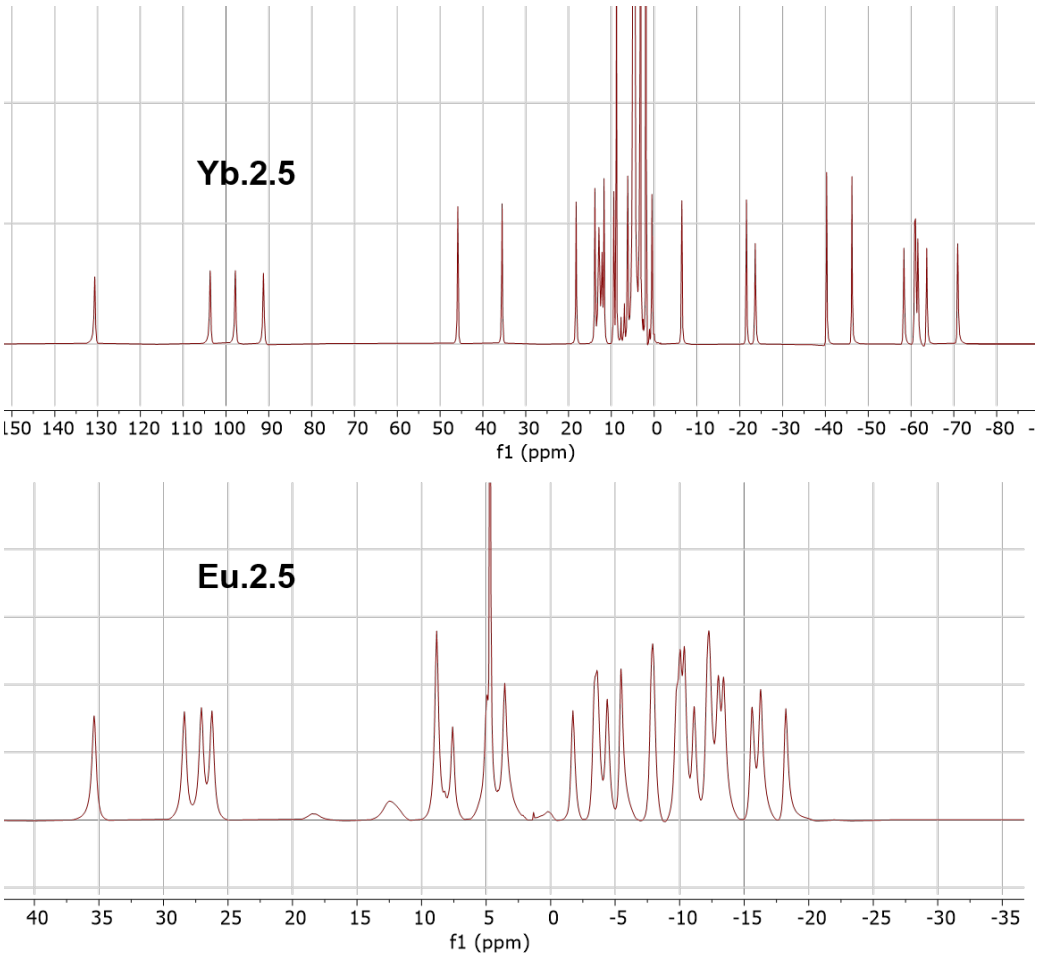

Figure 2.12: *^{1}H NMR of azidophenacylDO3A Yb/Eu Complexes*

The UV-vis absorption spectra of the azidophenacylDO3A ligand **2.4** and its lanthanide complexes **Ln.2.5** were measured in H_2O at 10^{-5} M. The spectra are shown in Figure 2.13. The ligands exhibit a broad absorption band at 295 nm in aqueous

solution which corresponds to the charge-transfer (CT) originating from the phenacyl chromophore. Upon complexation, a bathochromic shift is observed in the absorption spectrum. The Eu, Tb, Lu and Yb complexes all show absorption maxima at 320 nm. This red shift of the CT signal indicates there is substantial interaction between the carbonyl group on the azidophenacyl chromophore and lanthanide centre. The presence of the electropositive lanthanide ion in the macrocyclic cavity facilitates the polarisation of carbonyl group, while simultaneously stabilising the polar charge-transfer excited states, thus decreasing their energy.

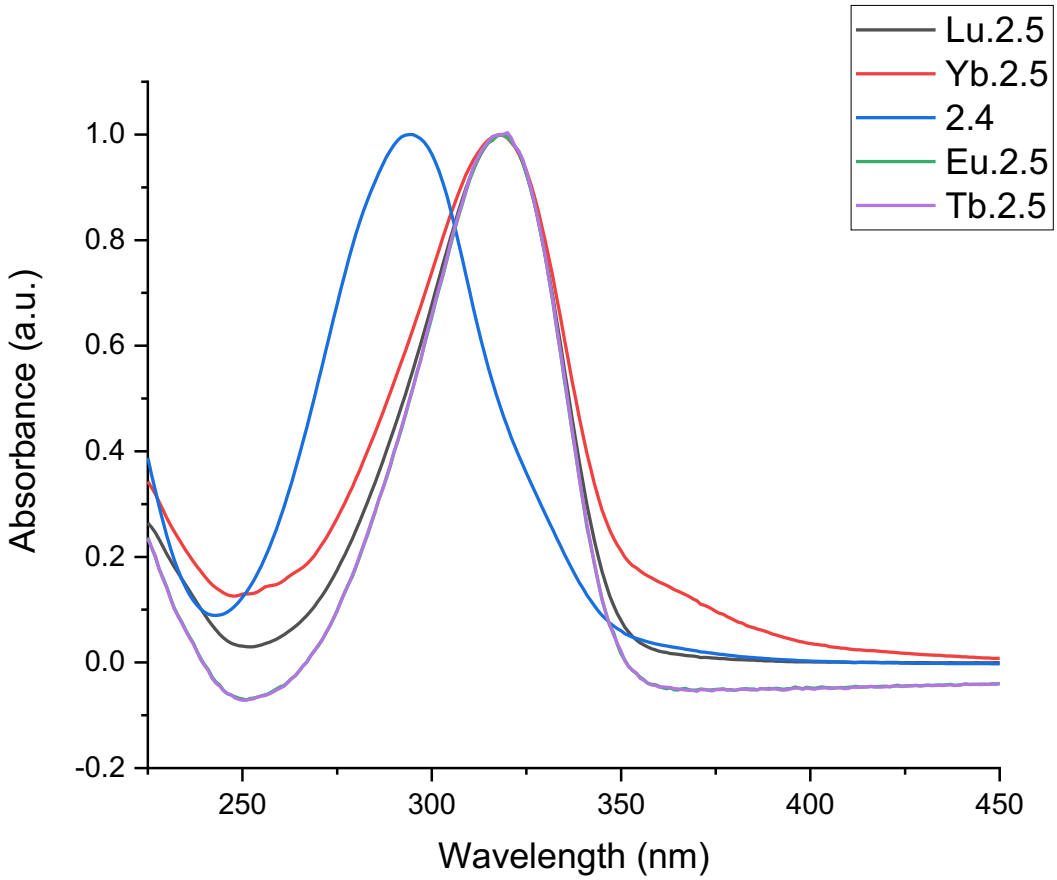

Figure 2.13: *Comparison of the UV-vis absorption spectra of azidophenacylDO3A Ln Complexes (D_2O, $10^{-4}M$)*

As shown in Figure 2.14, the luminescence spectroscopy of the **Eu.2.5** complex exhibited strong and characteristic Eu emission bands upon excitation in the chromophore band, with the peaks at 580 nm, 592 nm, 616 nm, 653 nm, 688 nm and

701 nm arising from the $^5D_0$ - ^7F_J (J = 0, 1, 2, 3, 4, 5) transition. The excitation spectrum shows a relatively broad band which is extended to the visible region. By employing two-photon excitation microscopy, it could be possible to use this molecule as an imaging agent under sensitisation with a NIR light source.

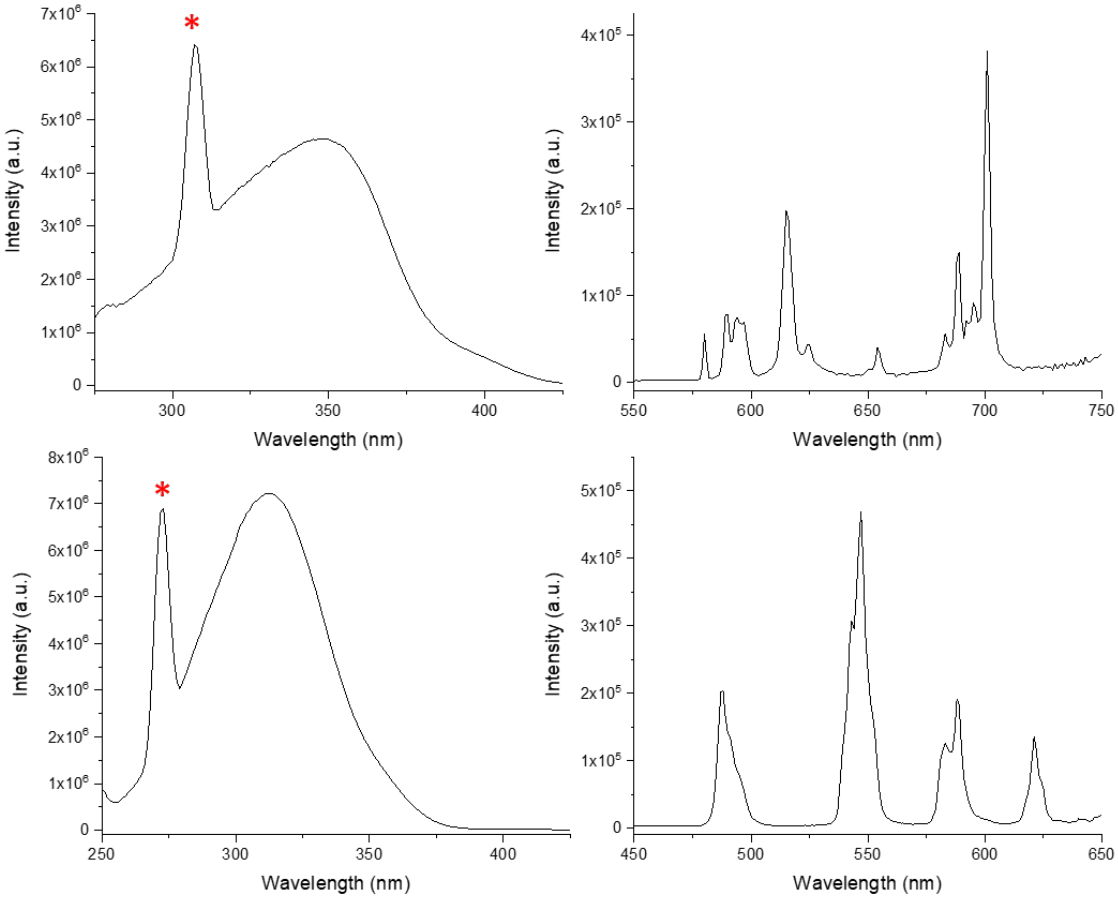

Figure 2.14: *Top left: Excitation spectrum of* ***Eu.2.5*** *(λ_{em} = 615 nm, slit width 5nm), *313 nm is artefact; top right: emission spectrum of* ***Eu2.5*** *(λ_{ex} = 357 nm, slit width 1 nm). Bottom left: Excitation spectrum of* ***Tb2.5*** *(λ_{em} = 549 nm, slit width 5 nm), *273 nm is artefact; bottom right: emission spectrum of* ***Tb.2.5****, (λ_{ex} = 357 nm, slit width 1 nm). All of the spectra were measured in water.*

The lifetimes of **Eu.2.5** in H_2O and D_2O were measured. From lifetimes, the hydration number *q* (the number of solvent molecules coordinated to the lanthanide centre) was determined by employing modified Horrocks' equation:

$$\boldsymbol{q} = A(k_H - k_D - B) \quad (2.1)$$

where A and B are parameters specific for each lanthanide, respectively, A_{Eu}= 1.2 ms and B_{Eu}= 0.25 ms^{-1}.

Table 2.1: *Tabulated luminescent lifetime of* ***Eu2.5*** *and its corresponding hydration number q.*

Complex	τ_{H2O}/ms	τ_{D2O}/ms	q
Eu.2.5	0.51	1.22	1.06

The hydration number q obtained for **Eu.2.5** indicates that the complex is octadentate species in solution, where the ketone actively participates in the coordination, and there is only one water molecule coordinated in the axial position.

2.3.3 Synthesis of the propargyl appended diethyl malonate

Figure 2.15 depicts the synthetic approach to a propargyl diethyl malonate compound **2.6**. Starting from diethyl malonate, the ethoxide ion from sodium ethoxide was used to deprotonate the hydrogen atom from the diethyl malonate. Subsequently the enolate ion underwent alkylation reaction with propargyl bromide which yielded in the alkylated malonate ester. The crude product was obtained via the extraction between water and dichloromethane as a yellow oil. The resulting crude product was then purified by flash column chromatography on silica gel with ethyl acetate and petroleum ether. The pure product was characterised by NMR spectroscopy and mass spectrometry. The side product of this reaction was also purified by the flash column chromatography, ^{1}H NMR and mass spectrometry indicated that small amount of bis-alkylated product was formed from the reaction.

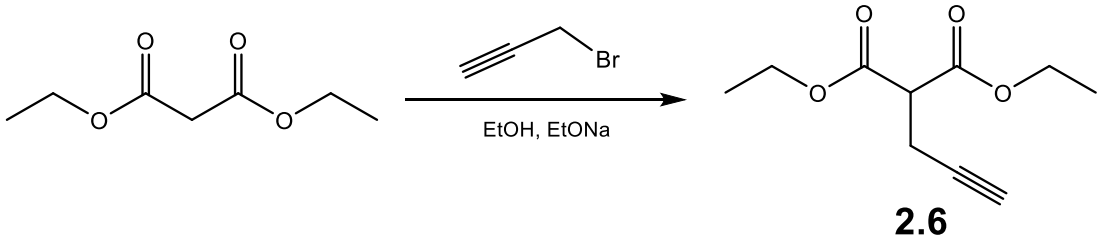

Figure 2.15: *synthetic pathway for formation of propargyl diethyl malonate (yield: 92%).*

2.3.4 The CuACC click reaction

The preparations of malonate-appended lanthanide complexes were achieved via CuAAC click reactions. Compound **2.6**, **Ln.2.5**, sodium ascorbate and copper sulphate were dissolved in methanol. The Cu(II) was reduced to the Cu(I) catalyst *in situ* by sodium ascorbate. The conversion of the reaction was modest when using 1:1 equivalent of azide and alkyne. This issue could be rationalised by the bulky nature of the azidophenacylDO3A precursor and the low reactivity of the azide group. Hence an excess of alkyne was added, to drive the reaction to completion. The reaction was conducted at 40°C, and HPLC was used to monitor the process of the reaction. About 90% of the lanthanide precursor **Ln.2.5** was consumed after 48 hours.

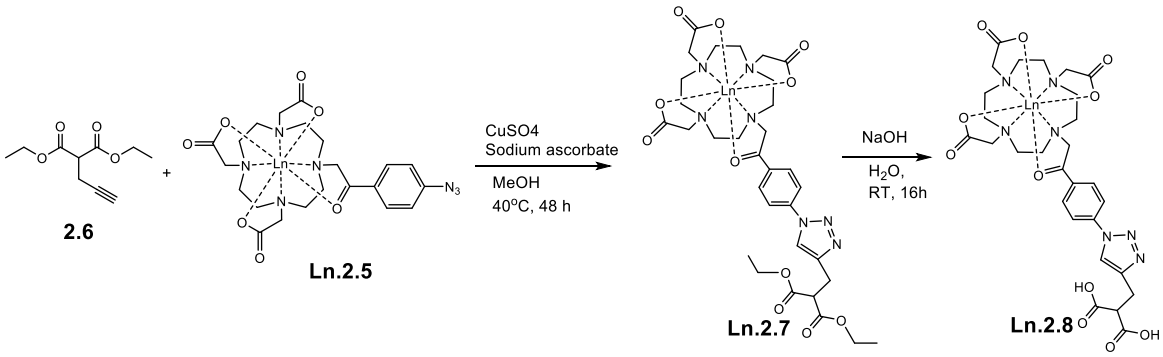

Figure 2.16: *synthetic pathway for the CuAAC reaction between* ***Ln.2.5*** *and compound* ***2.6*** *and the following ester deprotection of the click product.*

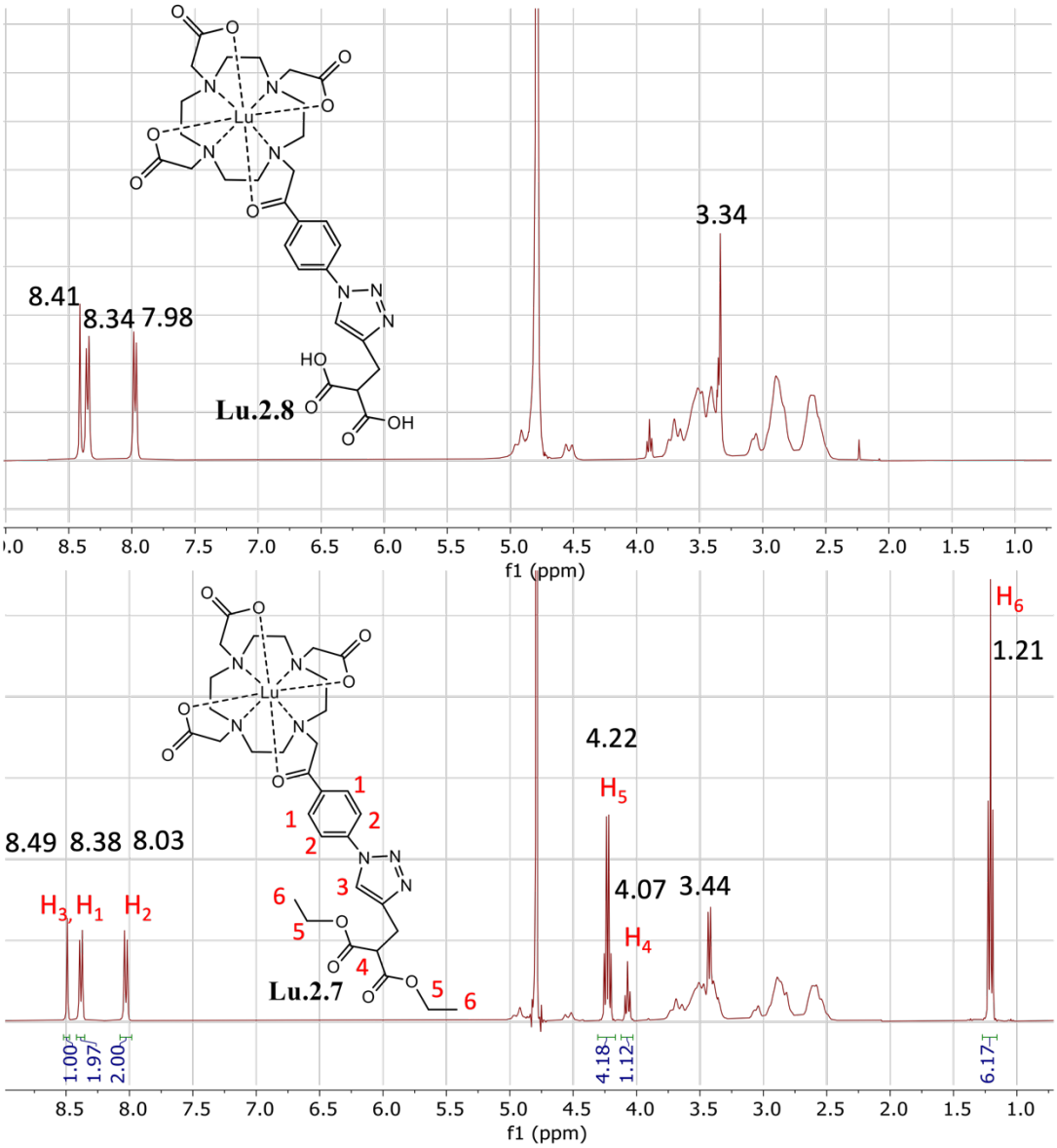

Figure 2.17: *^{1}H NMR spectra (D_2O, 400 MHz) of* ***Lu.2.7*** *(bottom) and complex* ***Lu.2.8****, the disappearance of the H_5 and H_7 indicate the deprotection of the malonic ester.*

Reverse-phase HPLC was adopted to purify the targeted product **Ln.2.7**. This purification was conducted on a HPLC C_{18} column, which successfully removed the residue of alkyne precursors and catalytic copper source. Details of the HPLC method can be found in the experimental methods section of this thesis. Briefly, acidic eluent conditions were employed using a shallow H_2O/MeOH gradient. The product was collected by mass detection at $[M+H]^+$. Re-injection of the product determined the purity of the ligand by analytical HPLC. The diethyl malonate lanthanide complexes

were then dissolved in water. 1 M sodium hydroxide solution was used to adjust the solution to pH 12 until no longer changing, and the reaction mixture was stirred at room temperature overnight which resulted in the cleavage of the ethyl groups. Purification of the product was attempted with both reverse-phase HPLC and 500 MWCO cellulose membrane. Both methods were found to be successful. Figure 2.17 shows the ^{1}H NMR spectra of the Lu complexes before and after the deprotection of the ethyl groups.

2.3.5 The Pt coordination and oxidation

cis-[$Pt(NH_3)_2I_2$] was synthesised by stirring potassium tetrachloroplatinate with 10 equivalents of potassium iodide in water for 30 minutes. To the resulting potassium tetraiodide platinum complex, 2 equivalents of ammonium chloride was added to the solution, replacing two of the *cis* iodides. After stirring in water at pH 10 for 2 hours, the *cis*-[$Pt(NH_3)_2I_2$] was formed as an orange solid. Pure *cis*-[$Pt(NH_3)_2I_2$] was recrystallized from DMF. Aquation of the *cis*-[$Pt(NH_3)_2I_2$] in the presence of 2 equivalents of silver nitrate resulted in formation of silver iodide as a pale yellow precipitate which was removed by filtration. The clear filtrate containing **Pt.2.9** was used directly in the next step.

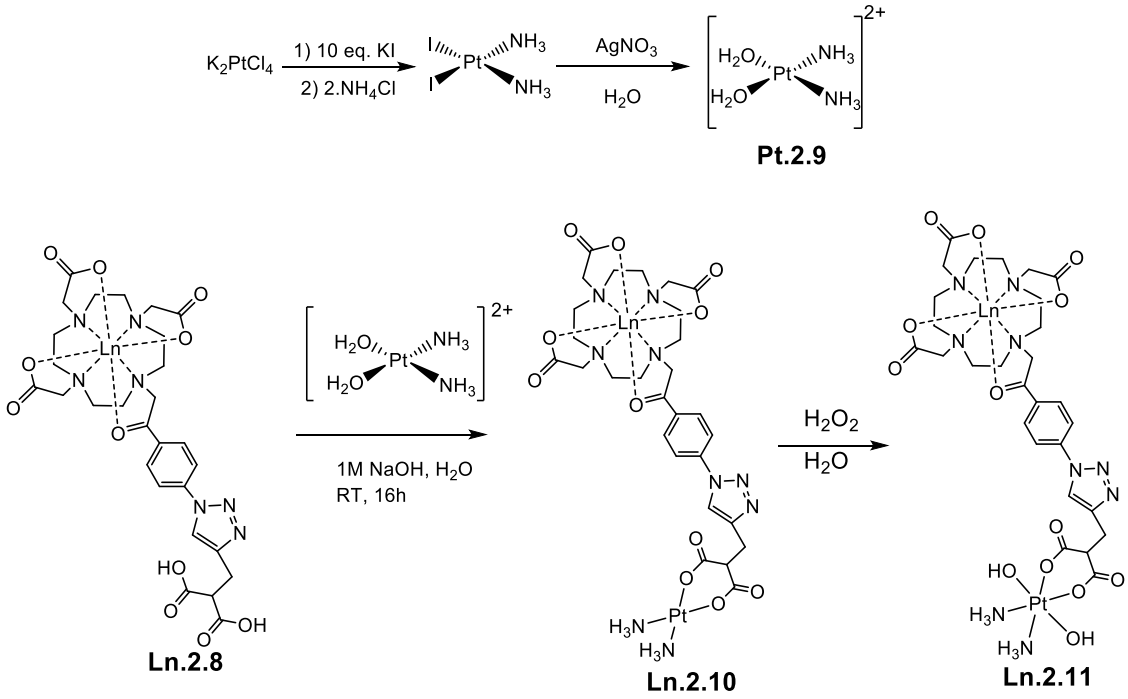

Figure 2.18: *synthetic pathway for making the Ln-Pt complex 2.10 and the oxidisation of the Pt(II) centre using H_2O_2.*

Pt.2.9 bound to the malonate appended lanthanide complexes **Ln.2.8** yielded the **Ln.2.10** complexes. 1 equivalent of **Ln.2.8** was added to the **Pt.2.9** water solution. 1M sodium hydroxide solution was added dropwise to adjust the pH of the solution to 9, and the resulting solution was stirred at room temperature for 24 hours. The reaction was monitored by reverse-phase HPLC, and the product was also purified by preparative HPLC using the same condition for isolating **Ln.2.8** complexes. The pH of the reaction turned out to be crucial for this reaction, basic sodium hydroxide was added to deprotonate the proton of the malonic acid which could accelerate the binding between the malonate and the platinum. However, the first attempt of this reaction in pH 12 resulted in insoluble black solid which was believed to be metallic Pt(0). This hypothesis was supported by a previous report that pH affects the interconversion between Pt(II) and Pt(0).[26] Later attempts of the reactions were all conducted at pH 9, and stirred at room temperature for 24 hours.

The oxidisation of the **Ln.2.10** complexes was achieved by stirring the purified **Ln.2.10**

complexes in 5% of hydrogen peroxide solution. The resulting product was purified by using reverse-phase HPLC, or 1000 MWCO cellulose membrane.

2.3.6 Photophysical characterisation of Eu-malonateDO3A-Pt complexes

Figure 2.19 depicts the UV-vis spectra of **Eu.2.8**, **Eu.2.10** and **Eu.2.11** complexes in H_2O at 10^{-4} M. The **Eu.2.8** complex exhibit a broad band at 280 nm in aqueous solution, which can be attributed to the ILCT transition located on the phenacyl triazole moiety. This shown a hypsochromic shift compared to the **Eu.2.5** complex (320 nm as shown in Figure 2.13). Both of the Eu-Pt(II) (**Eu.2.10**) and Eu-Pt(IV) (**Eu.2.11**) complexes exhibits a broad absorption band centred at 295 nm in aqueous solution which shows a bathochromic shift compared to **Eu.2.8**. This can be rationalised by the bidentate binding of the platinum to the malonate which results in the stabilisation of the charge-transfer excited states of the chromophore.

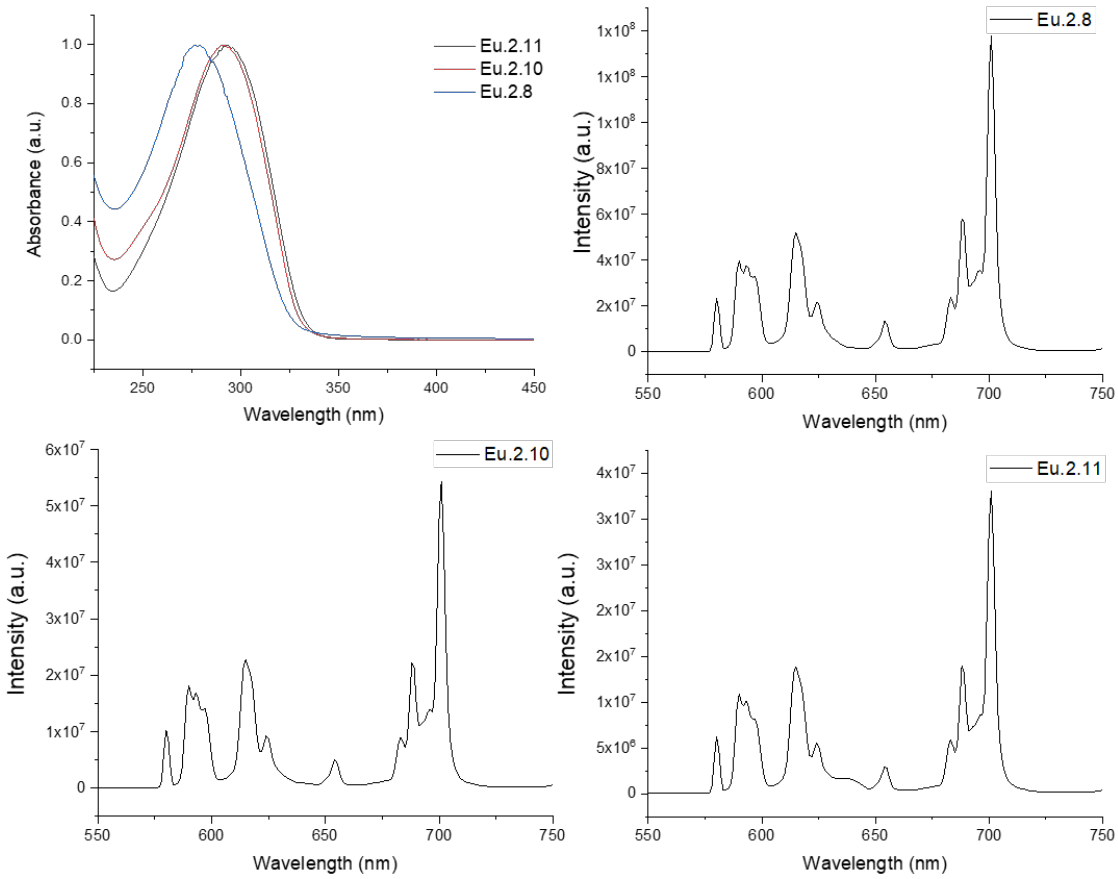

Figure 2.19: *Top left: UV-vis absorption spectra of the* ***Eu.2.8***, ***Eu.2.10*** *and* ***Eu.2.11****; top right: emission spectrum of* ***Eu.2.8****; bottom left: emission spectrum of* ***Eu.2.10*** *(Eu-Pt(II) complex), bottom right: emission spectrum of* ***Eu.2.11*** *(Eu-Pt(IV) complex). All of the spectra were measured in water,* λ_{ex} *= 357 nm, slit width 1nm.*

All of the peak shapes, especially the hypersensitive peaks of the three Eu complexes: **Eu.2.8**, **Eu.2.10** and **Eu.2.11**, are similar to each other. The $\triangle J_2/\triangle J_1$ ratio of the three Eu complexes are 1.35, 1.35 and 1.33 respectively. This indicates both binding of the Pt centre to the malonic ligand and the oxidation of the Pt barely affects the local symmetry of the Eu ion. This can be explained by the long distance between the lanthanide ion and the malonate bidentate ligand, which means modification on the malonate does not affect the coordination environment of the lanthanide.

2.3.7 ^{1}H and ^{195}Pt NMR characterisation

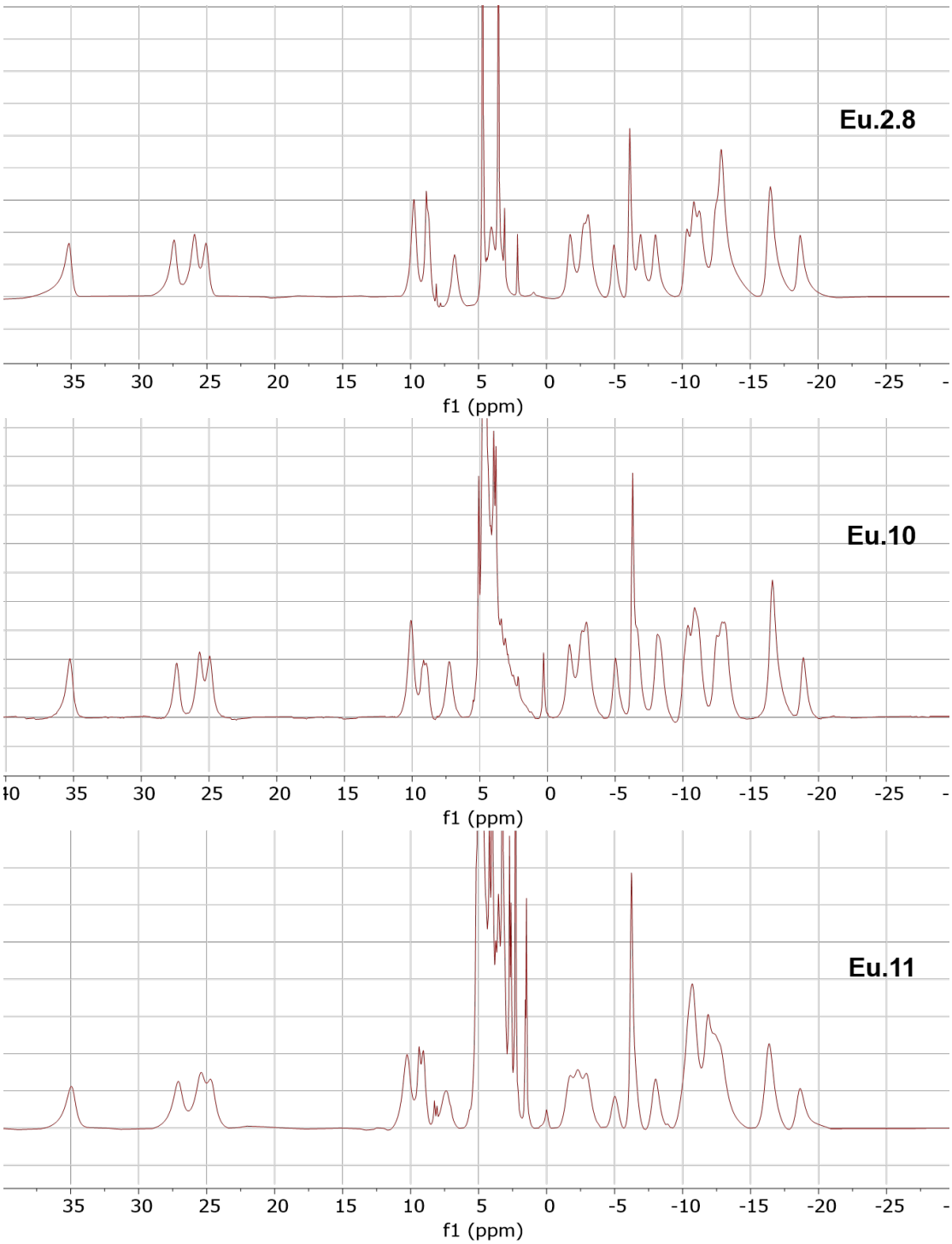

Figure 2.20: *The ^{1}H NMR spectra (D_2O, 400 MHz) of* ***Eu2.8*** *(top),* ***Eu.2.10*** *(Eu-Pt(II), middle) and* ***Eu.2.11*** *(Eu-Pt(IV), bottom) complexes.*

The ^{1}H NMR spectra of the three Eu complexes are shown in Figure 2.20, in all the three complexes, the exchanges of SAP and TSAP isomers were slow enough so that

the isomers can be distinguished obviously. The highly shifted peaks in the region around 35-25 ppm are assigned to the axial protons of the SAP isomers, while resonances observed in the spectra around 10 ppm indicate the presence of the TSAP. The chemical shifts of the SAP and TSAP peaks in the three Eu complexes are similar to each other. In all the three complexes, the ratio of the integration between SAP/TSAP isomers are all close to 1. The similarity of the chemical shifts and the same ratio of the integration of SAP/TSAP protons indicate that the binding of the platinum(II) and platinum(IV) moieties does not affect the coordination environments of the europium ions, which agrees with the luminescence results we discussed in the last section.

The ^{195}Pt NMR spectra of the Ln-Pt complexes with different Pt oxidation state were measured and shown in Figure 2.21. The chemical shifts of ^{195}Pt are consistent with Pt(II) and Pt(IV) oxidation states. The ^{195}Pt chemical shift of *cis*-$[Pt(NH_3)_2(H_2O))_2]^{2+}$ (complex **Pt.2.9**) was also measured as a reference to the **Ln.2.10** complex. The ^{195}Pt chemical shift of complex **Pt.2.9** is at -1596 ppm, upon binding to the malonate ligand, the ^{195}Pt resonance shifted upfield dramatically to -2098 ppm. This results from the replacement of the two neutral coordinated water molecules to the negative malonic bidentate ligand, which lead to the higher electron density around the Pt centre, thus the greater shielding effect. The Lu-Pt(IV) complex **Lu.2.11** has a ^{195}Pt signal at 1085 ppm. Different lanthanide centres did not affect the chemical shift of the ^{195}Pt NMR signal, as the ^{195}Pt chemical shift of the Eu-Pt(IV) complex **Eu.2.11** is 1084 ppm, which - within error - is the same as for the Lu-Pt(IV) complex as shown in Figure 2.21 bottom graph. This echoes with the luminescence and ^{1}H NMR result of Eu –Pt(II/IV) complexes discussed previously: the binding of the platinum and the oxidation states of the bound Pt centre do not affect the Eu centre because of the long distance between the Pt and the Ln. In this case, the paramagnetic Eu does not affect the ^{195}Pt resonance

as well.

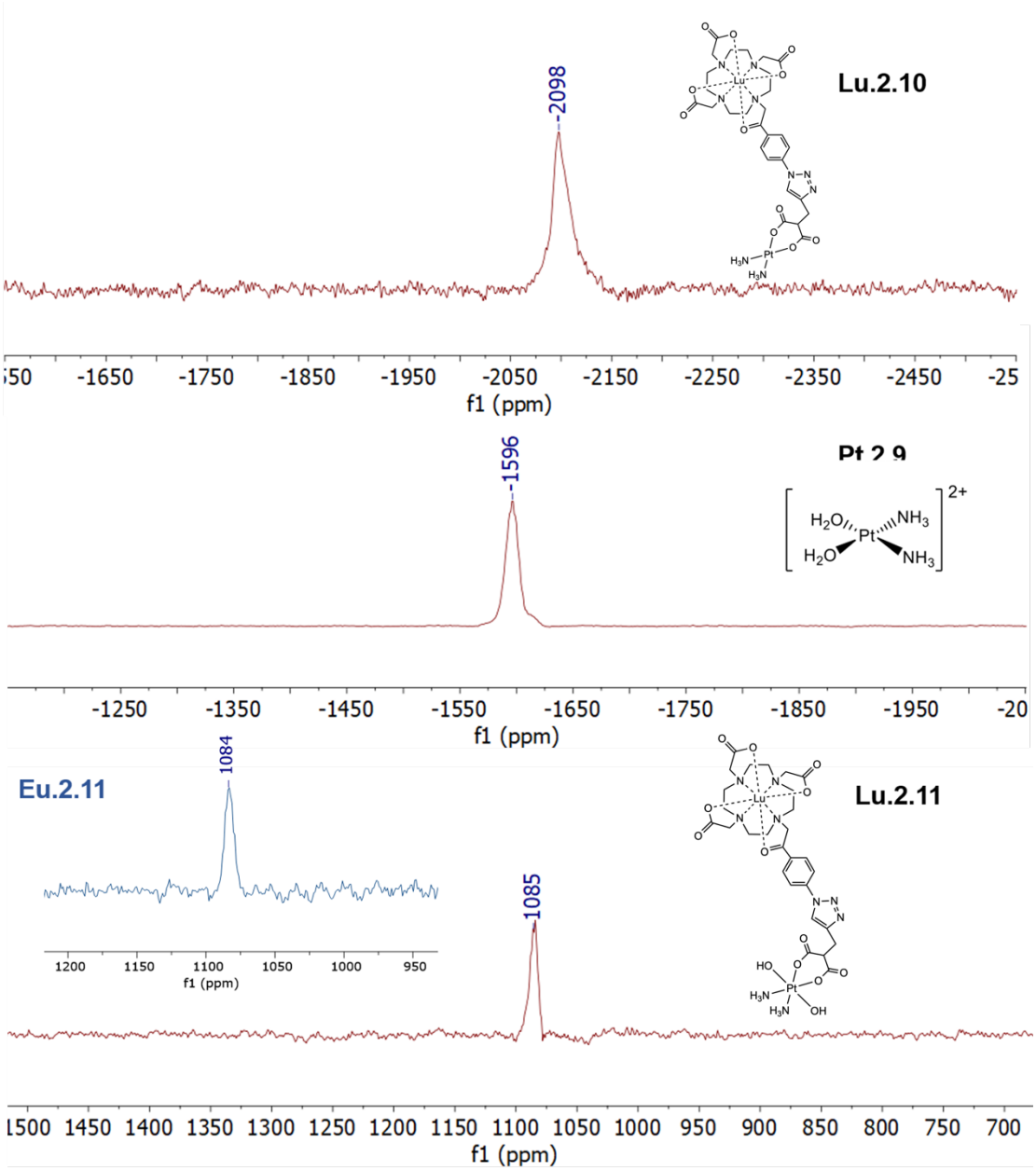

Figure 2.21: *The ^{195}Pt NMR spectra of* ***Lu.2.10*** *(top),* ***Pt.2.9*** *(middle) and* ***Lu.2.11*** *(bottom)* ***Eu.2.11*** *(bottom inset) in D_2O.*

2.4 Conclusion

This chapter described the synthesis and characterisation of a series of Ln-Pt bimetallic complexes in which the lanthanide ion is coordinated by a DO3A octadentate macrocyclic ligand with a pendent malonic arm, and the platinum is binding to the malonate ligand. The malonate ligand was coupled to the DO3A moiety via the CuAAC reaction. The advantages of using such an approach are the CuAAC reaction has been intensively utilised in coupling functional building blocks together, and the synthesis has proved to be straightforward. However, residual traces of copper ions from the catalyst may lead to undesirable cytotoxic effects, which would be a drawback if we want to apply these Ln-Pt complexes in *vivo*. Thus, effective ways of removing the residual copper salt need to be further investigated before the biological application of the complexes. Otherwise, alternative methods need to be applied to couple the lanthanide and the platinum moieties to avoid using a copper catalyst, which we will discuss in the following chapters. Other future work can involve modifying the axial ligands of the Pt(IV) complexes, so that - for example -imaging probes or drug molecules can be conjugated to the hydroxide group on the platinum to achieve multi-modality imaging or multi- function therapy.

References

1 H. C. Kolb, M. G. Finn and K. B. Sharpless, *Angew. Chemie - Int. Ed.*, 2001, **40**, 2004–2021.

2 V. V. Rostovtsev, L. G. Green, V. V. Fokin and K. B. Sharpless, *Angew. Chemie - Int. Ed.*, 2002, **41**, 2596–2599.

3 C. W. Tornøe, C. Christensen and M. Meldal, *J. Org. Chem.*, 2002, **67**, 3057–3064.

4 J. E. Moses and A. D. Moorhouse, *Chem. Soc. Rev.*, 2007, **36**, 1249–1262.

5 R. F. H. Viguier and A. N. Hulme, *J. Am. Chem. Soc.*, 2006, **128**, 11370–11371.

6 M. Jauregui, W. S. Perry, C. Allain, L. R. Vidler, M. C. Willis, A. M. Kenwright, J. S. Snaith, G. J. Stasiuk, M. P. Lowe and S. Faulkner, *J. Chem. Soc. Dalt. Trans.*, 2009, 6283–6285.

7 G. J. Stasiuk and M. P. Lowe, *Dalt. Trans.*, 2009, 9725–9727.

8 M. Tropiano, N. L. Kilah, M. Morten, H. Rahman, J. J. Davis, P. D. Beer and S. Faulkner, *J. Am. Chem. Soc.*, 2011, **133**, 11847–11849.

9 L. Frullano, C. Catana, T. Benner, A. D. Sherry and P. Caravan, *Angew. Chemie - Int. Ed.*, 2010, **49**, 2382–2384.

10 C. Szíjjártó, E. Pershagen and K. E. Borbas, *Dalt. Trans.*, 2012, **41**, 7660–7669.

11 P. A. Sukerkar, K. W. MacRenaris, T. R. Townsend, R. A. Ahmed, J. E. Burdette and T. J. Meade, *Bioconjug. Chem.*, 2011, **22**, 2304–2316.

12 M. Tropiano, C. J. Record, E. Morris, H. S. Rai, C. Allain and S. Faulkner, *Organometallics*, 2012, **31**, 5673–5676.

13 A. K. R. Junker, M. Tropiano, S. Faulkner and T. J. Sørensen, *Inorg. Chem.*, 2016, **55**, 12299–12308.

14 M. Tropiano, A. M. Kenwright and S. Faulkner, *Chem. - A Eur. J.*, 2015, **21**, 5697–5699.

15 T. C. Johnstone, K. Suntharalingam and S. J. Lippard, *Chem. Rev.*, 2016, **116**, 3436–3486.

16 M. A. Jakupec, M. Galanski, V. B. Arion, C. G. Hartinger and B. K. Keppler, *Dalt.*

Trans., 2008, 183–194.

17 Y. Xing, L. Lou, X. Chen, Q. Ye, Y. Xu, C. Xie, J. Jiang and W. Liu, *Bioorganic Med. Chem. Lett.*, 2012, **22**, 2239–2241.

18 J. Zhao, S. Gou and F. Liu, *Chem. - A Eur. J.*, 2014, **20**, 15216–15225.

19 A. Rosenfeld, J. Blum, D. Gibson and A. Ramu, *Inorganica Chim. Acta*, 1992, **201**, 219–221.

20 M. T. Wlodarczyk, S. A. Dragulska, O. Camacho-Vanegas, P. R. Dottino, A. A. Jarzęcki, J. A. Martignetti and A. J. Mieszawska, *ACS Biomater. Sci. Eng.*, 2018, **4**, 463–467.

21 D. Griffith, M. P. Morgan and C. J. Marmion, *Chem. Commun.*, 2009, 6735–6737.

22 H. P. Varbanov, S. Göschl, P. Heffeter, S. Theiner, A. Roller, F. Jensen, M. A. Jakupec, W. Berger, M. Galanski and B. K. Keppler, *J. Med. Chem.*, 2014, **57**, 6751–6764.

23 B. R. Hoffmeister, M. Hejl, M. S. Adib-Razavi, M. A. Jakupec, M. Galanski and B. K. Keppler, *Chem. Biodivers.*, 2015, **12**, 559–574.

24 M. S. Adib-razavi, M. A. Jakupec, M. Galanski and B. K. Keppler, 2012, **9**, 1840–1848.

25 C. Armstrong, *Korean Chem. Soc.*, 2003, **24**, 407-408.

26 D. S. Helfer and J. D. Atwood, *Organometallics*, 2002, **21**, 250–252.

Chapter 3: Photoactivatable Pt(IV) Triazole Anticancer complexes and Copper-free Click Reaction of Ln-Pt Complexes

3.1 Introduction

3.1.1 Photoactivatable anticancer drugs

Photoactivated chemotherapy (PACT) is a treatment involving photoactivatable drugs which are non-toxic under dark conditions, and can be photoactivated with light irradiation for medical applications. One of the advantages of PACT, compared to conventional photodynamic therapy (PDT), is that there is no requirement for molecular oxygen in order to instigate a photocytoxic effect. For solid tumours which are often hypoxic (i.e. low oxygen levels) this is particularly relevant.

Transition metals have been studied as photoactivatable anticancer drugs, of which Rh(III) and Ru(II) have been some of the most exploited over recent years.[1–7] Under 440 nm light irradiation, the Rh(III) complexes with cyclometalated ligands can cause DNA cleavage. Barton *et al.* reported a $[Rh(bpy)_2(chrysi)]^{2+}$ complex with a bulky cyclometalated chrysi ligand (5,6-chrysenequinone diamine) in 1999, and observed that the Rh(III) complexes show selective binding towards DNA upon activation.[1] In 2009, Sadler *et al*. presented the first case where a Ru(II) complex can selectively lead to photo-cleavage of a pyridine ligand upon visible-light irradiation, resulting in a reactive species which can bind to nucleobases.[5]

Metal complexes containing Fe(III),[8,9] Cu(II)[10] and V(VI)[11] were also explored as

photoactive anticancer agents, some of which can be activated by visible and near-IR light. Moreover, they are able to generate reactive oxygen species such as singlet oxygen ($^1O_2$) and enable the detection of photo-dissociation or DNA photo-binding activities.

Luminescent Pt(II) complexes have been studied thoroughly for applications in cell imaging due to their photophysical properties; and as photoactivated drugs because of their photochemical properties. Most of the Pt(II) complexes studied for these purposes are cyclometalated.[12–14] More recently, Pt(IV) prodrugs have been intensively studied to reduce the side-effects of Pt(II) anti-cancer drugs, because as low-spin d_6 complexes Pt(IV) complexes are more kinetically inert to substitution and require reduction to Pt(II) before exerting a cytotoxic effect. One strategy is the development of photoactivatable Pt(IV) complexes as anti-cancer prodrugs as they are relatively inert and non-toxic under dark conditions, but can undergo controlled and localised reduction to generate cytotoxic species. Bednarski *et al.* reported the first generation of photoactivatable Pt(IV) anticancer drugs.[15,16] As shown in Figure 3.1, the general formula of the diiodo Pt(IV) complex is *trans, cis*-[Pt(X)$_2$I$_2$(en)], where en = ethylenediamine and X = Cl-, OH-, acetate or methylsulfonate. The ethylenediamine bidentate ligand was chosen to produce a "*cis*" geometry of non-leaving groups, since - by extrapolation from cisplatin and transplatin - the *trans*-Pt(II) was not thought to be able to form lethal intrastrand DNA cross-links required for cytotoxic activity. It was advantageous to use the iodides as the ligands due to its low energy ligand-to-metal charge-transfer (LMCT) transition resulted from the fact that the iodide is a weak field ligand. For example, *cis*-[Pt(OAc)$_2$I$_2$(en)] and *trans,cis*-[Pt(OH)$_2$I$_2$(en)] had the UV-vis spectroscopic absorption bands centred at λ = 389 and 384 nm respectively, with a tail up to *ca.* 550 nm.[15] However, these complexes showed no significant difference between their dark and

light toxicities. This may be because they are too easily reduced by thiols in a cellular environment.[15,17]

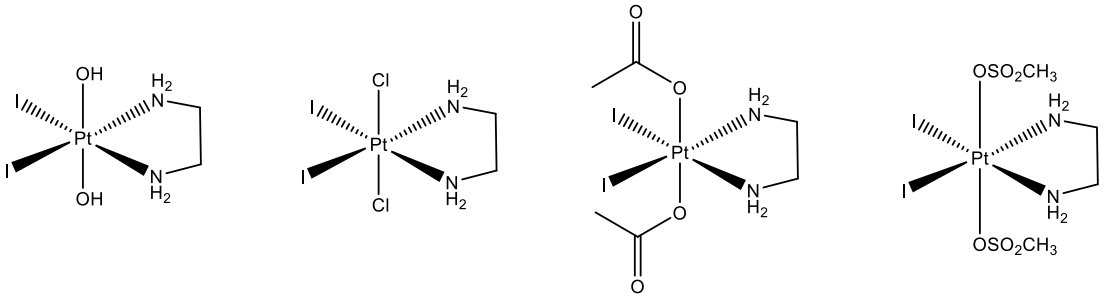

Figure 3.1: *Photoactivatable diiodo Pt(IV) complexes.*

The photochemical reduction of Pt(IV)-azido complexes was first reported by Vogler *et al*., which presented that *trans*-$[Pt(CN)_4(N_3)_2]^{2-}$ was converted to $[Pt(CN)_4]^{2-}$ upon irradiation with UV light (300 nm).[18] Following this, Sadler and Bednarski *et al*. developed and reported the second generation of photoactivatable Pt(IV) anticancer prodrugs, Pt(IV) diazidodihydroxido complexes, containing azides instead of iodides as the photo-cleavage groups.[19–26] Both the *cis* and *trans* diazido diammine Pt(IV) complexes as shown in Figure 3.2 (complex A and B) were studied and showed strong LMCT bands around 250 and 290 nm with the absorption tails ending around 480 nm. The initial UV-vis studies showed that the *cis* Complex A was activated slower than the *trans* Complex B which could be rationalised by the UV-vis absorption band of Complex B showing a 29 nm bathochromic shift compared to Complex A and the higher extinction coefficient of Complex B. Furthermore, the cytotoxic study also showed higher cytotoxicity for Complex B following photoactivation towards different human cancer cells.

Complex C and Complex D were synthesised and investigated with the ammine groups replaced by pyridine. Both complexes showed high stability in solution in the dark. Upon irradiation with UVA (365 nm) or blue light (420 nm), these complexes evolve azido radicals. Complex C and Complex D can be rapidly reduced to Pt(II)

species upon irradiation to form Pt(II) - 5'-GMP adducts in the presence of 5'-GMP used to mimic the binding of species to guanine in nucleic acids in aqueous solution.

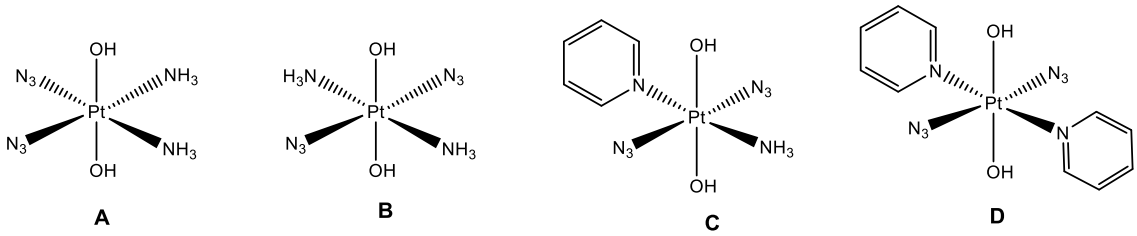

Figure 3.2: *Photoactivatable diazido Pt(IV) complexes.*

Further studies of the complexes were carried out using NMR spectroscopy,[27] EPR spectroscopy[28] and computational methods.[24] Functionalisation of the prodrugs in the axial position of the Pt[29] and replacing the pyridine with N-(heterocyclic) imine groups was also investigated.[30,31]

3.1.2 Copper-free azide-alkyne cycloadditions

Click chemistry has been expanded to develop Cu-free click reactions. It is advantageous since it avoids the use of a cytotoxic Cu catalyst.[32] For example, the strain-promoted azide-alkyne cycloaddition (SPAAC) reactions is a typical Cu-free click reaction. These are used in various biorthogonal reactions for labelling biomolecules,[32] achieving bifunctional drugs[33] and functionalising nanoparticles[34] *etc*. There is a major difference between CuAAC and SPAAC reactions: the product distribution. Normally for the Cu(I)-catalysed reactions resulting in asymmetrical compounds, one of the products is favoured over the other, while in the case of the SPAAC, both possible isomers are typically obtained (Figure 3.3).[35]

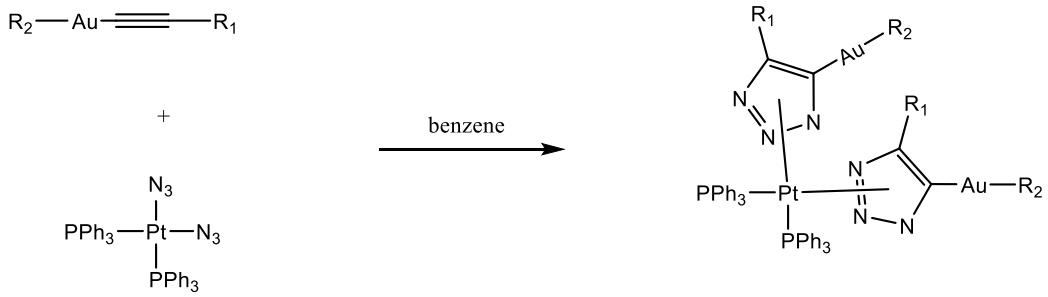

Figure 3.3: *Illustration of a copper-free click reaction between Au(I) and Pt(II) complexes, rearrangement could happen between Pt and the N atoms from triazole groups*.

A number of d-block metal azido complexes have been reported to undergo Cu-free cycloaddition reactions with unsaturated compounds, such as Au(I), Ru(II) and Pt(II).[36–41] Pt(IV) azido complexes were first reported for their Cu-free click reaction with alkynes by our group in 2018.[42] This research presented the study of the reactivity of a series of electron-deficient alkynes and *trans,trans,trans*-$[Pt(N_3)_2(OH)_2(py)_2]$. Since azido groups on Pt(IV) are considerably less electron-rich than those on Pt(II), the azido groups on Pt(IV) are considered to be likely to undergo cycloaddition with electron-deficient acetylenes.[43] However, it was shown that reactions can take place in mild conditions without a Cu catalyst using internal alkynes, producing both *mono* and *bis* click products. Terminal alkynes (HC≡CR) could undergo azide-acetylene ligand exchange with metal azides, rather than 1,3-dipolar cycloaddition. This was also reported by Pombeiro that *cis*-$[Pt(N_3)_2(PPh_3)_2]$ reacts with phenylethyne to give *trans*-$[Pt(C{\equiv}CPh)_2(PPh_3)_2]$.[44]

There are also some examples of lanthanide complexes that undergo SPAAC reactions. Most of them are lanthanide complexes with an appended arm that contain a strained alkyne such as dibenzylcyclo-octyne (DBCO), which undergoes click reactions with azido functional groups to achieve coupling.[45,46]

3.1.3 Aim of this chapter

The previous chapter described using a CuAAC reaction to couple an azido-containing lanthanide building block with an alkyne-containing building block that coordinates to platinum moieties. However, the drawback of the CuAAC method is that the copper is toxic in biological systems, and the presence of copper(I) could also lead to the unexpected reduction of platinum(IV). Therefore, we investigated an alternative way to link the lanthanide-containing and platinum-containing building blocks by using strained alkynes which do not require a Cu catalyst for the click reaction to occur.

Following the synthetic success of the SPAAC reactions between *trans,trans,trans*-$[Pt(N_3)_2(OH)_2(py)_2]$ and the strained alkynes discussed previously, in this section we extended the studies of SPAAC reactions of the Pt(IV) complex with another two strained alkyne - 1,4-diphenyl-2-butyne-1,4-dione and 5,6,11,12-tetradehydrodibenzo[a,e]- cyclooctene (Sondheimer diyne). We have not only studied the synthesis and characterisation of the click products, but also investigated in their photophysical and photochemical properties and their potential as photoactivatable anticancer drugs. We then employed the SPAAC reaction of *trans,trans,trans*-$[Pt(N_3)_2(OH)_2(py)_2]$ and azidophenacylDO3A Ln complexes, to couple the lanthanide and platinum moieties together under mild conditions.

3.2 Phenyl Click Platinum Complexes

3.2.1 Synthesis and purification

The reaction scheme of between *trans,trans,trans*-$[Pt(N_3)_2(OH)_2(py)_2]$ (Complex **3.1**) and 1,4-diphenyl-2-butyne-1,4-dione (Complex **3.2**) is illustrated in Figure 3.4. The synthesis of Complex **3.1** followed the method that was previously reported in 2010.[47]

We investigated various conditions of the SPAAC reactions including different solvents. When the reaction was conducted in methanol it resulted in decomposition with formation of a black Pt(0) precipitate, while in acetonitrile the reaction afforded cycloaddition products. Thus, the solvent plays an important role in the cycloaddition reaction. We also determined that adventitious residual H_2O_2 contaminant in the **3.1** (remaining from the final synthesis step of this compound) has a significant effect on the product formation, which will be discussed in detail in later sections.

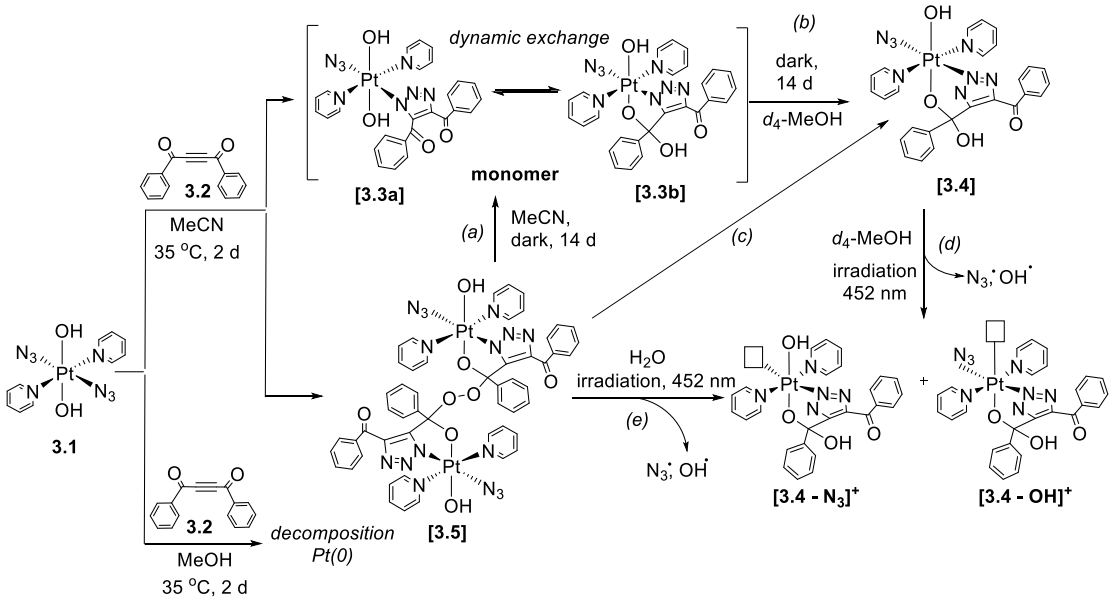

Figure 3.4: *The reaction scheme of SPAAC reaction between **3.1** and **3.2**.*

Following the reaction scheme shown in Figure 3.4, Complex **3.1** and alkyne **3.2** were dissolved in acetonitrile. The reaction was stirred at 35°C for 48 h, after which the solvent was removed by rotary evaporation, and the crude product was obtain as pale yellow solid. The crude solid was purified by reverse-phase HPLC under neutral conditions, as shown in Figure 3.5, the first fraction at t_R = 0.66 min corresponding to unreacted **3.1**, the second fraction at t_R = 4.01 min was the *bis*-nuclear species **3.5** in which the two Pt moieties was linked by O-O bond, the third fraction at t_R = 4.31 min was the *mono*-nuclear complex **3.3**. The residual H_2O_2 of **3.1** from oxidation reaction

was found to have a significant effect on the *bis*-nuclear product, the more H_2O_2 present in the starting materials **3.1** the more dimer is formed. When HPLC-purified **3.1** was used for the reaction (which meant there was no residual H_2O_2) there was only *mono*-nuclear product was formed according to the HPLC and the ^{1}H NMR spectra results. Both the monomer and dimer products were collected by mass-directed HPLC. The molecular weight of the dimer exceeded the detection limit of the HPLC mass spectrometer (1250 m/z), both the monomer and dimer were collected as the same fragmentation product [**3.3 - OH**]$^+$ at 688 *m/z* as shown in Figure3.6. We were initially unaware of that **3.5** was a dinuclear species, until the X-ray crystallographic structure was obtained (Figure 3.13), HRMS and NMR spectroscopic data helped to confirm the structure.

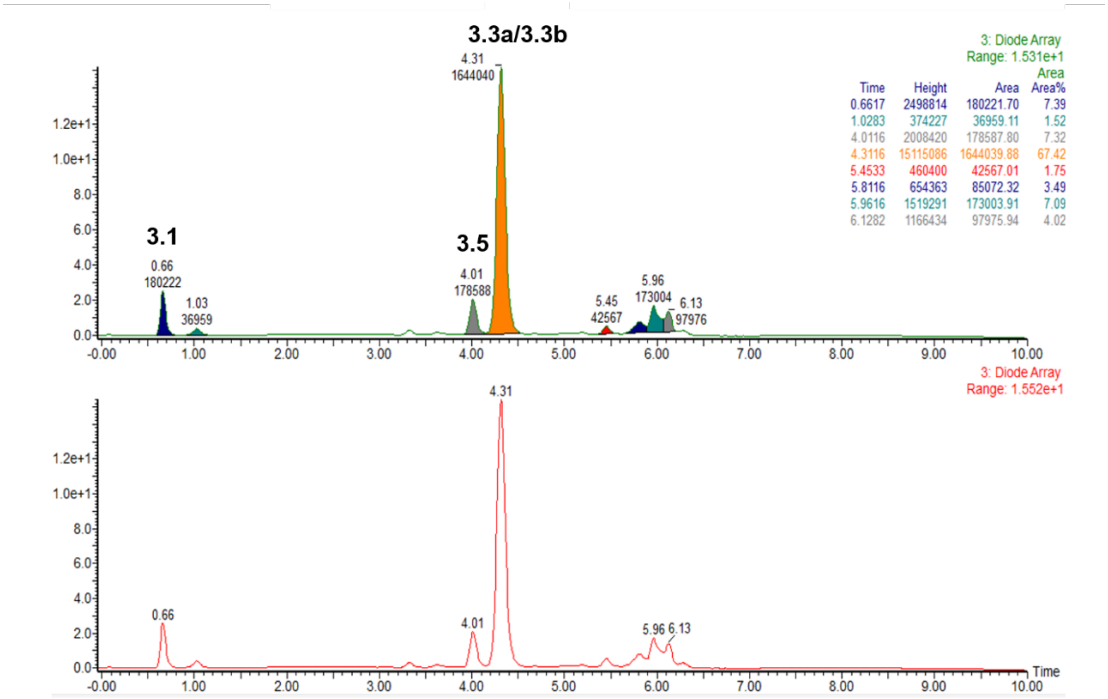

Figure 3.5: *HPLC trace of crude mixture from reaction between complex **3.1** and **3.2** showing product distribution. t_R = 4.01 min (3.**5, 8%**), 4.31 min (complex **3.3a/3.3b, 73%**).*

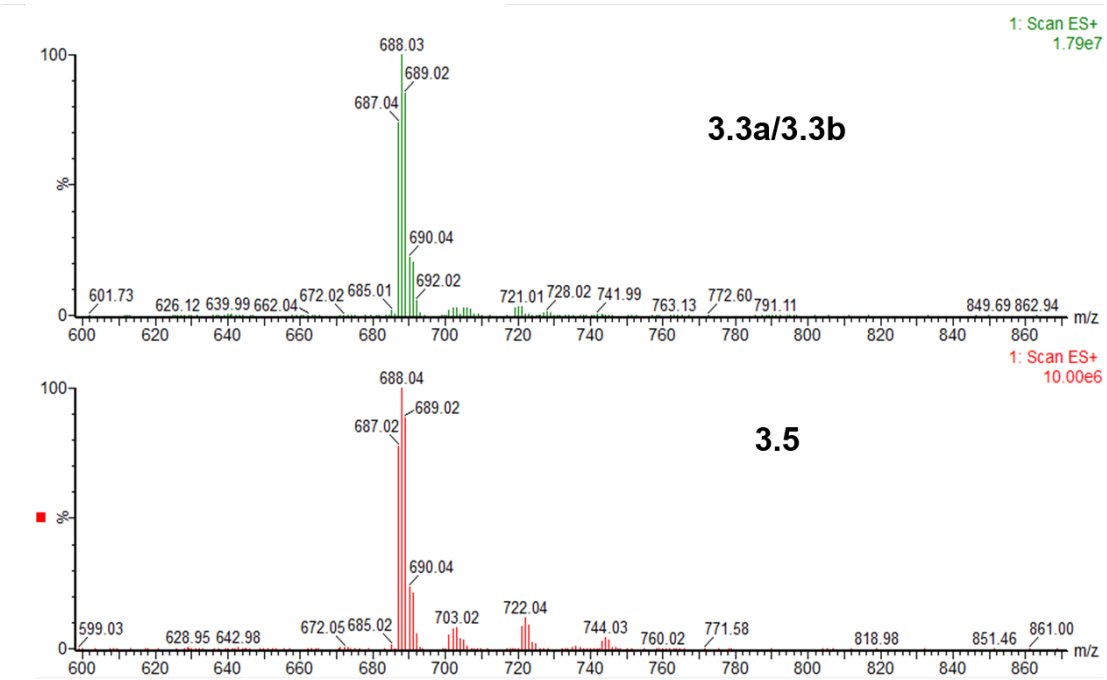

Figure 3.6: *Extracted ESI-MS spectra of* ***3.5*** *and* ***3.3a/3.3b*** *from the HPLC traces.*

3.2.2 Characterisation of the monomer

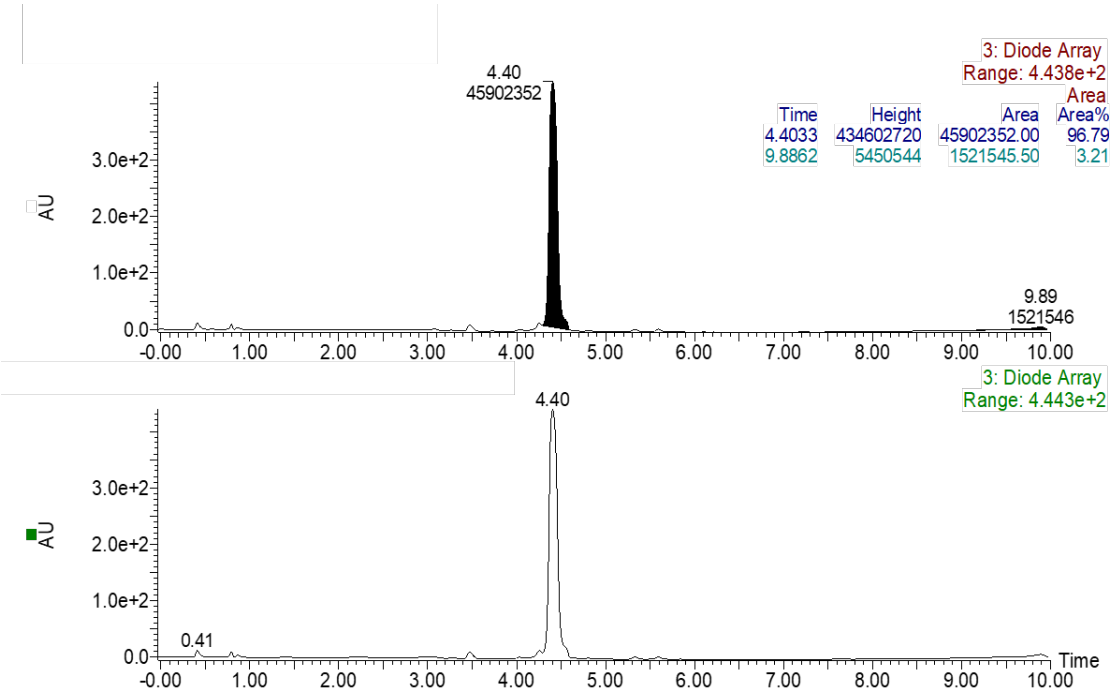

Figure 3.7: *Analytical RP-HPLC trace of* ***3.3*** *showing co-elution of the two interconverting isomers* ***3.3a*** *and* ***3.3b****.*

After HPLC purification, the HPLC eluent of the collected fractions was removed by freeze-drying. Although on re-injection for analytical HPLC the fraction of monomer

eluted as a single peak (Figure 3.7), in d_3-MeCN solution at 25 °C, the monomer existed in dynamic equilibrium between two isomers in a 1:1 ratio. ^{1}H and ^{13}C NMR spectral resonances of complexes **3.3a** and **3.3b** were fully characterised by 1D and 2D (COSY/ROESY/HSQC/HMBC) spectroscopic techniques. Figure 3.8 illustrates the ^{1}H NMR of **3.3a/3.3b** with full assignment. Figure 3.9 is the ^{1}H-^{195}Pt HMBC NMR spectroscopy of the **3.3a/3.3b** in d_3-MeCN, which revealed two distinct ^{195}Pt environments, for **3.3a** (689 ppm) and **3.3b** (785 ppm) respectively. Addition of D_2O to the d_3-MeCN NMR sample resulted in the loss of the **3.3b** C-OH ^{1}H NMR spectral resonance at 4.93 ppm, as a result of proton/deuterium exchange. The equilibrium species **3.3a/3.3b** were stable in d_3-MeCN (in the dark), for a period of at least 6 months. Although in the HPLC mass spectrum, complex **3.3** was shown as [**3.3 - OH**]$^{+}$ (688.04 m/z), in HRMS, [**3.3 + H**]$^{+}$ (706.15 m/z) was observed (**Figure 3.10**).

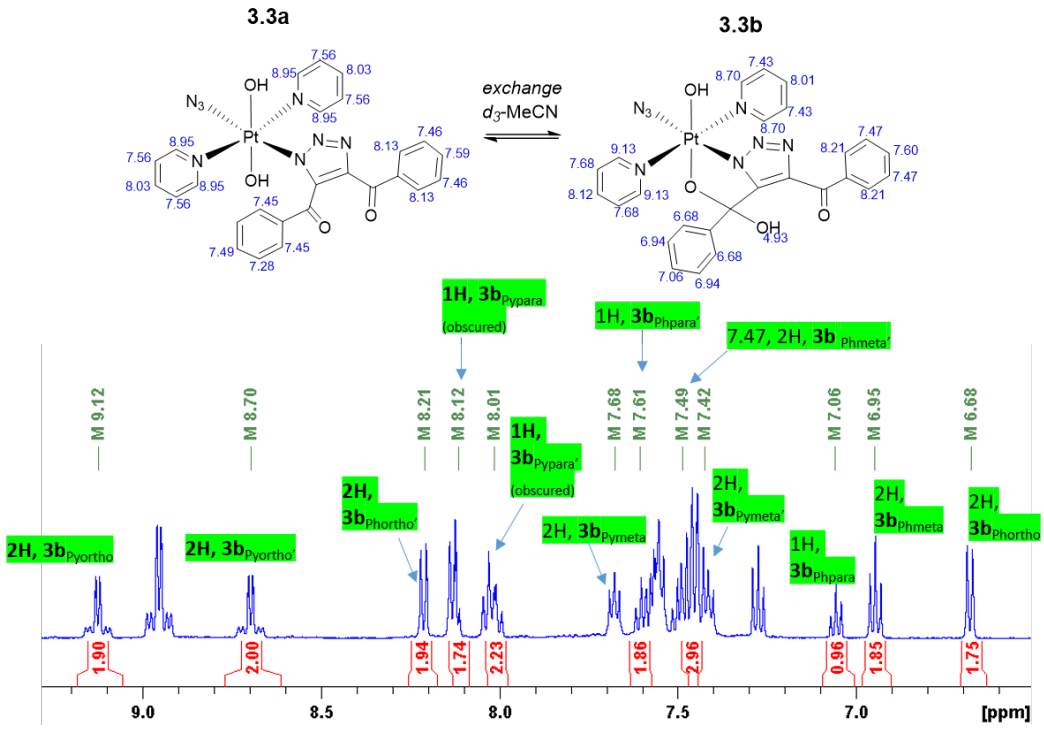

Figure 3.8: *^{1}H NMR spectrum of complex **3.3a/3.3b** with assignments.*

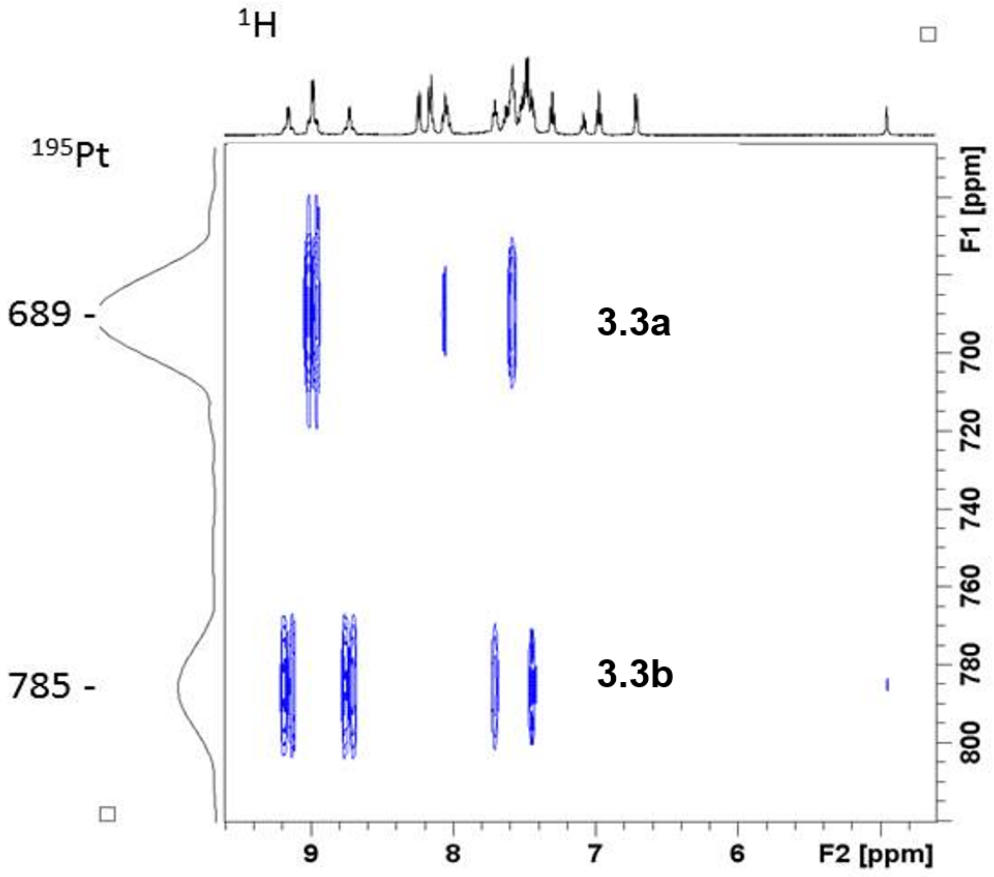

Figure 3.9: *^{1}H-^{195}Pt HMBC NMR (proton at 500 MHz) spectrum of complex **3.3** in d_3-MeCN, showing the presence of two isomers **3.3a** and **3.3b**.*

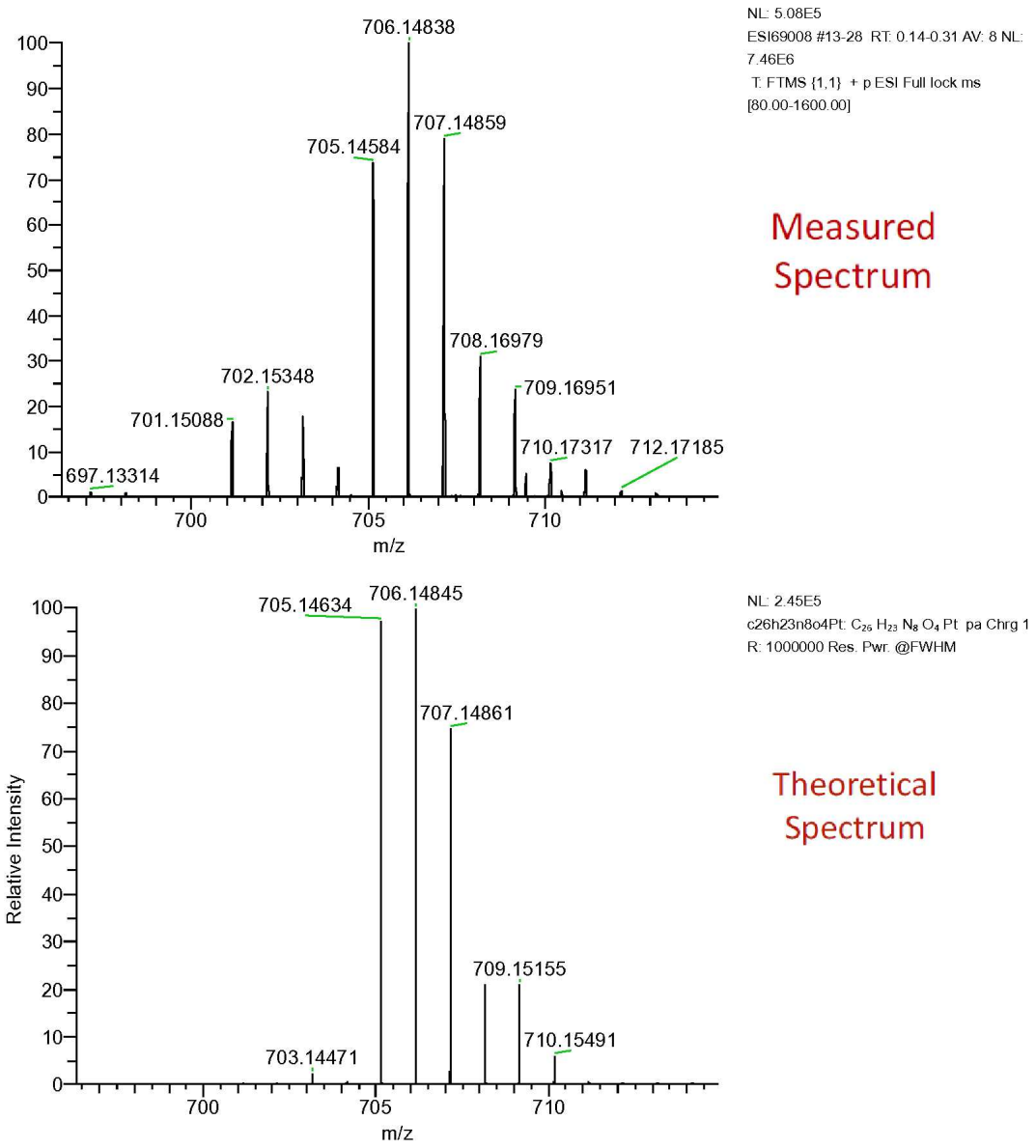

***Figure 3.10**: HRMS of complex **3.3** species [**3.3**+**H**]$^+$ (706.1484 m/z), mass error:0.1 ppm.*

The crystals of **3.3b** were grown by a Part II student – Sam Hare as yellow crystals, by vapour diffusion of tetrahydropyran into a concentrated MeCN solution of HPLC-purified **3.3**. Single crystal X-ray crystallography revealed the structure of the *mono*-click product (**3.3b**) which had cyclised *via* attack of the Pt-OH ligand at the PhCO group to form a 5-membered ring, the crystal structure was shown in Figure 3.11.

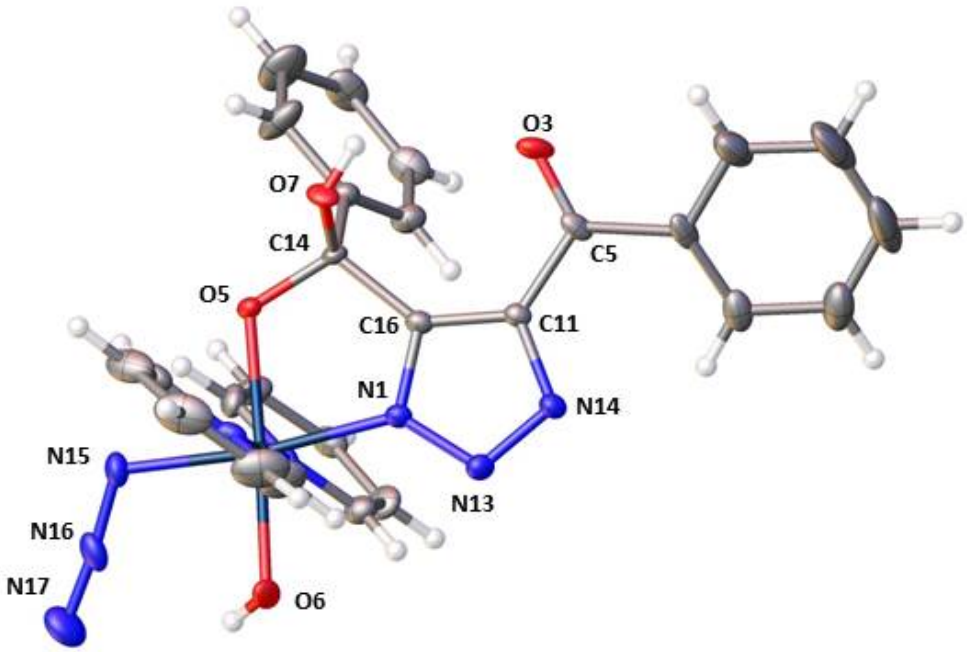

Figure 3.11: *X-Ray crystallographic structure of **3.3b** with thermal ellipsoids display at 50% probability. Pt-azido group naming convention; N15 = N_α, N16= N_β and N17 = N_γ.*

Both the azido (Pt-N_α-N_β-N_γ) ligand angle and bond lengths are very similar to those seen in the diazido precursor complex; (174.8(6)° in **3.3b** vs 174.4(4)/175.3(4)° in diazido Pt(IV) complex **3.1**);[47] and 1.218(6)/1.215(4), 1.218(5) Å (N_α-N_β) and 1.142(6)/1.139(4),1.146(5) Å (N_β-N_γ) in **3.3b** and **3.1** respectively. The angle subtended at Pt-N_α-N_β is more acute for complex **3.3b** (114.2(3)°) compared to complex **3.1** (118.0(3)°, 120.3(2)°). The Pt-N1 triazole bond length is 1.998(4) Å, which, compared to reported Pt(II) N1-coordinated 1,4-disubstituted triazole complexes with lengths of 2.149(2) Å - 2.139(2) Å, is indicative of relatively strong bonding.[48]

3.2.3 Purification and characterisation of the dimer 3.5

The HPLC-purified complex **3.5** was dried by lyophilisation. **3.5** was noticeably less soluble than complex **3.3** in organic solvents (MeCN, MeOH). In mass-direct HPLC, **3.5** was collected as 688 *m/z* due to its molecular mass exceeding the detection limit, in HRMS, [**3.5** + **Na**]$^+$ (1465.26 m/z) was detected as shown in Figure 3.12 with the mass error 0.73 ppm.

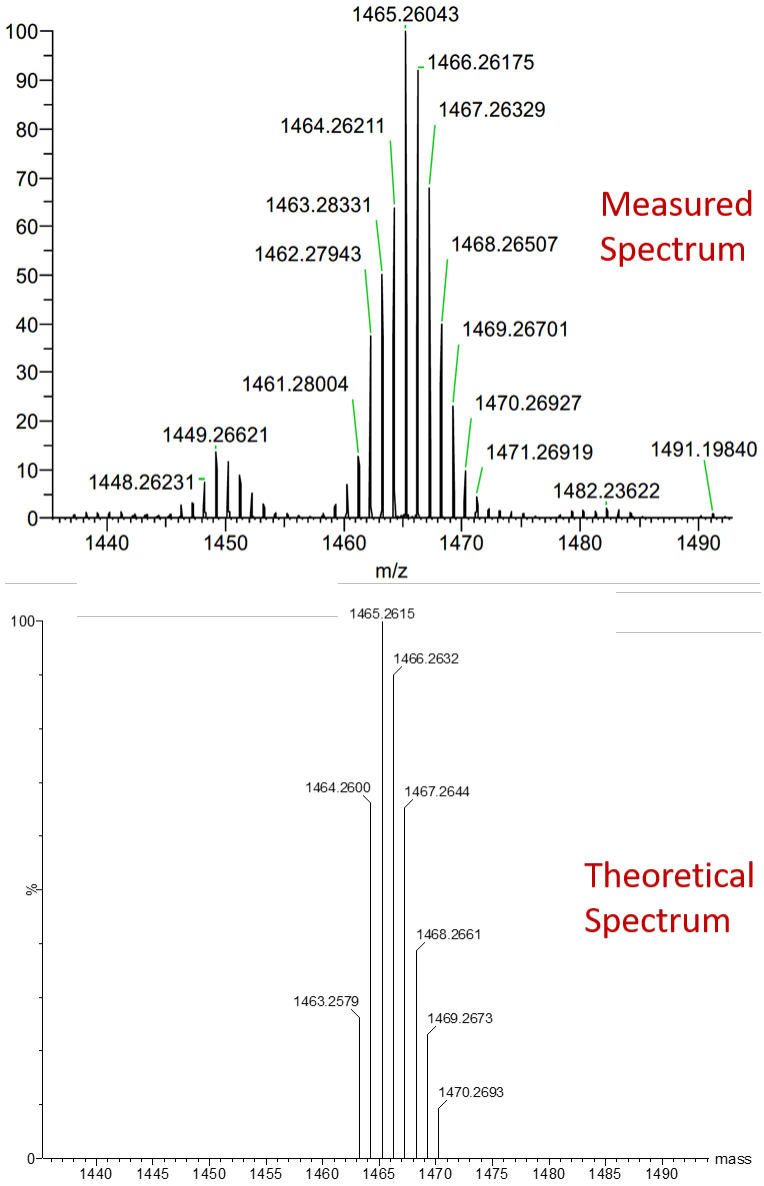

Figure 3.12: *HRMS of complex [**3.5** +**Na**], 5.6 ppm error.*

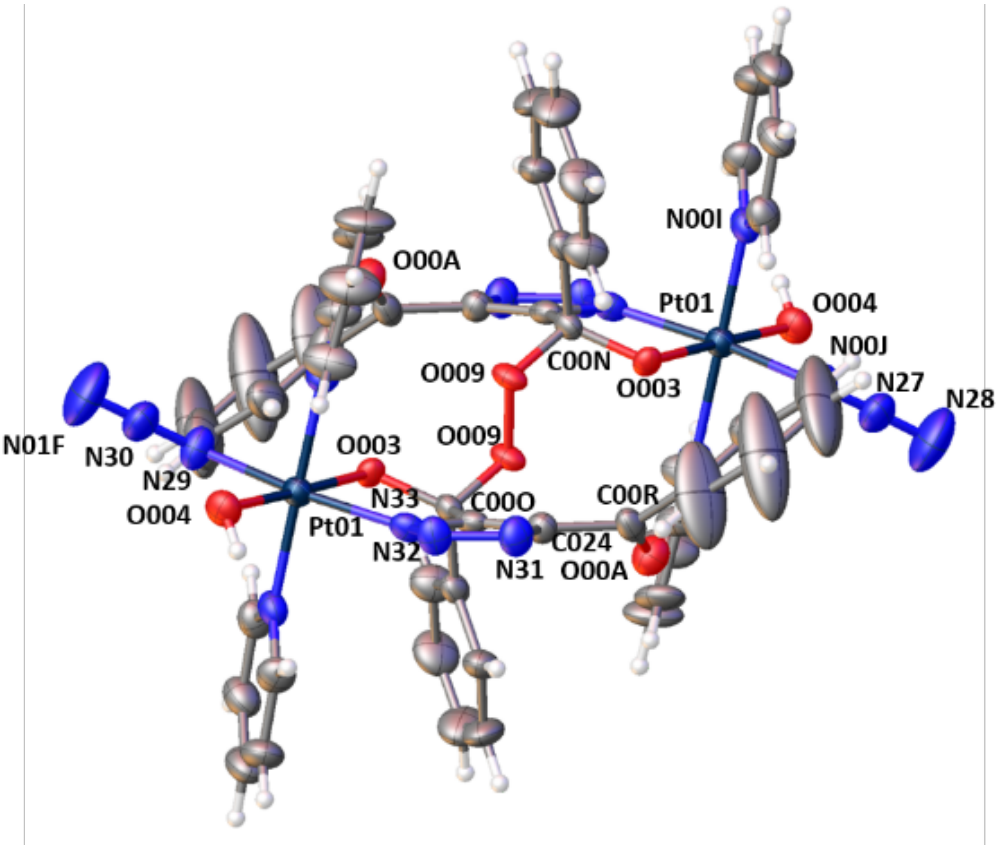

Figure 3.13: *X-Ray crystallographic OLEX2 structure of the peroxide dimer 3.5 with thermal ellipsoids displayed at 50 %. fully labelled structure is given in Experimental section.*

The X-ray crystal structure of 3.**5** shows an O-O bond length of 1.475(8) Å, consistent with a bond order of **3.1**[49] and it also exhibits a C00N-O009 (peroxide) bond length of 1.432(8) Å. The Pt-N azido (Pt-N29-N30-N01F) ligand shows slightly greater linearity (176.8(9)°) than is observed in the azido ligand(s) contained in both **3.3b** and **3.1**. The bond lengths within the azido ligand are very similar to **3.3b** and to **3.1**; 1.210(9) Å (N29-N30) and 1.147(9) Å (N30-N01F). The angle subtended at Pt-N29-N30 (116.0(5)°) is intermediate between that seen for complex **3.3b** and complex 3.**1**, and the Pt-N33 triazole bond length is 2.011(6) Å, slightly elongated in comparison to **3.3b**.[50]

^{1}H and ^{13}C NMR spectral resonances of **3.5** were fully characterised by 1D and 2D spectroscopic techniques. Figure 3.14 and Figure 3.15 illustrate the ^{1}H NMR and ^{13}C NMR spectra of the **3.5** with full assignment respectively. Although the determination

of the resonances of the two pyridines are tentative. Most of the ^{1}H NMR spectroscopic features resemble the monomer complex **3.3a/3.3b**: the protons in the *ortho* positions of the pyridine ligands are in chemical shifts around 9 ppm and have sharp ^{195}Pt NMR satellites. A singlet was observed at 9.16 ppm in **3.5**, which underwent exchange with the residual water peak.This may correspond to protons of the associated/coordinated H_2O_2. Assignment of the ^{13}C NMR spectra was aided HSQC and HMBC experiments. Many features of the ^{13}C NMR spectrum of **3.5** were similar to that of **3.3a/3.3b**, including the observation of a $^{2}J_{CPt}$ coupling of 43.8 Hz for one of the quaternary triazole carbon resonances in **3.5** (150.5 ppm).

Figure 3.16 is the ^{1}H-^{195}Pt HMBC NMR spectrum of **3.5** in d_3-MeCN, the ^{195}Pt NMR resonance of **3.5** is at 776 ppm, while in the same solvent the monomers **3.3a/3.3b** give rise to two resonances at 689 ppm and 785 ppm respectively. This suggests that dynamic exchange processes are similar to those seen for **3.3** do not occur in **3.5**, consistent with the carbonyl/hydroxyl group of the triazole ligand being part of the stable peroxide bond.

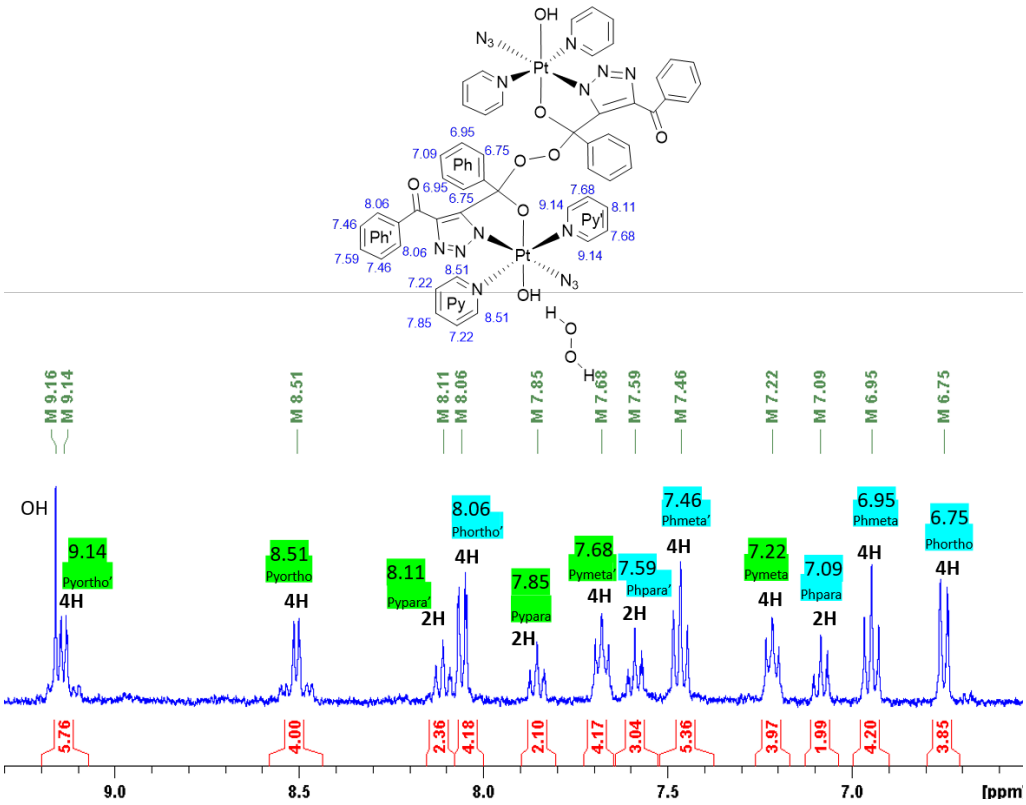

Figure 3.14: *^{1}H NMR spectrum of **3.5** (d_3-MeCN) with assignments.*

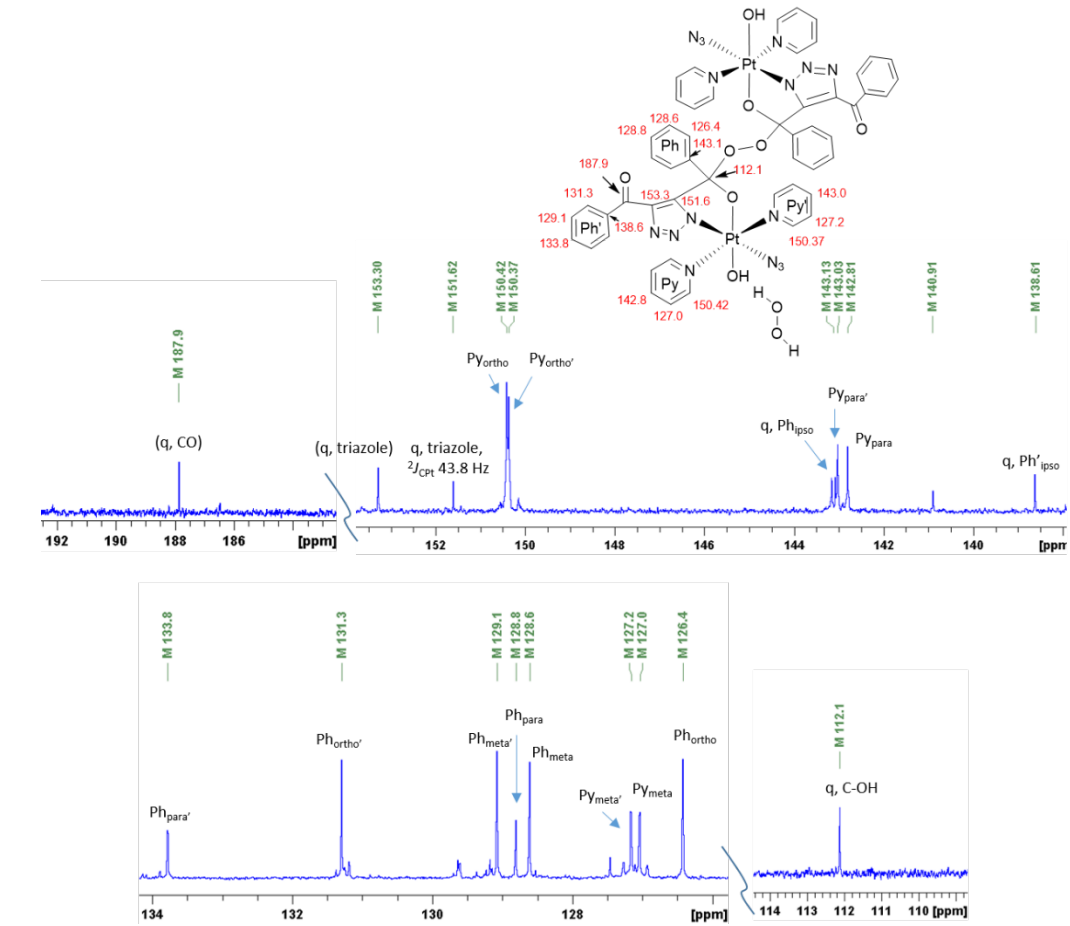

Figure 3.15: *^{13}C NMR spectrem of **3.5** (d_3-MeCN) with assignments.*

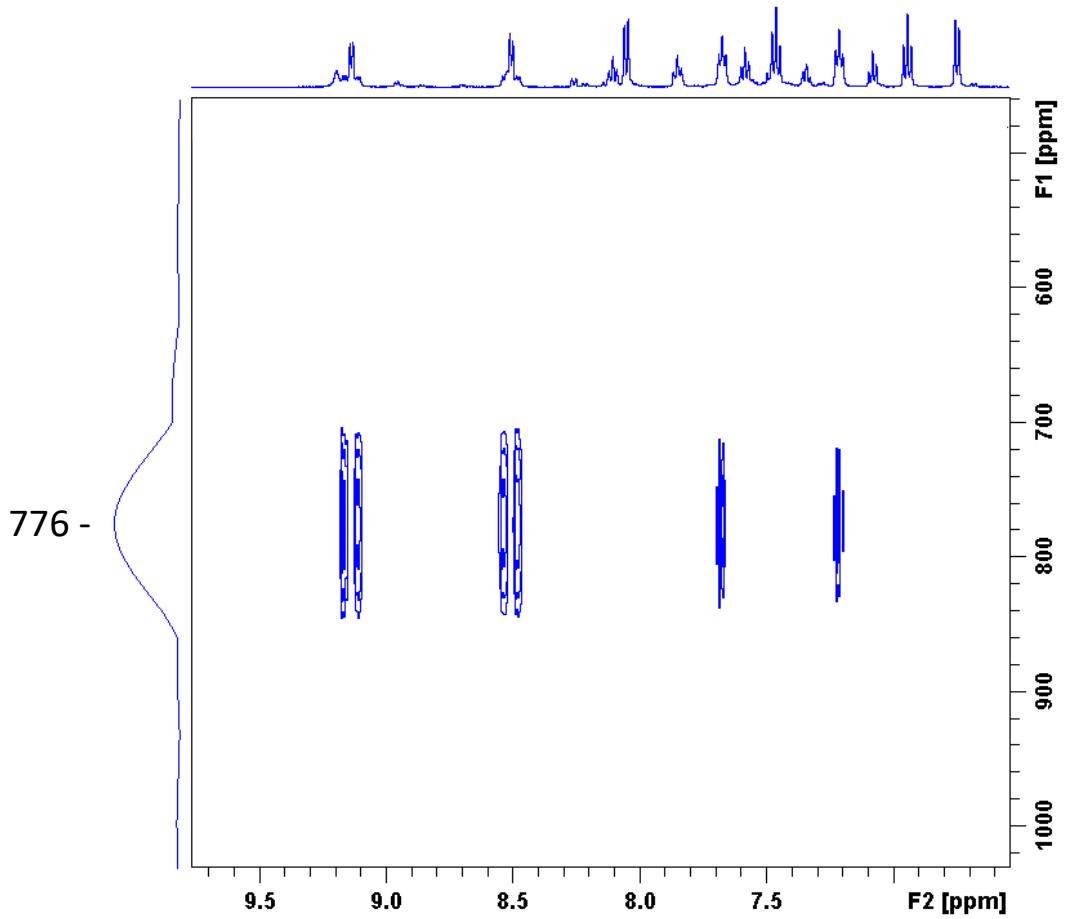

Figure 3.16: *^{1}H-^{195}Pt HMBC NMR (proton at 500 MHz) spectrum of complex **3.5** in d_3-MeCN.*

UV-vis spectroscopy of **3.3a/3.3b** was consistent with partial loss of a N_3→Pt LMCT band, with the λ_{max} moving to shorter wavelengths, from 299.5 nm (complex **3.1**) to 261.5 nm (complex **3.3**) (Figure 3.17). The UV-vis absorption spectrum of complex **3.5** was broadly similar to the spectrum of **3.3a**.

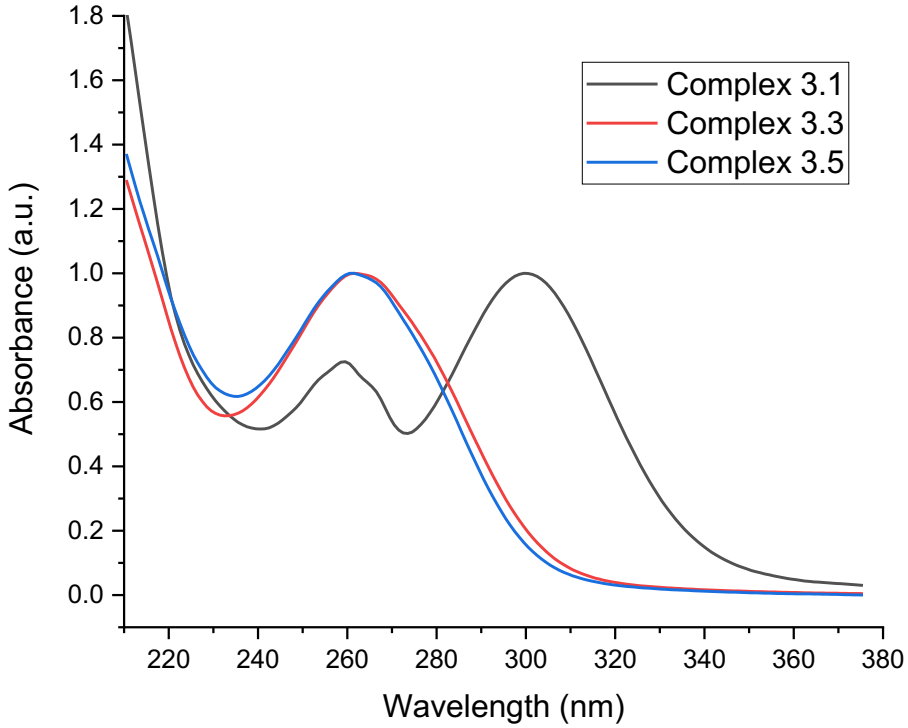

Figure 3.17: *Comparison of the UV-vis absorption spectra of complex **3.1**, **3.3** and **3.5**.*

IR spectroscopy of a freshly prepared d_4-MeOD sample of complex **3.3** showed a sharp peak at 2048 cm^{-1} arising from the strong asymmetric N_3 stretch. The IR spectroscopy of **3.5** in d_4-MeOD revealed a sharp peak at 2049 cm^{-1}.This was slightly weaker compared to the starting diazido complex **3.1** (2051 cm^{-1}, solid),[51] but is similar to the value reported for the cyclometallated mono triazole DMAD complex *trans,trans,trans*-[$Pt(N_3)(C_5H_3N_3O_4)(OH)(py)_2$] (2047 cm^{-1}).[42]

3.2.4 Interconversation of 3.3 and 3.5 in solution

a. Conversion of 3.3a/3.3b to 4 in d_4-MeOD

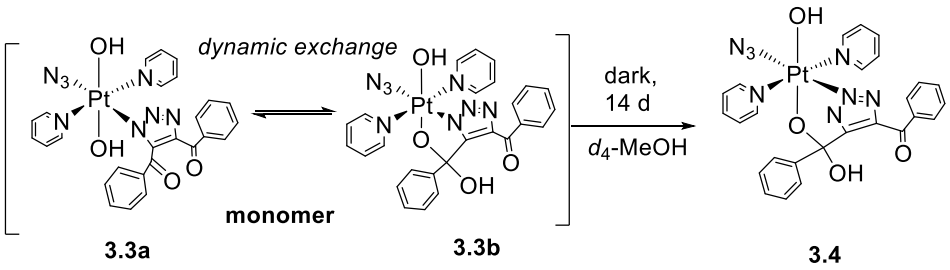

Figure 3.18: *illustration of the conversion of complex **3.3a/3.3b** to complex **3.4** in d_4-MeoD.*

When the synthesis of **3.3a/3.3b** was conducted in MeCN followed by solvent removal and resuspension of solid **3.3a/3.3b** in protic solvents, it did not result in decomposition. Instead, **3.3a/3.3b** underwent a conversion to a new complex (**3.4)** in d_4-MeOH (Figure 3.18). By the time ^{13}C, ^{1}H-^{13}C HSQC and HMBC NMR spectral data had been acquired for a freshly prepared solution of **3.3a/3.3b** in d_4-MeOH, partial conversion to **4** had already begun. Complete conversion of **3.3a/3.3b** to **3.4** was relatively slow, with 100% conversion after 22 d (^{1}H NMR spectroscopy, d_4-MeOH, Figure 3.19). During this time, the ^{195}Pt NMR spectral resonances at 832 ppm (**3.3a**) and 784 ppm (**3.3b**) converged to a single resonance at 824 ppm for **3.4** (d_4-MeOH).

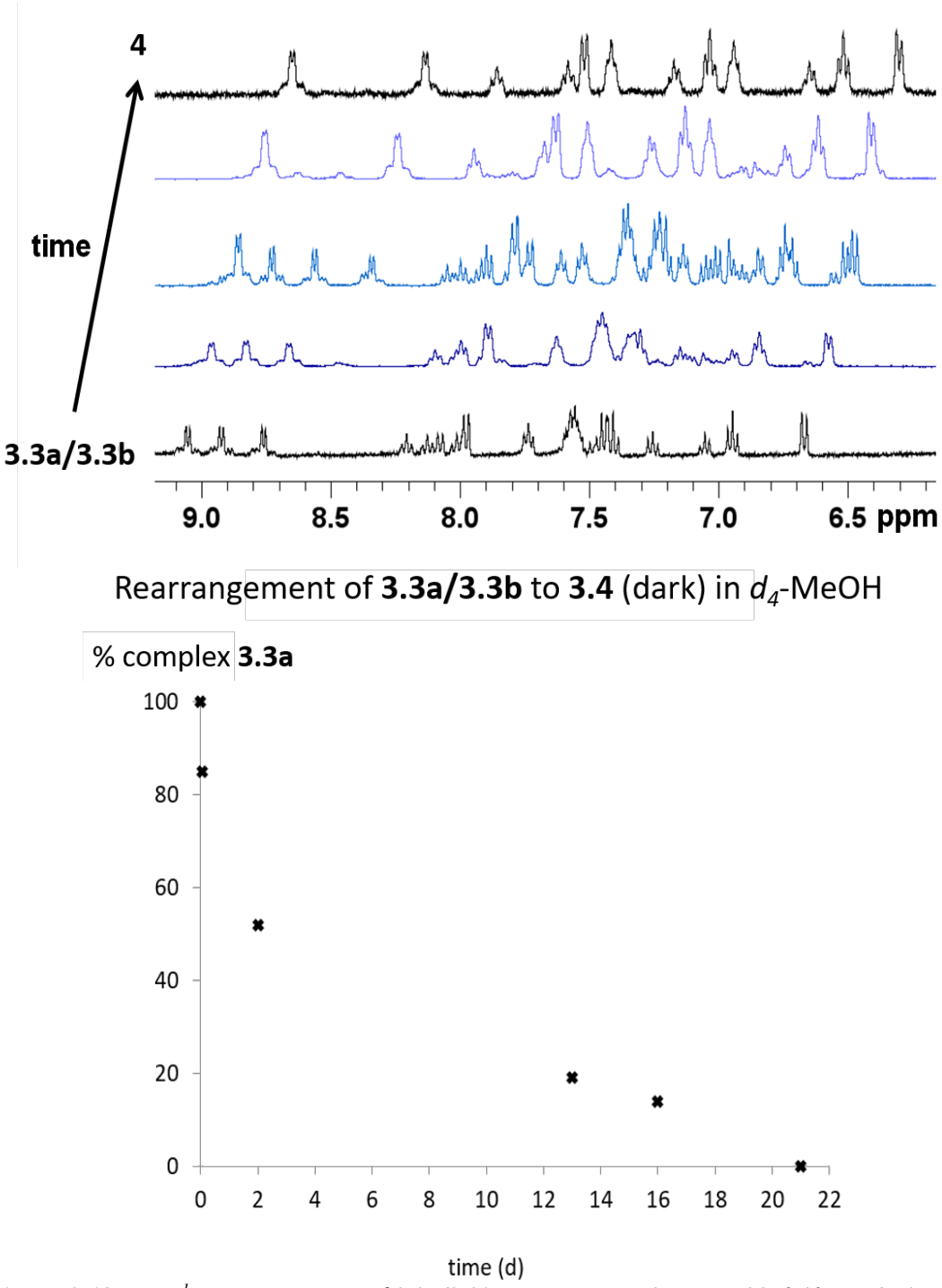

Figure 3.19: *Top: ^{1}H NMR spectra of **3.3a/3.3b** converting to **3.4** over 22 d (d_4-MeOH) at 20 ^{o}C. Bottom: Conversion of **3.3a/3.3b** to **3.4** in the absence of light (d_4-MeOH) measured by normalised summed integration of Py_{ortho} ^{1}H NMR spectral resonances for **3.3a** (4H, at 8.93 ppm) and **3.4** (4H at 8.54 ppm).*

b. Conversion of complex 3.5 to 3a/3b in d_3-MeCN

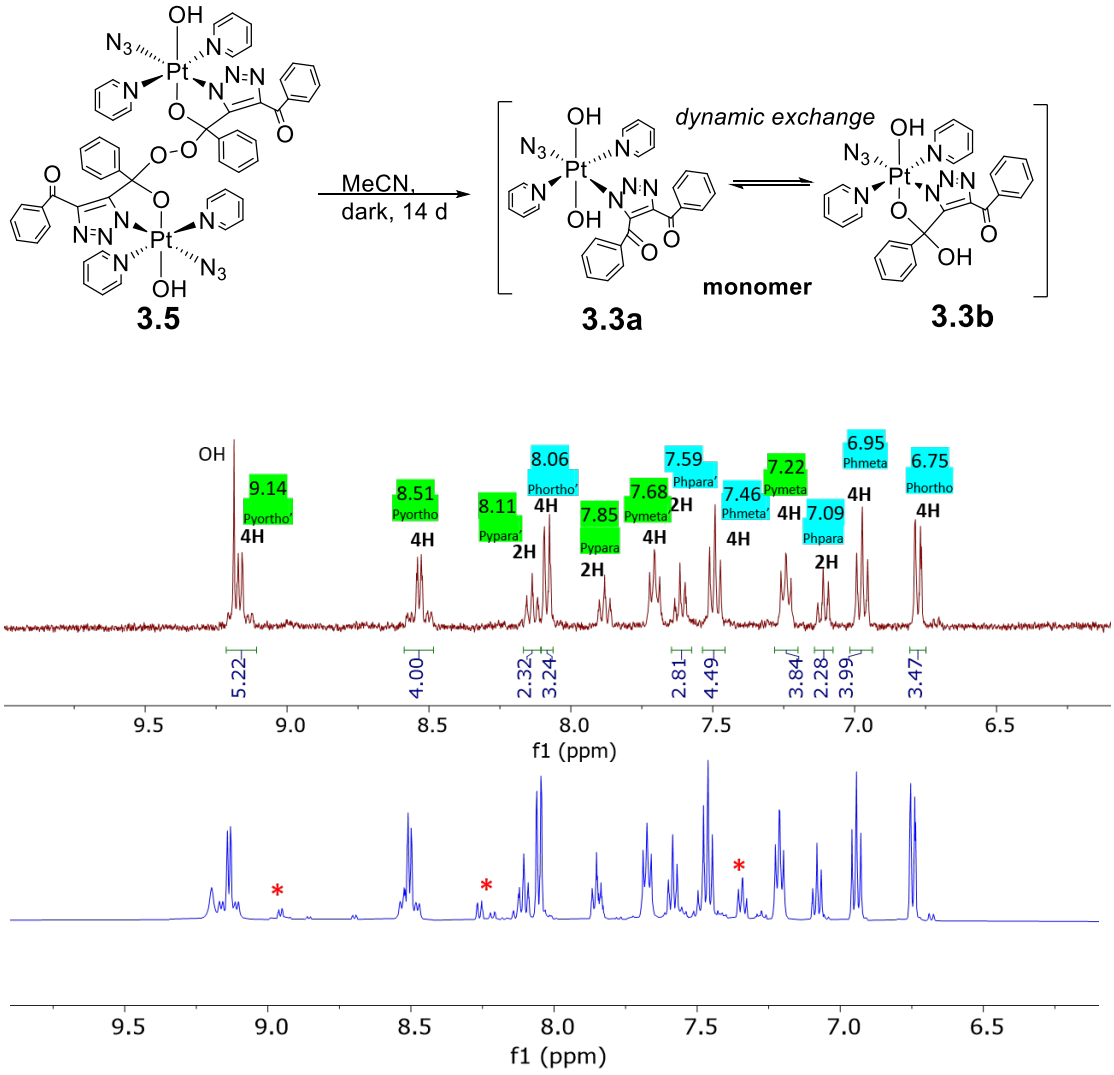

Figure 3.20: *Top: illustration of complex **3.5** convert to complex **3.3a/3.3b** in MeCN. Bottom: ^{1}H NMR spectra obtained immediately in d_3-MeCN (red) and ^{1}H NMR spectrum acquired of the same sample after 6 h (blue).*

Complex **3.5** was unstable in MeCN solution, changing over time in the absence of light. Comparing ^{1}H NMR spectra obtained immediately following dissolution (Figure 3.20 top) with ^{1}H NMR spectrum acquired later the same day (Figure 3.20 bottom), new resonances can already be seen appearing in the later spectrum marked with * in Figure 3.20, which indicates **3.3a/b** ware formed.

3.2.5 Photochemical studies

a. Photochemistry of complex 3.3

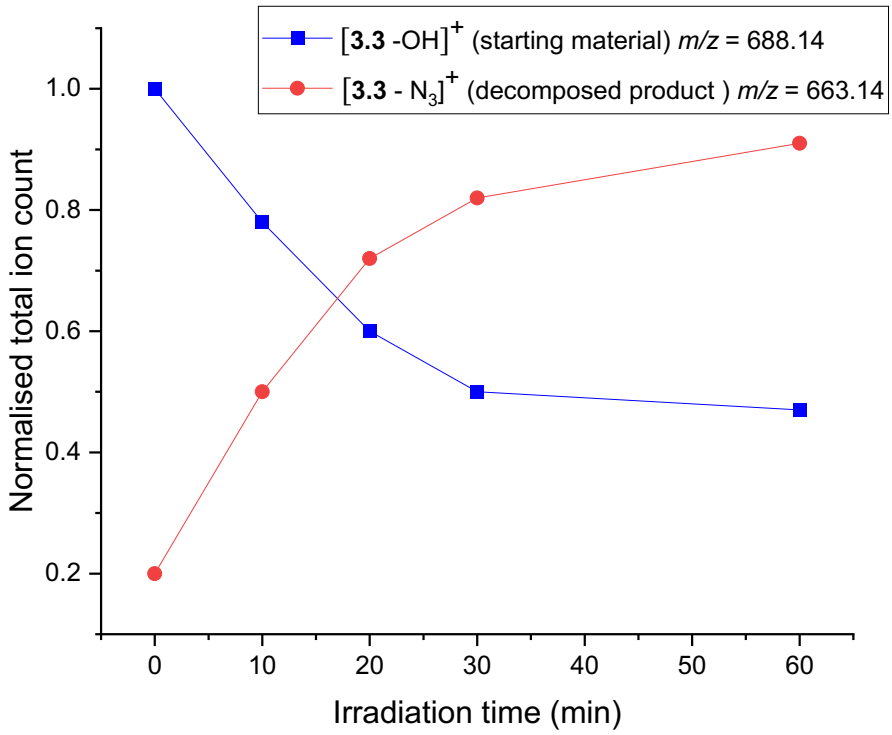

Figure 3.21. *Irradiation of **3.3** (detected by ESI-MS predominantly as [**3.3 – OH**]$^+$) in the presence of 5'-GMP with UVA irradiation in PBS solution; resulted in photo-release of N_3 and formation of [**3.3 – N_3**]$^+$, as monitored by HPLC.*

The photochemical properties of **3.3** were investigated with 5'-GMP (5 equiv.). The irradiation reactions were carried out in phosphate-buffered saline (PBS) solution UVA light (365 nm) and the reaction monitored by HPLC (Figure 3.21). Upon irradiation, azide release was observed, through detection of the [**3.3 – N_3**]$^+$ fragment (663.16 *m/z*). The identity of this main photoproduct was also confirmed by HRMS (663.1318 *m/z*). Meanwhile, the decrease [**3.3 - OH**]$^+$ (688.14 m/z) which represent complex **3.3** was observed, which indicates the decomposition of the complex.

^{195}Pt NMR spectroscopy was also used to investigate the decomposition of complex **3.3** in d_3-MeCN. Two new ^{195}Pt NMR peaks was observed at 858 ppm and 810 ppm

after irradiation, corresponding to the photoproducts [**3.3 – N_3**]$^+$. No ^{195}Pt signals were observed in the Pt(II) region of the spectrum. This supported the hypothesis that upon irradiation, **3.3** does not form Pt(II) photoproducts, unlike for the precursor diazido complex **3.1** which forms a variety of photoproducts, including Pt(II) species. When complex **3.3** was irradiated in the presence of 5'-GMP, no adducts were detected. Pt(IV) diazido complexes have demonstrated evolution of azidyl and hydroxyl radicals under irradiation, which is considered to contribute to their potent photocytotoxic effects.[52–54]

b. Photochemistry of complex 3.4

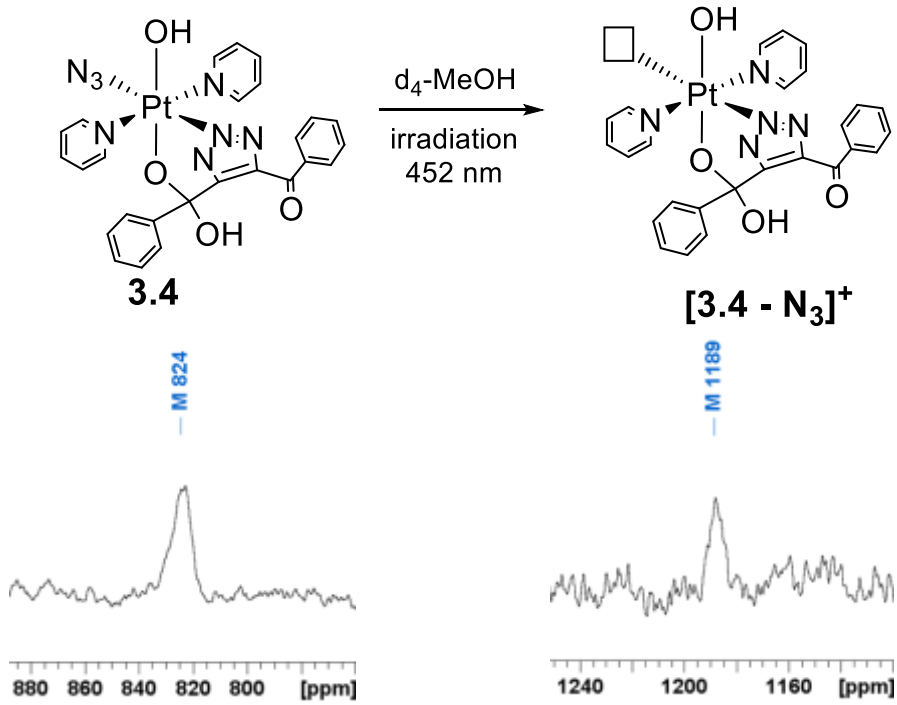

Figure 3.21. *^{195}Pt NMR spectra (d_4-MeOH) of complex **3.4** a) before irradiation (86.1 MHz) and b) after irradiation with blue light, forming [**4** - N_3]$^+$ (107.6 MHz).*

^{195}Pt NMR spectroscopy of **3.4** (d_4-MeOH) under irradiation also showed conversion from the resonance at 824 ppm (**3.4**) to 1189 ppm [**3.4 - N_3**]$^+$ in the Pt)(IV) region of the spectrum (Figure 3.21). This is consistent with previous discussion of the photochemistry of **3.3a/3.3b** (d_3-MeCN), which showed the ^{195}Pt resonances move to a

more deshielded position following irradiation and release of azide.

c. EPR irradiation studies of complex 3.3 and complex 3.5

EPR spin-trapping experiments under irradiation (440 - 480 nm) were also carried out with freshly prepared **3.3a/3.3b** and **3.5** in the presence of DMPO. The EPR spectroscopic results were measured and analysed by Arnau Bertran and Dr. Alice Bowen. The formation of DMPO•-N_3 and DMPO•-OH radical adducts indicated evolution and trapping of N_3• and OH• radicals in both cases.

For **3.3a/3.3b**, a steady state radical adduct concentration (5.5 ± 0.6 μM) was reached after ~30 min of continuous irradiation and remained constant during the period of irradiation (~3 h) (Figure 3.22b). For **3.5**, the radical adduct concentration peaked after ~30 min irradiation (3.1 ± 0.3 μM) and then decayed (Figure 3.22d).

The comparatively low concentration of **3.5** in the experiment was due to its reduced solubility in H_2O. DMPO•-N_3 : DMPO•-OH molar ratios of 90 : 10 and 95 : 5 were determined by spectral simulation for **3.3a/3.3b** and **3.5**, respectively (Figure 3.22a and 3.22c). The DMPO•-N_3 signals quickly disappeared after irradiation ceased, with a lifetime of ~7 min, demonstrating that radical evolution in aqueous solution can be switched on and off by blue light irradiation. The persistance of the DMPO•-OH signal is due to the much longer lifetime of that radical adduct in comparison to DMPO•-N_3,[55] rather than due to the evolution of OH• radicals in the dark from **3.3a/3.3b**. Evolution of OH• radicals from **3.3a/3.3b** in H_2O is induced by irradiation, as it can be seen from the initial rise in the DMPO•-OH signal (Figure 3.22b, red trace), while it seems to be light-independent for **3.5**.H_2O_2 (Figure 3.22d, red trace), with the same weak DMPO•-OH signal under irradiation as is observed in the dark.

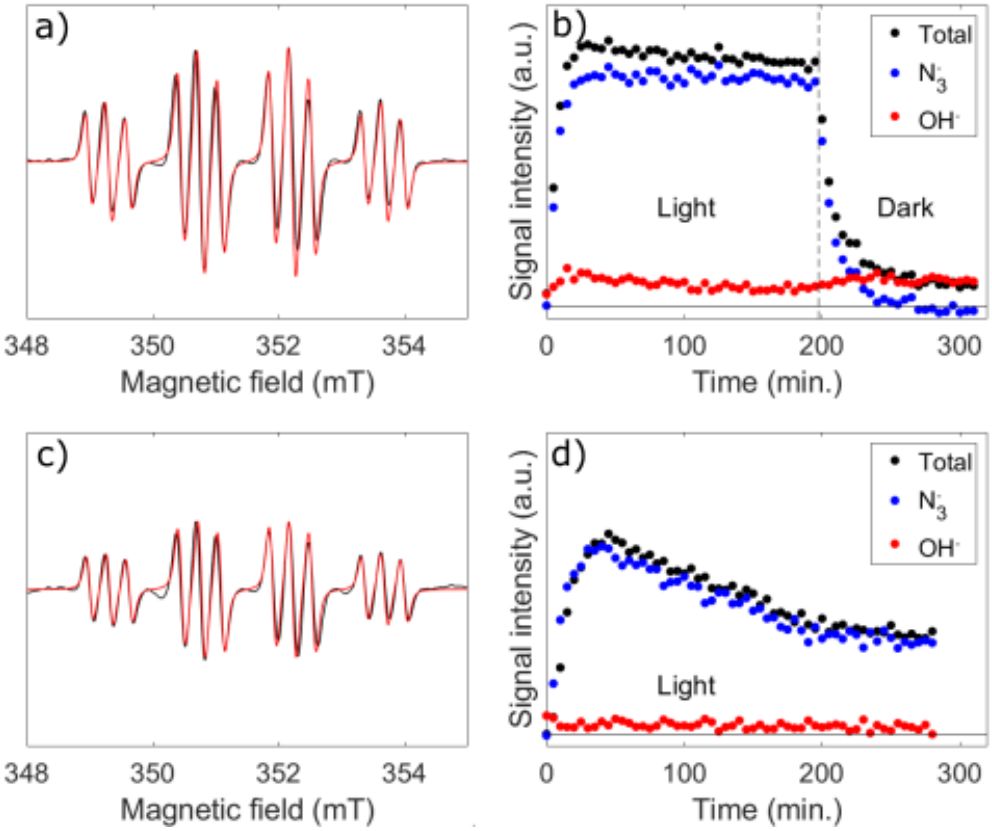

Figure 3.22: *EPR spin trapping experiments under irradiation of* ***3.3a/3.3b*** *at 10.5 mM in H_2O (a, b) and* ***3.5***.H_2O_2 *at < 1 mM (c, d) in the presence of 21 mM DMPO. (a, c) Experimental spectra averaged for 100 min under continuous illumination (black) and simulations with a DMPO•-N3 : DMPO•-OH molar ratio of 90 : 10 (a) and 95 : 5 (b) (red). (b, d) EPR intensities of the total radical adduct signal (black), DMPO•-N3 signal (blue) and DMPO•-OH signal (red). Vertical axes have the same scale in (a, c) and (b, d), respectively, for comparison.*

We did not detect photo-ejection of the triazole ligand from the Pt centre of **3.3, 3.4** or **3.5** in any of our irradiation experiments, possibly due to the additional stability afforded by cyclisation of the biphenyl ligand, resulting in bidentate coordination. MS/MS studies of **3.3** also confirmed the strong binding of the triazole ligand. Irradiation of **3.3** in the presence of the DNA model 5'-GMP with either UVA or 452 nm light did not produce any detectable 5'-GMP-Pt products, which confirms the stability of the Pt-triazole coordination.

The photocytotoxic mechanisms of diazido complexes such as **3.1** are complicated, since azidyl radicals, hydroxyl radicals, $^1O_2$ various DNA-binding Pt(IV) and Pt(II)

fragments can be produced upon irradiation.[54] The relatively simple photochemistry observed for complex **3.3** may enable us to better understand the photocytotoxic role and relative importance of the azidyl radical when released *in cellulo*. Such azidyl-releasing complexes in the same line as photoCORMS (CO-releasing)[56] and NORMS (NO releasing)[57] complexes may find application as phototherapeutics since azidyl radicals and azide anions are cytotoxic; one pathway by which azidyl radicals may exert their cytotoxic activity is via oxidative attack of tryptophan residues in proteins;[28] and sodium azide inhibits cytochrome oxidase in the mitochondrial electron transport chain causing cell death.[58]

3.3 Platinum Diyne Double Click Complexes

Based on the study of the click reaction between *trans,trans,trans*-[$Pt(N_3)_2(OH)_2(py)_2$] and 1,4-diphenyl-2-butyne-1,4-dione, we looked at the click reaction between *trans,trans,trans*-[$Pt(N_3)_2(OH)_2(py)_2$] and a di-alkyne compound - Sondheimer diyne. The two alkynes of the Sonheimer diyne can react with two azides in a concerted manner, which provides the possibility of forming multi-nuclear Pt(IV) triazolato azido complexes.

3.3.1 Synthesis and characterisation

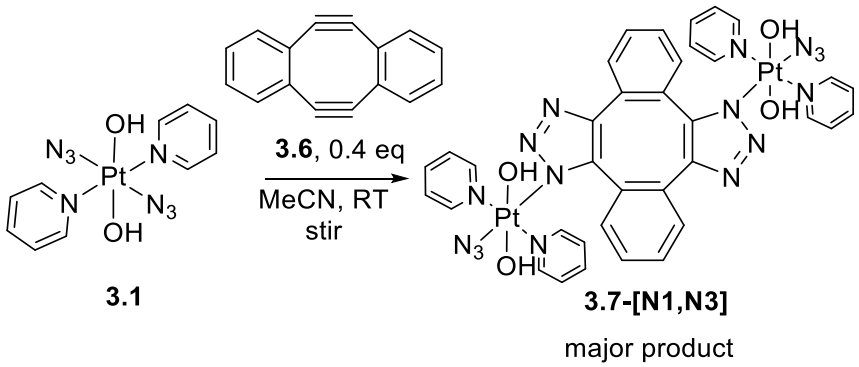

Figure 3.23: *Synthetic scheme between the diazido Pt(IV) complex* ***3.1*** *and Sondheimer diyne* ***3.6****.*

The Sondheimer diyne was synthesised according to the reported procedure and purified by flash column chromatography.[59,60] The SPACC reaction between diyne **3.6** and **3.1** was conducted in acetonitrile at room temperature by adding a diyne acetonitrile solution to a solution of **3.1** in acetonitrile dropwise. The reaction was monitored by LCMS and was judged to be completed after 2 days. No mono-Pt(IV) cycloaddition intermediates were detected by ESI-MS during the course of the reaction. This is consistent with DFT calculations of the reactivity profile of the diyne, which indicates

that the activation energy for the second cycloaddition is lower than for the first, due to the highly distorted alkyne bond in the mono-substituted intermediate, arising from steric repulsion between the substituent on the triazole ring and the hydrogen atom on the benzene ring.[61] The product was purified by mass-directed HPLC under neutral conditions, which was detected as both $[M + H]^+$ (1143.20 *m/z*) and $[M + Na]^+$ (1165.36 *m/z*).

The isolated product is a mixture of two regioisomers, which co-eluted with a purity of 95% as shown in Figure 3.24. Different isomers could arise from the rearrangements between the Pt and the triazole N atoms as demonstrated in Figure 3.3. The major isomer was purified by recrystallization: yellow crystals were formed from the acetonitrile solution of the HPLC purified products on standing for 24 h. The crystals were analysed by X-ray crystallography which helped us to determine the structure of the major isomer (Figure 3.25).

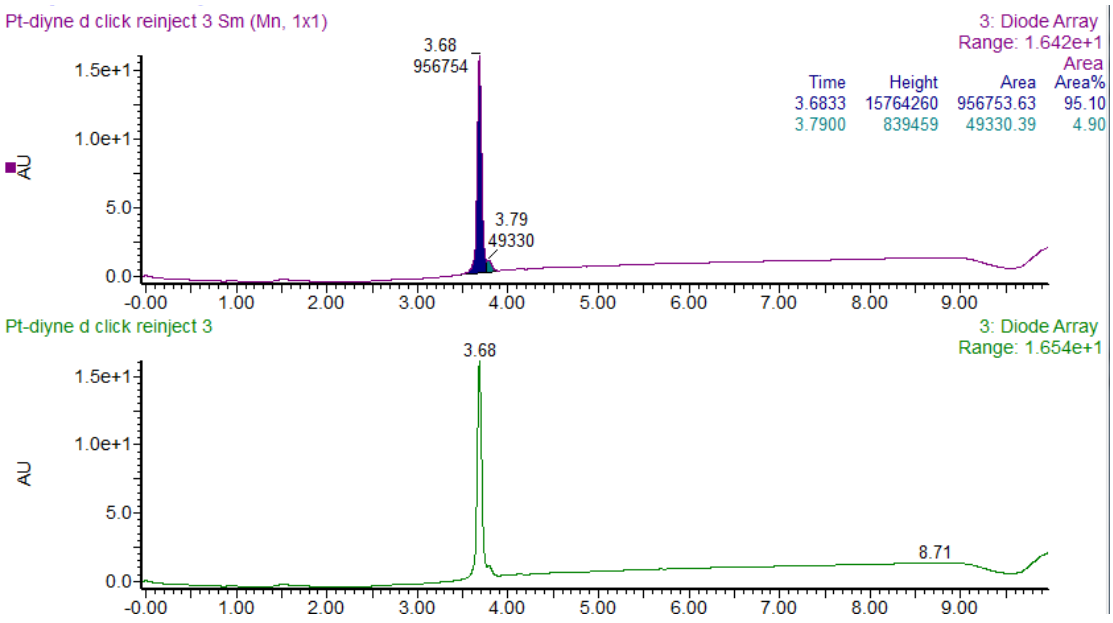

Figure 3.24: *HPLC trace of reinjected complex* ***3.7-[N1,N3]*** *for purity testing.* t_R *= 3.7 min (3-[N1,N3]****, 95%****). Relative intensities are calculated by relative UV-Vis spectral absorbance integrated over the range 210 nm – 400 nm.*

The crystal structure revealed the ligand interactions around the puckered chair of the cyclooctene ligand. The pyridine ligands undergo π-π interactions with the cyclooctene ring ranging from 3.527 – 4.509 Å in length. A hydrogen-bond interaction of 2.178(3) Å was observed between Pt(1)-OH(2) and triazole N(2); the corresponding interaction on the other side of the molecule measured 2.242 Å (Pt-OH(3) to triazole N(5)).

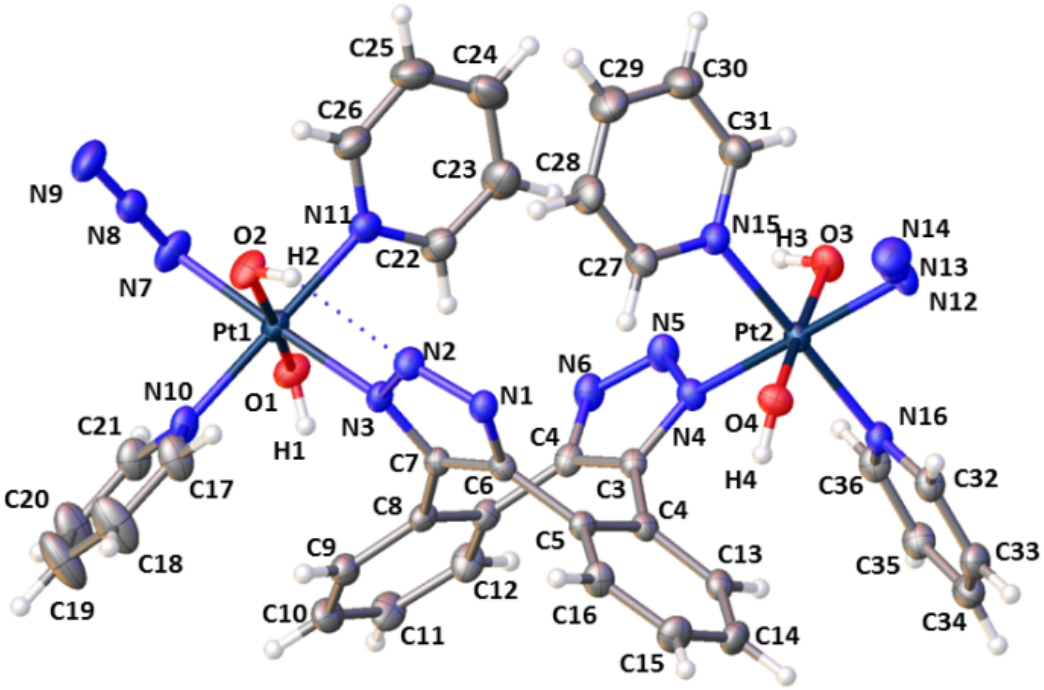

Figure 3.25: *X-ray crystallographic structure of* ***3.7-[N1, N3]*** *with thermal ellipsoids displayed at 50% probability.*

The identity of **3.7** was also confirmed by HRMS [**3.7** + **H**]$^{+}$ ($C_{36}H_{32}N_{16}O_4Pt_2H$)*:* 1143.2123 *m/z* found; 1143.2069 *m/z* calcd., 4.7 ppm error) as shown in Figure 3.26.

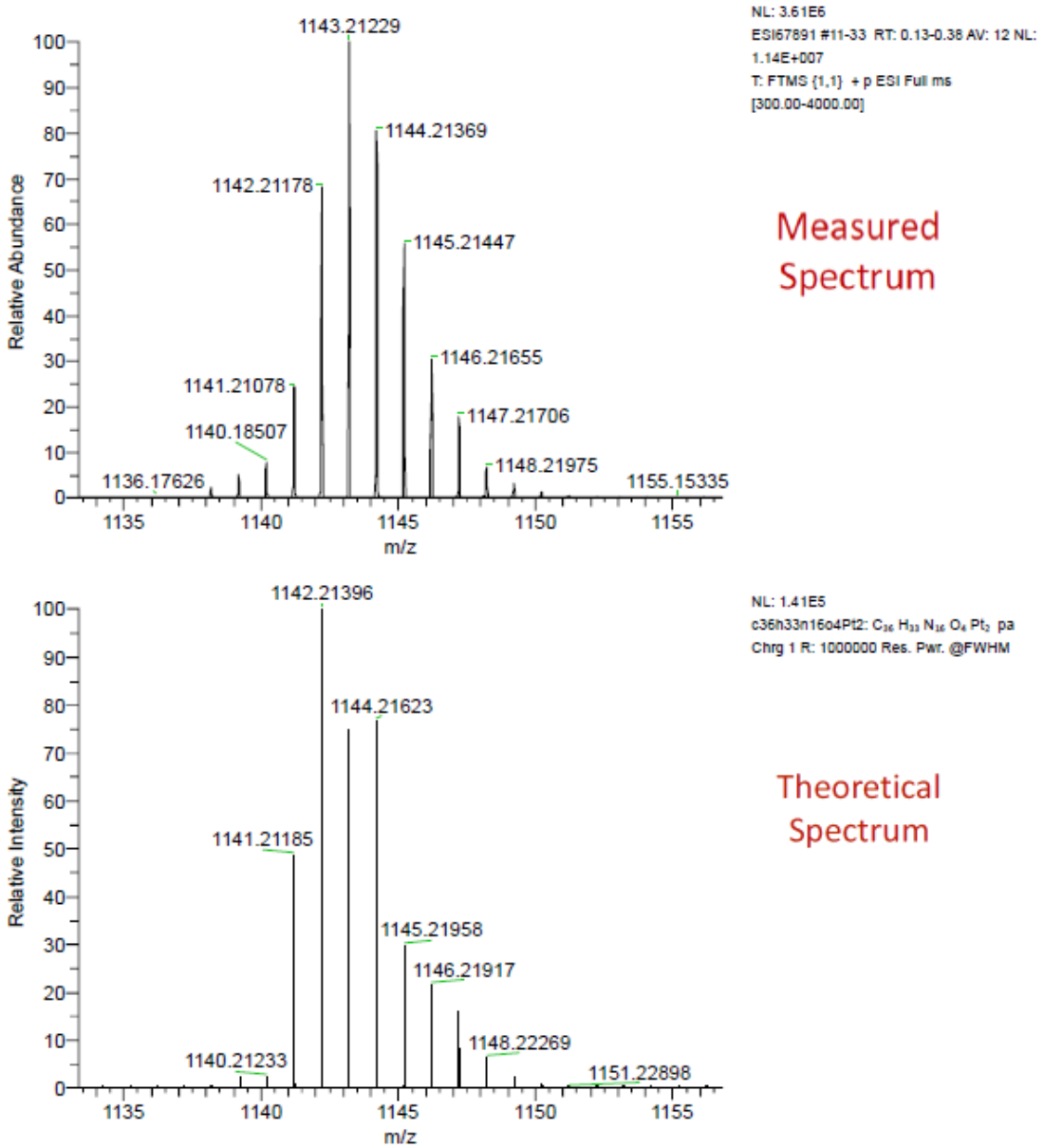

Figure 3.26: *HRMS of [M + H]$^{+}$ ($C_{36}H_{32}N_{16}O_4Pt_2H$): 1143.2123 m/z found; 1143.2069 m/z calc (4.7 ppm error).*

The **3.7-[N1, N3]** complex was fully characterised by ^{1}H , ^{195}Pt and ^{13}C NMR spectra. Figure 3.27 illustrates the ^{1}H NMR spectrum of the complex with full assignment. Most of the resonances of the pyridine protons resemble the diazido Pt(IV) starting substrate,

with the *ortho* proton on the pyridine rings process the characteristic sharp ^{195}Pt satellites. Figure 3.28 shows the ^{1}H-^{195}Pt HMBC NMR spectroscopy of the complex in D_2O, the ^{195}Pt NMR resonance of **3.7-[N1, N3]** is at 723 ppm.

The **3.7-[N1, N3]** complex was found to be stable in d_3-MeCN for a period of at least 5 weeks judging by ^{1}H NMR spectroscopy. Different NMR solvents can change the ^{195}Pt NMR chemical shift of [N1,N3] significantly: as shown in Figure 3.29, when the NMR solvents changed from d_3-MeCN to D_2O, the peaks shift towards upfield significantly. The ^{1}H-^{195}Pt HMBC NMR also showed that ^{195}Pt NMR resonance change from 723 ppm (d_3-MeCN) to 886 ppm (D_2O). This solvent effect is reversible.

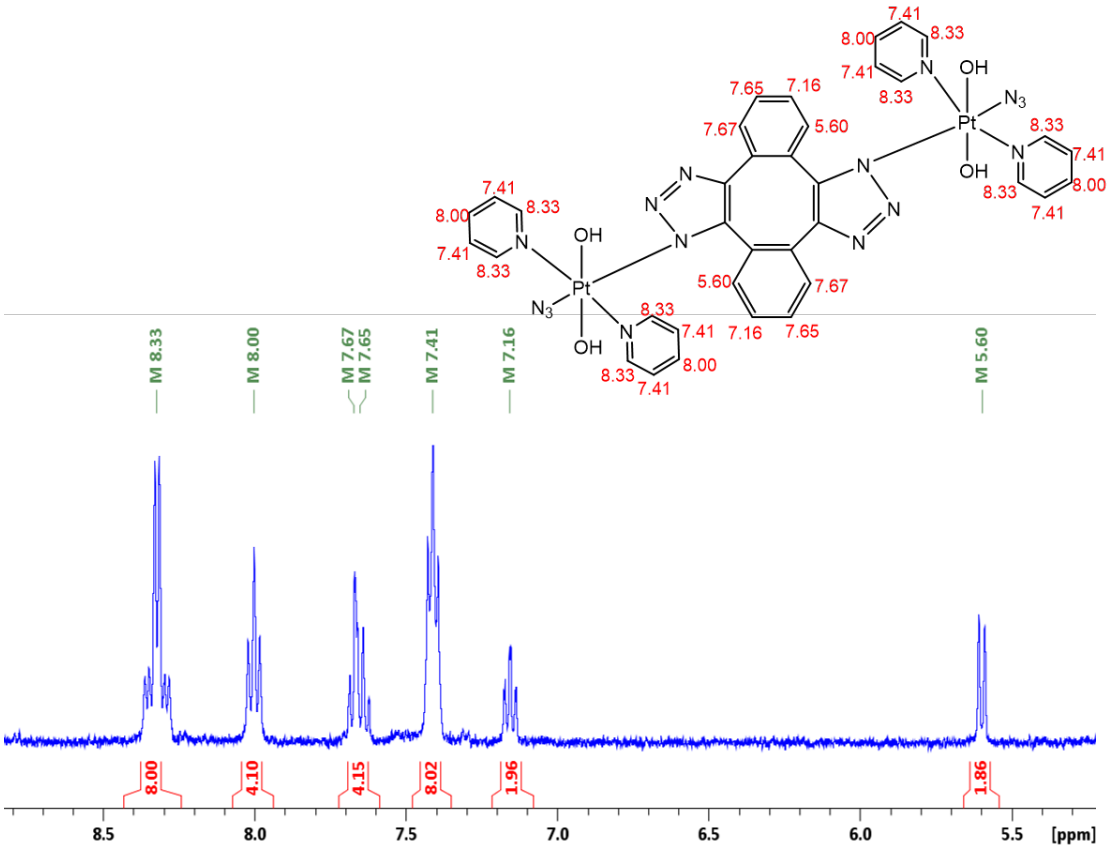

Figure 3.27: *^{1}H NMR spectrum of **3.7-[N1, N3]** with assignments in D_2O.*

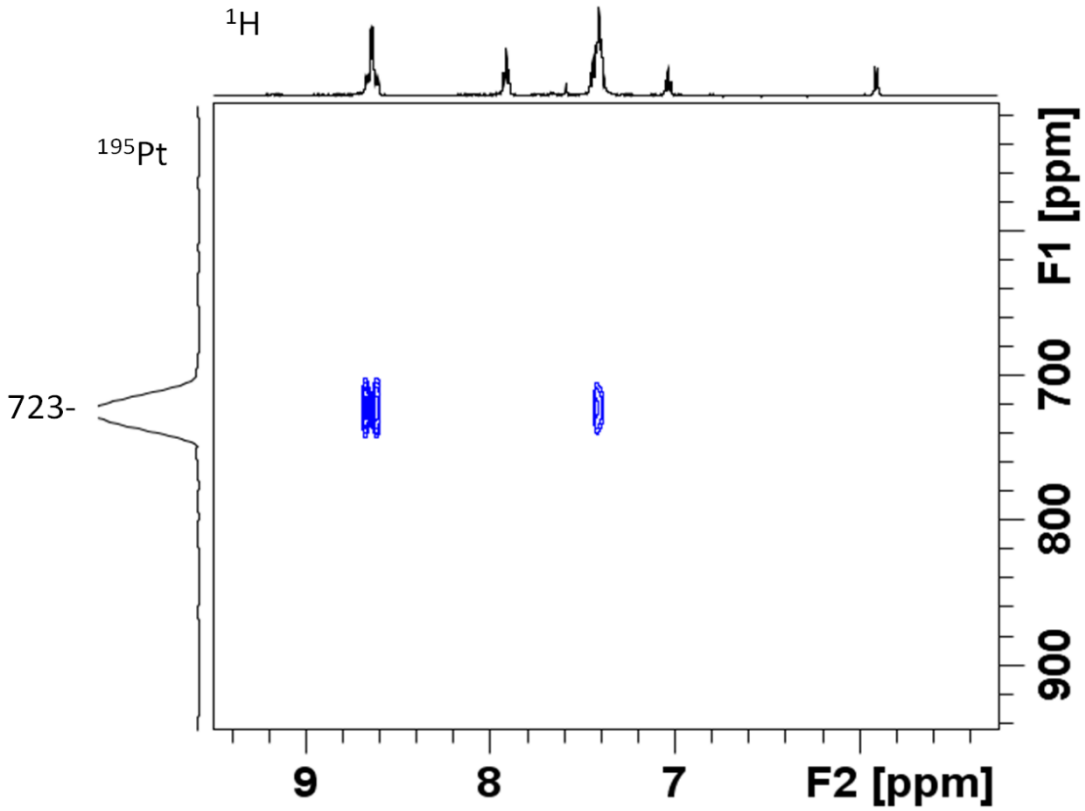

Figure 3.28: *^{1}H-^{195}Pt HMBC NMR spectrum of* ***3.7-[N1, N3]*** *in d_3-MeCN.*

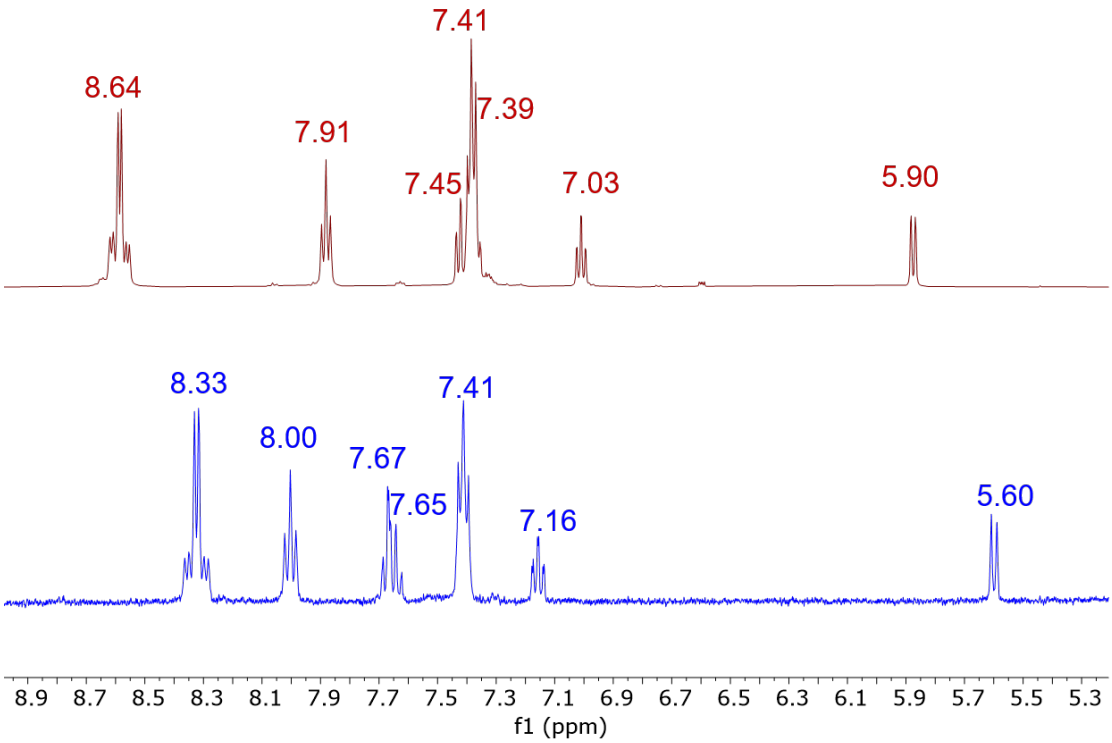

Figure 3.29: *^{1}H NMR spectra of* ***3.7-[N1, N3]*** *in d_3-MeCN (top), and D_2O (bottom).*

The UV-Vis spectrum of **3.7**-[**N1,N3**] (Figure 3.30) showed a long shoulder with λ_{max}

ca. 252 nm and a tail into the visible region corresponding to the N_3→Pt LMCT transition band, with increased intensity at shorter wavelengths compared to **3.1.** due to the presence of the diyne aromatic groups. IR spectroscopy of a freshly parepared d_3-MeCN sample of Pt-diyne-Pt showed a sharp peak at 2043 cm^{-1} arising from the strong asymmetric N_3 stretch. This was slightly weaker compared to the starting diazido complex **3.1 (2051** cm^{-1}, solid) and the Ph Pt click product (both the monomer 2048 cm^{-1} and dimer 2049 cm^{-1}).

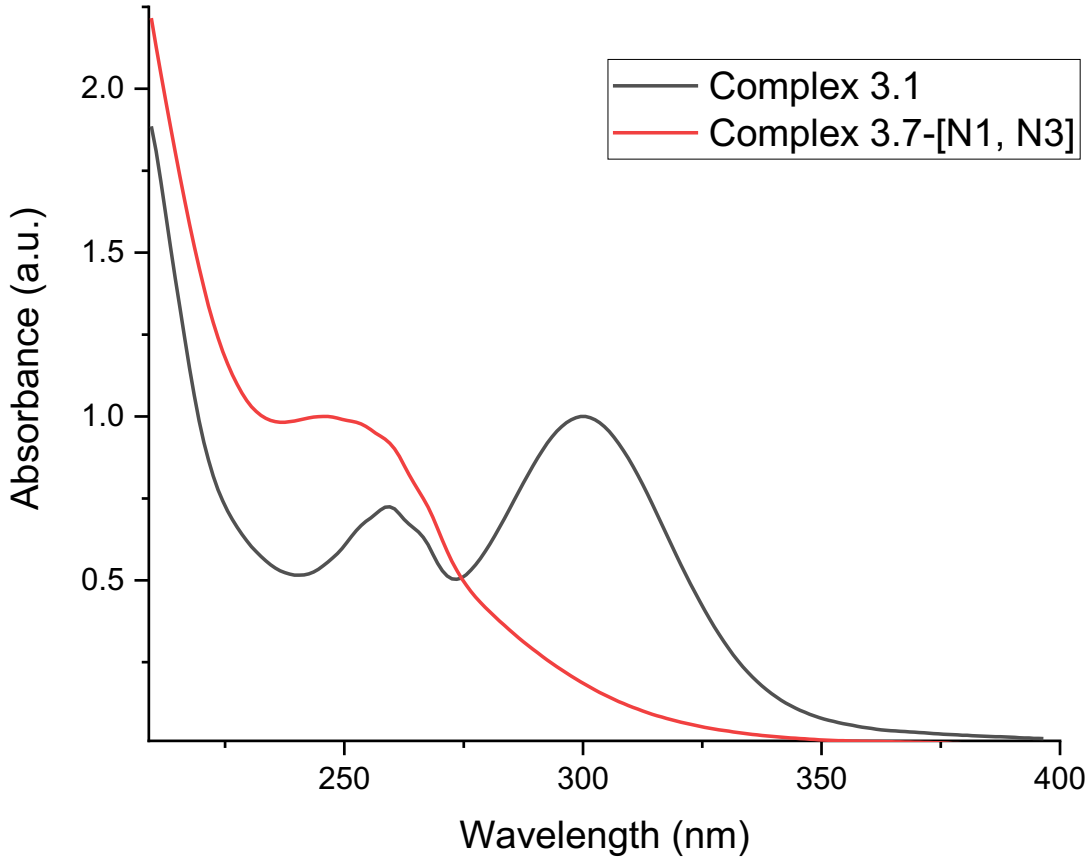

Figure 3.30: *Comparison of the UV-vis absorption spectra of complex* ***3.1****(black) and* ***3.7-[N1, N3]*** *(red)*

3.3.2 Photochemical studies

The photochemistry of **3.7-[N1,N3]** was monitored by ^{1}H–^{195}Pt HMBC and 1D ^{195}Pt NMR spectroscopy at 22 mM, λ_{irr} = 452nm, for 180 min. During irradiation, the

intensity of the ^{195}Pt NMR spectroscopic resonance corresponding to [N1,N3] (854 ppm) decreased, with small amounts of new Pt(IV) species (1267, 1350 ppm) and two more intense Pt(II) signals appearing (-2224 ppm and -2369 ppm). These spectra indicate the formation of multiple Pt(II) and Pt(IV) photoproducts.

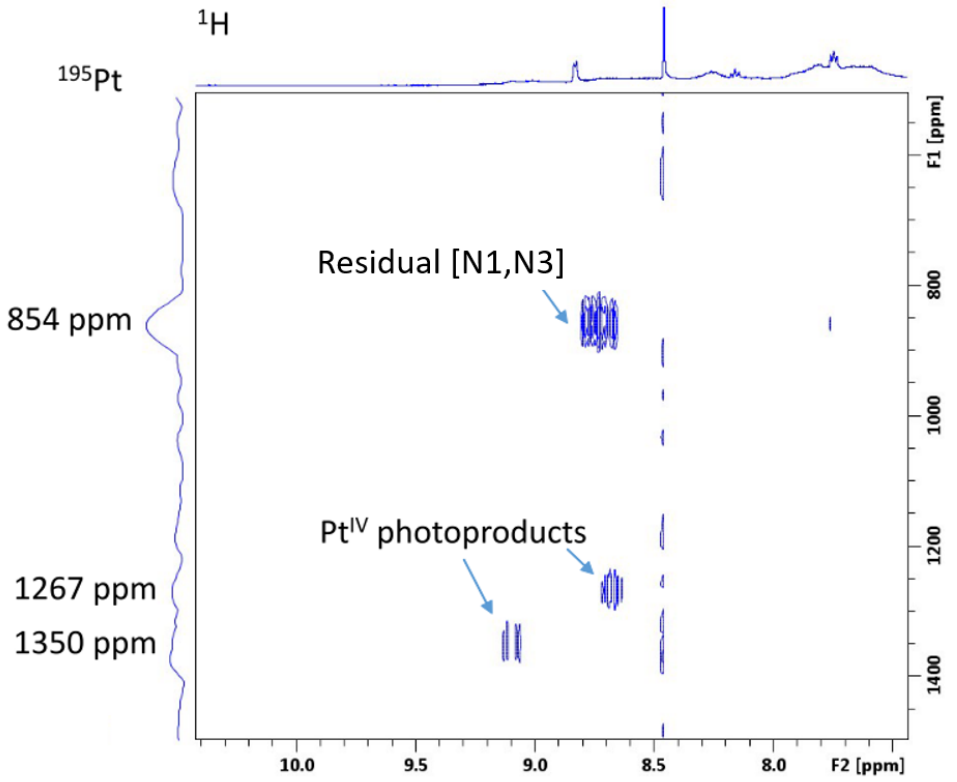

Figure 3.31: *^{1}H-^{195}Pt HMBC NMR spectra of* ***3.7-[N1, N3]*** *in d_3-MeCN*

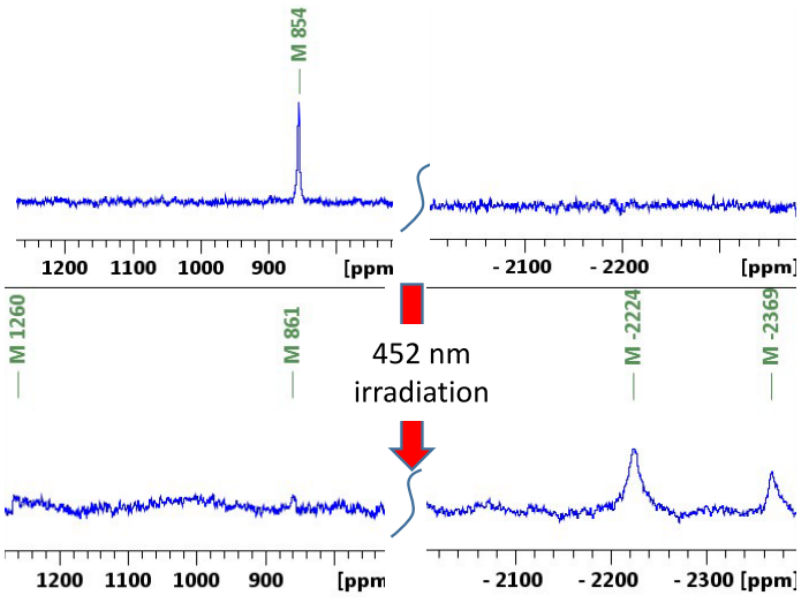

Figure 3.32: *^{195}Pt NMR spectra of a solution of 1.5 mM* ***3.7-[N1,N3]*** *and 2 mol. equiv. of 5'-*

GMP showing formation of new Pt(II) species following irradiation (bottom).

Irradiation of a solution of **3.7-[N1,N3]** (1.15 mM) and 5,5-dimethyl-1-pyrroline N-oxide (DMPO, 20 mM) monitored by EPR spectroscopy in either water or cell-free lysate (KNS42) generated azidyl ($N_3^{\cdot}$) and hydroxyl ($OH^{\cdot}$) radical species, trapped in a 85 : 15 and 90 : 10 molar ratio, respectively, with a maximum trapped radical concentration of 7 mM. The signals started to decay after 30 min irradiation. The inclusion of 5'-GMP in the solution of **3.7-[N1,N3]** in lysate had a significant effect; the maximum trapped radical concentration reduced to 3 mM with a 95:5 $N_3^{\cdot}$:$OH^{\cdot}$ molar ratio and radical trapping slowed down.

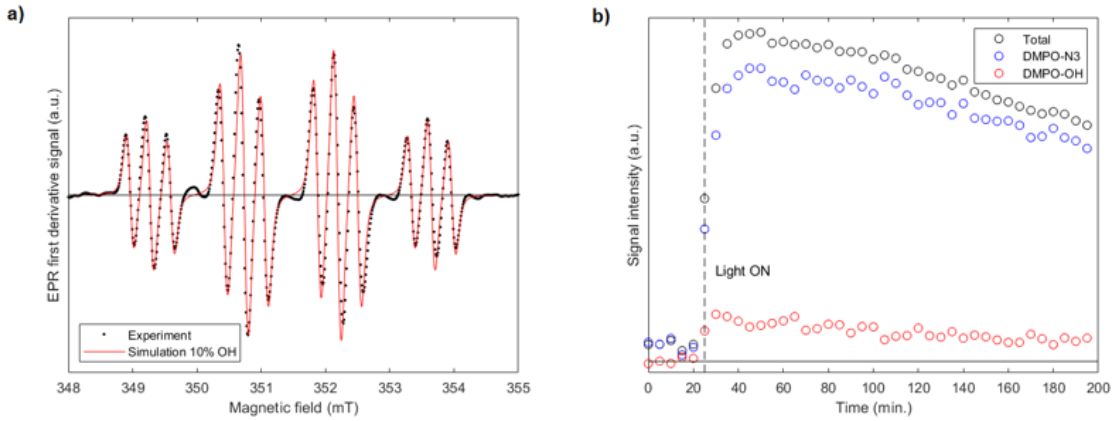

Figure 3.33: *cw-EPR spectrum a) showing trapping of azido ($N_3^{\cdot}$) and hydroxyl ($OH^{\cdot}$) radicals in freshly prepared KNS42 lysate (λ_{irr} 440 – 480 nm; spectra averaged over 1 h of maximum signal intensity) and b) deconvoluted kinetic profiles for the two radical adducts DMPO-N_3 and DMPO-OH.*

3.4 Double Click Ln-diyne-Pt Complexes

Based on the studies of double-click **3.7-[N1,N3]** synthesis, we substituted one of the Pt azido substrates to an azidophenacylDO3A Ln complex. By doing that, we synthesised a Ln-Pt complex in which the both the lanthanide and platinum moieties were linked to the Sondheimer diyne via SPAAC reactions.

3.4.1 Synthesis and characterisation

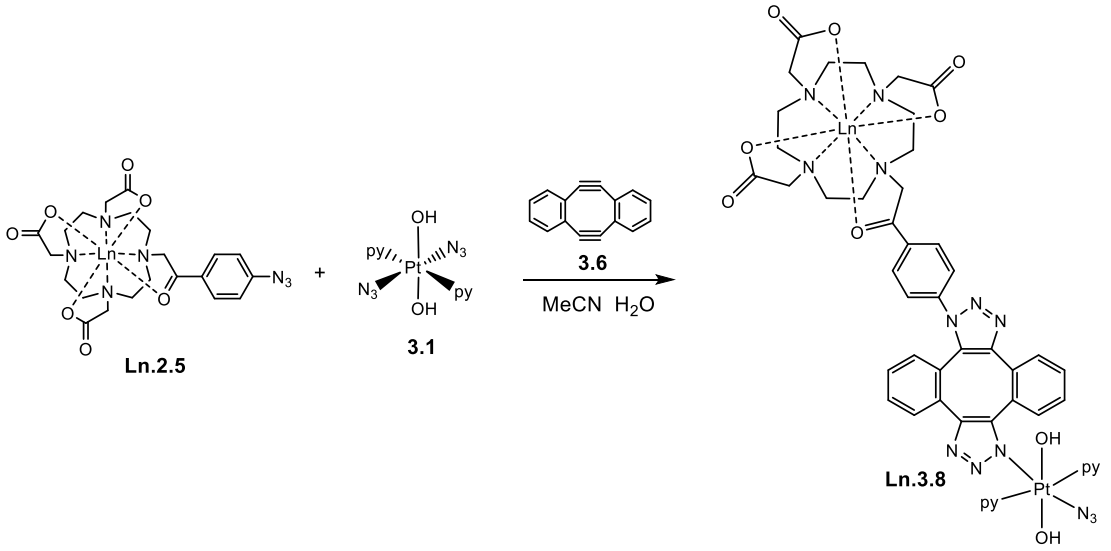

Figure 3.34: *The illustration of the double click reaction between complex* ***Ln.2.5****,* ***3.1*** *and* ***3.6****.*

The synthesis of azidophenacylDO3A lanthanide complexes **Ln.2.5** followed the same procedure as described in Chapter 2. The SPACC reaction between diyne **3.6** azidophenacylDO3A lanthanide **Ln.2.5** and *trans,trans,trans*-[$Pt(N_3)_2(OH)_2(py)_2$] **3.1** was conducted in acetonitrile/water solution at room temperature. 1:1 mixture of **3.1** and **Ln.2.5** azido complexes was dissolved in acetonitrile, the minimum amount of water was added to fully dissolve the mixture as the **Ln.2.5** complex was only sparingly soluble in acetonitrile. To this solution of azido compounds, a solution of diyne **3.6** in acetonitrile was added dropwise over 30 min. The reaction was monitored by LCMS and was judged to be completed after 2 d. The solvent was removed by rotary evaporation at 40 ^{o}C, the resulting crude product was purified by reverse phase HPLC

at neutral pH. Since the molecular weight of the compound exceeded the detection limit of the HPLC mass spectrometer, the fractions were collected using UV/Vis absorption as the detection method, which were submitted to the departmental mass spectrometry facility to identify the target products. Side products such as di-Ln and di-Pt double click product were also observed by mass spectrometry. Figure 3.35 shows the high-resolution mass spectra of di-Yb side product (left) and **Yb.3.8** complex(right) with mass error at 1.28ppm and 0.14ppm respectively. HPLC re-injection was used to confirm the purity of the HPLC isolated product, as shown in Figure 3.39, the re-injection trace shows 100% purity of the **Yb.3.8** complex.

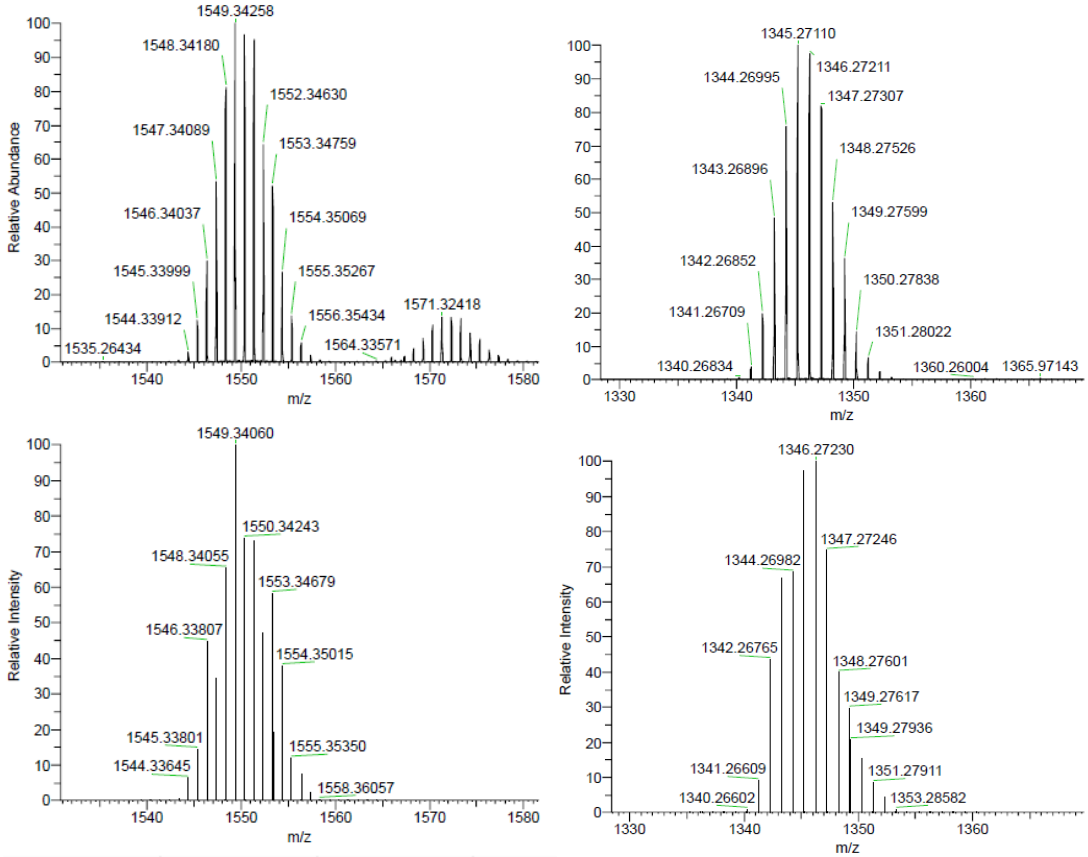

Figure 3.35: *High resolution mass spectra of of di-Yb side product (left) and* ***Yb.3.****8 (right) measured in negative mode. Top are spectra measured, and the bottom are theoretical spectra.*

Figure 3.36 shows the proton NMR spectra of the **Yb.2.5** and **Yb.3.8** complexes. In both complexes, the exchange of SAP and TSAP isomers are slow enough so that the

isomers can be distinguished obviously, where peaks between 140-80 ppm are assigned SAP while resonances around 50-14 ppm are assigned TSAP. Peaks in the conjugated complexes are broader than the non-conjugated one which could result from the higher rigidity of the conjugated complex.

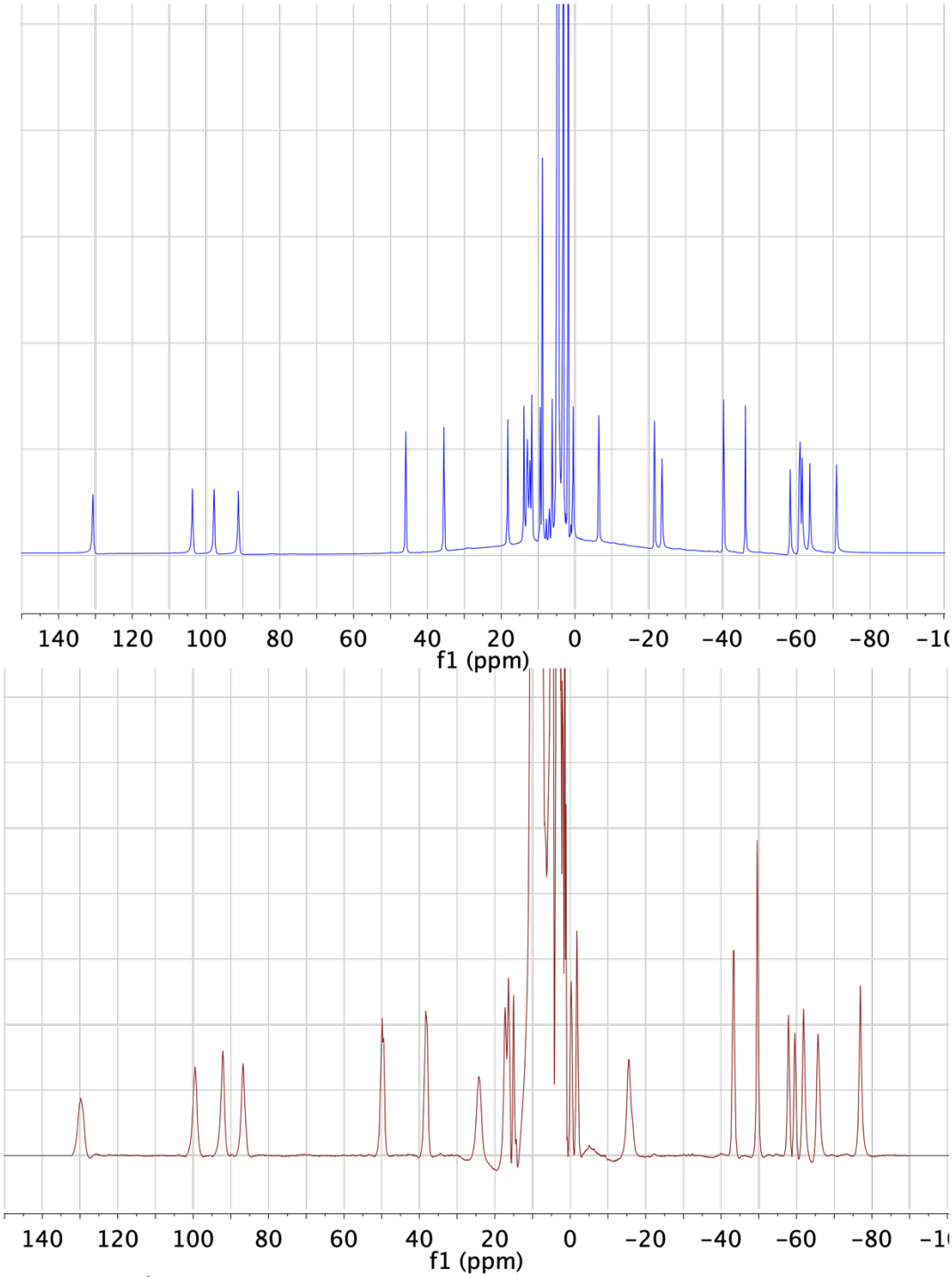

Figure 3.36: *^{1}H NMR spectra of* ***Yb.2.5*** *(top) and* ***Yb.3.8*** *(bottom) complexes in D_2O.*

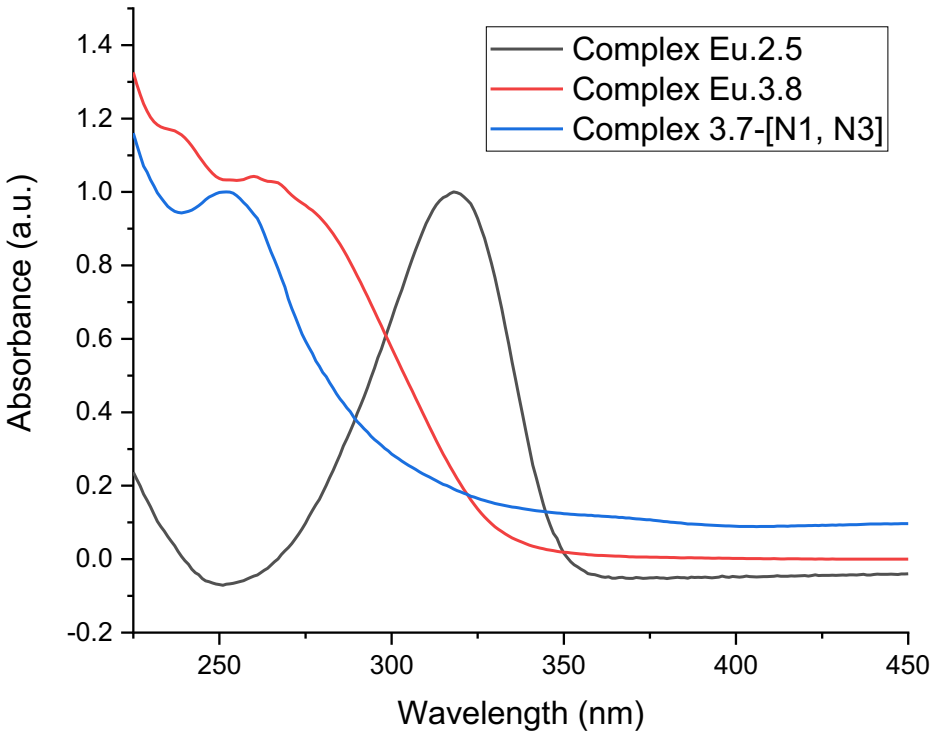

Figure 3.37: *Comparison of the UV-vis absorption spectra of complex **Eu.2.5** (black), di-Pt complex **3.7-[N1, N3]** (blue) and **Eu.3.8** (red).*

The Eu version of the complex was also synthesised, and its photophysical properties were studied. The UV-vis spectrum of **Eu.3.8** is shown in Figure 3.37, λ_{max} *ca.* 265 nm, with a tail extend towards to visible wavelength. Compared to the starting Eu substrate **Eu.2.5**, the UV-vis absorption showed a blue shift which indicated the formation of a triazole group. The λ_{max} is relatively close to the di-Pt complex **3.7-[N1, N3]** (252 nm). The shorter wavelength absorption can result from the diyne structure. The luminescence spectra of **Eu.3.8** is shown in Figure 3.38 exhibited characteristic Eu emission bands, with the peaks in 580 nm, 592 nm, 616 nm, 653 nm, 688 nm and 701 nm arise from the $^5D_0$ - ^7F_J (J=0, 1,2,3,4,5).

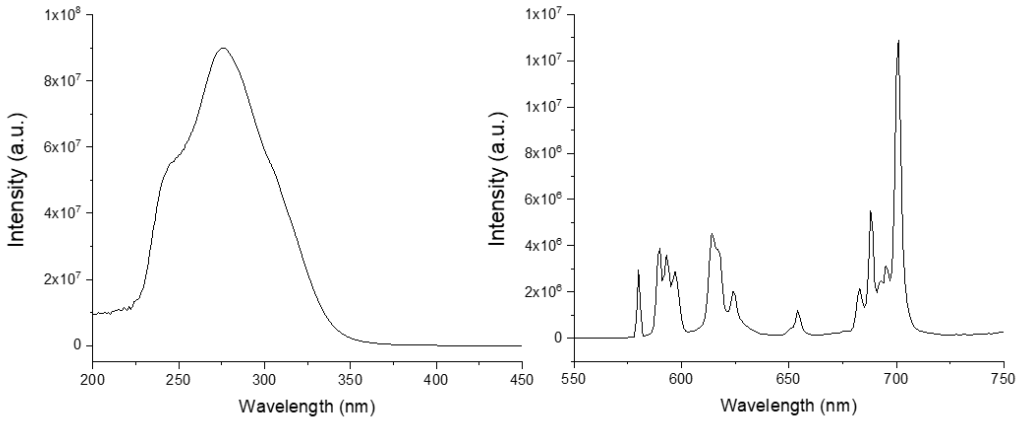

Figure 3.38: *Left: Excitation spectrum of* ***Eu.3.8****; right: emission spectrum of* ***Eu.3.8****.*

Table 3.1: *Tabulated luminescent lifetime of complex* ***Eu.2.5*** *and* ***Eu.3.8*** *and their corresponding hydration number q.*

Complex	τ H2O/ms	τ D2O/ms	q
Eu.2.4	0.51	1.22	1.06
Eu.3.8	0.63	1.23	0.63

The luminescence lifetimes of complexes **Eu.2.5** and **Eu.3.8** are tabulated in **Table 3.1**. From their values in D_2O and H_2O, the number of coordinated solvent molecules was determined according to the modified Horrocks' equation. The hydration number *q* obtained for complex **Eu.2.5** indicate that the complex is octadentate species in solution, where the ketone actively participates in the coordination and only one water molecule coordinates in the axial position. Upon SPAAC reaction, the Pt coupled compound **Eu.3.8** was observed with a smaller hydration value $q = 0.63$, which is due to the bulky structure of the complex reducing water coordination.

3.4.2 Stability study

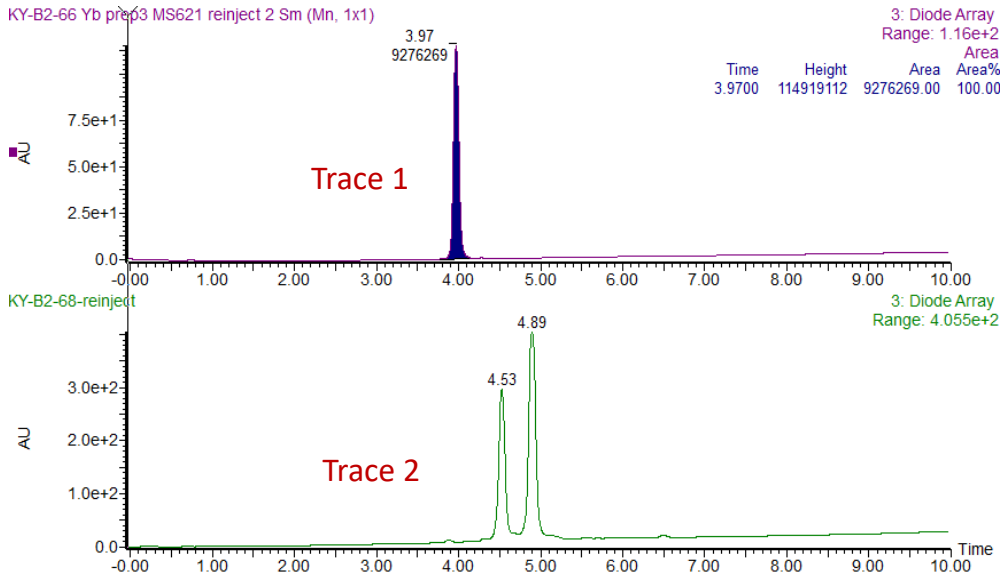

Figure 3.39: *Top: HPLC trace of reinjected* ***Yb.3.8*** *for purity testing. tR = 3.97 min (100%). Relative intensities are calculated by relative UV-Vis spectral absorbance integrated over the range 210 nm – 450 nm. Bottom: HPLC of* ***Yb.3.8*** *after standing in 1:1 MeCN:H_2O for 2 weeks.*

When the HPLC-purified **Ln.3.8** complex remained in solution in protic solvents over time, different species formed. Figure 3.39 trace 1 is the re-injection HPLC of the isolated complex just after HPLC purification, which shows 100% purity; trace 2 is the HPLC of same complex suspended in 1:1 acetonitrile: water for 14 d showing two peaks at different retention times which indicates the complex has converted to new species. We proposed that the rearrangement could happened between the triazole and the platinum centre as discussed previously in the complex **3.4**. The chemical structures of three possible isomers of Pt-triazole rearrangement products are depicted in Figure 3.40.

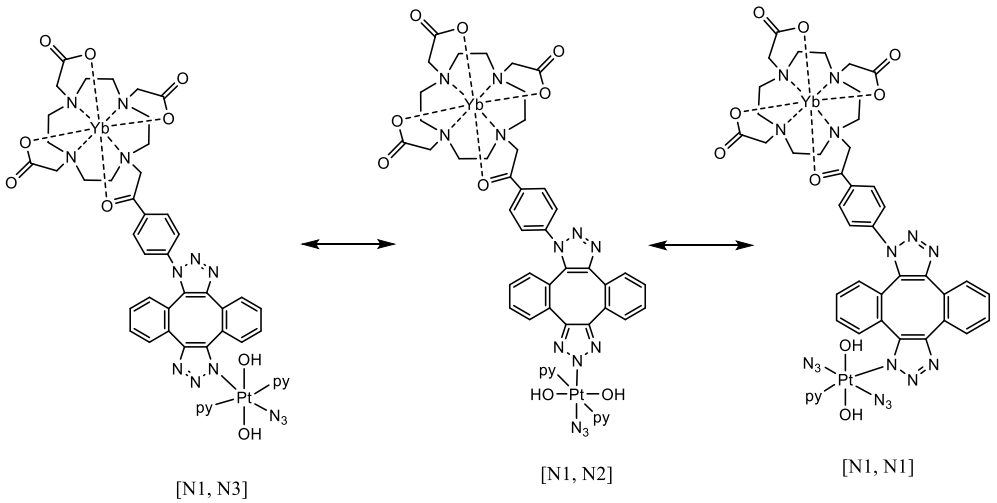

Figure 3.40: *The structure of three* ***Yb.3.8*** *isomers rearranging the Pt-triazole bond.*

^{195}Pt NMR spectra were used to further understand the isomerisation of the complex, as shown in Figure 3.41, as shown in the top graph is the isolated **Lu.3.8** in D_2O, the major peak at 910 ppm is related to the main product just after the reaction. Because there was about 6 h delay between dissolving the sample in D_2O and acquiring ^{195}Pt NMR spectra, we started to see a minor peak at around 890 ppm during which time correlated to the newly formed isomers. The middle and bottom graph in Figure 3.41 show the ^{195}Pt NMR spectra of the same sample stayed in D_2O for 13 days and 21 days which the peak at 910 pm was decreasing while the peak at 890 ppm is increasing. Mild heating (45^{o}C) was used to accelerate the conversion between the isomers, however the NMR solution was found to form precipitate after 3 hours of heating, which means the complex was not stable in water solution upon heating. The precipitate was soluble in methanol and its methanol solution shows the correct mass of [**Lu.3.8**+**H**$^+$]$^+$ in mass spectroscopy. Thus, the precipitate could be a polymer of the complex. Further study needs to be done to confirm this hypothesis.

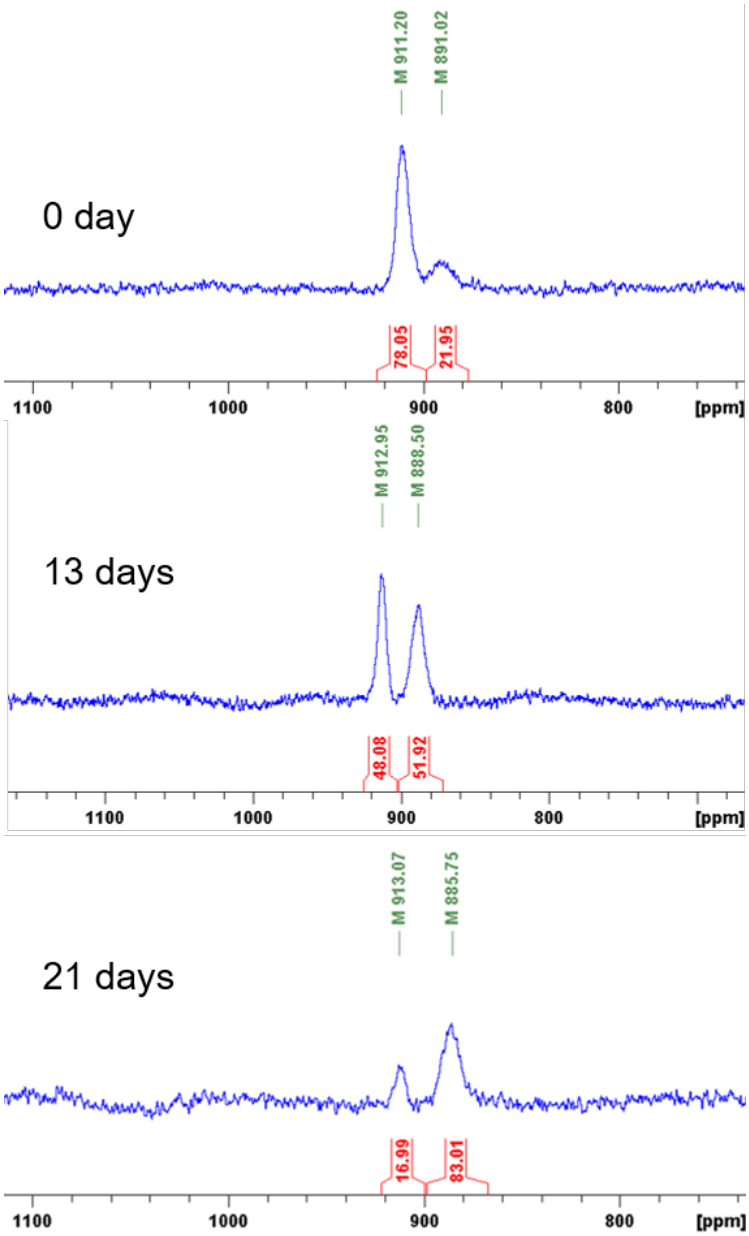

Figure 3.41: *^{195}Pt NMR spectra of* ***Lu.3.8*** *in D_2O over 21 days, showing formation of new isomer.*

3.5 Conclusion and Future Work

This chapter presented the synthesis, characterisation and photochemical studies of diazido Pt(IV) complex **3.1** with two different strained alkynes and extended the study to the synthesis of a Ln(III)-Pt(IV) complex through a double-click SPAAC reaction. The work associated with the synthesis, characterisation and properties of diazido Pt(IV) complex **3.1** with two strained alkyne - 1,4-diphenyl-2-butyne-1,4-dione and 5,6,11,12-tetradehydrodibenzo[a,e]- cyclooctene (Sondheimer diyne) was published.[62–64] Results show that the mono azido-, mono triazole- click product turn out less potential to be a photoactivatable complex compared to the diazido Pt(IV) substrate, but could still have potential photo-cytotoxicity. Further study is needed. The coupling of Ln-Pt utilising SPACC reaction was successful under mild conditions without using the cytotoxic copper catalyst. Using mixed azido compounds as reaction substrates with the Sondheimer diyne results in undesired side-products due to the nature of reaction: di-Pt and di-Ln complexes are also formed as side-products. Furthermore, without the control afforded by a Cu catalyst, multiple isomers can be formed, although there is evidence that suspension of the mixture of products in protic solvents (MeOH, H_2O) can induce triazole rearrangement of the click product at the Pt(IV) centre, which is anticipated to overcome the latter issue.

References

1 B. A. Jackson, V. Y. Alekseyev and J. K. Barton, *Biochemistry*, 1999, **38**, 4655–4662.

2 M. J. Rose and P. K. Mascharak, *Coord. Chem. Rev.*, 2008, **252**, 2093–2114.

3 Y. Liu, R. Hammitt, D. A. Lutterman, L. E. Joyce, R. P. Thummel and C. Turro, *Inorg. Chem.*, 2009, **48**, 375–385.

4 C. Moucheron, *New J. Chem.*, 2009, **33**, 235–245.

5 S. Betanzos-Lara, L. Salassa, A. Habtemariam and P. J. Sadler, *Chem. Commun.*, 2009, 6622–6624.

6 U. Schatzschneider, *Eur. J. Inorg. Chem.*, 2010, 1451–1467.

7 L. Zayat, O. Filevich, L. M. Baraldo and R. Etchenique, *Philos. Trans. R. Soc. A Math. Phys. Eng. Sci.*, 2013, 371, **1995**, 1-12.

8 B. Maity, M. Roy, B. Banik, R. Majumdar, R. R. Dighe and A. R. Chakravarty, *Organometallics*, 2010, **29**, 3632–3641.

9 U. Basu, I. Khan, A. Hussain, P. Kondaiah and A. R. Chakravarty, *Angew. Chemie - Int. Ed.*, 2012, **51**, 2658–2661.

10 S. Roy, S. Saha, R. Majumdar, R. R. Dighe and A. R. Chakravarty, *Polyhedron*, 2010, **29**, 2787–2794.

11 P. K. Sasmal, S. Saha, R. Majumdar, S. De, R. R. Dighe and A. R. Chakravarty, *Dalt. Trans.*, 2010, **39**, 2147–2158.

12 R. W. Y. Sun, A. L. F. Chow, X. H. Li, J. J. Yan, S. S. Y. Chui and C. M. Che, *Chem. Sci.*, 2011, **2**, 728–736.

13 S. W. Lai, Y. L, D. Zhang, B. Wang, C. N. Lok, C. M. Che, M. Selke, *Photochem. Photobiol*., 2011, **23**, 1–7.

14 T. Zou, C. N. Lok, Y. M. Eva Fung and C. M. Che, *Chem. Commun.*, 2013, **49**, 5423–5425.

15 N. A. Kratochwil, M. Zabel, K. J. Range and P. J. Bednarski, *J. Med. Chem.*, 1996, **39**, 2499–2507.

16 N. A. Kratochwil and P. J. Bednarski, *Arch. Pharm. (Weinheim).*, 1999, **332**, 279–285.

17 P. J. Bednarski, R. Grünert, M. Zielzki, A. Wellner, F. S. Mackay and P. J. Sadler, *Chem. Biol.*, 2006, **13**, 61–67.

18 A. Vogler, A. Kern and J. Hüttermann, *Angew. Chemie Int. Ed. English*, 1978, **17**, 524–525.

19 F. S. Mackay, J. A. Woods, H. Moseley, J. Ferguson, A. Dawson, S. Parsons and P. J. Sadler, *Chem. - A Eur. J.*, 2006, **12**, 3155–3161.

20 F. S. Mackay, J. A. Woods, P. Heringova, J. Kašpárková, A. M. Pizarro, S. A. Moggach, S. Parsons, V. Brabec and P. J. Sadler, *Proc. Natl. Acad. Sci. U. S. A.*, 2007, **104**, 20743–20748.

21 N. J. Farrer, J. A. Woods, L. Salassa, Y. Zhao, K. S. Robinson, G. Clarkson, F. S. MacKay and P. J. Sadler, *Angew. Chemie - Int. Ed.*, 2010, **49**, 8905–8908.

22 N. J. Farrer, J. A. Woods, V. P. Munk, F. S. MacKay and P. J. Sadler, *Chem. Res. Toxicol.*, 2010, **23**, 413–421.

23 L. Ronconi and P. J. Sadler, *Dalt. Trans.*, 2011, **40**, 262–268.

24 H. C. Tai, Y. Zhao, N. J. Farrer, A. E. Anastasi, G. Clarkson, P. J. Sadler and R. J. Deeth, *Chem. - A Eur. J.*, 2012, **18**, 10630–10642.

25 Y. Zhao, J. A. Woods, N. J. Farrer, K. S. Robinson, J. Pracharova, J. Kasparkova, O. Novakova, H. Li, L. Salassa, A. M. Pizarro, G. J. Clarkson, L. Song, V. Brabec and P. J. Sadler, *Chem. - A Eur. J.*, 2013, **19**, 9578–9591.

26 E. Shaili, M. Fernández-Giménez, S. Rodríguez-Astor, A. Gandioso, L. Sandín, C. García-Vélez, A. Massaguer, G. J. Clarkson, J. A. Woods, P. J. Sadler and V. Marchán, *Chem. - A Eur. J.*, 2015, **21**, 18474–18486.

27 S. J. Berners-Price, L. Ronconi and P. J. Sadler, *Prog. Nucl. Magn. Reson. Spectrosc.*, 2006, **49**, 65–98.

28 V. Venkatesh, C. J. Wedge, I. Romero-Canelón, A. Habtemariam and P. J. Sadler, *Dalt. Trans.*, 2016, **45**, 13034–13037.

29 A. Gandioso, E. Shaili, A. Massaguer, G. Artigas, A. González-Cantó, J. A. Woods, P. J.

Sadler and V. Marchán, *Chem. Commun.*, 2015, **51**, 9169–9172.

30 A. M. Pizarro, R. J. McQuitty, F. S. Mackay, Y. Zhao, J. A. Woods and P. J. Sadler, *ChemMedChem*, 2014, **9**, 1169–1175.

31 E. Shaili, L. Salassa, J. A. Woods, G. Clarkson, P. J. Sadler and N. J. Farrer, *Chem. Sci.*, 2019, **10**, 8610–8617.

32 P. V. Changa, J. A. Preschera, E. M. Sletten, J. M. Baskin, I. A. Miller, N. J. Agard, A. Lo and C. R. Bertozzi, *Proc. Natl. Acad. Sci. U. S. A.*, 2010, **107**, 1821–1826.

33 R. K. Pathak, C. D. McNitt, V. V. Popik and S. Dhar, *Chem. - A Eur. J.*, 2014, **20**, 6861–6865.

34 D. J. Nieves, N. S. Azmi, R. Xu, R. Lévy, E. A. Yates and D. G. Fernig, *Chem. Commun.*, 2014, **50**, 13157–13160.

35 L. Liang and D. Astruc, *Coord. Chem. Rev.*, 2011, **255**, 2933–2945.

36 J. A. Krause Bauer, T. M. Becker and M. Orchin, *J. Chem. Crystallogr.*, 2004, **34**, 843–849.

37 L. Henry, C. Schneider, B. Mützel, P. V. Simpson, C. Nagel, K. Fucke and U. Schatzschneider, *Chem. Commun.*, 2014, **50**, 15692–15695.

38 T. J. Del Castillo, S. Sarkar, K. A. Abboud and A. S. Veige, *Dalt. Trans.*, 2011, **40**, 8140–8144.

39 L. Waag-Hiersch, J. Mößeler and U. Schatzschneider, *Eur. J. Inorg. Chem.*, 2017, **2017**, 3024–3029.

40 A. R. Powers, X. Yang, T. J. Del Castillo, I. Ghiviriga, K. A. Abboud and A. S. Veige, *Dalt. Trans.*, 2013, **42**, 14963–14966.

41 L. Busetto, A. Palazzi and R. Ros, *Inorganica Chim. Acta*, 1975, **13**, 233–238.

42 N. J. Farrer, G. Sharma, R. Sayers, E. Shaili and P. J. Sadler, *Dalt. Trans.*, 2018, **47**, 10553–10560.

43 D. Sturmayr and U. Schubert, *Eur. J. Inorg. Chem.*, 2004, **3**, 776–782.

44 S. Mukhopadhyay, J. Lasri, M. F. C. Guedes da Silva, M. A. Januário Charmier and A. J. L. Pombeiro, *Polyhedron*, 2008, **27**, 2883–2888.

45 M. E. Martin, S. G. Parameswarappa, M. S. O'Dorisio, F. C. Pigge and M. K. Schultz, *Bioorganic Med. Chem. Lett.*, 2010, **20**, 4805–4807.

46 S. C. Bishop, R. Winefield, A. Anbanandam and J. N. Lampe, *bioRxiv*, 2019, 1–16.

47 N. J. Farrer, J. A. Woods, L. Salassa, Y. Zhao, K. S. Robinson, G. Clarkson, F. S. MacKay and P. J. Sadler, *Angew. Chemie - Int. Ed.*, 2010, **49**, 8905–8908.

48 B. Schulze and U. S. Schubert, *Chem. Soc. Rev.*, 2014, **43**, 2522–2571.

49 P. L. Holland, *Dalt. Trans.*, 2010, **39**, 5415–5425.

50 K. Yao, A. Bertran, J. Morgan, S. M. Hare, N. H. Rees, A. M. Kenwright, K. Edkins, A. M. Bowen and N. J. Farrer, *Dalt. Trans.*, 2019, **2**, 6416–6420.

51 R. R. Vernooij, T. Joshi, E. Shaili, M. Kubeil, D. R. T. Appadoo, E. I. Izgorodina, B. Graham, P. J. Sadler, B. R. Wood and L. Spiccia, *Inorg. Chem.*, 2016, **55**, 5983–5992.

52 J. S. Butler, J. a Woods, N. J. Farrer, M. E. Newton and P. J. Sadler, *J. Am. Chem. Soc.*, 2012, **134**, 16508–11.

53 Y. Zhao, N. J. Farrer, H. Li, J. S. Butler, R. J. McQuitty, A. Habtemariam, F. Wang and P. J. Sadler, *Angew. Chemie - Int. Ed.*, 2013, **52**, 13633–13637.

54 C. Vallotto, E. Shaili, H. Shi, J. S. Butler, C. J. Wedge, M. E. Newton and P. J. Sadler, *Chem. Commun.*, 2018, **54**, 13845.

55 F. A. Villamena, C. M. Hadad and J. L. Zweier, *J. Phys. Chem. A*, 2003, **107**, 4407–4414.

56 U. Schatzschneider, *Inorganica Chim. Acta*, 2011, **374**, 19–23.

57 E. Orlowska, M. V. Babak, O. Dömötör, E. A. Enyedy, P. Rapta, M. Zalibera, L. Bučinský, M. Malček, C. Govind, V. Karunakaran, Y. C. S. Farid, T. E. McDonnell, D. Luneau, D. Schaniel, W. H. Ang and V. B. Arion, *Inorg. Chem.*, 2018, **57**, 10702–10717.

58 D. Ji, T. A. Kamalden, S. Del Olmo-Aguado and N. N. Osborne, *Apoptosis*, 2011, **16**, 425–437.

59 H. N. C. Wong and F. Sondheimer, *Tetrahedron*, 1981, **37**, 99–109.

60 A. Orita, D. Hasegawa, T. Nakano and J. Otera, *Chem. - A Eur. J.*, 2002, **8**, 2000–2004.

61 I. Kii, A. Shiraishi, T. Hiramatsu, T. Matsushita, H. Uekusa, S. Yoshida, M. Yamamoto, A. Kudo, M. Hagiwara and T. Hosoya, *Org. Biomol. Chem.*, 2010, **8**, 4051–4055.

62 K. Yao, A. Bertran, A. Howarth, J. M. Goicoechea, S. M. Hare, N. H. Rees, M. Foroozandeh, A. M. Bowen and N. J. Farrer, *Chem. Commun.*, 2019, **55**, 11287–11290.

63 K. Yao, A. Bertran, J. Morgan, C. Greenhalgh, K. Edkins, A. M. Bowen and N. J. Farrer, *Eur. J. Inorg. Chem.*, 2021, 1397-1040.

64 K. Yao, A. Bertran, J. Morgan, S. M. Hare, N. H. Rees, A. M. Kenwright, K. Edkins, A. M. Bowen and N. J. Farrer, *Dalt. Trans.*, 2019, **48**, 6416–6420.

Chapter 4: Cell-permeable SalicylateDO3A Ln-Pt complex

4.1 Introduction

4.1.1 INDIANA

In collaboration with Professor Andrew Baldwin and Dr Gogulan Karunanithy, a ^{1}H diffusion NMR method has recently been developed by them to indicate whether the contrast agent is intracellular.[1] This method was developed to distinguish between intracellular and extracellular water based on the fact that water diffusion in intracellular fluids is defined by the boundaries of the cell. Since the cell is much smaller than the voxel (volume pixel) in an MRI image, this means that intracellular fluid can be treated as a slow diffusing pool, whilst extra-cellular fluid is treated as a fast diffusing pool. The INDIANA (IN cell DIffusion Analysis) methodology allows these two pools and their properties to be quantitatively described, including the relaxation rates. In this chapter, we will use the INDIANA method to investigate the cellular uptake of the Gd complexes.

4.1.2 Switch-on luminescent sensor

The general concept of generating “switch-on” luminescence following reduction of a platinum(IV) prodrug to platinum(II) is a highly promising strategy for tracking (sub)cellular distribution and reduction of platinum(IV) prodrugs. Previously reported strategies include axial platinum(IV) coordination of quenched fluorophores such as fluorescein[2] and selective fluorescence reporting from organic probes following the

reaction with specific platinum(II) reduction fragments.[3]

Lanthanides provide a significant advantage over purely organic fluorophores, by producing a highly distinctive emission profile when excited, from which background autofluorescence can also be effectively removed through time-gating.[4] There were examples for using lanthanide complexes as responsive probes based on the modulation of the emission intensity, lifetime or polarisation. The lanthanide probes have been applied to report on local pH, pM (M = Zn, Na, K …) or the concentration of anions, such as bicarbonate, citrate, lactate, bicarbonate, or urate.[5-9]

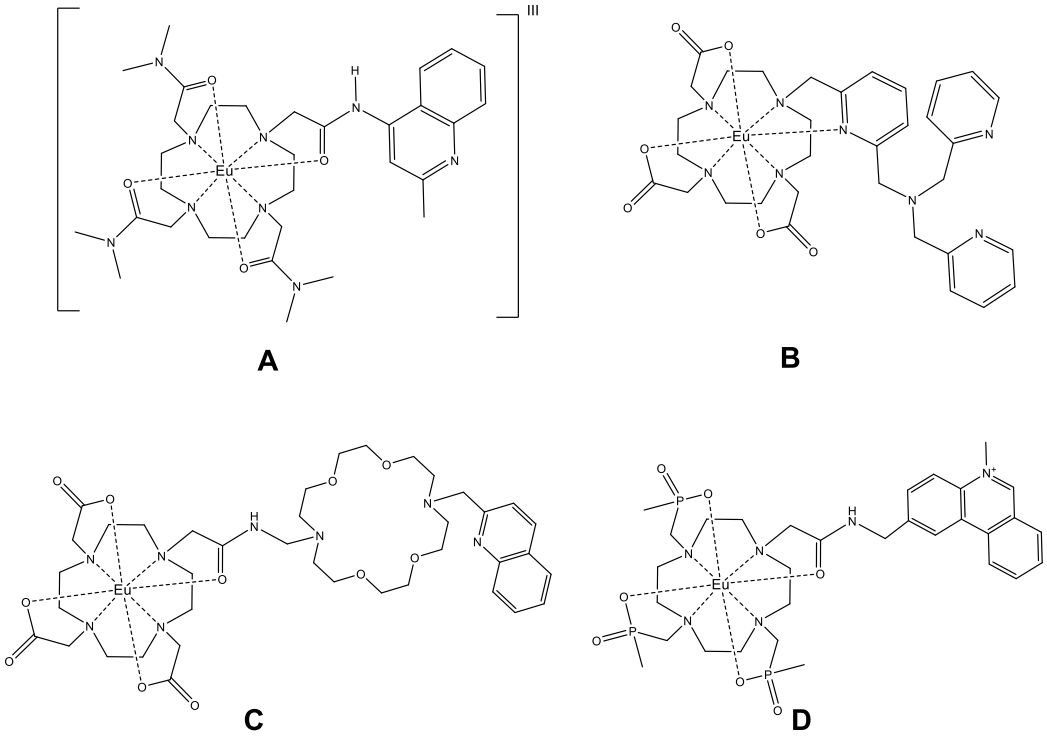

Figure 4.1: *Complex A: Eu pH sensor; complex B: Eu probe that emission would be quenched upon binding to Zn(II); complex C: Eu complex which showed modulation of emission in the presents of* Na^+ *and* K^+*; complex D: Eu complex used to detect hard anions such as carboxylates or phosphate.*[6]

The d-block metal complexes were found to sensitise the luminescence of multiple lanthanide complexes from visible to NIR emission. The d-f hybrids can be prepared by conventional synthesis and self-assembly. Ru(II), Pt(II), Pd(II), Re(I), Os(II) and Ir(III) complexes have been incorporated as sensitisers for luminescence from

lanthanides,[7,10-12] or at the other extreme quenching of lanthanide luminescence in the presence of a ^{3}MLCT state of lower energy can be used to signal the formation of a transition element complex.[6] Recently, several Ln-Pt(II) complexes was investigated in which the Pt(II) moieties acted as the antenna for the Ln emission. [10–16] Some of them were also studied as theranostic agents to achieve both imaging and therapeutic purpose.[17-20] The cellular uptake and localisation properties of the complexes were investigated by confocal microscopy. Wong *et al*.[18] found a Eu-Pt complex in which the binding of Pt was believed to quench the emission of the Eu (Figure 4.2 Complex C), as the energy absorbed by the antenna ligand is transferred to the dissociative states of the cis-Pt(II) moiety which means very limited energy can be transferred to the Eu(III) excited state for emission. Thus, the release of the cisplatin can be controlled by two-photon excitation *in vitro*, and the luminesce of Eu can be used to monitor this process.[18]

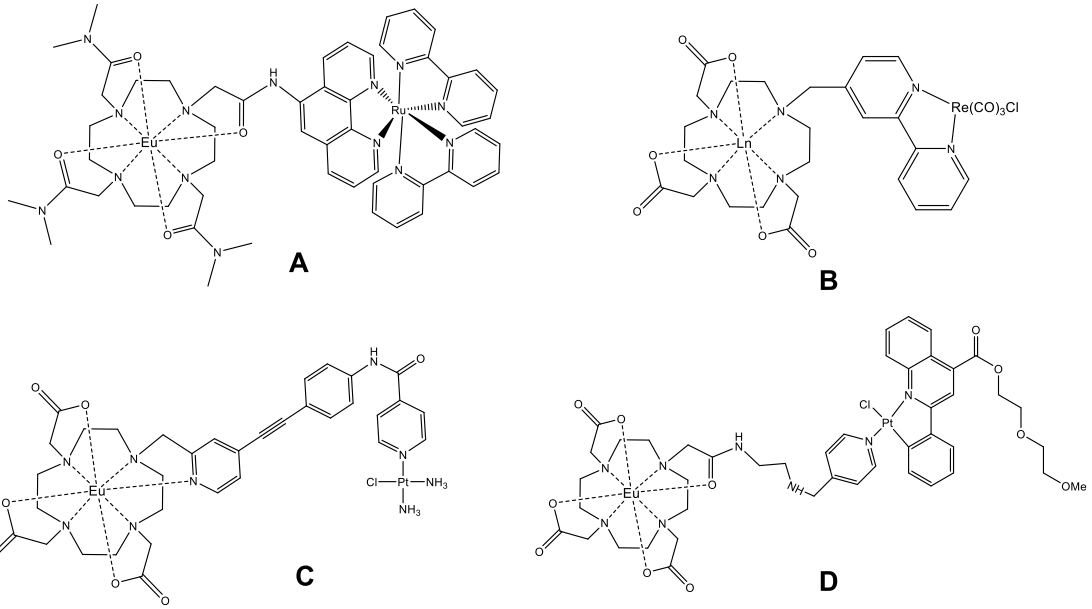

Figure 4.2: *Complex A and B:d-f complexes in which the d-block metals act as sensitiser for the lanthanide emission. Complex C and D: Ln-Pt complexes which can be used as theranostic agents.*

4.1.3 Salicylic acid and its platinum complexes

There are a few examples of synthesis and characterisation of salicylate-platinum.[21-26] I. Lampronti and S Hou have synthesised salicylate-platinum(II) complexes (Figure 4.3) and studied their anticancer activities. The presence of O-donors as anionic ligands is the common character of Pt-drugs provided with a better therapeutic index than cisplatin, namely carboplatin, oxaliplatin, nedaplatin and lobaplatin. The salicylate leaving group with O-donors may also result in better lipophilic properties for the platinum drugs comparing to cisplatin which leads to better cellular accumulation. The results of the papers have shown that the salicylate Pt(II) complexes shown in Figure 4.3 with R = $CH(CH_3)_2$ were all more potent than Carboplatin, Oxaliplatin and Eptaplatin against four human cancer cell lines 3AO, A59, NCI-H460 and SGC-790.[24]

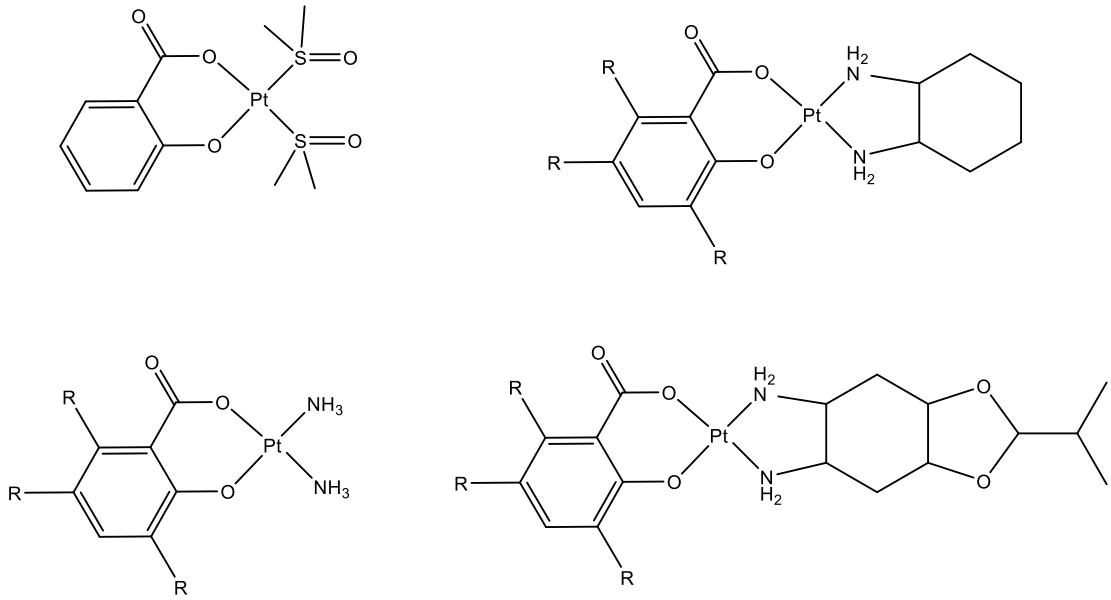

Figure 4.3: *Chemical structure of salicylate-platinum and derivatives which has been studied as anticancer drugs.*

4.1.4 Modifying the axial position of platinum complexes to increase their cellular uptake

As discussed previously in Chapter 1, the cellular uptake and rate of reduction of Pt(IV) prodrugs inside the cells depend strongly on the coordinated ligands. D. Osella *et. al* have reported the conjugation of the valproate (VPA) and octanoate (OA) ligands to the axial position of cisplatin (structure shown in Figure 4.4). In the case of *cis,cis,trans*-diamminedichloridobis(valproato)platinum(IV) complex, the valproate ligand was known as an anti-epileptic drug which has histone deacetylase inhibitor (HDACI) activity. The remarkably increased cytotoxicity was interpreted as the result of the increased cellular accumulation of the complex by virtue of its increased lipophilicity and of the synergy with the HDACI action of VPA. While in the case of *cis,cis,trans*-diamminedichloridobis(n-octanoato)platinum(IV), the complex exhibits a 106-fold enhancement in cellular accumulation in ovarian (A2780) cancer cells in comparison to its synthetic precursor, *cis,cis,trans*-diamminedichloridobishydroxideplatinum(IV). This results from the enhanced accumulation of the complex which origins from the higher lipophilicity.

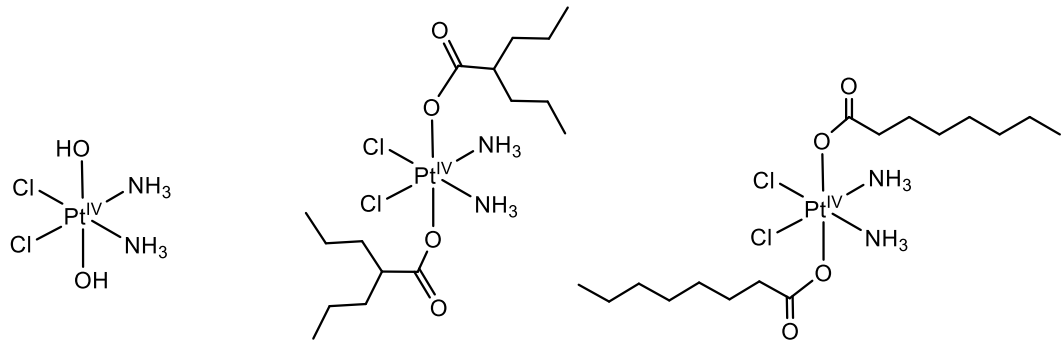

Figure 4.4: *Chemical structure of the cis-Pt(IV) precursor, the $[Pt(NH_3)_2(Cl_2)(VPA)_2]$ and $[Pt(NH_3)_2(Cl_2)(OA)_2]$ complexes.*

4.1.5 The design of salicylate-containing lanthanide complex

In this chapter, a series of Ln-Pt complexes were designed in which the lanthanide is bound in an octadentate DO3A binding site, while the pendent salicylic acid group can act as a ligand to a second metal centre – platinum. The salicylic ligand has the advantages of providing the phenyl carboxylic acid and hydroxide groups as the bidentate binding site and also providing an aromatic chromophore to sensitise the lanthanide emission. The axial position of the platinum(IV) complexes can be modified to octanoyl groups to improve the overall cellular uptake of the complexes. Alternating the lanthanide ions can allow different imaging technique, for example, the Gd complexes can be used in NMR related imaging so that the INDIANA NMR diffusion method can be applied, while Eu/Tb can be used in optical imaging.

4.2 Synthesis

4.2.1 Synthesis of salicylic appended lanthanide DO3Acomplexes

The synthesis started from 3-methylsalicylic acid, which reacted with acetyl chloride at 0-5^{o}C to give the 2-acetoxy-3-methylbenzoic acid product. The intermediate then undergoes a Fries rearrangement in the present of anhydrous aluminium chloride to obtain the 5-acetyl-2-hydroxy-3-methylbenzoic acid, proposed reaction scheme is shown in Figure 4.5.[27] However, the Fries rearrangement was found to generate multiple products which could be because the acetyl group rearranged to different positions of the aromatic ring.

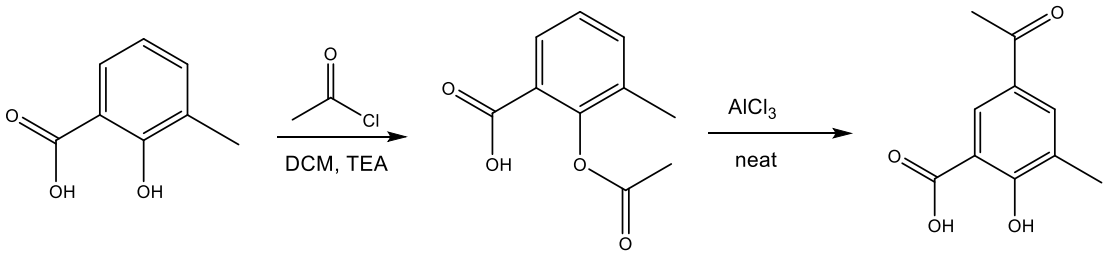

Figure 4.5: *Fries rearrangement reaction starting from 3-methylsalicylic acid and acetyl chloride.*

Since the Fries rearrangement discussed above was found to be not very effective, we decided to start with the commercially available methyl 5-acetylsalicylate, in which the methyl group of the carboxylate can be easily removed under basic condition. The acetyl group can be brominated and the resulting bromination product **4.1** can undergo alkylation with triester. Figure 4.6 depicts the synthetic pathway for formation of compound **4.1**. Bromination of aromatic carbonyl compounds with $CuBr_2$ was found to be effective and straightforward.[28] The reaction of methyl 5-acetylsalicylate with 2.2 equivalent of $CuBr_2$ was conducted in 1:1 mixture of chloroform and ethyl acetate. After filtering out the CuBr white precipitate and removing the solvent under reduced pressure, the crude product was obtained as pale-yellow oil. The pure product can be recrystallized from dichloromethane/hexane mixture after standing in freezer overnight. The product was characterised by ESI-MS, ^{1}H NMR and ^{13}C NMR.

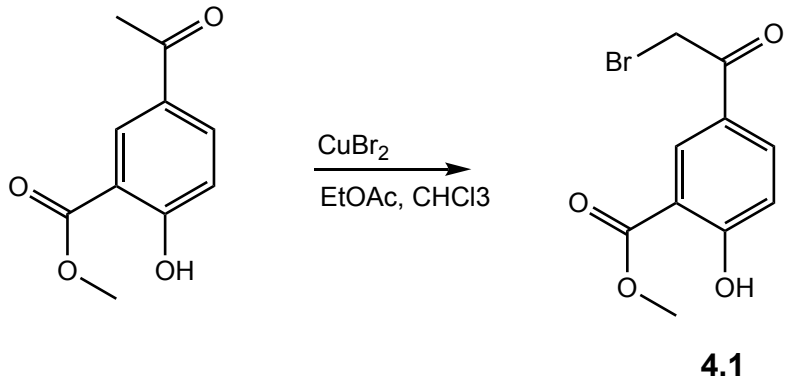

4.1

Figure 4.6: *Synthetic attempts of brominated 4-methylsalicylic acid.*

Bromination of 4-methylsalicylic acid was also attempted in order to generate the brominated methyl group. This can be used to prepare corresponding triester derivative which can act as a 7-coordinated position for the lanthanide. The bromination reaction with $CuBr_2$ was found to be unsuccessful as no brominated compound was found judging by TLC, mass spectroscopy and ^1H NMR. Alternative bromination approach using NBS was tested, although the ^1H NMR result indicated that the bromination happened in the aromatic ring rather than the methyl group.[29] Another bromination method starts from protecting the carboxylic acid with methyl group and then the brominate the methyl protected product with NBS in carbon tetrachloride. The reaction schemes are showed in Figure 4.7

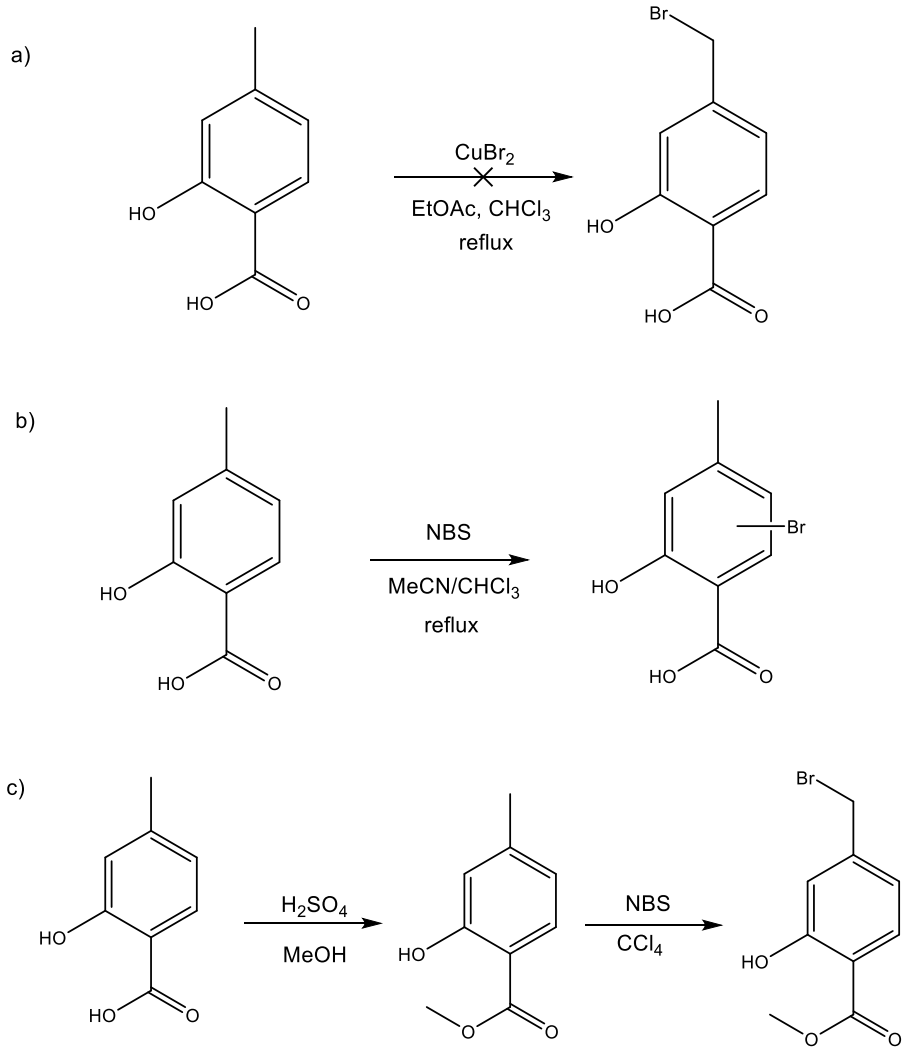

Figure 4.7: *Synthetic attempts of brominated 4-methylsalicylic acid.*

As shown in Figure 4.8, the reaction between methyl 5-bromoacetyl-2-hydroxybenzoate (**4.1**) and *tert*-butyl protected triester (**2.2**) in the presence of potassium carbonate resulted in the crude protected ligands. The purification of the crude product was achieved by the flash column chromatography on silica gel with acetonitrile and water as eluents (yield: 56%). The deprotection of the *tert*-butyl protection group was carried out in dichloromethane by adding the trifluoroacetic acid dropwise. The reaction was stirred at room temperature for 24 hours, after which the dichloromethane and most of the trifluroacetic acid were removed by rotary evaporation. The deprotected crude product was dissolved in minimum amount of methanol and precipitate with diethyl ether to yield the product as a pale yellow solid (yield: 82%). The lanthanide complexation of the deprotected ligand was carried out in methanol with the corresponding lanthanide triflate salt at 60^{o}C. After 48 hours, methanol was removed, and the complex was dissolved in 3-5 ml water. The pH of the water solution was adjusted to 10 by adding 1M sodium hydroxide solution dropwise to precipitate out the excess lanthanide ion. The $Ln(OH)_3$ solid was removed by centrifuging, the resulting supernatant was stirred at 50^{o}C for 24 hours with the pH maintained at 10. The methyl-deprotected ligand was purified by dialysis with 500 MWCO cellulose membrane (yield: 50%). The pure product **Ln.4.5** was characterised by ESI-MS, NMR spectroscopy, UV-vis spectroscopy and luminescence spectroscopy, the characterisation of **Ln.4.5** is in section 4.3.

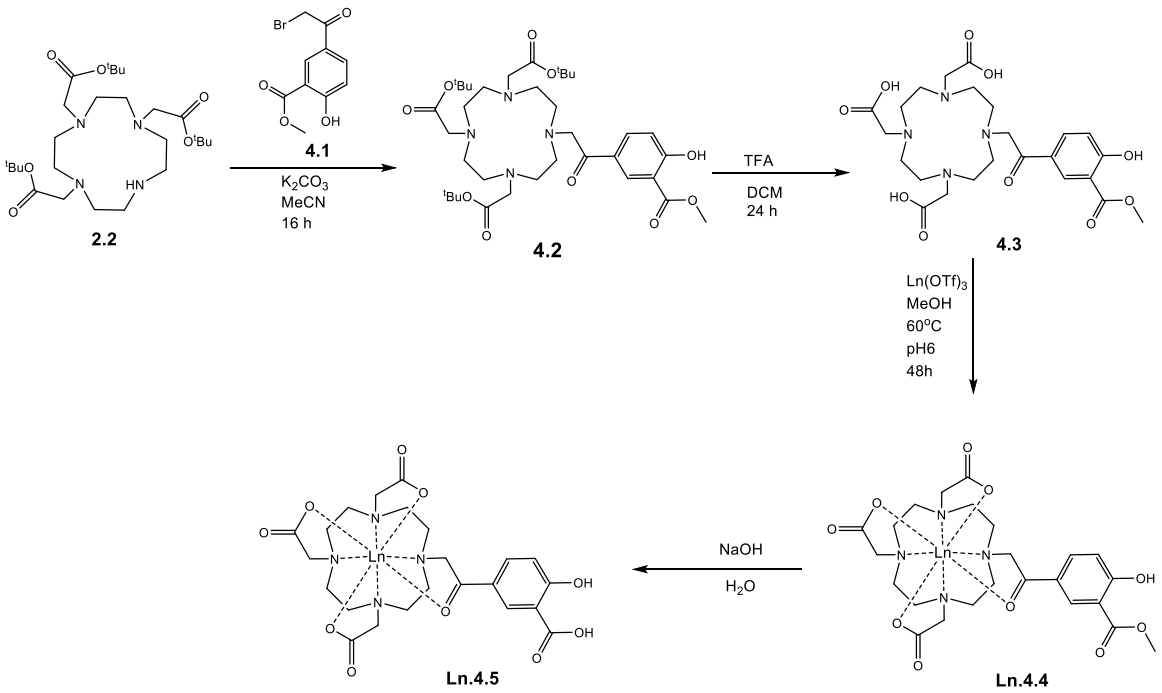

Figure 4.8: *Synthetic pathway for the preparation of a series of lanthanide DO3A complexes with a pendent salicylic ligand.*

4.2.2 Synthesis of lanthanide salicylicDO3A platinum complexes

Reaction of **Ln.4.5** with *cis*-[$Pt(NH_3)_2I_2$] yielded the heterometallic Ln-Pt(II) complex **Ln.4.6**. Previously, the platination was carried out with *cis*-[$Pt(NH_3)_2Cl_2$], which was found to be less effective. This may due to the much higher solubility product (Ksp) of AgCl (1.8×10^{-10}) compared to AgI (1.5×10^{-16}). The K_{sp} of the corresponding Ag salt was important because the halogen ligand of the *cis*-platinum complexes need to be precipitated as an Ag^+ salt before the platinum centre binds to the salicylic arm. The pH of the reaction was another vital factor of accelerating the platination reaction, as the deprotonation of the salicylic acid can help its coordination to the platinum. However, increasing the pH dramatically may cause the undesired formation of Ag(OH) solid and Pt(0) which will ultimately affect the yield of the product. Carrying out the reaction at pH = 8 with 1.2 equivalent of silver nitrate and *cis*-[$Pt(NH_3)_2I_2$] was found as the best

reaction condition. Oxidation was accomplished by treating the **Ln.4.6** complexes with 15% H_2O_2 aqueous solution to give the Pt(IV) di-hydroxido complex **Ln.4.7** complex. Reaction of **Ln.4.7** complexes with octanoyl chloride in the presence of pyridine afforded the Ln-Sali-Pt(IV) di-octanoic acid conjugate **Ln.4.8**. All lanthanide and lanthanide-platinum complexes can be purified by reverse-phase HPLC with an eluent system comprising of water + 0.1% formic acid/ acetonitrile + 0.1% formic acid.

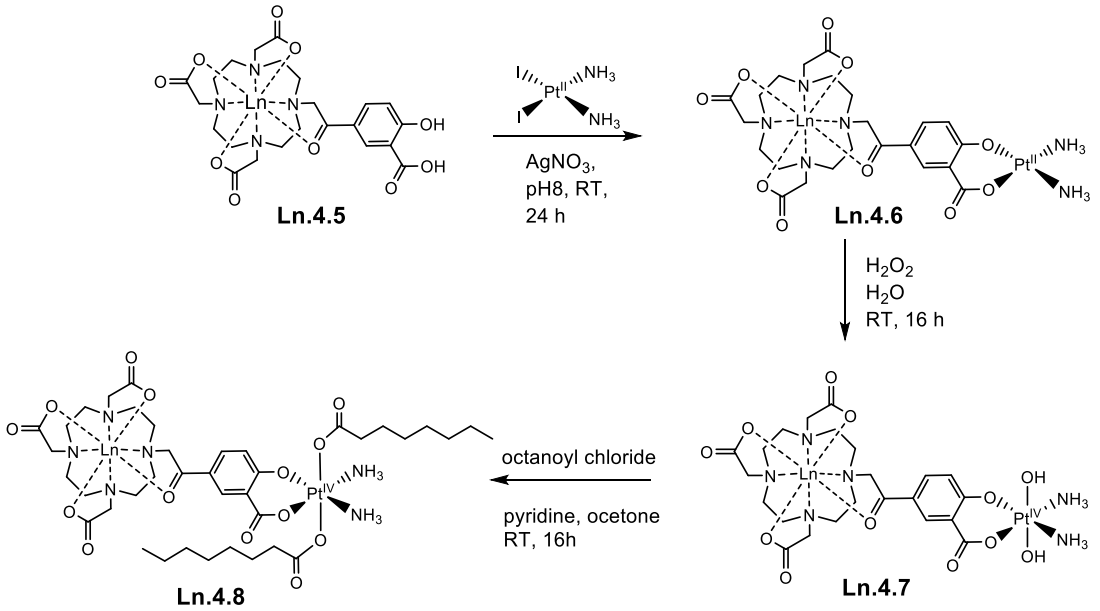

Figure 4.9: *Synthetic pathway for the preparation of a series of Ln-Pt(II) complexes* ***Ln.4.6****, the oxidisation of the* ***Ln.4.6*** *complexes and the axial modification of the Ln-Pt(IV) complexes* ***Ln.4.7*** *.*

4.3 Characterization of the Complexes

4.3.1 HPLC purification and high-resolution mass spectrometry (HRMS)

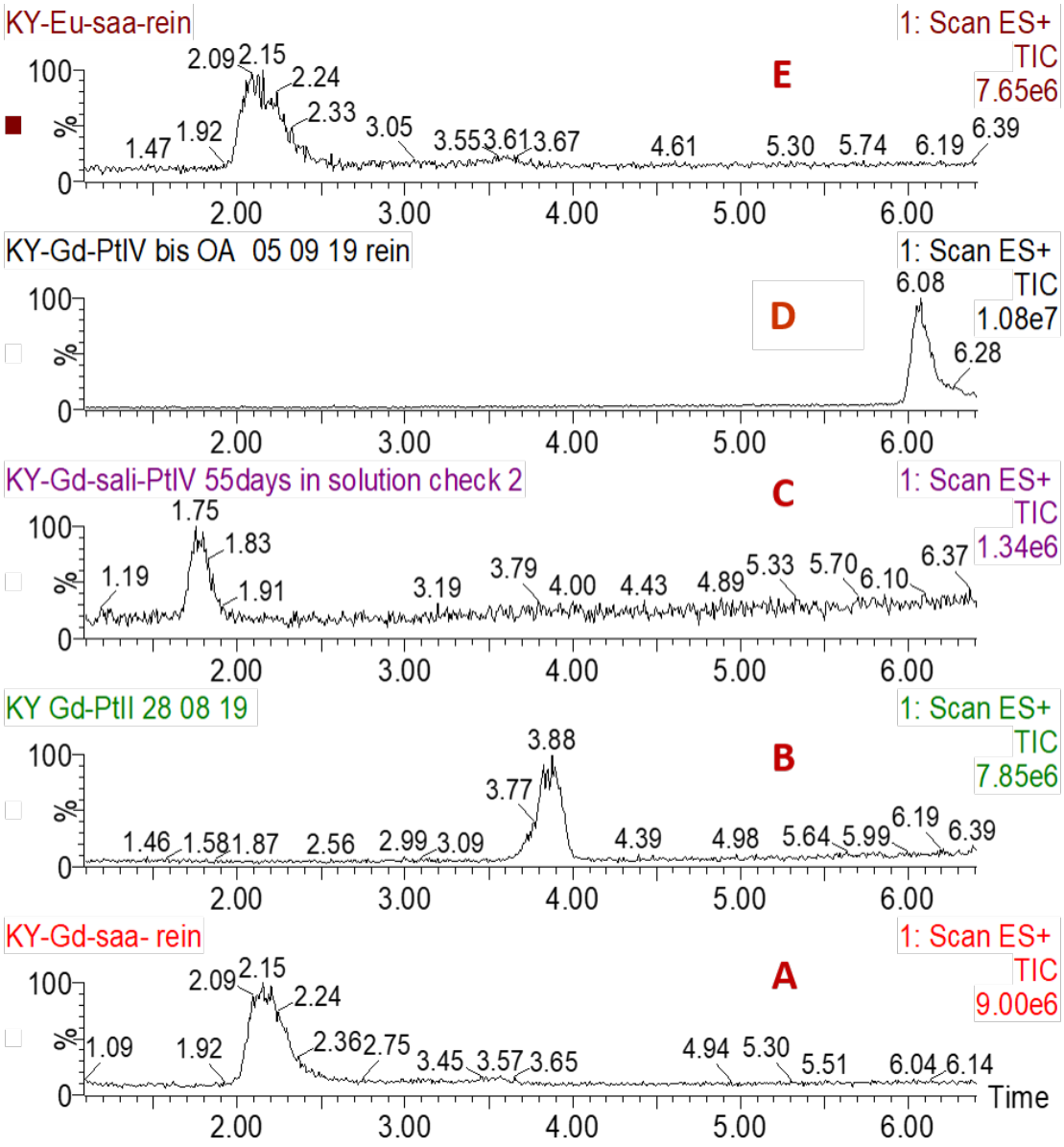

Figure 4.10: *HPLC traces of A)* ***Gd.4.5****,* t_R *= 2.15 min; B)* ***Gd.4.6****,* t_R *= 3.88 min; C)* ***Gd.4.7****,* t_R *= 1.75 min; D)* ***Gd.4.8,*** t_R *= 6.08 min and E)* ***Eu.4.5,*** t_R *= 2.15 min.*

Figure 4.10 shows the LCMS re-injection traces of Gd-Pt complexes **4.5-4.8**. Trace A is the reinjection of **Gd.4.5** complex with the retention time at 2.15 min. For trace B the peak at 3.88 min is the Gd-Pt(II) complex **Gd.4.6**, while in trace C and D with the peaks

at 1.75 min and 6.08 min are associated with the Gd-Pt(IV) and di-octanoic Gd-Pt(IV) complexes **Gd.4.7** and **Gd.4.8** respectively. All complexes are stable in aqueous solution for at least 50 days according to the LCMS reinjections results of the solutions. The LCMS results also indicated that changing the lanthanide ion of the lanthanide ion did not affect the retention time of the complex, as shown in the Figure 4.10, **Eu.4.5** has the same retention time as **Gd4.5**. Thus, the same HPLC purifying method can be applied to complexes with different lanthanide ions (Eu/Gd/Tb/Yb/Lu) without further modification. The HPLC purifications were achieved by mass-directed method, all complexes were observed as $[M + H]^+$ and $[M + Na]^+$ ions, while in HRMS the complexes were preferably observed as $[M + 2H]^{2+}$ ion (Figure 4.11).

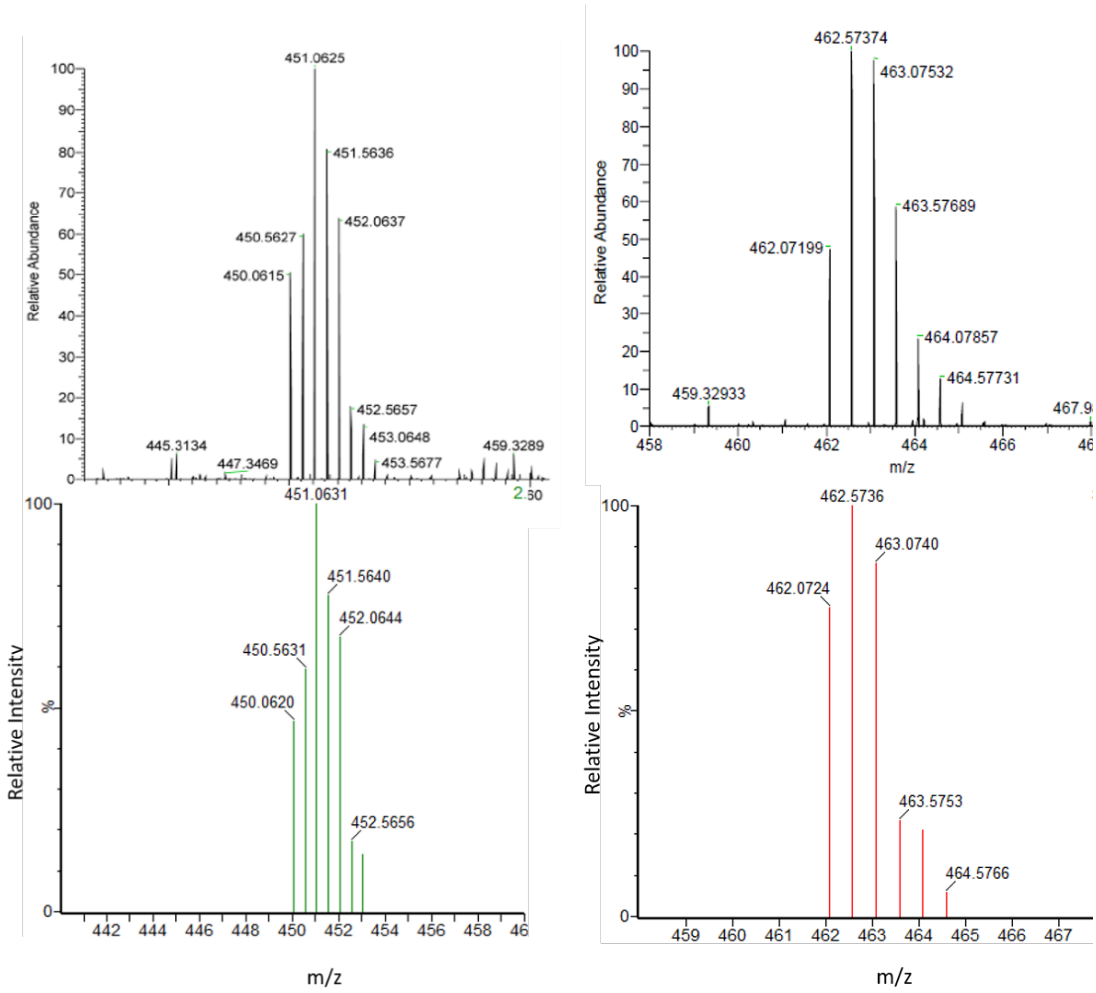

Figure 4.11: *HRMS of* ***Ln.4.6*** *in MeOH, Left:* ***Eu.4.6****, molecular formula:* $C_{23}H_{35}EuN_6O_{10}Pt$*, measured as* $[M+2H^+]^{2+}$*, mass error: 1.3 ppm; right:* ***Lu.4.6****, molecular formula:*

$C_{23}H_{35}LuN_6O_{10}Pt$, , measured as $[M+2H]^{2+}$, mass error: 0.3 ppm. Top: measured spectra, bottom: predicted spectra.

4.3.2 NMR characterization

4.3.2.1 ^{1}H NMR

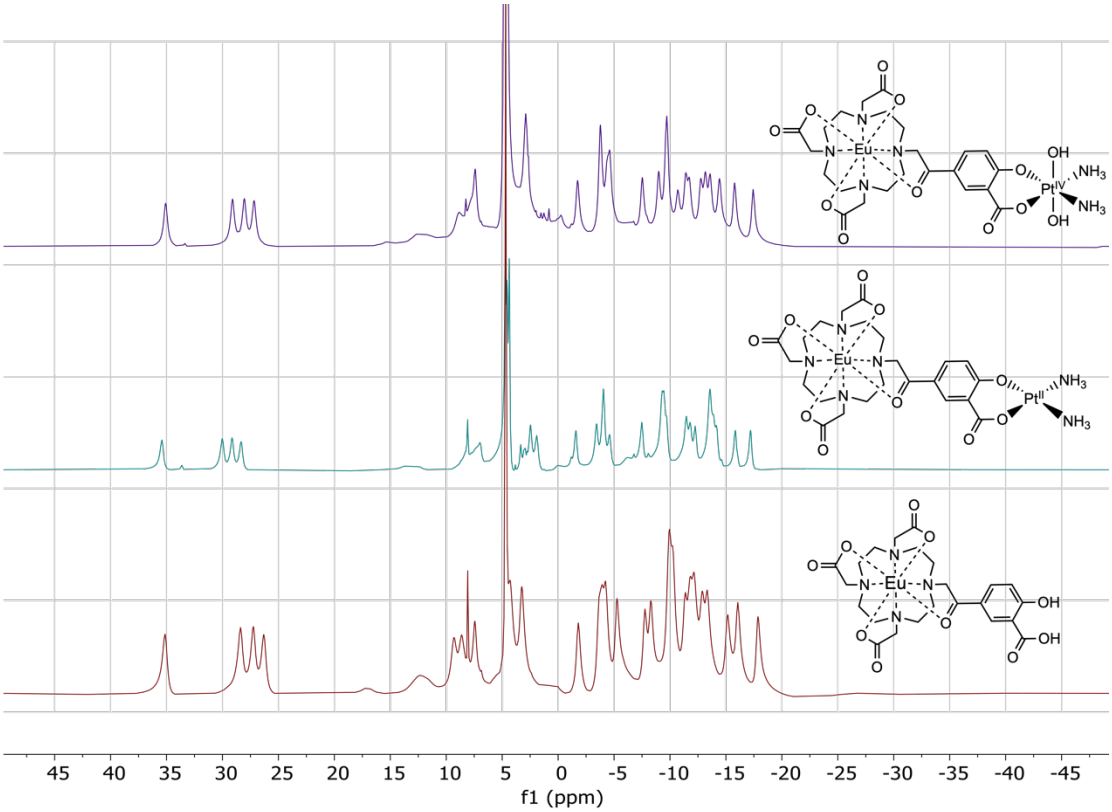

Figure 4.12: *^{1}H NMR spectra of **Eu.4.7** (top), **Eu.4.6** (middle) and **Eu.4.5** (bottom)*

The 1H-NMR spectrum of europium complexes – **Eu.4.5, Eu.4.6** and **Eu.4.7** all exhibited similar NMR spectra compared to DO3A europium analogues with shifted resonance peaks, as shown in Figure 4.12. The four main resonances between 25 and 35 ppm show four different proton environments on the macrocycle backbone, indicating the square antiprismatic (SAP) geometry predominates, whereas the resonances from the twisted squared antiprismatic (TSAP) have much lower chemical shifts around 8 ppm. The axial proton of the SAP isomers in the Pt(II) (**Eu.4.6**) and Pt(IV) (**Eu.4.7**) become broader comparing to the Eu only complex (**Eu.4.5**), while the

TSAP peaks of the three complexes are all relatively sharp compared to the SAP proton. Among the three complexes, the chemical shifts of the resonances stay almost the same. The similarity of the ^{1}H-NMR spectra suggests that all three europium(III) complexes (**Eu.4.5, Eu.4.6** and **Eu.4.7**) adopted very similar structures in solution, and indicates the binding of the Pt(II) or the oxidisation of the Pt(II) centre to Pt(IV) would not affect the ^{1}H NMR chemical shifts of the DO3A ligand.

The ^{1}H NMR spectra of **Yb.4.5** and **Yb.4.6** also exhibited similar forms. The relatively sharp peaks imply that the complex is an eight-coordinate complex where the ketone is actively engaged in the coordination. Peaks between 140-80 ppm are assigned to typical axial protons of SAP isomers while resonances around 50-15 ppm are assigned to axial protons of TSAP protons.

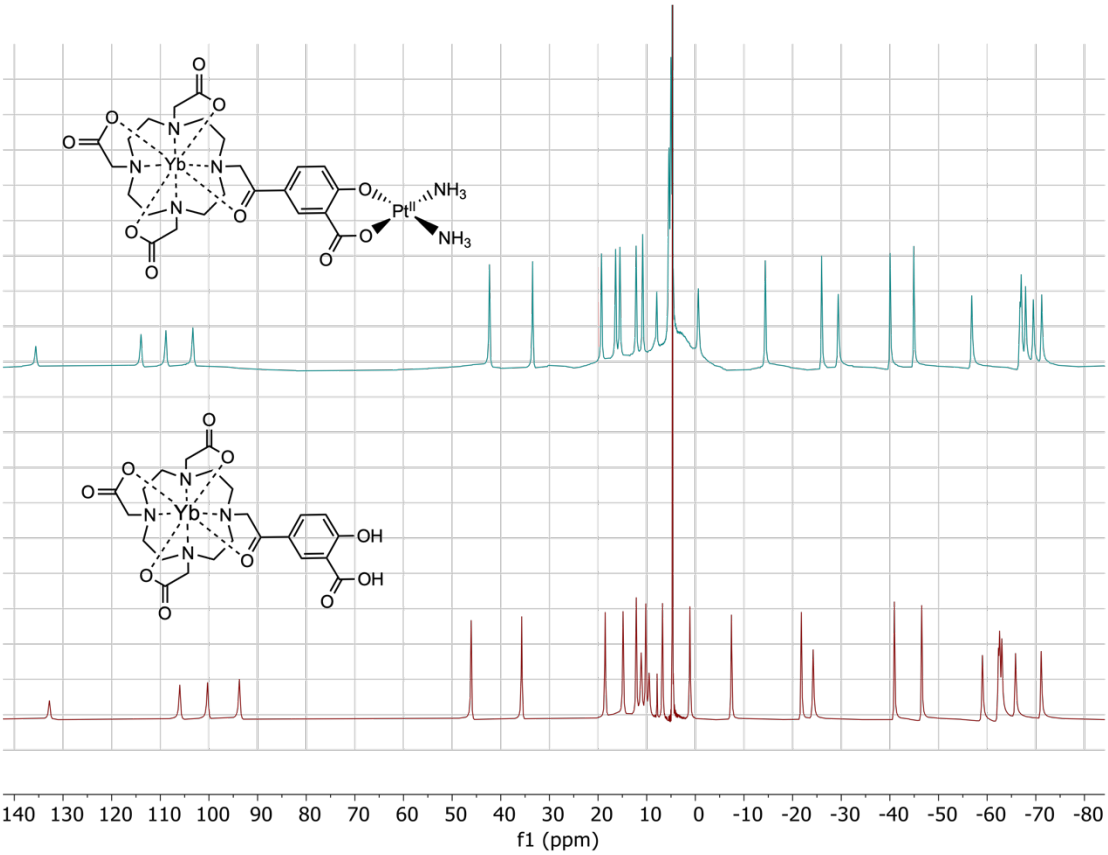

Figure 4.13: *^{1}H NMR spectra of* ***Yb.4.6*** *(top) and* ***Yb.4.5*** *(bottom)*

4.3.2.2 ^{191}Pt NMR

The ^{195}Pt NMR of all complexes measured are consistent with Pt(II) and Pt(IV) oxidation states. ^{195}Pt NMR of **Lu.4.6** revealed a single resonance at -1608 ppm (D_2O, Figure 4.14). The ^{195}Pt NMR resonance of **Eu.4.6** is identical to its Lu counterpart, while the resonances Tb and Yb complexes (**Tb.4.6** and **Yb.4.6**) are slightly different, which are -1622 ppm and -1631 ppm respectively as shown in Figure 4.14. Overall, the differences in ^{195}Pt NMR of different Ln-Pt(II) complexes are all within 2%, which means the paramagnetic lanthanide centre only has minor effect on the ^{195}Pt resonance. The Lu-Pt(IV) complex **Lu.4.7** has the resonance at 1691 ppm, which is consistent with typical ^{195}Pt(IV) NMR chemical shift in literature. While the ^{195}Pt resonance of **Lu.4.6** was observed as a singlet, the the ^{195}Pt resonance **of Lu.4.7** was revealed as a quintet (Figure 4.15), which is resulted from the coupling to the two equivalent quadrupolar (I = 1) ^{14}N nuclei of the NH_3 ligands. The coupling constant of between Pt and N is 213 Hz. The same coupling phenomenon was observed in the di-octanoic Gd-Pt(IV) complex **Gd.4.8** with a couple constant = 210 Hz. The magnitude of the ^1J (^{195}Pt, ^{14}N) coupling constant (213 Hz, 210 Hz) is consistent with other ^1J (^{14}N, ^{195}Pt) constants that was previously observed in the Pt(IV) species, for example , *cis,cis,cis*-$[Pt(N_3)_2(OH)_2(NH_3)_2]$ (167 Hz). After modifying the axial position of the platinum centre by adding the octanoic groups, the platinum resonances were changed significantly. The ^{195}Pt NMR signal for the mono-octanoic Gd-Pt(IV) complex **Gd.4.7** was observed at 1777 ppm, while the resonance of di-octanoic Gd-saili-Pt(IV) complex **Gd.4.8** was observed at 1918 ppm (Figure 4.16). The ^{195}Pt chemical shift of **Gd.4.7** shifted downfield from the di-hydroxide axial ligands to mix axial ligands and to di-octanoic axial ligands is due to the decreasing electron density around the platinum nucleus.

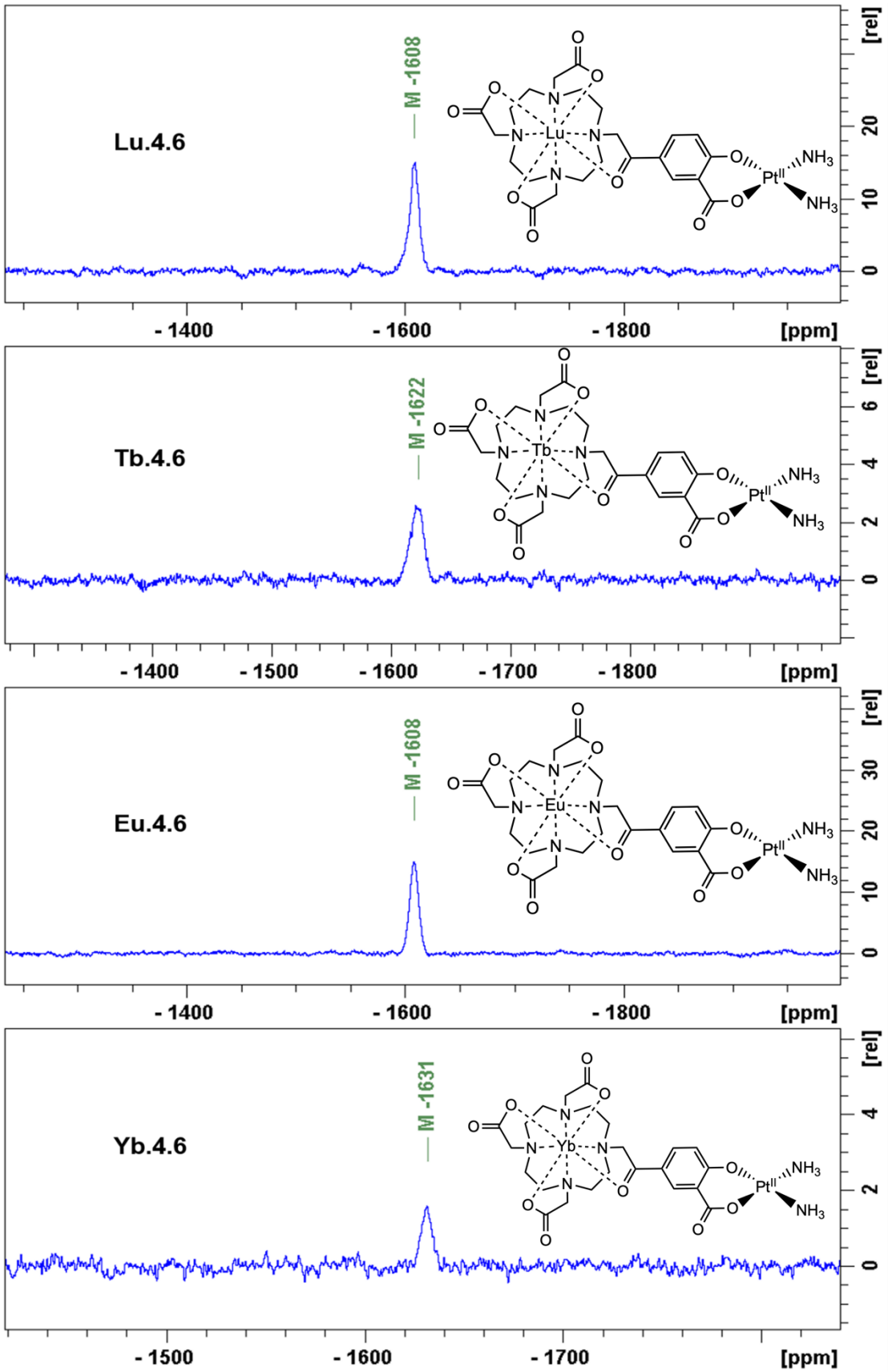

Figure 4.14: *^{195}Pt NMR spectrum (108 MHz, D_2O) of* ***Lu.4.6***, ***Tb.4.6 Eu.4.6*** *and* ***Yb.4.6***.

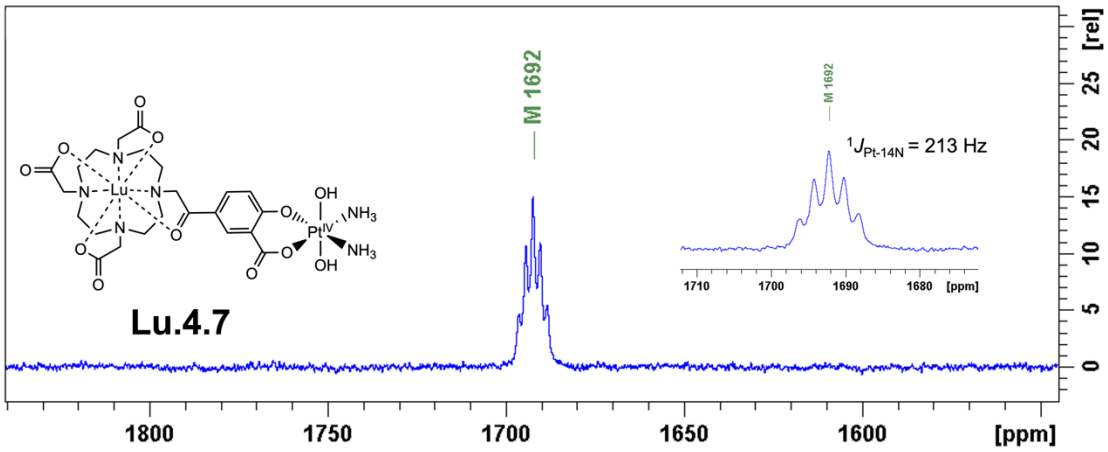

Figure 4.15: *^{195}Pt NMR spectrum (108 MHz, D_2O) of* ***Lu.4.7****.*

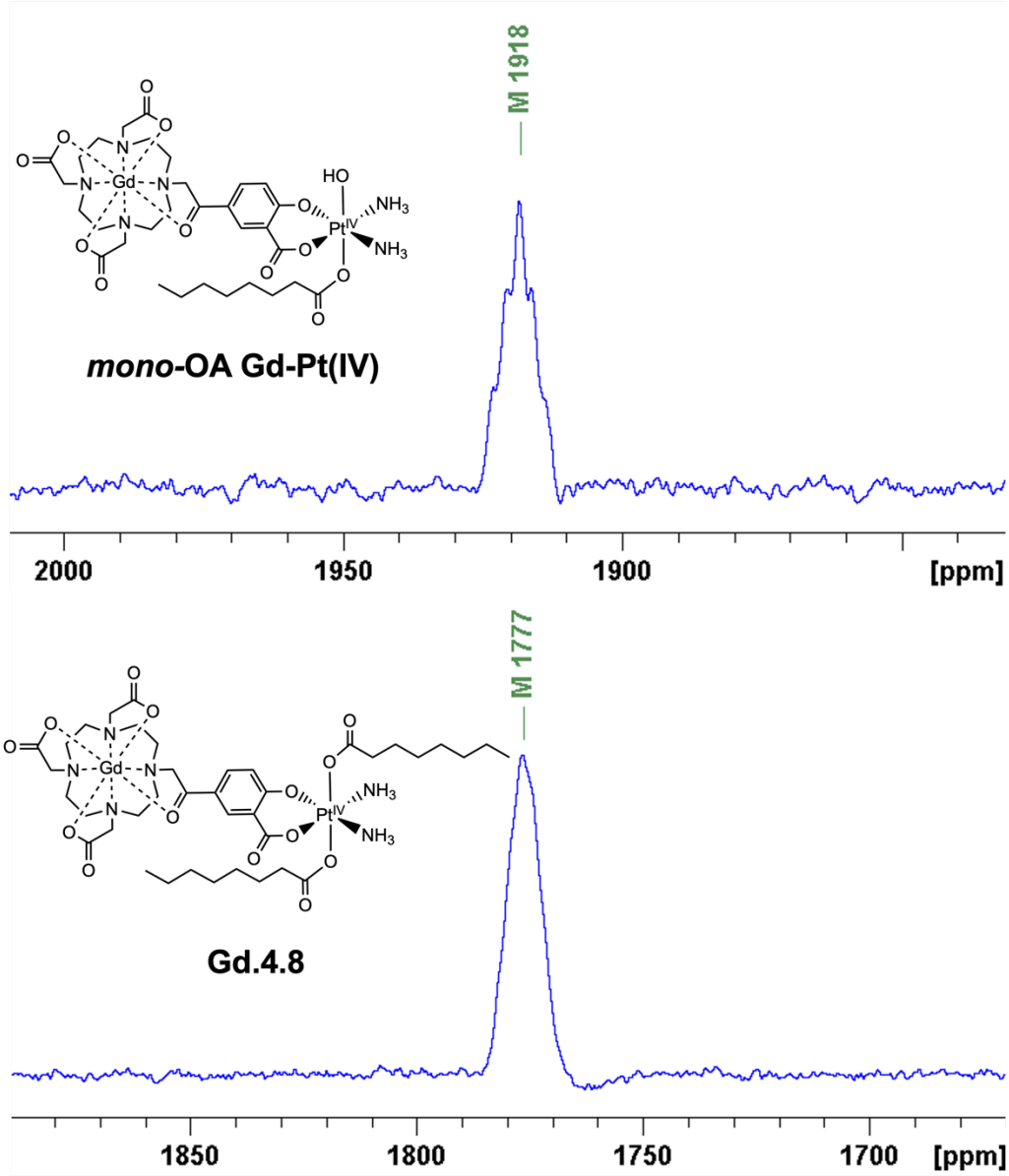

Figure 4.16: *top: ^{195}Pt NMR spectrum (108 MHz, D_2O) of mono-octanoic Gd-Pt(IV)* ***Gd4.7****; bottom: ^{195}Pt NMR spectrum (108 MHz, D_2O) of* ***Gd.4.8****.*

4.3.3 Crystal data

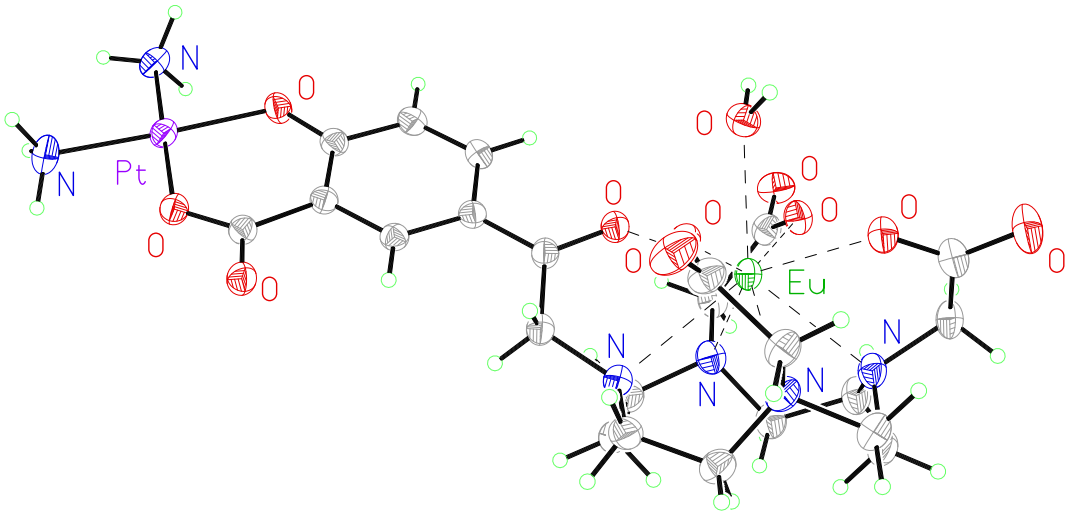

Figure 4.17: *Molecular structure of* ***Eu.4.6*** *from single crystal X-ray diffraction studies; thermal ellipsoids are drawn at 20% probability and water in the solvent sphere is omitted for clarity。*

Crystals suitable for X-ray analysis of **Eu.4.6** were grown by slowly cooling the saturated water solution of the complex. The structure was solved and analysed by Dr. Amber L. Thompson and Dr. Kirsten E. Christensen. They solved the structure by charge-flipping using 'Superflip' and refined by full-matrix least squares on F^2 using CRYSTALS suite. The structure demonstrated a monocapped square antiprism (SAP) configuration of the Eu centre. The crystal structure also showed that there is one water molecular coordinated to the Eu centre. The hydration state agrees with the result of calculated by employing the modified Horrocks' equation. To the best of our knowledge, this is the first reported europium-platinum X-ray single crystal structure; bond lengths and angles are essentially consistent with other previously reported Ln(III)-Pt(II) complexes. Full bond lengths and angles data are listed in Experimental chapter.

4.3.4 Relaxivity study

^{1}H T_1 relaxation times can be a good indicator of the type of binding between the water

molecules and the Gd complexes in solution. Measurement of the T_1 relaxation enhancements obtained with complexes **Gd.(4.5-4.8)** offers further insights into their solution-state structure. The relaxivity of the complexes was determined by observing the variation of $1/T_1$ with complex concentration in media (DMEM) as shown in Figure 4.18. In all cases, the resulting plots showed a linear response to concentration across a wide range, indicating that all complexes were essentially stable in solution and that their properties are not changed by their local environment (since a change in speciation would be expected to result in curvature of the plots). All the **Gd.(4.5-4.8)** exhibit relaxivities consistent with a single water molecule in their inner coordination sphere.

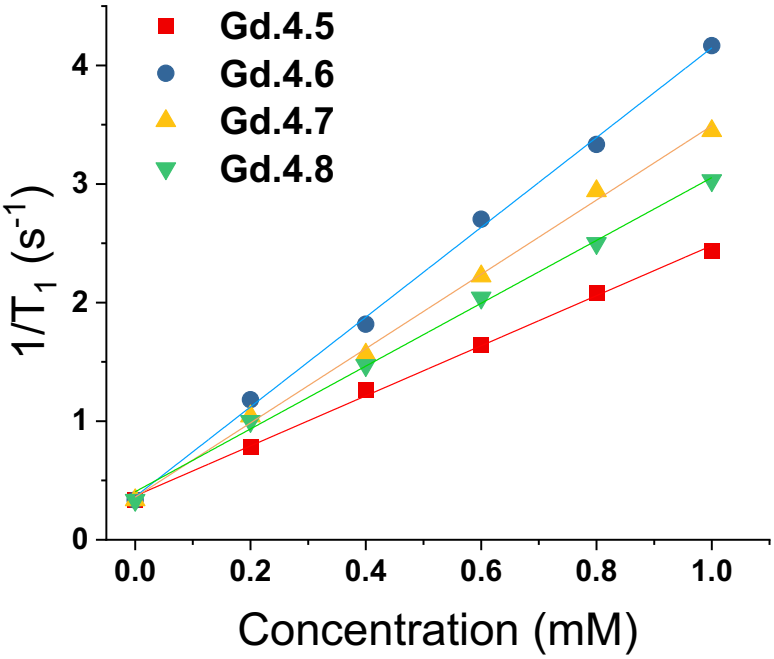

Figure 4.18: *Variation of $1/T_1$ with concentration of gadolinium for complexes* ***Gd.(4.5-4.8)*** *at different concentrations (at 25°C, in DMEM, 14.1 T).*

The relaxivity $r_1 = 1/[Gd]T_1$ is a concentration-independent term that can be used to compared different contrast agents. It is a useful measure of the effectiveness of a complex as a contrast agent; the best contrast agents will have large relaxivities per mmol of gadolinium, effectively meaning that good images can be obtained with lower concentrations of contrast agent. r_1 values of the complexes **Gd.(4.5-4.8)** are 2.21, 3.79,

3.13 and 2.65 $mM^{-1}s^{-1}$, respectively. The **Gd4.5** complex has the lowest relaxivity, while the **Gd4.6** complex has the highest relaxivity. The differences between the relaxivities can be resulted from the different pendent Pt moieties that affect the residence time of solvent (τ_m)

4.3.5 INDIANA study

As discussed previously, using the INDIANA model, the diffusive behaviour of water within cellular systems can be robustly described using a two-pool model with the water residing in either an intra- or extra-cellular pool. This results from the intrinsic diffusion of water being slower in the viscous intra-cellular compartment and its maximum displacement being restricted by the presence of the cell membrane. The model also explicitly accounts for exchange between the two environments.

The Diffusion NMR data acquisition and analysis were carried out by Dr. Gogulan Karunanithy and Prof. Andrew Baldwin. When fitting variable diffusion delay data from ^1H NMR spectroscopic experiments, it is possible to derive a number of system properties including intra- and extra-cellular diffusion coefficients, populations of water in the two environments, exchange rate of water over the membrane, average cell radius and, crucially for this study, intra- and extra-cellular longitudinal relaxation rates of water. Due to the relaxation enhancement caused by MRI imaging reagents, by comparing the difference in relaxation rates in the presence and absence of these agents in cellular systems, we can quantitatively assess the degree to which they are localised within cells.

As the relaxivities of the four complexes are different, this must be considered when using an increased intra-cellular relaxation rate as a proxy for cellular uptake of imaging agent. To address this, we used the relaxivity of the complexes measured in

DMEM (Figure 4.18). To estimate the partitioning of the four complexes between extra- and intra-cellular environments, we assumed that the relaxivity of the compounds inside cells could be approximated by their relaxivity in media. Using the INDIANA method described above, we found the extra- and intra-cellular longitudinal relaxation and compared this to the values in the absence of any complex to give ΔR_1 for each compound in the two environments. This value was then divided by the relaxivity to show how the compound was partitioned.

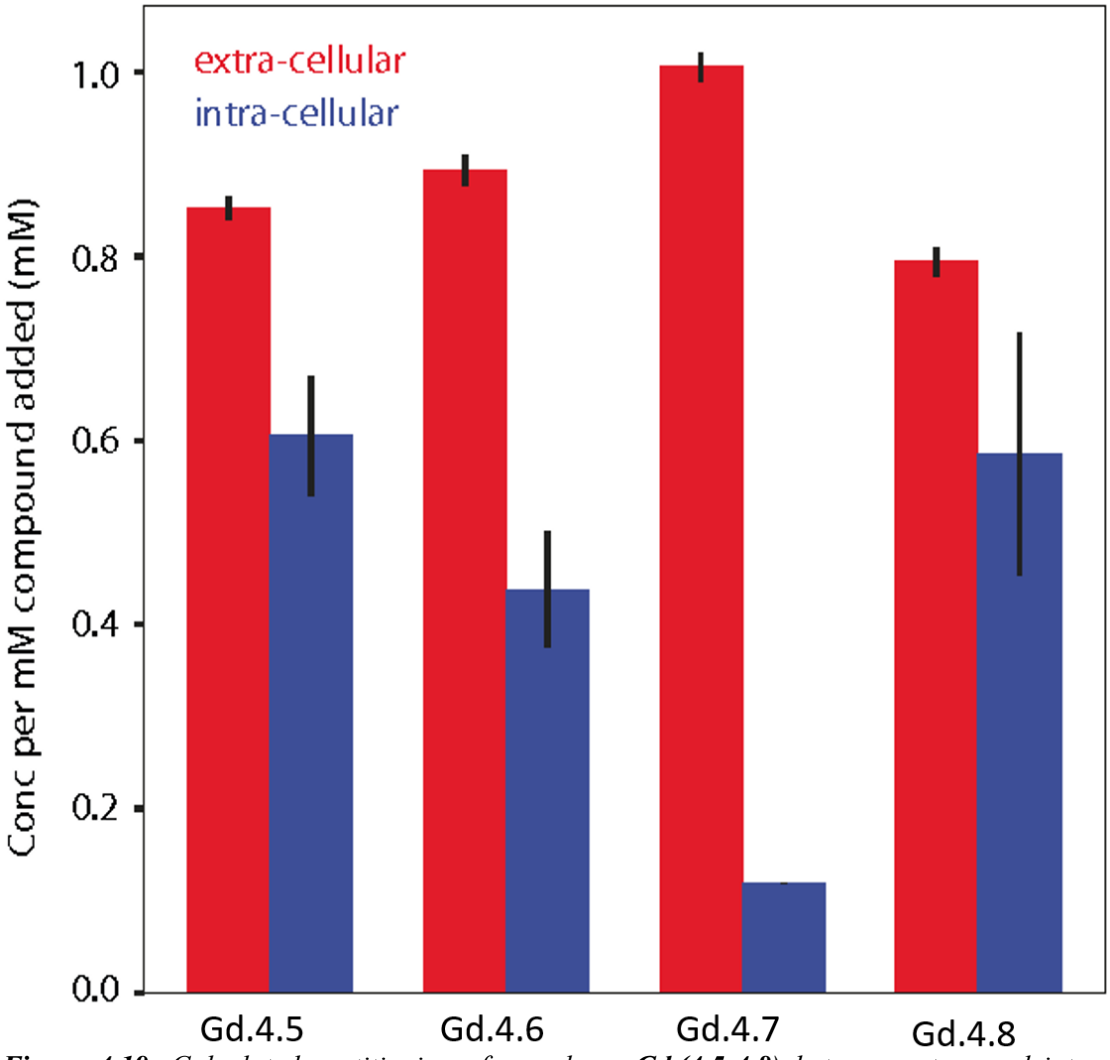

Figure 4.19: *Calculated partitioning of complexes* ***Gd.(4.5-4.8)*** *between extra- and intra-cellular environments following 1.5 h incubation with KNS42 cells. The concentration of complexes in the two environments is found by comparing longitudinal relaxation rates in the presence and absence of the compounds (ΔR_1) and then dividing by the relaxivity. The error bars are calculated by propagating the error in ΔR_1 for three independent samples and taking the standard deviation.*

The results of our analysis are shown in Figure 4.19. The ^{1}H diffusion measurements were used to quantify the accumulation of the compounds within cells. Complexes **Gd.4.5-4.8** accumulated relatively well in the cells, whilst there was a reduction in accumulation for **Gd.4.6** which incorporated the Pt(II) group. Gadolinium complexes enter cells predominantly by micropinocytosis,[30,31] whereas platinum(II) complexes enter cells through a combination of copper transporters, anion/cation transporters and passive diffusion.[32] Significantly lower cellular accumulation was observed for the platinum(IV) compound, **Gd.4.7**, consistent with the oxidation state and ligand sphere of the Pt modulating the ability of the complex to enter cells. The copper transporter mechanism is less viable for platinum(IV) complexes, since there are no vacant positions available in the octahedral platinum(IV) coordination sphere. Cellular uptake of platinum(IV) complexes is therefore thought to occur through a combination of passive diffusion and active pathways.[33] Finally, **Gd.4.8**, which incorporates two OA ligands, showed a similar uptake to **Gd.4.5**, demonstrating the notable effect of the modified coordination sphere of the platinum(IV) on the degree of cellular accumulation. If diffusion is the predominant cellular uptake mechanism for **Gd.4.7**, increasing the lipophilicity through inclusion of octanoic acid groups as in **Gd.4.8** would be anticipated to significantly enhance uptake, and the data are consistent with this, although without discounting the possibility of uptake through micropinocytosis. The dominant route(s) of cellular uptake for other lanthanide-platinum conjugates are unknown, since only a handful of examples have been reported, with either labile,[34,35] or kinetically inert lanthanide chelation.[36,37] From these data, we suggest that the route(s) vary significantly depending on the coordination sphere of the platinum. These diffusion results are particularly enlightening in combination with the cytotoxicity results (below) to give an overall picture of the cellular behaviour of the complexes.

4.4 Cytotoxicity Study

Table 4.1. *Cytotoxicity (IC_{50}, μM) values of compounds* ***Gd.(4.5-4.8)*** *in KNS42 cell line. Cells were exposed to ½ log serial dilutions of compounds for 1.5, 24, 48 and 72 h. IC_{50} values were determined using a 3-parameter log inhibitor vs. concentration curve fit.*

Complex	Gd.4.5		Gd.4.6	
Time / h	IC_{50}	95% CI	IC_{50}	95% CI
1.5	>1000	-	637.9	446.1 – 934.3
24	>1000	-	316.7	226.6 - 445.9
48	>1000	-	75.3	65.79 - 86.25
72	>1000	-	75.7	64.68 - 88.82
Complex	Gd.4.7		Gd.4.8	
Time / h	IC_{50}	95% CI	IC_{50}	95% CI
1.5	227.6	183.2 - 283.7	>1000	-
24	96.5	80.13 - 116.4	>1000	-
48	91.4	73.43- 114.0	747.5	644.4 -871.2
72	53.2	43.34- 65.50	142.8	111.2 - 84.5

Cell cytotoxicity study of the Gd complexes in KNS42 cell line (paediatric glioblastoma) was conducted with the help from Dr. Alison Howarth. Complex **Gd.4.5** was well-tolerated by KNS42 cells (viability > 90%) across all concentrations and time-points tested. This indicated minimal cytotoxicity for **Gd.4.5**, with IC_{50} values exceeding 1000 μM (Table 4.1, Figure 4.20). The Gd(III)-Pt(II) complex **Gd.4.6** demonstrated increasing cytotoxicity after 1.5 h exposure (IC_{50} = 637.9 μM at 1.5 h incubation). The Gd(III)-Pt(IV) complex **Gd.4.7** was significantly more cytotoxic than complex **Gd.4.6** after 1.5 h and 24 h exposure. However, no significant difference in cytotoxic effect between **Gd.4.6** and **Gd.4.7** was observed at longer (48 h and 72 h) exposure times. Complex **Gd.4.8** was less cytotoxic than **Gd.4.6** and **Gd.4.7** at all

exposure times, with IC_{50}> 1000 μM at 1.5 h and 24 h, with increasing cytotoxicity after 48 h exposure. Whilst complex **Gd.4.5** showed no toxicity towards cells up to a concentration of 1000 μM, the platinum-containing bimetallic complexes **Gd.(4.6-4.8)** displayed varying degrees of cytotoxicity. As kinetically-inert $5d^6$ complexes, platinum(IV) complexes are suggested to reduce to platinum(II) intracellularly before ligand exchange and binding to cellular targets (*e.g.* DNA, proteins) can occur.[38] Complexes **Gd.(4.7-4.8)** all demonstrated increased cytotoxicity towards the cells with prolonged contact time. However, complex **Gd.4.8** showed a more pronounced "latent" period of initial lower cytotoxicity, compared with complexes **Gd.4.6** and **Gd.4.7**, consistent with an outer-sphere mechanism of reduction for **Gd.4.8** which is likely to be slower than an inner-sphere mechanism of reduction for **Gd.4.7**. For **Gd.4.7**, the reduction mechanism could involve bridging to one or both axial hydroxido groups,[39] which is not possible for **Gd.4.8**.

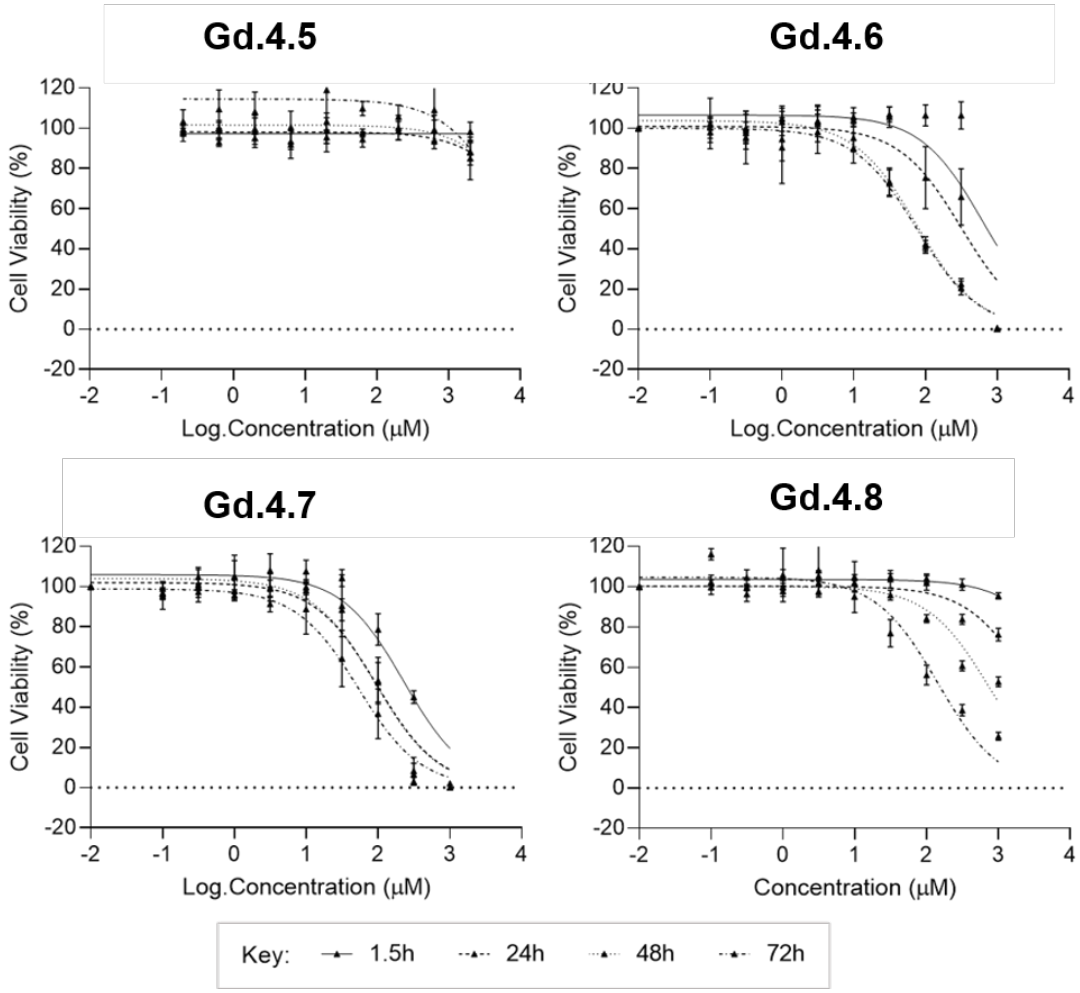

Figure 4.20: *KNS42 compound toxicity. KNS42 cells were exposed to ½ log serial dilutions of test compounds for 1.5, 24, 48 and 72 h. IC_{50} values were determined in Graphpad prism using a 3 parameter log inibitor vs. concentration curve fit. Three independent replicates were performed.*

4.5 ICP-MS Study

Stability of the Gd complexes in DMEM media was tested by ICP-MS analysis. 5 repeat samples of each complexes were prepared, and control samples were DMEM only samples where no Gd complexes were used. The results were tabulated in Table 4.2: for **Gd.4.5** complex, the ratio of Gd : Pt is 1 : 0 as there is no Pt in the complex. For the other three Gd-Pt bimetallic complexes, the Gd : Pt ratio were all around 1 : 1 which indicated the complexes are stable in DMEM media (detailed ratio of Gd:Pt was listed in Experimental Chapter). We have also done the elemental analysis of KNS42 cell, by

incubating the complexes containing media with the cell at 37^0C for 1.5 hours, following by the removal of the media by centrifuging and digestion of the cell. The ICP-MS results of cell showed that the complexes entered the cell, however at the condition we conducted the experiment, the detected concentration of Gd and Pt were only at μM level. The low concentration might affect the ICP-MS measurement, as the measured Gd:Pt ratios of the cell sample in different replicate varied a lot (showed in Experimental Chapter), so that the results were not accurate enough for us to investigate the ratio of Gd and Pt in cell. To improve the ICP-MS measurement accuracy in cells, more cells can be used in the incubation step to increase the overall metal concentration after digestion. The cell concentration we did for the ICP-MS measurement was $4.5e^4$/ml, while the cell concentration for the cell diffusion NMR study was $6e^7$/ml. Thus, conducting the cell ICP-MS analysis at cell concentration around $1e^7$/ml might be reasonable next step to improve the ICP-MS analysis accuracy.

Table 4.2*: Elemental concentrations of Pt and Gd in complexes* ***Gd.(4.5-4.8)*** *determined over 5 replicates (R1 - R5).*

	Total Pt concentration (mM)				
Replicate	Control	**Gd.4.5 (1 mM)**	**Gd.4.6 (0.5 mM)**	**Gd.4.7 (0.5 mM)**	**Gd.4.8 (1 mM)**
R1	0.0	0.0	0.5	0.4	0.7
R2	0.0	0.0	0.5	0.4	0.9
R3	0.0	0.0	0.5	0.4	0.9
R4	0.0	0.0	0.5	0.4	0.8
R5	0.0	0.0	0.5	0.4	0.9

	Total Gd concentration (mM)				
Replicate	Control	**Gd.4.5 (1 mM)**	**Gd.4.6 (0.5 mM)**	**Gd.4.7 (0.5 mM)**	**Gd.4.8 (1 mM)**
R1	0.0	1.0	0.6	0.4	0.7
R2	0.0	1.0	0.5	0.4	0.8
R3	0.0	1.0	0.5	0.4	0.8
R4	0.0	1.1	0.5	0.4	0.8
R5	0.0	1.1	0.5	0.3	0.8

4.6 Photophysical Study

4.6.1 UV-vis

Figure 4.21 displays the normalised absorption spectra of the Ln-Pt complexes. For all complexes, only changing the lanthanide barely change their absorption bands. The absorption spectra of **Ln.4.5** complexes all show an absorption band at 309 nm which corresponds to the π-π* absorption of the salicylate chromophore. The Ln-Sali-Pt(II) complexes **Ln.4.6** shows an red shifted absorption band at 343 nm, which is the MLCT of the salicylatePt(II). When the Pt(II) centre was oxidised to Pt(IV), we observed a blue shift of the absorption.

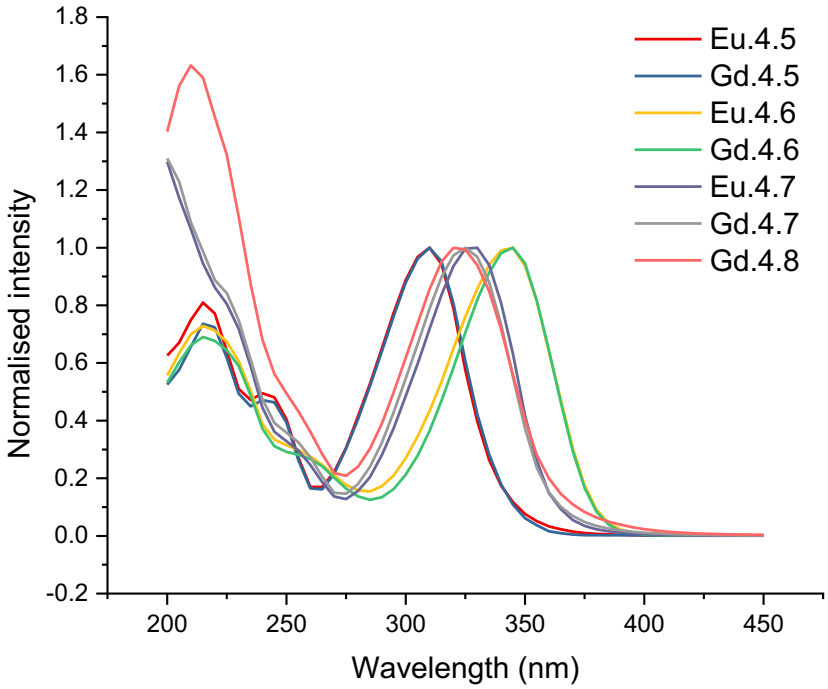

Figure 4.21: *UV-Vis absorption of Eu and Gd complexes,* ***Ln.4.5****: 309nm,* ***Gd.4.8****: 324nm,* ***Gd.4.7****: 325nm,* ***Eu.4.7****: 330nm,* ***Ln.4.6****: 345 nm*

4.6.2 Luminescence study

As shown in Figure 4.22, the luminescence spectra of the both **Eu.4.5** and **Eu.4.6** complexes exhibited strong and characteristic Eu emission bands upon excitation in the chromophore band, with the peaks in 580nm, 592nm, 616nm, 653nm, 688nm and

701nm arising from the transitions the $^5D_0$ - ^7F_J (J = 0, 1,2,3,4,5). The hypersensitive emission band $^5D_0$ - $^7F_2$ at 616 nm in **Eu.4.6** shows significant increase compared to **Eu.4.5** which indicate the binding of salicylic acid to the platinum centre perturbs the coordination environment of the europium. The excitation spectrum shows a relatively broad band which is extended to around 380 nm, which makes the luminescence lanthanide complexes excitable by employing two-photon excitation in the near-IR optical window 700-820 nm that has the best penetration of cells and tissues. So that the complexes can be used as cellular imaging probe by two-photon excitation microscopy.

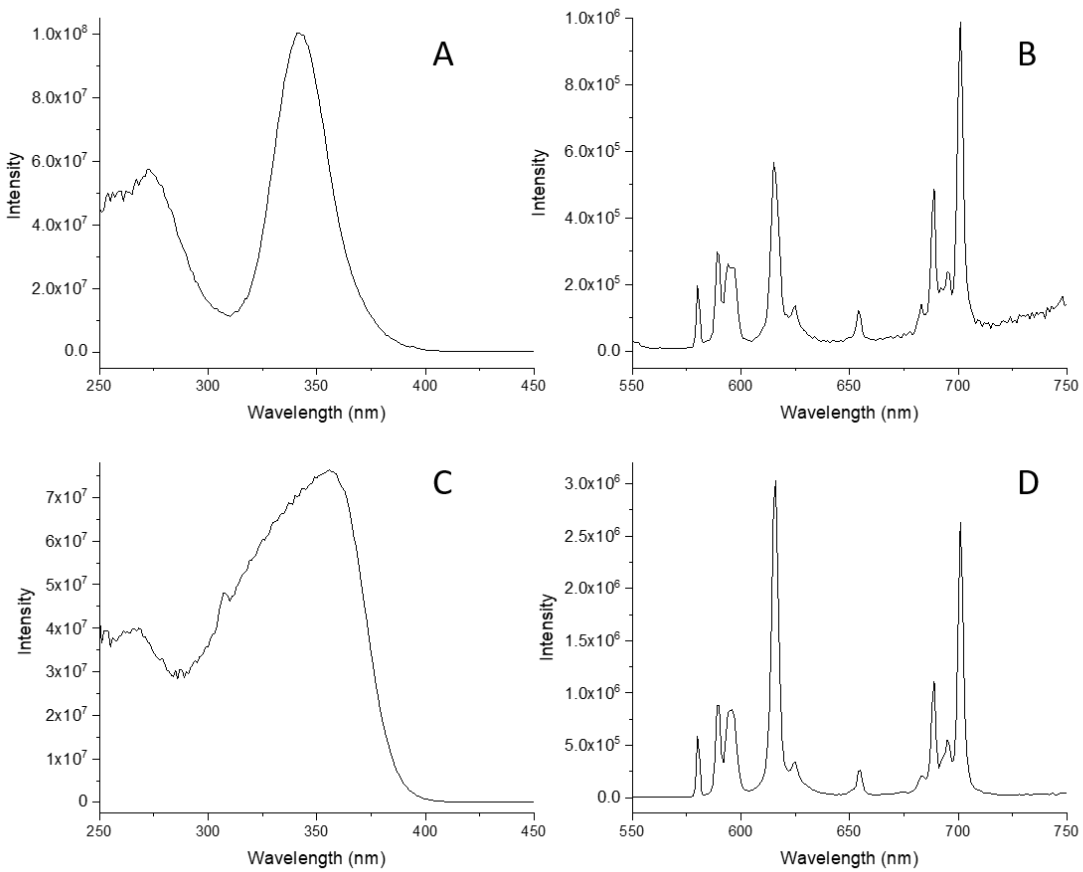

Figure 4.22: *A): Excitation spectrum of **Eu.4.5**, B) Emission spectrum of **Eu.4.5**, C): Excitation spectrum of **Eu.4.6**, D) Emission spectrum of **Eu.4.6**. All samples are equimolar 10^{-4} M in H_2O.*

The terbium(III) complexes **Tb.4.5** and **Tb.4.6** also exhibited strong characteristic emission bands as shown in Figure 4.23. The excitation spectra of **Tb.4.5** and **Tb.4.6** exhibited broad bands centred on 350 nm and 310 nm respectively.

The lifetimes of the four Eu/Tb complexes in H_2O and D_2O obtained by fitting the luminescence decay curve. The lifetime values are demonstrated in Table 4.3 and hydration number *q* of each complexes were calculated according to Horrocks' equation. The *q* numbers are all close to one, further indicating the carbonyl oxygen is strongly coordinated to the metal and the ligands are octadentate species in solution.

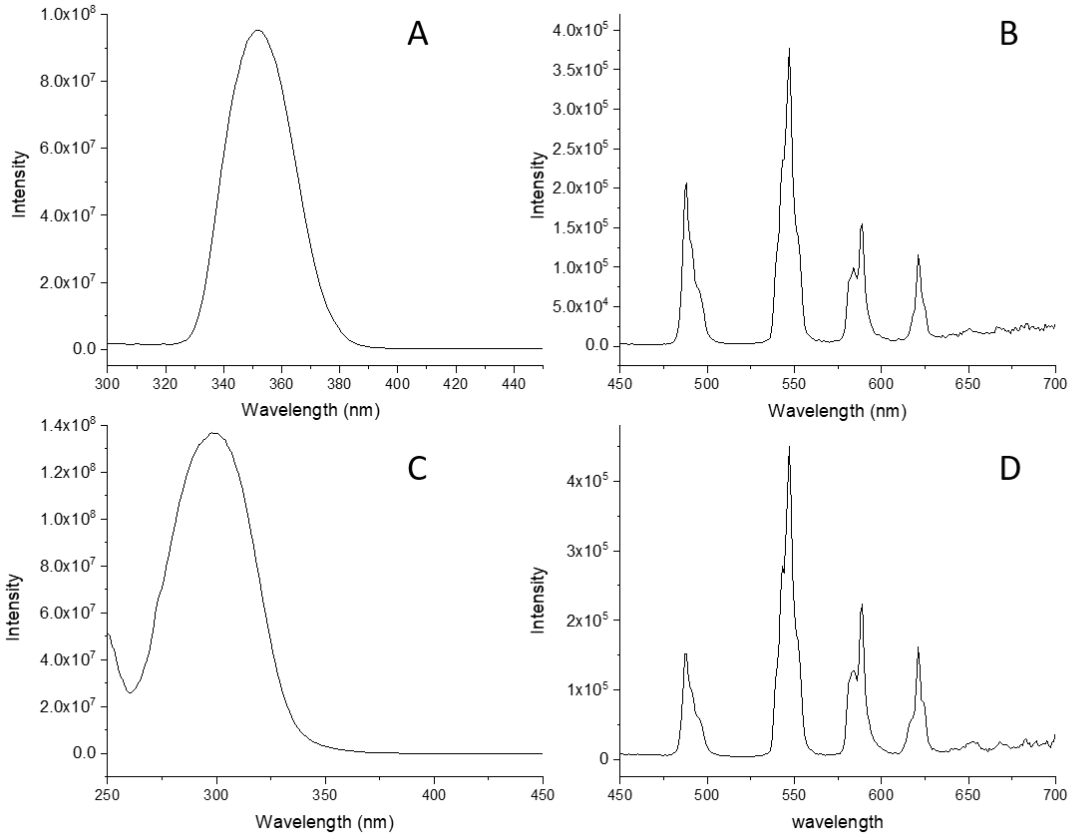

Figure 4.23: *A): Excitation spectrum of* ***Tb.4.5****, B) Emission spectrum of* ***Tb.4.5****, C): Excitation spectrum of* ***Tb.4.6****, D) Emission spectrum of* ***Tb.4.6****. All samples are equimolar 10^{-4} M in H_2O.*

Table 4.3. *Lifetime values of the excited states of the luminescent* ***Eu.4.5****,* ***Eu.4.6, Tb.4.5*** *and* ***Tb.4.6.*** *The measurement of the lifetimes of luminescence in water and D_2O allowed the determination of the hydration number using the modified Horrocks' equation.*[40]

Complex	λ_{ex}/nm	λ_{em}/nm	τ_{H2O}/µs	τ_{D2O}/µs	q
Eu.4.5	348	616	657	2131	0.96
Eu.4.6	348	616	609	1869	1.03
Tb.4.5	350	547	1736	2903	0.85
Tb.4.6	310	547	1702	2596	0.71

4.6.3 Switch-on luminescence study

Although the both the salicylic acid and salicylic-Pt(II) sensitised the emission of the lanthanide effectively, the salicylic-Pt(IV) was found to quench the lanhtanide emission. This provided us a method to monitor the reduction process of Ln-Pt(IV) drugs as well as the distribution of the drug.

In comparison, **Eu.4.7** and **Eu.4.8** exhibited only very weak luminescence, and poor signal-to-noise ratios were obtained (the emission and excitation spectra can be found in Experimental Chapter). However, when the platinum (IV) centre in **Eu.4.7** and **Eu.4.8** were treated with ascorbic acid (AA), dramatic enhancements in luminescence intensity were observed in both complexes. In the case of **Eu.4.7,** the incubation of AA resulted in a 35-fold enhancement of signal on regenerating **Eu.4.6** (Figure 4.24) over a period of 216 hours, while in the case of **Eu.4.8** the enhancement was 13-fold (Figure 4.25). The excited-state manifold of the platinum (IV) complex acts to quench the europium emission, meaning that switching on of signal can potentially be used to observe reduction of the complex *in situ*. The enhancements of emission of different Eu-Pt(IV) complexes were different, which indicate the reduction rate of Pt(IV) to Pt(II) in different complexes are different. This can result from the reduction potential differences origin from the varied axial groups of the Pt(IV) complexes. Ultimately, different reduction potential can result in different cytotoxicity in various time points as we observed in the cytotoxic study in KNS42 cell. However, the “switch-on” luminescence study of these Eu-Pt complexes can be further studied in cellular environment and the emission changes can be correlate to the cytotoxicity of the complexes.

The mono-octanoic acid platinum(IV) complex also showed a “switch-on” in luminescence when reduced with ascorbic acid, the luminescence spectrum is shown in

Figure 6.2 (Experimental Chapter). The “switch-on” spectra of the three Eu-Pt(IV) complexes measured with more time points are shown in Figure 6.1, 6.2 and 6.3 (Experimental) The “switch on” effect we observed here is consistent with other Pt(IV)/Pt(II) couples that display reductive “switch on” fluorescence; the quenching in the Pt(IV) state being thought to arise from the presence of metal-based d-orbitals energetically positioned between the HOMO and LUMO of the fluorophore.[41,42] Luminescence in the Pt(IV) oxidation state is more likely to be observed if one or more ligands are cyclometallated.[43,44] Although the mechanism of reduction *in cellulo* is likely to be complicated and involve more than one reducing species,[45] ascorbate acid-mediated reduction gives an initial insight into the potential for monitoring the reduction of these compounds through fluorescence microscopy.

However, verification of the “switch on” mechanism requires more photophysical investigation, the validation of the hypothesis is outside the scope of this work and hence has not been conducted.

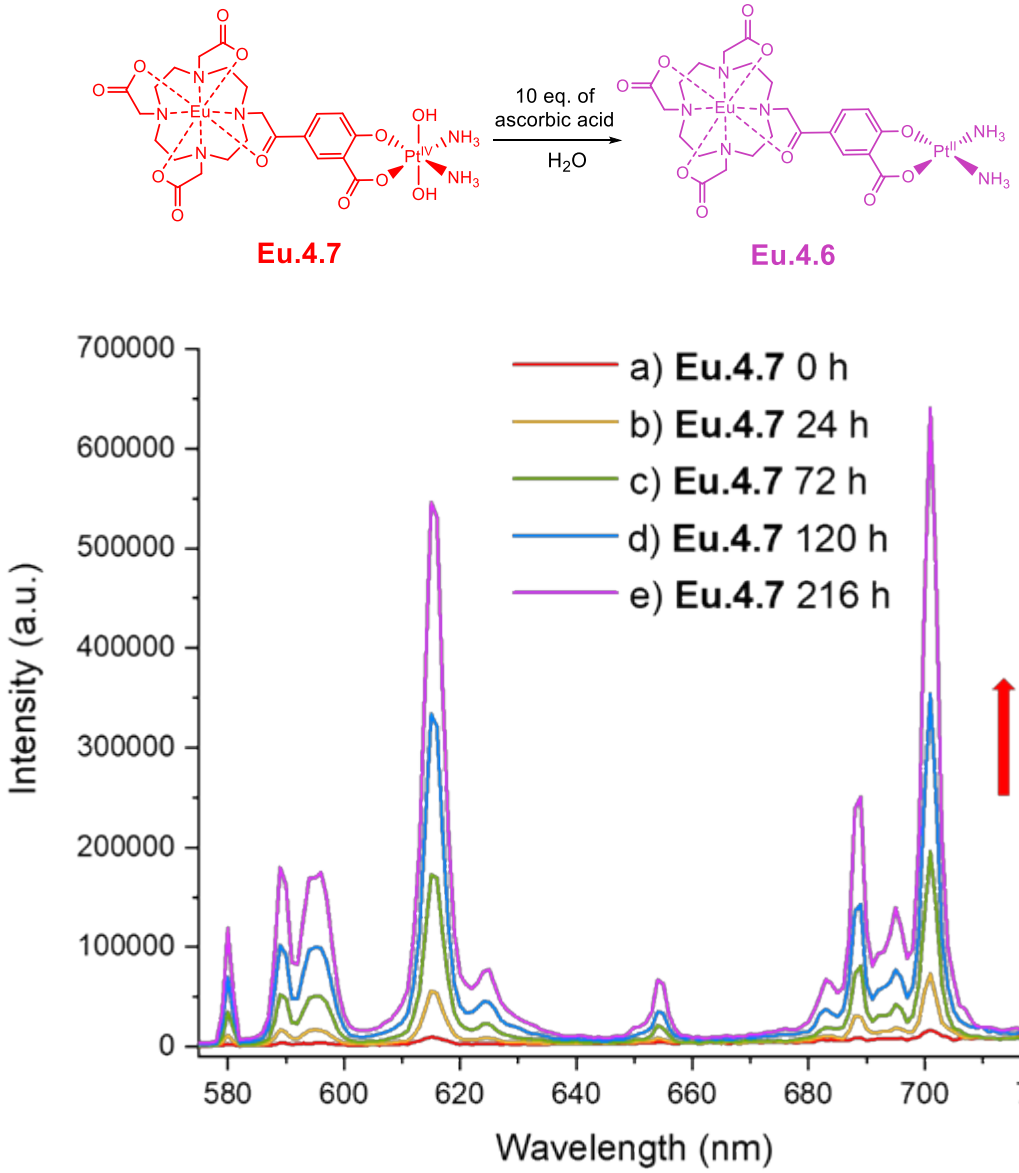

Figure 4.24: *Luminescence spectrum of* ***Eu.4.7****; λ_{ex} = 330 nm, emission slit = 1 nm. a) before addition, b) 24 h after addition of excess (20-fold) ascorbic acid (AA) and c) 72 h after addition of AA, d) 120 h after addition of AA, e) 216 h after addition of AA. The red arrow shows that as time increases the intensity of emission increases.*

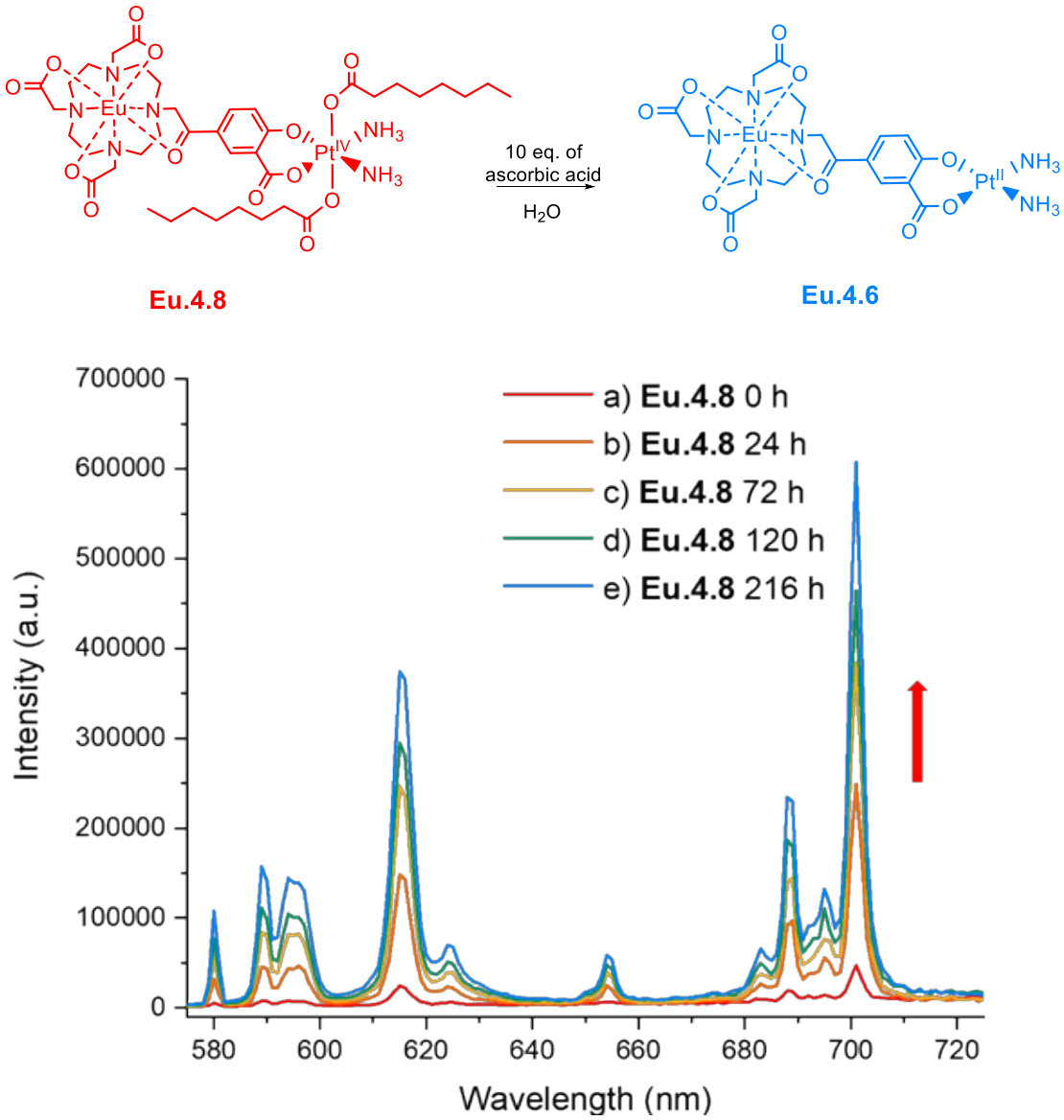

Figure 4.25: *Luminescence spectrum of* ***Eu.4.8****;* λ_{ex} *= 330 nm, emission slit = 1 nm. a) before addition, b) 24 h after addition of excess (20-fold) ascorbic acid (AA) and c) 72 h after addition of AA, d) 120 h after addition of AA, e) 216 h after addition of AA. The red arrow shows that as time increases the intensity of emission increases.*

4.7 Conclusion and Next Step

A series of Ln-salicylateDO3A-Pt complexes were synthesis and fully characterised by mass spectroscopy, NMR spectroscopy and UV-vis and luminescence spectroscopies. The ICP-MS confirmed the Ln:Pt ratio and the structure of crystal X-ray crystallography demonstrated a monocapped square antiprism (SAP) configuration of the Eu centre. The cytotoxic studies showed different toxicities of the complexes at varied time points. The INDIANA diffusion NMR study reveal the cellular update profile of different Gd-Pt complexes. Optical microscopy is considered as the next step to investigate the subcellular localisation of the complexes. The synthesis of the naphthalene as chromophore can also be continued to enable longer wavelength of light to excite to emission of complexes. A "switch-on" luminescence of Eu-Pt(IV) to Eu-Pt(II) was observed, further study of this phenomenon in cell environment can reveal more details of the action of the complexes in cell and can be compared with the cytotoxicity and INDIANA result we already obtained. The luminescence behaviour of the Yb version can give us further information of the energy transfer mechanism to the Ln centre, i.e. the possibility of Dexter energy transfer mechanism. Lastly, the Ln-salicylateDO3A complexes is possible to detect metal ion environment as the salicylic acid can bind to the metal ion which eventually perturb the lanthanide luminescent or magnetic properties.

Reference

1 G. Karunanithy, R. J. Wheeler, L. R. Tear, N. J. Farrer, S. Faulkner and A. J. Baldwin, *J. Magn. Reson.*, 2019, **302**, 1–13.

2 A. L. Barabasi, N. Gulbache, J. Loscalzo, *Nat. Rev. Genet.*, 2011, **23**, 56–58.

3 J. X. Ong, C. S. Q. Lim, H. Van Le and W. H. Ang, *Angew. Chemie - Int. Ed.*, 2019, **58**, 164–167.

4 S. Faulkner, S. J. A. Pope, B. P. B. Pye, S. Faulkner, S. J. A. Pope and B. P. B. Pye, *Appl. Spectrosc. Rev.*, 2017, **40**, 1–31.

5 E. J. New, D. Parker, D. G. Smith and J. W. Walton, *Curr. Opin. Chem. Biol.*, 2010, **14**, 238–246.

6 C. Dossantos, A. Harte, S. Quinn and T. Gunnlaugsson, *Coord. Chem. Rev.*, 2008, **252**, 2512–2527.

7 T. Gunnlaugsson, J. P. Leonard, K. Sénéchal and A. J. Harte, *Chem. Commun.*, 2004, **4**, 782–783.

8 S. J. Butler and D. Parker, *Chem. Soc. Rev.*, 2013, **42**, 1652–1666.

9 M. C. Heffern, L. M. Matosziuk and T. J. Meade, *Chem. Rev.*, 2014, **114**, 4496–4539.

10 N. M. Shavaleev, L. P. Moorcraft, S. J. A. Pope, Z. R. Bell, S. Faulkner and M. D. Ward, *Chem. Commun.*, 2003, 1134–1135.

11 S. J. A. Pope, B. J. Coe and S. Faulkner, *Chem. Commun.*, 2004, **44**, 1550–1551.

12 T. Lazarides, D. Sykes, S. Faulkner, A. Barbieri and M. D. Ward, *Chem. - A Eur. J.*, 2008, **14**, 9389–9399.

13 P. B. Glover, P. R. Ashton, L. J. Childs, A. Rodger, M. Kercher, R. M. Williams, L. De Cola and Z. Pikramenou, *J. Am. Chem. Soc.*, 2003, **125**, 9918–9919.

14 S. J. A. Pope, A. M. Kenwright, S. L. Heath and S. Faulkner, *Chem. Commun.*, 2003, 1550.

15 N. M. Shavaleev, L. P. Moorcraft, S. J. A. Pope, Z. R. Bell, S. Faulkner and M. D. Ward, *Chem. - A Eur. J.*, 2003, **9**, 5283–5291.

16 T. K. Ronson, T. Lazarides, H. Adams, S. J. A. Pope, D. Sykes, S. Faulkner, S. J. Coles, M. B. Hursthouse, W. Clegg, R. W. Harrington and M. D. Ward, *Chem. - A Eur. J.*, 2006, **12**, 9299–9313.

17 O. J. Stacey, A. J. Amoroso, J. A. Platts, P. N. Horton, S. J. Coles, D. Lloyd, C. F. Williams, A. J. Hayes, J. J. Dunsford and S. J. A. Pope, *Chem. Commun.*, 2015, **51**, 12305–12308.

18 H. Li, R. Lan, C. F. Chan, L. Jiang, L. Dai, D. W. J. Kwong, M. H. W. Lam and K. L. Wong, *Chem. Commun.*, 2015, **51**, 14022–14025.

19 K. Singh, S. Singh, P. Srivastava, S. Sivakumar and A. K. Patra, *Chem. Commun.*, 2017, **53**, 6144–6147.

20 A. Chandra, K. Singh, S. Singh, S. Sivakumar and A. K. Patra, *Dalt. Trans.*, 2016, **45**, 494–497.

21 L. Kumar, K. H. Puthraya and T. S. Srivastava, *Inorganica Chim. Acta*, 1984, **86**, 173–178.

22 Q. S. Ye, L. G. Lou, W. P. Liu, Y. Yu, X. Z. Chen, S. Q. Hou, W. Q. Gao and Y. Liu, *Bioorganic Med. Chem. Lett.*, 2007, **17**, 2146–2149.

23 W.-P. Liu, Q.-S. Ye, Y. Yu, X.-Z. Chen, S.-Q. Hou, L.-G. Lou, Y.-P. Yang, Y.-M. Wang and Q. Su, *Platin. Met. Rev.*, 2008, **52**, 163–171.

24 Y. Yu, L. G. Lou, W. P. Liu, H. J. Zhu, Q. S. Ye, X. Z. Chen, W. G. Gao and S. Q. Hou, *Eur. J. Med. Chem.*, 2008, **43**, 1438–1443.

25 F. A. Thomet, P. Pinyol, J. Villena G. and P. G. Reveco, *Inorganica Chim. Acta*, 2012, **384**, 255–259.

26 P. Bergamini, L. Marvelli, V. Ferretti, C. Gemmo, R. Gambari, Y. Hushcha and I. Lampronti, *Dalt. Trans.*, 2016, **45**, 10752–10760.

27 N. Puttaswamy, G. S. Pavan Kumar, M. Al-Ghorbani, V. Vigneshwaran, B. T. Prabhakar and S. A. Khanum, *Eur. J. Med. Chem.*, 2016, **114**, 153–161.

28 L. Carroll, I. I. Bromide and G. K. Ostrum, 1964, **3459**, 3459–3461.

29 X. Marguerettaz, R. O'Neill and D. Fitzmaurice, *J. Am. Chem. Soc.*, 1994, **116**, 2629–2630.

30 E. J. New and D. Parker, *Org. Biomol. Chem.*, 2009, **7**, 851–855.

31 E. Mathieu, A. Sipos, E. Demeyere, D. Phipps, D. Sakaveli and K. E. Borbas, *Chem. Commun.*, 2018, **54**, 10021–10035.

32 H. C. Tai, Y. Zhao, N. J. Farrer, A. E. Anastasi, G. Clarkson, P. J. Sadler and R. J. Deeth, *Chem. - A Eur. J.*, 2012, **18**, 10630–10642.

33 A. Karlsson, K.; Svensson, *Mol. Pharmacol*, 1990, **77**, 887–894.

34 I. M. Etchells, M. C. Pfrunder, J. A. G. Williams and E. G. Moore, *Dalt. Trans.*, 2019, **48**, 2142–2149.

35 Z. Zhu, X. Wang, T. Li, S. Aime, P. J. Sadler and Z. Guo, *Angew. Chemie - Int. Ed.*, 2014, **53**, 13225–13228.

36 C. J. Adams and T. J. Meade, *Chem. Sci.*, 2020, **11**, 2524–2530.

37 G. Thiabaud, G. He, S. Sen, K. A. Shelton, W. B. Baze, L. Segura, J. Alaniz, R. M. MacIas, G. Lyness, A. B. Watts, H. M. Kim, H. Lee, M. Y. Cho, K. S. Hong, R. Finch, Z. H. Siddik, J. F. Arambula and J. L. Sessler, *Proc. Natl. Acad. Sci. U. S. A.*, 2020, **117**, 7021–7029.

38 N. Graf and S. J. Lippard, *Adv. Drug Deliv. Rev.*, 2012, **64**, 993–1004.

39 E. Wexselblatt and D. Gibson, *J. Inorg. Biochem.*, 2012, **117**, 220–229.

40 A. Beeby, I. M. Clarkson, R. S. Dickins, S. Faulkner, D. Parker, L. Royle, A. S. de Sousa, J. A. G. Williams and M. Woods, *J. Chem. Soc. Perkin Trans. 2*, 1999, **2**, 493–504.

41 J. E. Expósito, M. Álvarez-Paíno, G. Aullón, J. A. Miguel and P. Espinet, *Dalt. Trans.*, 2015, **44**, 16164–16176.

42 J. J. Wilson and S. J. Lippard, *Inorganica Chim. Acta*, 2012, **389**, 77–84.

43 J. E. Expósito, M. Álvarez-Paíno, G. Aullón, J. A. Miguel and P. Espinet, *Dalt. Trans.*, 2015, **44**, 16164–16176.

44 J. C. López-López, D. Bautista and P. González-Herrero, *Chem. - A Eur. J.*, 2020, **26**, 11307–11315.

45 E. Wexselblatt and D. Gibson, *J. Inorg. Biochem.*, 2012, **117**, 220–229.

Chapter 5: Conclusion and Future Works

This work has investigated the development of several Ln-Pt theranostic complexes. The work started with the investigation of Ln-Pt bimetallic complexes in which the Ln and Pt building blocks were conjugated by CuAAC click reactions. To avoid using cytotoxic Cu salts, Ln-Pt conjugates using SPAAC methods were investigated utilising the diazido Pt(IV) complex, azidophenacylDO3A lanthanide complex and Sondheimer diyne. The SPACC reaction of the Pt(IV) complexes was first studied in full details including reaction condition, characterisation and photoactivatable properties, and the results of the investigation have been published as three papers.[1–3] The third Ln-Pt system is the cell-permeable Ln-Pt complex, of which the relaxivity and cell diffusion NMR of the Gd complexes were studied in detail and the photophysical properties of the switch-on Eu complexes was also investigated, the results have been summarised and published.[4] Possible new approaches to investigate Ln-Pt theroanostic complexes are detailed below:

1. Ln-Pt Complexes with Extended Chromophore:

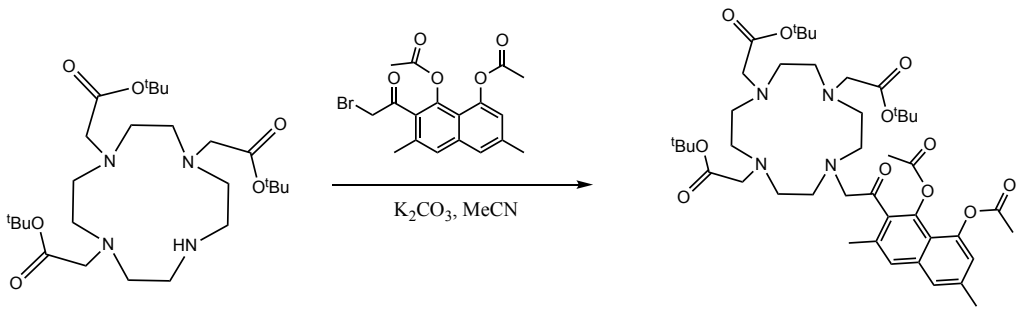

Figure 5.1: *The proposed naphthalene-diol containing ligand.*

Following the success of synthesizing Ln-salicylateDO3A-Pt complexes in Chapter 4, the investigation of a chromophore that contained a naphthalene-diol group to substitute the salicylate group has also been intitiated. There are two advantages of using this new chromophore group: 1. the naphthalene chromophore can be excited at longer wavelength; 2. the lower excited state of chromophore can transfer energy more effectively to a lanthanide centre, especially specific lanthanides which emit NIR light (Yb, Nd).

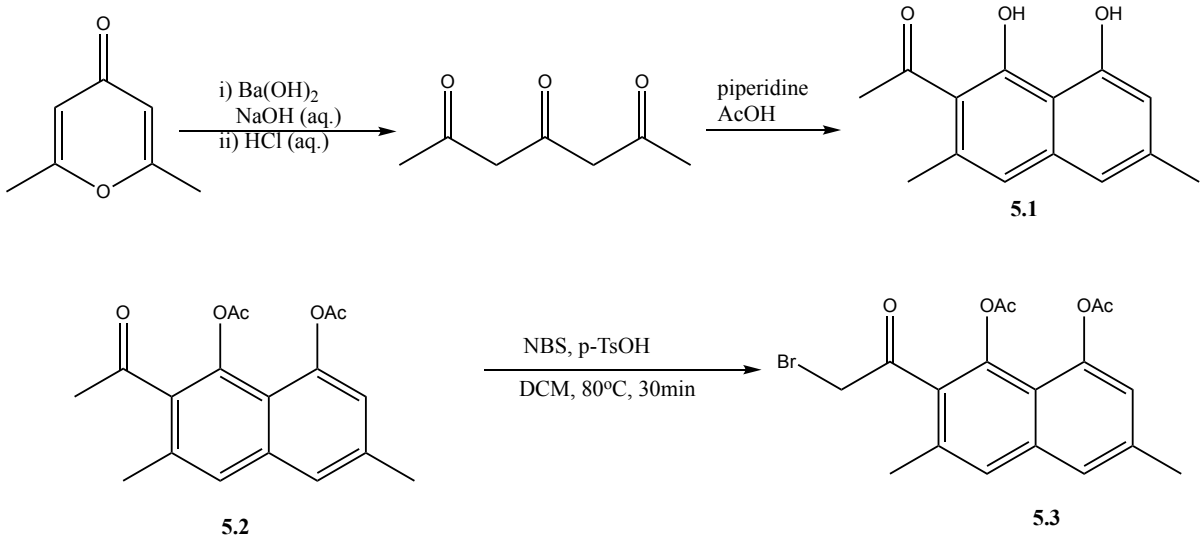

Figure 5.2: *Top: the reaction scheme for synthesising compound* ***5.1****. Bottom: bromination of the Ac-protected naphthalene-diol compound* ***5.2*** *which resulted in* ***5.3****.*

The reaction scheme for synthesising the naphthalene-diol compound **5.1** is illustrated in Figure 5.2.[5,6] The ring opening of 2,6-dimethyl-γ-pyrone was induced by $Ba(OH)_2$. Hydrochloric acid was used to hydrolyse the intermediate Ba^{2+}-chelate complex affording the diacetylacetone. The naphthalene core structure was established by condensation of two molecules of diacetylaceone in a mixture of piperidine and acetic acid. The product was purified by flash column chromatography and characterised by NMR spectroscopy and mass spectroscopy.

Compound 5.1 was protected by acetyl groups before the bromination reaction. Different reaction conditions of the Ac-protected compound were tested, including brominating agents, solvents, reaction time and heat. The best reaction condition was found to be using N-bromosuccinimide as brominating agent, dichloromethane as solvent, and heated under microwave for 30 minutes. The side-product of the reaction is the bi-brominated product which was removed by flash column chromatography. The product **5.3** was purified by flash column chromatography and characterised by NMR spectroscopy, mass spectroscopy and UV-vis spectroscopy with a maximum absorption band at 391 nm.

The alkylation reaction of the brominated chromophore to the triester was subsequently investigated, however, the *tert*-butyl protected ligand was found to decompose under TFA deprotecting condition. Thus, alternative deprotecting or alkylating strategies need to be found to achieve the synthesis of the target ligand shown in Figure 5.1.

2. Ln(III)-Pt(IV) axial complexes:

Development of the Ln(III)-Pt(IV) complexes in which the Ln moiety is attached to the axial position of the Pt centre is another approach to investigate the Ln-Pt theronostic complexes especially the behaviour of the Pt(IV) prodrugs. For example, in 2020, Meade and co-workers has reported a Gd(III)-Pt(IV) complex in which the Gd moiety was attached in the axial position of the Pt. Results showed the complex is an effective T_1-weighted MR contrast agent.[8]

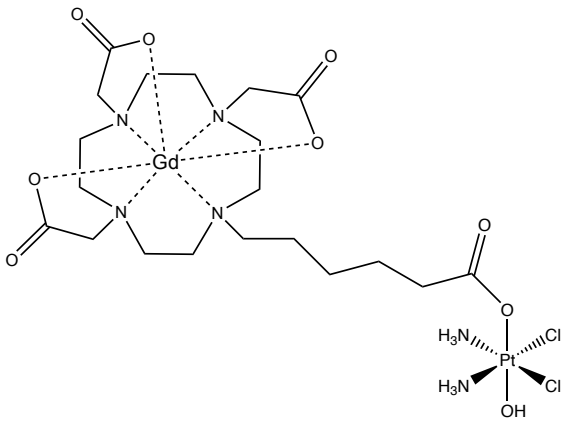

Figure 5.2*: structure of the Gd(III)-Pt(IV) complex.*[8]

Several strategies for achieving axial coupling of the lanthanide moity to the Pt complexes were evaluated, however none of them have satisfying results. A better coupling method therefore needs to be found to achieve axial coupling of lanthanide to platinum. The methods evaluated to date are shown below:

1. Using a coupling agent (HATU or HBTU), forming the activated NHS-ester, in different reaction conditions (solvent, pH, temperature). In these reactions I can observed the formation of activated esters, but no coupled products, and the activated ester decomposed over time. Figure 5.3 showed one of the reactions as an example.

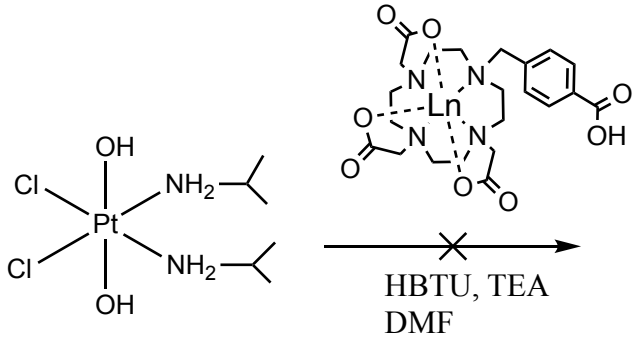

Figure 5.3*: one of the attempted coupling reactions between lanthanide and platinum.*

2. Click reaction between lanthanide and platinum complexes using both CuAAC and SPAAC strategies. In the case of Cu-catalysed reaction, the reaction was unsuccessful

potentially because the Pt(IV) complex can be reduced by the Cu(I) catalyst. In the case of SPACC reaction, the click reaction was found to be slow (less than 5% conversion after 5 days) and a large number of side products was generated.

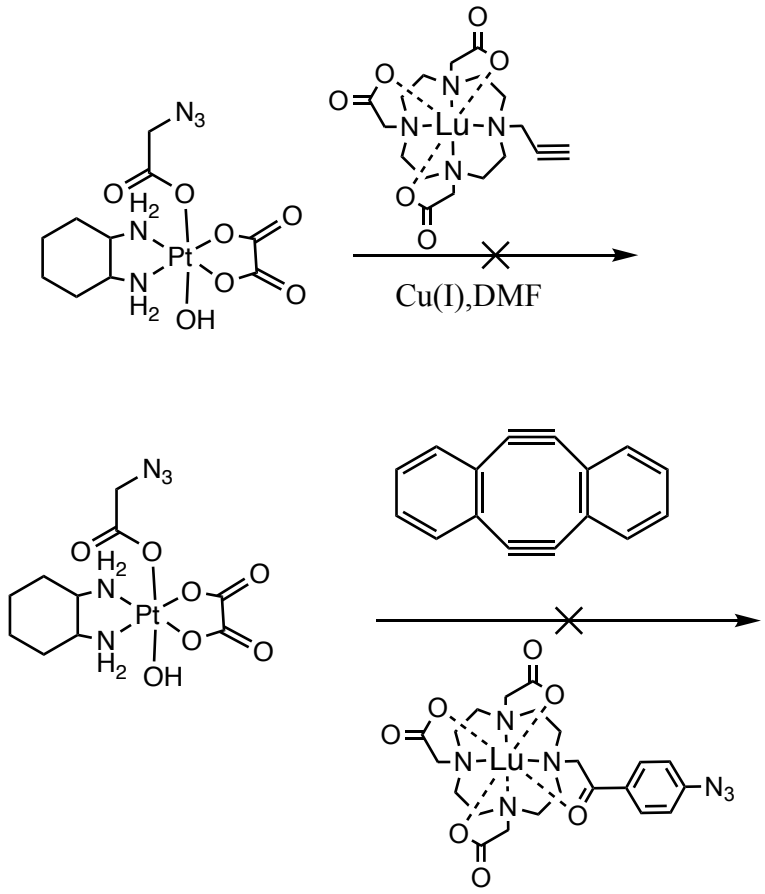

Figure 5.4*: Illustration of click reaction between lanthanide and platinum complexes.*

3. The third type of conjugation strategy was to conjugate the brominated chromophore to the Pt complex first, and then carry out an alkylation reaction between the Pt complex and the triester ligand. The reactions went well, and the alkylated Pt-triester ligand can be purified by HPLC or flash chromatography. However, when it came to the deprotection of the triester, the ester group between the Pt and the triester was proved to be unstable in both acidic and basic conditions, the bond between triester and Pt always disassociated before full deprotection of the triester, even under mild conditions (lower concentration or different acid like

formic acid, acetic acid).

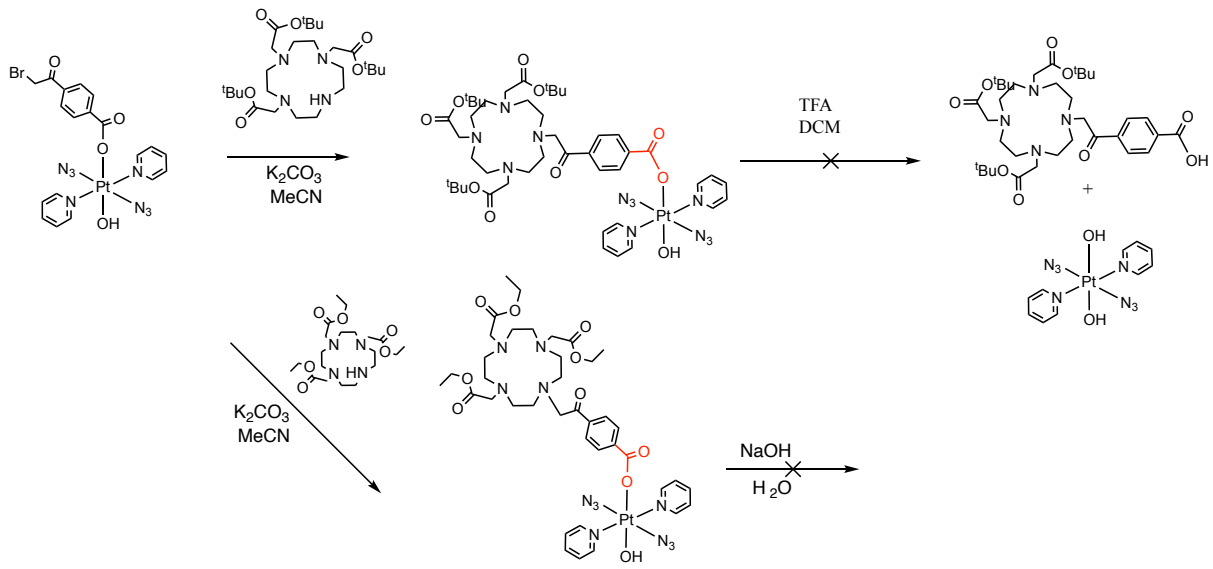

***Figure 5.5**: Illustration of alkylation reactions between Pt complex and triester, and the following deprotection reactions.*

3. Ln_2-Pt complexes:

When having the success on both attaching the Ln on the equatorial and axial position of the Pt centre respectively, a Ln_2-Pt complexes in which one of the Ln is on the axial position and the other one is on the equatorial position can be envisaged, as shown in Figure 5.3. By developing such complex, dual-modality imaging becomes possible. For example, putting Gd(III) and Eu(III) in the Ln building blocks would enable MR and luminescent imaging from the same complex simultaneously. Different lanthanide ions can be used without changing the ligand, and more details of the sub-cellular distribution and metabolism of the complex could be monitored.

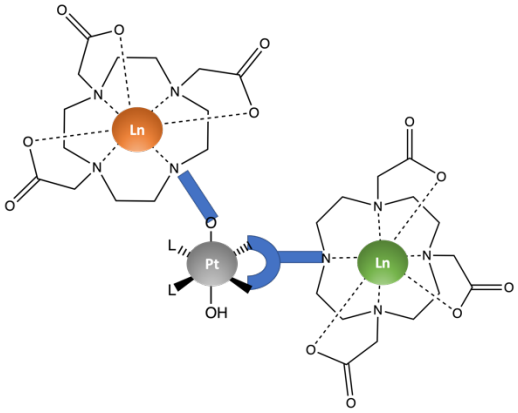

***Figure 5.3**: The illustration of Ln_2-Pt complexes.*

Reference

1 K. Yao, A. Bertran, J. Morgan, S. M. Hare, N. H. Rees, A. M. Kenwright, K. Edkins, A. M. Bowen and N. J. Farrer, *Dalt. Trans.*, 2019, **48**, 6416–6420.

2 K. Yao, A. Bertran, J. Morgan, C. Greenhalgh, K. Edkins, A. M. Bowen and N. J. Farrer, *Eur. J. Inorg. Chem.*, 2021.

3 K. Yao, A. Bertran, A. Howarth, J. M. Goicoechea, S. M. Hare, N. H. Rees, M. Foroozandeh, A. M. Bowen and N. J. Farrer, *Chem. Commun.*, 2019, **55**, 11287–11290.

4 K. Yao, G. Karunanithy, A. Howarth, P. Holdship, A. L. Thompson, K. E. Christensen, A. J. Baldwin, S. Faulkner and N. J. Farrer, *Dalt. Trans.*, 2021, **50**, 8761–8767.

5 S. Gatenbeck and R. Bentley, *Biochem. J.*, 1965, **94**, 478–481.

6 S. Schwolow, H. Kunz, J. Rheinheimer and T. Opatz, *European J. Org. Chem.*, 2013, 6519–6524.

7 S. Bhatt and S. K. Nayak, *Tetrahedron Lett.*, 2006, **47**, 8395–8399.

8 C. J. Adams and T. J. Meade, *Chem. Sci.*, 2020, **11**, 2524–2530.

Chapter 6: Experimental Method

6.1 General Procedure

Commercially available solvents and chemicals were purchased and used without further purification unless otherwise stated. Anhydrous solvents, where used, were degassed with nitrogen and dried by passing through a *MBraun MPSP-800* column, degassed by freeze-pump-thaw and then used immediately. Deionised water was obtained using an Elix® Essential water purification system. Propargyl bromide was used as 80 wt% solution in toluene. All other chemicals were used as received. TLC Silica gel 60 plates were purchased from Merck and used by cutting manually. TLC Aluminium oxide 60 F254 with 60 Å pore size (neutral Al2O3) were purchased from Merck. Geduran® Si 60 Silica gel for column chromatography was purchased from Merck (particle size 25 – 45 μm). Neutral alumina was purchased from Sigma-Aldrich (activated Al2O3, Type I, 70 – 290 mesh). Dialysis tubes (500, 1000MWCO) equipped with regenerated cellulose were purchased from Sigma-Aldrich and used to purify the lanthanide and lanthanide-platinum complexes. The dialysis tube was activated by 10% ethanol solution in deionised water followed by deionised water alone before being used. The corresponding complexes were dissolved in water and transferred into dialysis tube. The dialysis tube was placed in a 5L-beaker filled with deionised water. The dialysis lasts for at least two days under stirring and the deionised water was replaced with fresh deionised water more than three times during the course of dialysis.

NMR spectroscopy: NMR spectra were acquired at 298 K. 400 MHz ^{1}H, 86MHz ^{195}Pt NMR spectra were recorded on a Bruker Avance III HD nanobay NMR equipped with a 9.4T magnet. 500 MHz ^{1}H NMR, 107 MHz ^{195}Pt NMR spectra were recorded on a

Bruker Avance III NMR equipped with a 11.75T magnet. ^{13}C NMR spectra at 126 MHz were recorded on a Bruker Avance NMR spectrometer equipped with a 11.75 T magnet and a ^{13}C detect cryoprobe. All spectra are referenced to the residual solvent peak, unless otherwise stated. The chemical shifts (δ) are reported in parts per million (ppm) and coupling constants in Hz. NMR abbreviations used are as follows: singlet (s), doublet (d), triplet (t), quartet (q), multiplet (m) and broad (br).

NMR Spectroscopy (Diffusion Experiments): All diffusion NMR experiments were acquired at 298 K on a 14.1 T (600 MHz) Agilent DD2 NMR spectrometer equipped with a 5 mm z-axis gradient triple resonance room temperature probe. Gradients were calibrated using the known diffusion coefficient of residual HDO (1902 $\mu m^2 s^{-1}$) in a sample of D_2O at 298 K. The spectrometer temperature was calibrated with d_4-methanol. A stimulated echo pulse sequence with six variable diffusion delays (Δ = 50, 100, 200, 300, 400 and 500 ms) was used in all diffusion experiments. In all experiments δ= 2 ms, τ2, the time for which the magnetisation is transverse, was always set to 10 ms and eleven quadratically spaced gradient field strengths between 8 and 60 $G \cdot cm^{-1}$ were employed.

All spectra were Fourier transformed and phased using NMRPipe. Data were analysed in phase-sensitive mode, with the lowest gradient field strength and diffusion delay spectrum used to determine the phase parameters that are then applied to all other spectra. The water peak intensity in each spectrum was integrated and analysed using the INDIANA method[1] to determine the intra-cellular water mole fraction, cell radius, water exchange rate over the membrane and diffusion coefficients and longitudinal relaxation rates in both the intra- and extra-cellular spaces. Previous simulations have shown that while the INDIANA method is relatively insensitive to small changes in the

intra-cellular longitudinal relaxation rate it is sensitive to when this rate exceeds approximately 0.5 s^{-1}.

NMR Relaxivity Experiments: Relaxivity data were acquired at 298 K on a 14.1 T (600 MHz) Agilent DD2 NMR spectrometer equipped with a 5 mm z-axis gradient triple resonance room temperature probe. In all cases longitudinal relaxation rates were measured using an inversion recovery pulse sequence. To minimise radiation damping effects 100 µL of sample was placed in a co-axial NMR tube and $CDCl_3$ was placed in the outer tube to provide lock signal. For all experiments the recycle delay time was set to at least ten times the T1 time to ensure that the magnetisation relaxed fully back to equilibrium prior to the inversion pulse. Typically, fifteen different relaxation delays up to five times the T1 time were employed. Spectra were subsequently phased and Fourier transformed using NMRPipe. Peak intensities for each relaxation delay were integrated and fit to the equation: $S(t) = S(\infty)(1 - 2e^{-R_1 t})$ where S is the signal intensity and S(∞) and R_1 are fitting parameters using in-house python scripts that employ the LMFIT and nmrGlue modules.

Mass Spectrometry: Low-resolution mass spectra were acquired using either an Agilent Technology 1260 Infinity or a Waters LCT Premier XE spectrometer. LC-MS were measured by a Waters LCT Premier bench-top orthogonal acceleration time-of-flight LC-MS system. High resolution accurate mass spectra were recorded to 4 decimal places using Bruker µTOF and Micromass GCT systems.

Elemental analysis (Pt, Ln) of complexes: complexes were dissolved in DMEM media and analysed by ICP-MS analysis. Five repeat samples for each complex were prepared. The average of the replicates were calculated including error calculation. 50

µL of compound containing media was added to the PFA vials, to which 500 µL 16M HNO_3 and 100 µL of 30% H_2O_2 were added. The samples were digested overnight at 70° C. Following this digestion the samples were allowed to cool to room temperature, where they appeared transparent and yellow in colour. Following complete digestion, the samples were diluted to 15 mL with water.

Trace elemental analyses of Pt and Gd, were undertaken by inductively coupled plasma - mass spectrometry (ICP-MS), using a PerkinElmer NexION 350D ICP-MS at the Department of Earth Sciences, University of Oxford. All sample and standard measurements were blank corrected, using blank measurements taken periodically during the analytical run. The run was arranged so that every ten samples were bracketed by a gravimetrically prepared calibrant standard, as a gauge for analytical precision and accuracy. A secondary quality control standard was also measured to verify the validity of the calibration. Detection limits are calculated as three times the standard deviation of the blank series measured during the analysis (ca. n=19) and corrected for the sample dilutions.

Analytical HPLC: HPLC was performed using a Waters Autopurification system, equipped with an ACQUITY QDa performance mass spectrometer and UV-Vis absorption spectrometer. UV-Vis absorption spectra were acquired on the HPLC. MilliQ® water (Milipore, Merck) and HPLC-grade MeCN/MeOH were used as eluents A and B respectively.

Neutral conditions consisted of original solvents, basic conditions contain 0.05% NH_4OH (pH 8) in both solvents and acidic conditions contain 0.1% formic acid in both solvents (pH 2), gradient and column conditions are described in the chart below. Crude

samples were dissolved in 95:5 H2O/MeCN and filtered (nylon, ionic membrane, 0.2 μM).

prep-HPLC: Prep-HPLC used a Waters X-Bridge OBD semi-prep column (5 μm, 19 mm x 50 mm), with an injection loop of 1 ml. Samples (in H_2O/MeOH) were filtered (IM) and injected in 750 μL aliquots, with mass-directed purification with an ACQUITY QDa performance mass spectrometer.

Analytical HPLC: Analytical HPLC used the same solvents and a Waters X-Bridge OBD column (5 μm, 4.6 mm x 50 mm) and an injection loop of 0.02 ml.

Method 1, Column: Xbridge, flow rate: 1ml/min for analytical, 25ml/min for preparative run		
Time/min	Solvent A %	Solvent B %
0	95	5
5	50	50
5.5	5	95
6.5	5	95
9	95	5

Method 2, Column: Xbridge, flow rate: 1ml/min for analytical, 25ml/min for preparative run		
Time/min	Solvent A %	Solvent B %
0	95	5
1	95	5
2.5	70	30
8	30	70
9	95	5

Method 3, Column: Sunfire/Xbrdige, flow rate: 1ml/min for analytical, 20ml/min for preparative run		
Time/min	Solvent A %	Solvent B %
0	95	5
1	90	10
8	25	75
9	5	95
10	95	5

Method 4, Column: Xbridge, flow rate: 1ml/min for analytical, 20ml/min for preparative run		
Time/min	Solvent A %	Solvent B %
0	80	20
1	80	20
8	10	90
9	50	50
10	80	20

X-ray crystallography: Low temperature single crystal X-ray diffraction data were collected using a (Rigaku) Oxford Diffraction SuperNova A diffractometer. Raw frame data were reduced using CrysAlisPro and the structure was solved from the integrated intensities with charge-flipping using 'Superflip'.[2] The structure was refined using full-matrix least squares on F^2 using the CRYSTALS suite.[3–5] Crystallographic data have been deposited with the Cambridge Crystallographic Data Centre (CCDC: 1960280) and can be obtained via www.ccdc.cam.ac.uk/data_request/cif.

Infrared spectroscopy: Infrared spectra were recorded in solid-state using a Bruker Tensor 27 FT-IR spectrometer with an IR Diamond Attenuated Total Reflectance module.

Luminescence spectroscopy: HORIBA Jobin Yvon FluoroLog3 fluorimeter (Hamamatsu R928 detector and a double-grating emission monochromator) was used to acquire the luminescence spectra. The standard conditions for acquiring emission and excitation spectra are room temperature and steady-stated mode unless otherwise stated. HORIBA Jobin Yvon FluoroLog3 fluorimeter system equipped with a Xenon flash lamp was used to acquire emission lifetimes. Luminescence lifetimes were obtained by tail fit for Eu(III) complexes using Origin software.

6.2 Synthetic Methods

tBuDO3AH: 1,4,7-Tris(tert-butoxycarbonylmethyl)-1,4,7,10-tetraazacyclododecane, (2.2)[6]

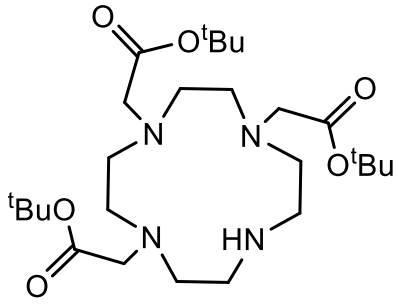

Cyclen (7.00 g, 40 mmol) was added to dry MeCN (175 mL) with sodium hydrogen carbonate (11.30 g, 134 mmol) and stirred for 20 minutes in an ice bath. Tert-butyl bromoacetate (19.75 mL, 134 mmol) dissolved in dry MeCN (75 mL) was added dropwise over 30 minutes. The solution was then allowed to warm to room temperature and stirred under nitrogen for 48 h. The inorganic solids were removed by filtration and the solvent removed under reduced pressure to give a pale cream solid. The solid was dissolved in a minimum amount of DCM, hexane added and triturated to remove excess tert-butyl bromoacetate. The resulting cream solid was washed with toluene and then recrystallized from hot toluene to yield the product as a white solid (7.65 g, 37%).

^{1}H-NMR (400 MHz, CDCl+): δ_H 9.97 (s, 1H), 3.32 (s, 4H), 3.26 (s, 2H), 3.06 (s, 4H), 2.90–2.83 (s, 12H), 1.42 (s, 27H) ppm. ^{13}C-NMR (126 MHz, $CDCl_3$): δ_C 170.67, 169.78, 82.01, 81.85, 58.41, 51.54, 49.38, 47.68, 28.39, 28.36 ppm. ESI-MS (MeOH): *m/z* cal. for $[M+H]^+$ 515.4, found *m/z* 515.4 $[M+H]^+$, 537.4 $[M+Na]^+$.

4-Azido acetophenone[7]

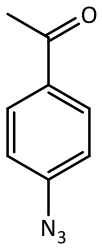

4-Aminoacetophenone (1 g, 7.4 mmol) was dissolved in mixture of 14 ml ethyl acetate and 2 ml H_2O, and this solution was left to cool in an ice-water bath for 10 minutes. To this a solution of $NaNO_2$ in 2.4 ml H_2O was added dropwise (0.87g, 12.6 mmol) stirred for 30 min. A solution of NaN_3 in 2.7ml H_2O was added dropwise (0.82, 12.6 mmol). After stirring for a further 30 min, the solution was diluted by 16 ml H_2O and washed with 2 × 20 ml ethyl acetate. The combined organic phase was wash with 1 M NaOH solution, then water, dried over Na_2SO_4 and concentrated *in vacuo* and dried in Schlenk line to give the target compound as pure yellow crystals (1.16 g, 93%).

^{1}H-NMR (400 MHz, $CDCl_3$) δ: 2.62 (s, 3H), 7.14 (d, J = 8.0 Hz, 2H), 7.98 (d, J = 8.0 Hz, 2H). IR (cm^{-1}): 2095 (N_3), 1683 (C=O).

1-(4-azidophenyl)-2-bromoethan-1-one (2.1)[8]

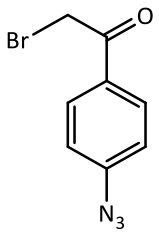

4-Azido acetophenone (1 g) was dissolved in 20 ml acetonitrile, *p*-toluenesulfonic acid monohydrate (2.08 g, 12 mmol) and N-bromosuccinimide (1.09 g, 6 mmol) were added. Stirred under reflux for 2 h. Removed solvent under reduced pressure, and redissolved in 50 ml DCM, washed with water, dried over $MgSO_4$ and removed solvent under

vacuum. The crude product was purified by silica gel chromatography (6:4 (*v:v*) DCM:hexane) to obtain a pale yellow solid (0.78 g, 54%).

^{1}H NMR (400 MHz, $CDCl_3$) δ: 8.01 (d, J = 8.5Hz, 2H), 7.11 (d, J = 8.4Hz, 2H), 4.45 (s, 2H). IR (cm^{-1}): 2096 (N_3), 1678 (C=O).

Tri-*tert*-butyl 2,2',2''-(10-(2-(4-azidophenyl)-2-oxoethyl)-1,4,7,10-tetraazacyclododecane-1,4,7-triyl)triacetate (2.3)[9]

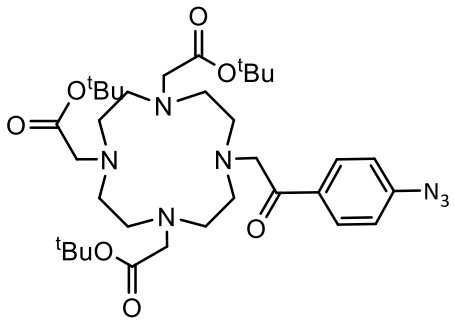

To a solution of triester (1g 1.9 mmol) in dry acetonitrile (40 ml), potassium carbonate was added (0.54 g, 3.8 mmol) followed by 1-(4-azidophenyl)-2-bromoethan-1-one (0.47 g, 1.9 mmol). The suspension was left stirring at RT under nitrogen for 3 h. The reaction was filtered and the solvent was removed by reduced pressure. The crude product was purified by silica gel column chromatography (9:1 (*v:v*) $CHCl_3$:MeOH) to obtain an orange solid. (1.42 g, 83%)

^{1}H-NMR (400 MHz; $CDCl_3$) δ: 7.92-8.13 m, 2H), 7.03-7.21 (m, 2H), 3.45 – 2.06 (m, 24H), 1.45 (s, 27H). ESI-MS: *m/z* cal. for $[M+Na]^+$ 696.4, found *m/z* 696.4.

2,2',2''-(10-(2-(4-azidophenyl)-2-oxoethyl)-1,4,7,10-tetraazacyclododecane-1,4,7-triyl)triacetic acid (2.4)[10]

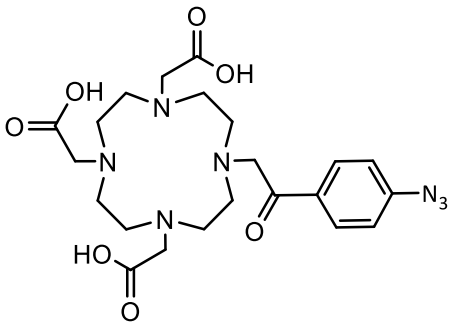

To a solution of Tri-*tert*-butyl 2,2',2''-(10-(2-(4-azidophenyl)-2-oxoethyl)-1,4,7,10-tetraazacyclododecane-1,4,7-triyl)triacetate (0.5g 0.74 mmol) in DCM (5 ml), TFA (5 ml) was added dropwise. The reaction was stirred at RT for 24 h, the solvent were removed under reduced pressure. The resulting solid was treated with a small amount of methanol following addition of diethyl ether to triturate the target product as white powder. The solvent was decanted and the solid was dried under vacuum to afford target ligand in quantitative yield. (0.31 g, 81%)

^{1}H-NMR (400 MHz, D_2O) δ 7.83-8.04 (m, 2H), 7.02-7.21 (m, 2H), 4.05 – 2.75 (m, 24H). ESI-MS: *m/z* cal. for $[M+H]^+$ 506.2, found *m/z* 506.2 for $[M+H]^+$

General method for synthesis of the azidophenylDO3A lanthanide complexes (Ln.2.5)[11]

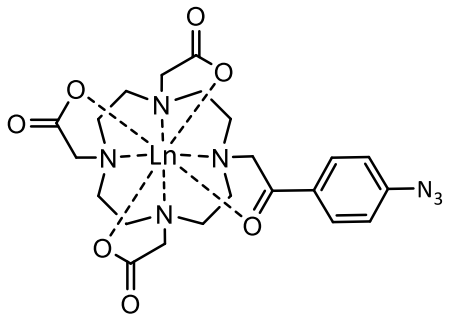

To a solution of the ligand **2.4** in methanol the appropriate lanthanide triflate salt was added (1.2 eq.) and the solution was stirred at 60ºC for 30 min. The pH was adjusted to 4 by adding 1 M NaOH dropwise. The reaction was left to stir at 60ºC for 48 h. The methanol was removed under vacuum, leaving an oil that was dissolved in water. The pH of this solution was adjust to 10 by addition of NaOH solution in order to precipitate excess lanthanide as its insoluble hydroxide, which was separate by centrifugation and the supernatant was filtered by a syringe filter. The aqueous solvent was removed by freeze-drying to obtain product.

(Ln: Eu). Yield: 86%. ^{1}H-NMR (400 MHz; D_2O) δ: 33.8, 32.0, 22.5, 20.3, 15.9, 9.7, -3.5, - 5.0, -7.3, -8.8, -9.8, -11.1, -11.7, -15.6, -17.1. Only resolved peaks outside 0 to 5 ppm are reported. ESI-MS: *m/z* cal. for $[M+Na]^+$ 678.1, found *m/z* 678.1 for $[M+Na]^+$.

(Ln: Yb). Yield: 82%. ^{1}H-NMR (400 MHz; D_2O) δ: 133.6, 126.5, 119.5, 90.5, 85.4, 81.9, 70.3, 67.1, 56.9, 43.6, 37.5, 30.5, 28.8, 25.8 23.6, 22.5, -24.6, -27.7, -35.0, -36.5, - 39.3, -42.7, -46.0, -48.1, -51.4, -66.5, -81.0. Only resolved peaks outside -20 to 20 ppm are reported. ESI-MS: *m/z* cal. for $[M+Na]^+$ 699.1, found *m/z* 699.1for $[M+Na]^+$.

(Ln: Lu). Yield: 87%. ^{1}H-NMR (400 MHz; D_2O) δ: 8.08(d, J = 8.8, 2H), 7.18 (d, J = 8.7, 2H), 4.02 (br, 16H), 3.21(br, 8H), 2.86 (br, 4H). ESI-MS: *m/z* cal. for $[M+Na]^+$ 700.1, *m/z* found 700.1 for $[M+Na]^+$.

diethyl 2-(prop-2-yn-1-yl)malonate (2.6)[12]

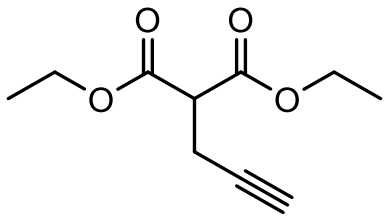

To a stirring solution of diethyl malonate (0.5g) in ethanol, 1.1 equivalent of sodium ethoxide was added and stirred for 15 min. 1 equivalent of propargyl bromide was added dropwise. The resulting solution was stirred at room temperature for 16 h. The solvent was removed by reduced pressure and the crude product was obtained as yellow oil. Flash column chromatography was used to purify the product (silica gel, ethyl acetate: petroleum ether = 6: 4). (1.14 g, 92%)

^{1}H NMR (400 MHz, $CDCl_3$) δ: 4.16 (qd, *J* = 7.2, 1.8 Hz, 4H), 3.49 (t, *J* = 7.7 Hz, 1H), 2.70 (dd, *J* = 7.7, 2.7 Hz, 2H), 1.96 (d, *J* = 5.4 Hz, 1H), 1.21 (t, *J* = 7.1 Hz, 6H). ESI-MS: *m/z* cal. for $[M+H]^+$ 199.1, found *m/z* 199.1 for $[M+H]^+$.

General method for the synthesis of the lanthanide complexes from Ln.2.5 and 2.6 (Ln.2.7)[13]

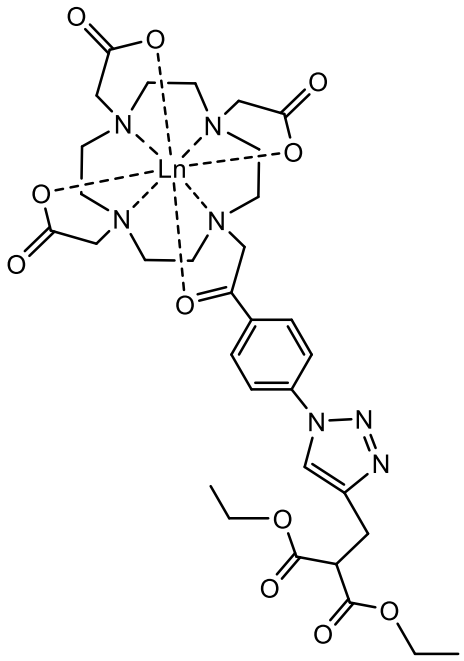

Ln complex **Ln.2.5** (0.2g) was dissolved in methanol, 1.5 equivalent of the alkyl compound **2.6**, 1.6 equivalent of sodium ascorbate and copper sulphate were added to the solution. The solution was stirred at 40°C for 48 h. HPLC (acidic conditions with 0.1% formic acid, HPLC method 3, Sunfire column) was used to monitor the reaction progress and purification of the crude product.

(Ln: Lu). Yield: 36%. ^{1}H NMR (400 MHz, D_2O) δ: 8.34 (s, 1H), 8.27 (d, *J* = 8.7 Hz, 2H), 8.15 (s, 1H), 7.90 (d, *J* = 8.3 Hz, 2H), 4.05 – 2.75 (m, 28H), 1.48 (t, *J* = 7.1 Hz, 6H). ESI-MS: *m/z* cal. for $[M+H]^+$ 876.2, ound *m/z* 876.2 for $[M+H]^+$.

(Ln: Eu). Yield: 45%. ^{1}H-NMR (400 MHz; D_2O) δ: 32.6, 31.5, 22.6, 21.0, 14.9, 8.9, -3.4, - 4.9, -7.2, -8.8, -9.6, -11.0, -11.6, -14.6, -17.0. Only resolved peaks outside 0 to 5 ppm are reported. ESI-MS: *m/z* cal. for $[M+H]^+$ 854.2 found *m/z* 854.2 for $[M+H]^+$.

General method for the ester deprotection of lanthanide complexes 2.7 (Ln.2.8)[14]

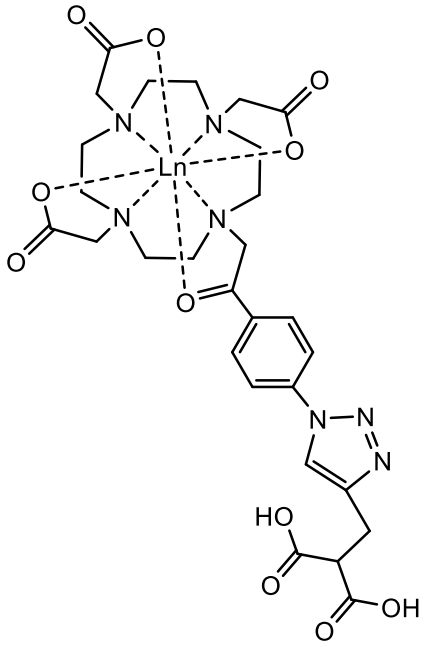

Ln complex **Ln.2.7** (0.15g) was dissolved in water and 1M NaOH solution was added dropwise until the pH of the solution reached 10. The resulting solution was stirred at 50°C for 16 h. The product was purified by 500 MWCO cellulose membrane.

(Ln: Lu). Yield: 85%. ^{1}H NMR (400 MHz, D_2O) δ: 8.32 (s, 1H), 8.25 (d, *J* = 8.5 Hz, 2H), 8.13 (s, 1H), 7.80 (d, *J* = 8.1 Hz, 2H), 4.05 – 2.75 (m, 24H). ESI-MS: *m/z* cal. for $[M+H]^+$ 820.2 found *m/z* 820.2 for $[M+H]^+$. UV-vis absorption (nm) 275.

(Ln: Eu). Yield: 88%. ^{1}H-NMR (400 MHz; D_2O) δ: 35.5, 32.4, 22.8, 21.5, 15.1, 9.9, -2.9, - 3.5, -6.2, -8.8, -9.8, -11.0, -12.5, -15.6, -18.5. Only resolved peaks outside 0 to 5 ppm are reported. ESI-MS: *m/z* cal. for $[M+H]^+$ 798.2, found *m/z* 798.2 for $[M+H]^+$. UV-vis absorption (nm) 275.

***cis*-[Pt(NH$_3$)$_2$I$_2$]**

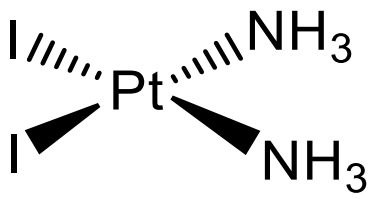

Potassium tetrachloroplatinate with 10 equivalents of potassium iodide were dissolved in water and stirred for 30 minutes. 2 equivalents of ammonium chloride was added to the solution. 2M KOH solution was added dropwise until the pH reached 10 and stay unchanged. The solution was left to stir for another 2 hours, the *cis*-[Pt(NH$_3$)$_2$I$_2$] was formed as orange solid. Pure product was recrystallized from DMF.

ESI-MS: *m/z* cal. for $[M+H]^+$ 483.96, found m/z 483.83 for $[M+H]^+$.

***cis*-[Pt(NH$_3$)$_2$(H$_2$O)$_2$]$^{2+}$ (Pt.2.9)**

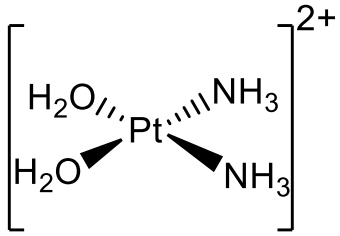

2 equivalents of silver nitrate was added to a water suspension of *cis*-[Pt(NH$_3$)$_2$I$_2$]. The silver iodide was formed as a pale-yellow precipitate. The suspension was stirred at room temperature for 24 h and the precipitate was removed by filtration. The clear filtrate containing **Pt.2.9** can be used directly in the next step.

^{195}Pt NMR (107 MHz, d_3-MeCN) δ: -1596.

General method for the ester deprotection of lanthanide-platinum complexes

Ln.2.10

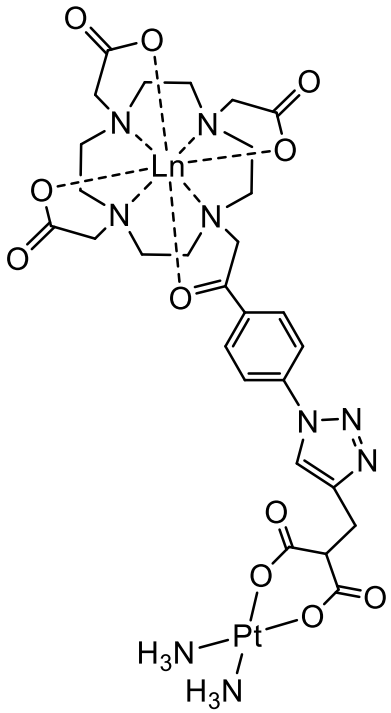

1 equivalent of **Ln.2.8** (0.12g) was added to the **Pt.2.9** (1.5 equivalent) water solution. 1M sodium hydroxide solution was added dropwise to adjust the pH of the solution to 9, and the resulting solution was stirred at room temperature for 24 hours. Solvent was removed by reduced pressure and the crude product was purified by HPLC (acidic condition with 0.1% formic acid, HPLC method 3, Sunfire column).

(Ln: Lu). Yield 33%. ^{1}H NMR (400 MHz, D_2O) δ: 8.33 (s, 1H), 8.27 (d, J = 8.5 Hz, 2H), 8.14 (s, 1H), 7.81 (d, J = 8.1 Hz, 2H), 4.06 – 2.75 (m, 24H). ^{195}Pt NMR (107 MHz, d_3-MeCN) δ: -2098. ESI-MS: *m/z* cal. for $[M+H]^+$ 1047.2, found *m/z* 1047.2 for $[M+H]^+$. UV-vis absorption (nm) 295.

(Ln: Eu). Yield:28%. ^{1}H-NMR (400 MHz; D_2O) δ: 35.2, 27.4, 25.7, 24.9, 10.1, 9.14, 7.2, -1.7, -2.5, - 5.1, -6.4, -8.6, -9.8, -11.0, -12.1, -13.1, -16.6, -19.0. Only resolved peaks outside 0 to 5 ppm are reported. ^{195}Pt NMR (107 MHz, d_3-MeCN) δ: -2096. ESI-

MS: *m/z* cal. for $[M+H]^+$ 1025.2 found *m/z* 1025.2 for $[M+H]^+$. UV-vis absorption (nm) 295.

General method for the ester deprotection of lanthanide-platinum complexes Ln.2.11

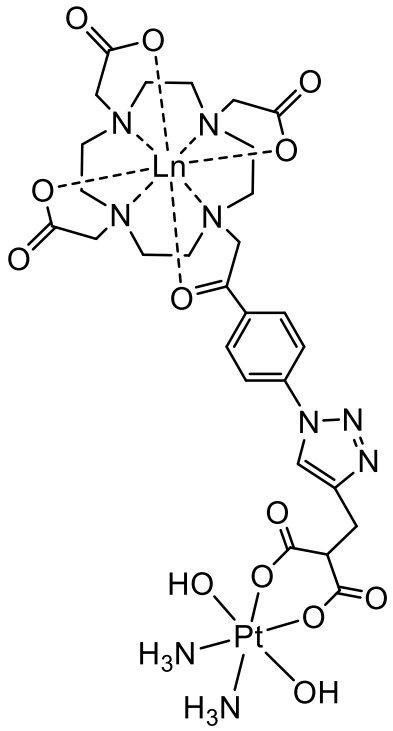

Complexes **Ln.2.10** (0.1 g) was dissolved in 2 ml of water, 0.5 mL 30% H_2O_2 solution was added dropwise to the solution. The resulting solution was stirred for 16 h. Solvent was removed by rotary evaporation and the crude product was obtain as yellow oil and purified by HPLC (acidic conditions with 0.1% formic acid, HPLC method 3, Sunfire column).

(Ln: Lu). Yield 76%. ^{1}H NMR (500 MHz, D_2O) δ: 8.66 (s, 1H), 8.32 (s 1H), 8.12 (d, *J* = 8.6 Hz, 2H), 8.05 (d, *J* = 8.6 Hz, 2H), 7.81 (d, *J* = 8.1 Hz, 2H), 4.06 – 2.75 (m, 24H). ^{195}Pt NMR (107 MHz, d_3-MeCN) δ: 1085. ESI-MS: *m/z* cal. for $[M+H]^+$ 1081.2, found *m/z* 1081.2 for $[M+H]^+$. UV-vis absorption (nm) 295.

(Ln: Eu). Yield 85% ^{1}H-NMR (400 MHz; D_2O) δ: 34.9, 27.1, 25.4, 24.7, 21.7, 10.3, 9.4, 9.1, 7.4, -1.7, -2.3, -2.9, -5.0, -8.0, -10.7, -11.8, -16.4, -18.6. Only resolved peaks outside 0 to 5 ppm are reported**. ^{195}Pt NMR** (107 MHz, d_3-MeCN) δ: 1084. ESI-MS: *m/z* cal. for $[M+H]^+$ 1089.2, found *m/z* 1089.2 for $[M+H]^+$. UV-vis absorption (nm) 295.

***trans,trans*-[Pt(py)$_2$Cl$_2$]**[15]

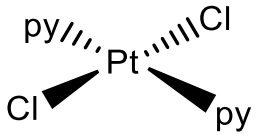

Pyridine (1.8g, 24 mmol) was added to a solution of K_2PtCl_4 (2g, 4.8 mmol) in distilled water (50 ml). The solution was stirred at 85 °C overnight until colourless, cooled and syringe filtered. The solvent was removed and the salt was washed with diethyl ether (3 ml). HCl (2M, 50 ml) was added and the solution was stirred at 75 °C for 24 hours. The resulting yellow suspension was put on ice and filtered by Buchner filter, and washed with cold minimal H_2O, methanol and diethyl ether to give the pale yellow product (1.66 g 82%).

^{1}H NMR (400 MHz, d_6-acetone) δ: 8.92 (dd, $^{3}J_{HPt}$ = 35 Hz, $^{3}J_{HH}$ = 7 Hz, 4H) 8.05 (tt, $^{3}J_{HH}$ = 7 Hz, 2H) 7.55 (dt, $^{3}J_{HH}$ = 7 Hz, 4H).

***trans,trans*-[Pt(N$_3$)$_2$(py)$_2$]**[15]

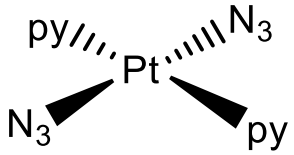

trans,trans-$[PtCl_2(py)_2]$ (1.60 g, 3.80 mmol) was suspended in H_2O (275 mL), $AgNO_3$ (1.28 g, 7.60 mmol) was added and the reaction stirred at 60 °C overnight. The grey solution was filtered (celite, then IM). NaN_3 (1.24 g, 19.00 mmol) was added and the

reaction was stirred at room temperature, after 4 h additional NaN_3 (1.24g, 19.00 mmol) was added, and the solution stirred for 4 h. The solution was placed on ice, filtered, and the yellow product washed with cold, minimal solvents (H_2O, ethanol, ether) to give the crude product (1.60 g, 3.68 mmol, 96%). The crude product was purified by recrystallisation from pyridine (in the ratio product/solvent of 1 g/37.5 mL, pre-heated to 40 °C), followed by filtration (IM), and cooling to 4 °C. The yellow product was isolated by filtration, washed and dried under vacuum. (1.38g, 87%)

^{1}H NMR (400 MHz, d_6-acetone) δ: 8.86 (d, $^3J_{HPt}$ = 36 Hz, $^3J_{HH}$ = 7 Hz, 4H), 8.08(t, $^3J_{HH}$ = 7 Hz 2H), 7.65 (t, $^3J_{HH}$ = 7 Hz, 4H).

***trans,trans,trans*-$Pt^{IV}(N_3)_2(py)_2(OH)_2$ (3.1)**[15]

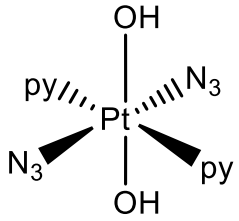

trans,trans-$[Pt(N_3)_2(py)_2]$ (500 mg, 1.14 mmol) was suspended in 30% H_2O_2 solution (35 ml) and left to stir at 45 °C for 3 hours. The solvent was reduced to 5 ml on a rotary evaporator at 50 °C. Ethanol (20 ml) was added and the solution was filtered (IM). Diethyl ether (60 ml) was added, the solution was allowed to cool and left in the freezer overnight. Yellow crystals were isolated on filtration (513 mg, 95%).

^{1}H NMR (400 MHz, D_2O) δ: 8.82 (d, $^3J_{HPt}$ = 27 Hz, $^3J_{HH}$ = 6 Hz, 4H) 8.30 (t, $^3J_{HH}$ = 8 Hz, 2H) 7.84 ppm (t, $^3J_{HH}$ = 7 Hz, 4H). ESI-MS (MeOH): *m/z* cal. for $[2M+H]^+$ 943.1, *m/z* = 965.1 $[2M + Na]^+$; 943.1 $[2M + H]^+$; 494.0 $[M + Na]^+$. IR (cm^{-1}): 2032.35 (N_3).

Reaction of 3.1 with 1,4-diphenyl-2-butyne-1,4-dione (3.2) to give complex 3.3(3.3a/3.3b)[16]

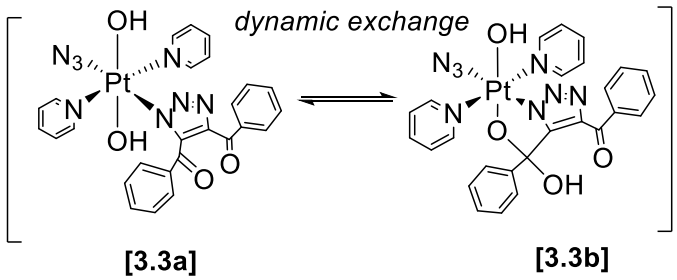

1,4-diphenyl-2-butyne-1,4-dione (70 mg, 0.299 mmol) was dissolved in MeCN (22 ml). *trans,trans,trans*-[$Pt(N_3)_2(OH)_2(py)_2$] (150 mg, 0.318 mmol) was added whilst stirring at 35 °C for 48 h. The solvent volume was reduced to 5 ml *in vacuo,* syringe filtered and purified by HPLC (neutral condition, HPLC method 1, Xbridge column). Complex **3a/3b** was isolated as a pale yellow solid (60 mg, 0.085 mmol, 28 %). Subsequent analysis of .3**3** confirmed that it was an equilibrium mixture of two isomers: **3.3a** and **3.3b**.

^{1}H NMR (500 MHz, d_3-MeCN) δ: 9.13 (dd, $^3J_{HPt}$ = 27.6, $^3J_{HH}$ = 6.7, 2H), 8.95 (dd, $^3J_{HPt}$ = 28.0, $^3J_{HH}$ = 6.7, 4H), 8.70 (dd, $^3J_{HPt}$ = 27.9, $^3J_{HH}$ = 6.7, 2H), 8.21 (d, $^3J_{HH}$ = 8.1, 2H), 8.13 (d, $^3J_{HH}$ = 7.5, 2H), 8.12 (m, 1H), 8.03 (m, 2H), 8.01 (m, 1H), 7.68 (dd, 2H), 7.60 (m, 1H), 7.58, (m, 1H), 7.56 (m, 4H) 8.03 (m, 2H), 7.49 (m, 1H), 7.47 (m, 2H), 7.46 (m, 2H), 7.45 (d, 2H), 7.43 (m, 2H), 7.26 (dd, $^3J_{HH}$ = 6.7, $^3J_{HH}$ = 6.7, 2H), 7.06 (t, $^3J_{HH}$ = 7.5, 1H), 6.94 (dd, $^3J_{HH}$ = 7.6, $^3J_{HH}$ = 7.6, 2H), 6.68 (d, $^3J_{HH}$ = 8.1, 2H), 4.93 (s).

^{13}C NMR (151 MHz, d_3-MeCN) δ: 190.3, 188.1, 186.4, 159.3, 150.5, 150.4, 150.1), 147.9 (q, $^3J_{CPt}$ = 25.8), 147.1 (q, $^4J_{CPt}$ = 13.6), 145.6 (q, $^3J_{CPt}$ = 33.1), 143.2, 143.0, 142.9, 142.2 (q, $^2J_{CPt}$ = 33.7), 138.1 (q), 137.7 (q), 134.3, 134.1, 134.0, 131.3, 131.2, 129.6, 129.3, 129.2,129.1, 128.5, 128.1, 127.2 ($^3J_{CPt}$= 26.5), 127.1 ($^3J_{CPt}$= 25.7), 127.0 ($^3J_{CPt}$= 27.4), 125.3, 103.0 (q).

^{195}Pt NMR (107 MHz, d_3-MeCN) δ: 689 (**3.3a**), 785 (**3.3b**).

ESI-MS (MeCN): *m/z* cal. for $[2M+Na]^+$ 1433.3, $[2M+Na]^+$ was found at 1433.3

Characterisation of complex 3.5[16]

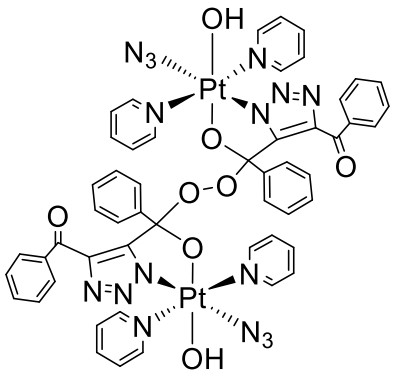

^{1}H NMR (500 MHz, d_3-MeCN) δ: 9.16 (s, br, 1H), 9.14 (dd, $^3J_{HPt}$ = 26.7, $^3J_{HH}$ = 6.7, 4H), 8.51 (dd, $^3J_{HPt}$ = 26.7, $^3J_{HH}$ = 6.6, 4H), 8.11 (t, $^3J_{HH}$ = 7.6, 2H), 8.06 (d, $^3J_{HH}$ = 8.3, 4H), 7.85 (t, $^3J_{HH}$ = 7.8, 2H), 7.68 (t, $^3J_{HH}$ = 7.8, 4H), 7.59 (t, $^3J_{HH}$ = 7.5, 2H), 7.46 (t, $^3J_{HH}$ = 7.8, 4H), 7.22 (t, $^3J_{HH}$ = 6.6, 4H), 7.09 (t, $^3J_{HH}$ = 7.4, 2H), 6.95 (t, $^3J_{HH}$ = 7.8, 4H), 6.75 (d,$^3J_{HH}$ = 8.3, 4H).

^{13}C NMR (151 MHz, d_3-MeCN) δ: 187.9 (q), 153.3 (q), 151.6 (q, $^2J_{CPt}$ 43.8 Hz), 150.42, 150.37, 143.1 (q), 143.0, 142.8, 138.6 (q), 133.8, 131.3, 129.1, 127.2 (t, $^3J_{CPt}$= 27.2), 127.0 (t, $^3J_{CPt}$= 26.2), 128.8, 128.6, 126.4, 112.1 (q).

^{195}Pt NMR (107 MHz, d_3-MeCN) 776 ppm. ESI-MS: *m/z* cal. for $[M.H_2O_2 +Na]^+$ 1465.3, $[M.H_2O_2 +Na]^+$ at 1465.3 *m/z*.

Characterisation of rearranged complex 3.4

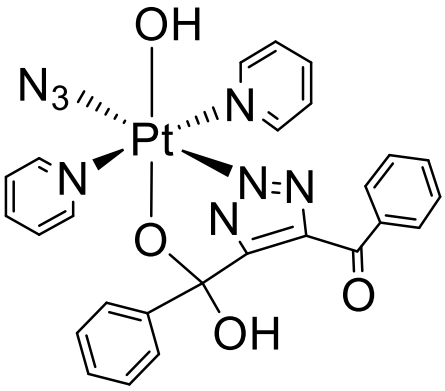

^{1}H NMR (400 MHz, d_4-MeOH) δ: 9.05 (d, $^{3}J_{HPt}$ = 25, $^{3}J_{HH}$ = 6, 2H), 8.54 (d, $^{3}J_{HPt}$ = 25, $^{3}J_{HH}$ = 6, 2H), 8.26 (dd, $^{3}J_{HH}$ = 6, 1H), 7.97 (dd,$^{3}J_{HH}$ = 6, 1H), 7.93 (d, $^{3}J_{HH}$ = 6, 2H), 7.81 (dd, $^{3}J_{HH}$ = 7, 2H), 7.57 (t, $^{3}J_{HH}$ = 7, 1H), 7.43 (dd, 2H, $^{3}J_{HH}$ = 7), 7.33 (dd, 2H), 7.04 (dd, 1H, $^{3}J_{HH}$ = 7), 6.91 (t, 2H, $^{3}J_{HH}$ = 7), 6.71 (d, 2H, $^{3}J_{HH}$ = 6).

^{13}C NMR (126 MHz, d_4-MeOH) δ: 188.0 (q), 152.0 (q), 151.3, 150.7, 145.3 (q), 143.8, 143.6 (q), 143.4, 138.8 (q), 134.1, 131.2, 129.9, 129.2, 128.8, 128.6, 128.1 ($^{3}J_{13C195Pt}$= 26), 127.6 ($^{3}J_{13C195Pt}$= 26), 126.3, 108.4 (q).

^{195}Pt NMR (107 MHz, d_4-MeOH) δ: 824

IR v cm^{-1} (d_4-MeOH): 3391.11 (br), 2508.44 (br), 2048.63 (sharp, $\nu_{asym}N_3$), 1654.70, 1613.38, 1597.02, 1460.08, 1405.16, 1254.93, 1213.32, 1106.53, 1013.34, 934.54, 894.13, 768.44, 691.38.

ESI-MS (MeOH) *m/z*: cal. for $[M+H]^+$ 705.7, found $[M + H]^+$ (*m/z*) = 705.7 and $[M – OH]^+$ (*m/z*) = 688.1)

***ortho*-(Phenylsulfonylmethyl)benzonitrile**[17]

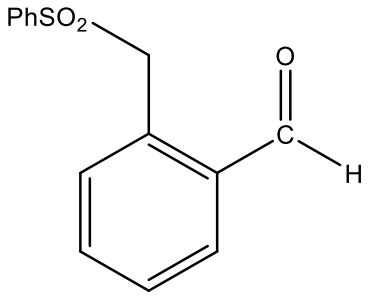

alpha-bromotolunitrile (4.01g) was added to benzene sulfinic acid sodium salt dihydrate (4.82 g, 24.0 mmol, ChemCruz) in DMF (30 ml) under an inert atmosphere. The reaction mixture was stirred at 80ºC for two hours and then cooled to room temperature. The reaction mixture was worked up with H_2O/EtOAc. The organic layer was isolated, dried with $MgSO_4$, filtered and the solvent removed in vacuo to yield 5.65 g of crude product. The crude product was then recrystallised with minimal hot EtOAc and hexane until the clouding point was reached, yielding the solid white product (2.54g, 50%).

^{1}H NMR (CDCl3) δ = 7.79 – 7.41 (m, 9H), 4.58 (s, 2H). ESI-MS *m/z:* cal. for $[M+H]^+$ 280.0, found m/z = 280.0 $[M+Na]^+$.

5,6,11,12-Tetradehydrodibenzo[a,e]cyclooctene (3.6)[17]

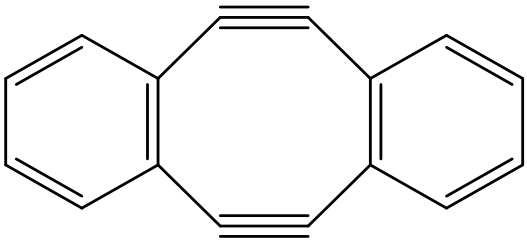

500 mg (1.93 mmol) of *ortho*-(phenylsulfonylmethyl)benzaldehyde was added to $ClPO(OEt)_2$ (0.33 ml, 2.3 mmol) and dry THF (50 ml) under an inert atmosphere. Lithium bis(trimethylsilyl)amide (LiHMDS, 1 M in THF, 3.9 ml, 3.9 mmol) was added at -78ºC. The reaction mixture was stirred at -78ºC for 30 minutes, then at room

temperature for 1.5 hours. Lithium diisopropylamide (LDA, 1 M, in THF / hexane, 9.6 ml, 9.6 mmol) was added dropwise at -78°C. The reaction mixture was stirred at -78°C for two hours and then quenched with aqueous NH_4Cl (100 ml, 1 M). The reaction mixture was worked up with H_2O (1 x 100 ml) and EtOAc (2 x 200 ml). The organic layers were combined and the solvent removed in vacuo to yield 870 mg of crude product. The product was purified by column chromatography (DCM:hexane 2:3) to yield 45 mg of pure product as a yellow solid (0.23 mmol, 11%).

^{1}H NMR ($CDCl_3$) = 6.92-6.95 (m, 4H), 6.71-6.77 (m, 4H). ESI-MS (MeCN) *m/z* cal. for $[2M+H]^+$ 401.3, found 401.3.

Reaction of 3.1 with diyne 3.6 to give complex 3.7 – [N1, N3][16]

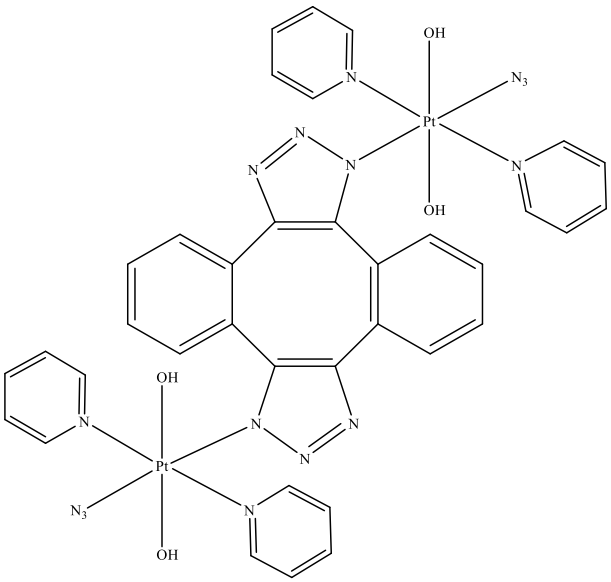

Diyne **3.6** (5,6,11,12-Tetradehydrodibenzo[a,e]cyclooctene) (60 mg, 0.3 mmol, 0.4 eq) was added to *trans,trans,trans*-$[Pt(N_3)_2(OH)_2(py)_2]$ (400 mg, 0.84 mmol) in MeCN (250 ml) and the reaction mixture stirred at room temperature for 48 h. The resulting yellow solution was concentrated, filtered and purified by HPLC (neutral condition, HPLC method 2, Xbridge column), the product **3.7** eluting as a single species at t_R =

4.01 min. The mixture of isomers of complex **3.7** was reconsituted in MeCN; crystals of **3.7 – [N1, N3]** formed on standing at room temperature (24 mg, 6 %).

^{1}H NMR (500 MHz, d_3-MeCN) δ: 8.64 (dd, 8H, $^{3}J_{HPt}$ = 27.5, $^{3}J_{HH}$ = 6.2) 7.91 (dd, 4H, $^{3}J_{HH}$ = 7.3, $^{3}J_{HH}$ = 7.3), 7.45 (d, 2H, $^{3}J_{HH}$ = 5.8), 7.41(dd, 8H, $^{3}J_{HH}$ = 6.7, $^{3}J_{HH}$ = 6.7), 7.39 (t, 2H, $^{3}J_{HH}$ = 8.3), 7.03 (t, 2H, $^{3}J_{HH}$ = 7.5, 1H), 5.90 (d, 2H, $^{3}J_{HH}$ = 7.8).

^{13}C NMR (126 MHz, d_3-MeCN) δ: 150.1, 147.3 (q), 142.9 (C_p), 141.0 (q), 134.3 (q), 131.5, (q), 130.8,130.7, 130.2, 128.9, 126.9 ($^{4}J_{13C\text{-}195Pt}$ = 27.3). ^{195}Pt NMR (107 MHz) δ: 723 in d_3-MeCN, 886 in D_2O. HRMS(*m/z*) *m/z* cal. for $[M+H]^+$ 1143.2139, found 1143.2123 $[M+H]^+$.

The double click lanthanide-platinum complex 3.8

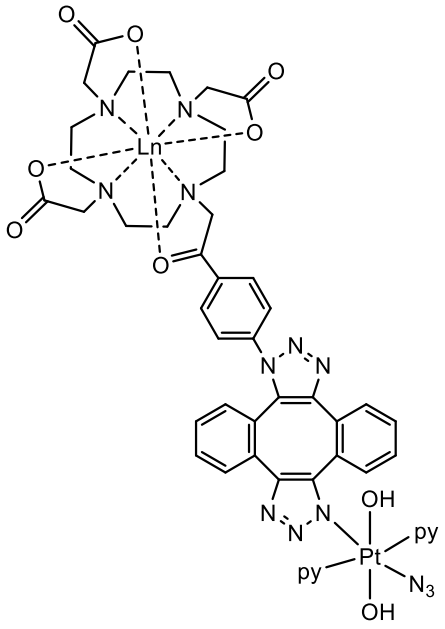

Ln DO3A-azidophenyl (75 mg, 0.11 mmol) and *trans,trans,trans*-[Pt $(N_3)_2(py)_2$] (52 mg 0.11 mmol)were dissolved in a mixture of 50ml H_2O and 50 ml MeCN, stirred for 20 min. A solution of Sondheimer diyne (22 mg, 0.11 mmol) in 10 ml MeCN was added dropwise over a period of 15 min. Stirred at RT for 48 h. Solvent was removed under reduced pressure, the resulting yellow solid was purified by HPLC (neutral

condition, HPLC method 2, Xbridge column) and 20 mg of product was isolated as a yellow solid.

(Ln: Eu) ^{1}H-NMR (400 MHz; D_2O) δ: 35.9, 28.1, 24.4, 23.7, 22.7, 11.2, 8.4, 8.1, 6.4, -1.6, -2.4, -2.8, -5.1, -8.2, -10.8, -12.8, -16.4, -18.6. Only resolved peaks outside 0 to 5 ppm are reported**.** HRMS found *m/z* 1324.2542 for $[M+H]^+$.

(Ln: Yb) ^{1}H-NMR (400 MHz; D_2O) δ: 130.1, 99.5, 92.1, 86.7, 49.7, 38.3, 24.0, -43.2, -49.5, -57.8, -59.6, -61.8 -65.6, -76.8. ^{195}Pt-NMR (500 MHz; D2O) δ: 911 HRMS *m/z* cal. for $[M + H]^+$ 1345.2713, found1345.2711.

Methyl 5-(2-bromoacetyl)-2-hydroxybenzoate (4.1)[18]

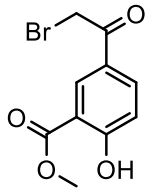

To a stirred solution of methyl 5-acetylsalicylate (1.0 g, 5.1 mmol) in $CHCl_3$/EtOAc (40 mL) was added copper (II) bromide (2.384 g, 10.8 mmol). The reaction mixture was gently refluxed at 45 °C. The progress of the reaction was monitored by TLC. After completion of the reaction, the reaction mixture was filtered and water (50 mL) and EtOAc (40 mL) were added to the reaction mixture. EtOAc layer was separated and aqueous layer was re-extracted with EtOAc (20 mL x 2). The EtOAc fractions were combined, dried over anhydrous $MgSO_4$, filtered, and the supernatant concentrated under reduced pressure to afford the crude 5-bromoacetyl-2-hydroxybenzoic acid methyl ester as a yellowish white solid. Crude product was recrystallized using CH_2Cl_2 and hexane. (1.131g, 82%) ^{1}H NMR (400MHz, $CDCl_3$) δ: 11.33 (s, 1H), 8.52 (d, 1H), 8.11(dd,1H), 7.07(d, 1H), 4.40(s, 2H), 4.01 (s, 3H) ppm**.** ^{13}C NMR (126 MHz; $CDCl_3$)

δ: 189.4, 170.0, 166.0, 136.2, 132.3, 125.7, 118.6, 112.5, 53.0, 30.4. ESI-MS (MeOH): *m/z* cal. for $[M + H]^+$ 272.9, found 272.9.

2,2',2''-(10-(2-(4-hydroxy-3-(methoxycarbonyl)phenyl)-2-oxoethyl)-1,4,7,10-tetraazacyclododecane-1,4,7-triyl)triacetic acid (4.3)[19]

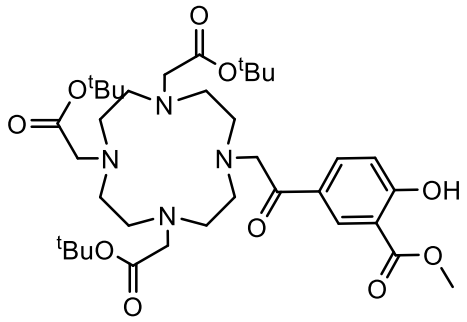

To a solution of **L1**(0.772g 1.5 mmol) (*1*) in dry acetonitrile (35 ml), potassium carbonate was added (0.415g, 3 mmol) followed by the addition of **benzoate** (0.408g, 1.5mmol). The suspension was left stirring at ambient temperature under an inert (N_2) atmosphere overnight. The potassium carbonate was removed by filtration and the solvent was removed from the filtrate by reduced pressure. The crude product was purified by silica gel column with MeOH and CH_2Cl_2. The resulting product was deprotected with TFA (6 mL) in DCM (12 mL) (0.452g, 56%). ^{1}H NMR (400MHz, D2O): 8.43 (d, 1H), 8.24(s, 1H), 8.07(dd, 1H), 3.98(s, 3H), 3.94-2.88 (br, 24H) ppm. ^{13}C NMR (126 MHz; $CDCl_3$) δ: 169.4, 165.9, 164.0, 135.0, 131.5, 117.9, 112.7, 52.9, 48.8, 57.1-46.8(br). ESI-MS (MeOH) *m/z m/z* cal. for $[M + H]^+$ 707.4, found 707.4.

2,2',2''-(10-(2-(4-hydroxy-3-(methoxycarbonyl)phenyl)-2-oxoethyl)-1,4,7,10 tetraazacyclododecane-1,4,7-triyl)triacetic acid (4.3)[19]

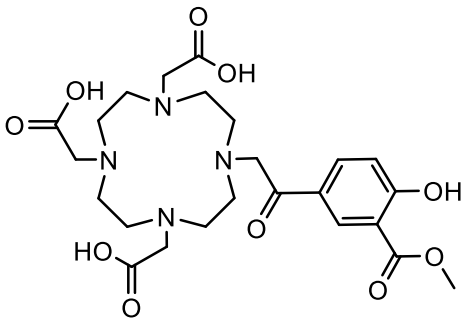

To a solution of compound **4.2** (0.5g 0.74 mmol) in DCM (5 ml), TFA (5 ml) was added dropwise. The reaction was stirred at RT for 24 h, the solvent were removed under reduced pressure. The resulting solid was treated with a small amount of methanol following addition of diethyl ether to triturate the target product as white powder. The solvent was decanted and the solid was dried under vacuum to afford target ligand in quantitative yield.

^{1}H NMR (500 MHz, D_2O) δ: 8.13 (d, *J* = 13.9 Hz, 3H), 7.85 (dd, *J* = 8.8, 2.3 Hz, 2H), 6.82 (d, *J* = 8.8 Hz, 2H), 4.31 (s, 1H), 3.82 (s, 5H), 3.75 (s, 6H), 3.69 (s, 4H), 3.37 (s, 12H), 3.23 (s, 1H). ^{13}C NMR (126 MHz, D_2O) δ: 173.76, 169.39, 165.92, 163.96, 134.95, 131.44, 126.17, 117.94, 112.69, 58.05, 55.74, 52.90, 51.18, 49.46, 48.82, 48.24. ESI-MS *m/z:* cal. for $[M + H]^+$ 539.2, found *m/z* 539.2 for $[M+H]^+$.

General procedure for the synthesis of salicylateDO3A lanthanide complexes (Ln.4.4)[19]

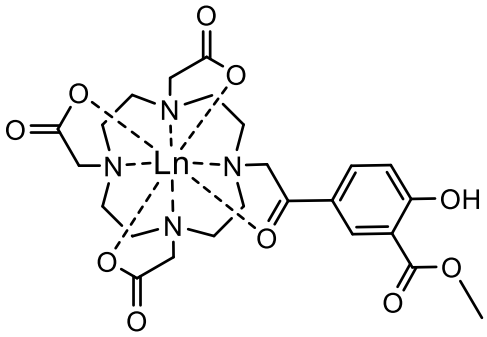

To a solution of the **4.3** in methanol the appropriate lanthanide triflate salt was added (1.2 eq.) and the solution was stirred at 60ºC for 30 min. The pH was adjusted to 4 by adding 1 M NaOH dropwise. The reaction was left to stir at 60ºC for 48 h. The methanol was removed under vacuum, leaving an oil that was dissolved in water. The pH of this solution was adjusted to 10 by addition of NaOH solution in order to precipitate excess lanthanide as its insoluble hydroxide, which was separate by centrifugation and the supernatant was filtered by a syringe filter. The aqueous solvent was removed under freeze dryer to obtain product.

(Ln: Lu) ^{1}H NMR (400 MHz, D_2O) δ: 8.11 (d, J = 13.9 Hz, 3H), 7.8 (dd, J = 8.8, 2.3 Hz, 2H), 6.80 (d, J = 8.8 Hz, 2H), 4.30-3.23 (m, 27H). ESI-MS *m/z:* cal. for $[M + H]^+$ 711.1, found 711.1.

(Ln: Eu) ^{1}H-NMR (400 MHz; D_2O) δ: 34.9, 27.1, 25.4, 24.7, 21.7, 10.3, 9.4, 9.1, 7.4, -1.7, -2.3, -2.9, -5.0, -8.0, -10.7, -11.8, -16.4, -18.6. Only resolved peaks outside 0 to 5 ppm are reported. ESI-MS *m/z:* cal. for $[M + H]^+$ 689.1, found 689.1.

General procedure for the synthesis of salicylic acidDO3A lanthanide complexes (4.5)

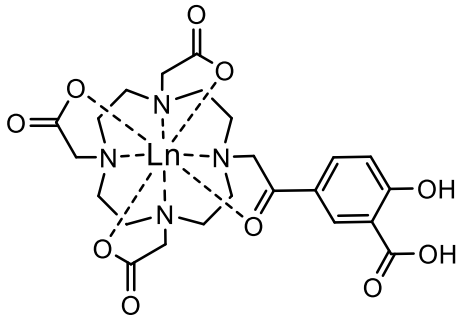

1.1 equivalents of $Ln(OTf)_3$ was added to a solution of **L2** (100 mg, 0.19 mmaol) in MeOH (3 mL). The solution was stirred at 60 ^oC for 30 min, the pH adjusted to 5 using 1M NaOH aqueous solution, and the resultant solution stirred at 60 ^oC for 2 d. The MeOH was removed under reduced pressure, leaving an oil that was dissolved in H_2O (3 mL), and the pH was adjusted to 10 by dropwise addition of aqueous NaOH (1M) to remove excess Ln^{3+} ions precipitates by centrifuge.

The resulting supernatant was stirred at 50^oC overnight. Formic acid (1M) was added to adjust pH to 7. The resulting product was purified by mass-directed HPLC and the solvent removed to give the title compound as an off-white powder.

(Ln: Lu) Yield: 48%. ^1H NMR (400MHz, D_2O) δ: 8.59 (d, 1H), 8.14 (dd, 1H), 6.95 (d, 1H), 3.91-2.37 (br, 24H)ppm, ESI-MS *m/z:* cal. for $[M + H]^+$ 697.1, found 697.1 for $[M+H]^+$.

(Ln: Eu) Yield: 32%. ^1H NMR(400MHz,D_2O) δ: 35.05, 28.17, 27.24, 26.27, 17.08, 12.40, 9.18, 8.65, 7.27, -1.76, -3.91, -4.35, -5.41, -7.76, -8.35, -10.01, -10.26, -11.38, -11.82, -12.16, -13.04, -13.38, -15.29, -16.16, -17.91ppm. Only resolved peaks outside the 0 to 5 ppm region are reported. ESI-MS *m/z:* cal. for $[M + H]^+$ 675.1, found *m/z* 675.1 for $[M+H]^+$. UV-Vis (H_2O): λ_{max} = 309 nm.

(Ln: Gd). Yield: 52%. ESI-MS *m/z:* cal. for $[M + H]^+$ 680.1, found *m/z* found *m/z* 680.1 for $[M+H]^+$, UV-Vis (H_2O): λ_{max} = 309 nm, ICP-MS Pt: Gd = 0:1

General procedure for the synthesis of salicylic acidDO3A lanthanide-platinum(II) complexes (4.6)

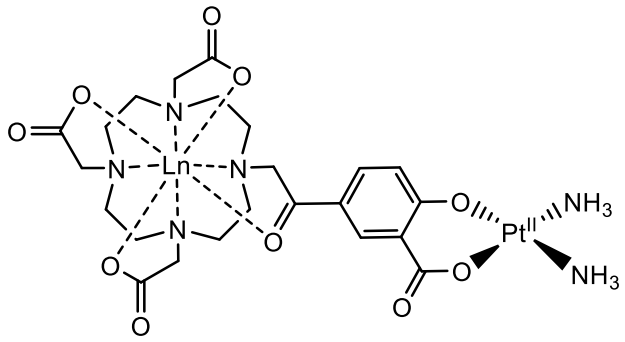

Complex Ln.4.5, 1 equivalent $PtI_2(NH_3)_2$ (73mg, 0.15 mmol) and 2 equivalent AgNO3 (51 mg, 0.30 mmol) were dissolved in 5 mL H_2O, saturated Na_2CO_3 solution was added to adjust pH to 9, stirred at room temperature overnight. The resulting grey precipitates were removed by centrifuge and the crude product was purified by HPLC in acidic condition (acidic condition, HPLC method 3, Xbridge column).

(Ln: Lu). Yield: 23%. ^{1}H NMR(400MHz,D_2O) δ: 8.78 (d, 1H), 7.96 (dd, 1H), 6.84 (d, 1H), 4.28-4.19 (s, 3H), 4.18-4.08 (s, 3H) 3.71-2.35 (br, 24H)ppm, ^{13}C NMR(500MHz,D_2O): 215.31, 180.76, 169.36, 166.01, 164.86, 139.43, 133.46, 132.67, 122.82, 120.93, 118.35, 65.64, 55.31, 46.42, 36.82, 31.30, 30.22, 8.09 ppm. ^{195}Pt NMR (500 MHz, D_2O): -1608 ppm. HRMS (MeOH/D_2O) found *m/z* 462.57374 for $[M+2H]^{++}$.

(Ln: Eu). Yield: 18%. ^{1}H NMR(400MHz,D_2O): 35.42, 33.63, 30.02, 29.14, 28.33, 13.81-12.29(br), 8.08, 6.97, -1.59, -3.46, -4.06, -4.60, -7.63, -9.28, -9.47, -11.47, -11.80, -12.26, -13.57, -13.89, -14.17, -15.84, -17.20ppm. Only resolved peaks outside the 0 to 5 ppm region are reported. HRMS (MeOH) *m/z* cal. for $[M+2H]^{++}$ 451.0631, found *m/z* 451.0625. UV-Vis (H2O): λ_{max} 345 nm.

(Ln: Gd). Yield: 26%. HRMS (MeOH) *m/z* cal. for $[M+2H]^{++}$ 453.5639, found *m/z* 453.5641 $[M + 2H]^{++}$. UV-Vis (H_2O): λ_{max} 345 nm. ICP-MS Pt: Gd = 0.97:1 (Std Dev: 0.07).

General procedure for the synthesis of salicylic acidDO3A lanthanide-platinum(IV) complexes (4.7)

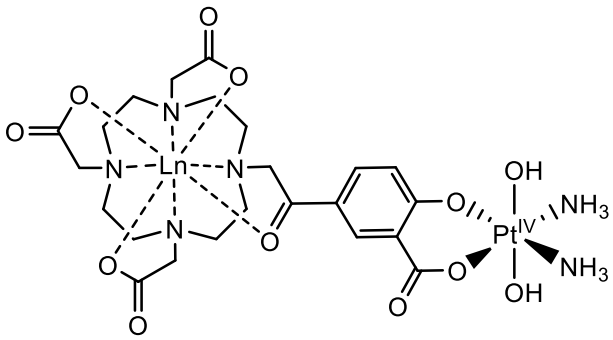

To a solution of 0.02 mmol **2** in 1ml H2O, 80µL H_2O_2(30%wt) solution was added dropwise. The solution was stirred at room temperature overnight.

3.Eu. Yield: 60%. **^{1}H NMR**(400MHz,D_2O): 35.08(s), 33.35(s), 29.10(s), 28.04(s), 27.18(s), 15.23-10.05(br), 8.86(s), 8.25(s), 7.41(s), -1.74(s), -3.77(s), -4.37(s), -4.59(s), -7.52(s), -8.98(s) -9.70(s), -10.69(s), -11.40(s), -11.74(s), -12.74(s), -13.14(s),-13.58(s), -14.41(s), -15.77(s), -17.43(s) ppm. Only resolved peaks outside the 0 to 5 ppm region are reported. **HRMS** (MeOH): *m/z* cal. for $[M+H]^+$ 935.1240 found 935.1234. UV-Vis (H2O): λ_{max} 330 nm.

3.Gd. Yield: 58%. **HRMS** (MeOH): *m/z* cal. for $[M+H]^+$ 942.1275, found 942.1274. UV-Vis (H2O): λ_{max} 325 nm. UV-Vis (H_2O): λ_{max} 325 nm, **ICP-MS** Pt: Gd = 1.07:1 (Std Dev: 0.15).

General procedure for the synthesis of salicylic acidDO3A lanthanide-platinum(IV) bis octanoic acid complexes (4)

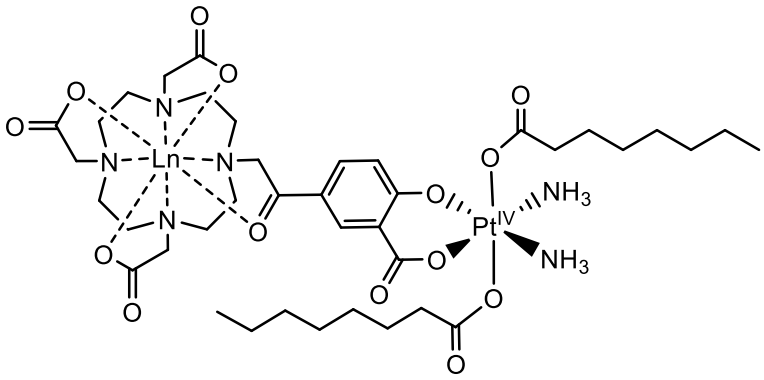

Figure S7. Compound **4.Ln**

3 (0.08 mmol) and pyridine (4 equiv.) was added to 3 ml acetone, a solution of n-octanoyl chloride (2.5 equivalent) in 2ml of acetone was added dropwise (over 15min). The reaction mixture was stirred overnight at room temperature. Solvent was reduced under reduced pressure and the crude product was purified by HPLC (acidic condition, HPLC method 4, Xbridge column).

HRMS (MeOH): *m/z* cal. for $[M+H]^+$ 1192.3360, found 1192.3359. UV-Vis (H2O): λ_{max} 324 nm. **ICP-MS** Pt: Gd = 1.08:1 (Std Dev: 0.07).

ICP-MS

Table 6.1*. The Gd:Pt ratio in complexes* ***Gd.(4.5-4.8)*** *determined over 5 replicates (R1 - R5).*

Complex / Replicate	R1	R2	R3	R4	R5
1.Gd Gd:Pt	1 : 0	1 : 0	1 : 0	1 : 0	1 : 0
2.Gd Gd:Pt	1.2 :1	1 : 1	1 : 1	1 : 1	1 : 1
3.Gd Gd:Pt	1 : 1	1 : 1	1 : 1	1 : 1	0.8 : 1
4.Gd Gd:Pt	1 : 1	0.9 : 1	0.9 : 1	1 : 1	0.9 : 1

Cell concentration: $4.5e^4$/ml for ICP-MS sample.

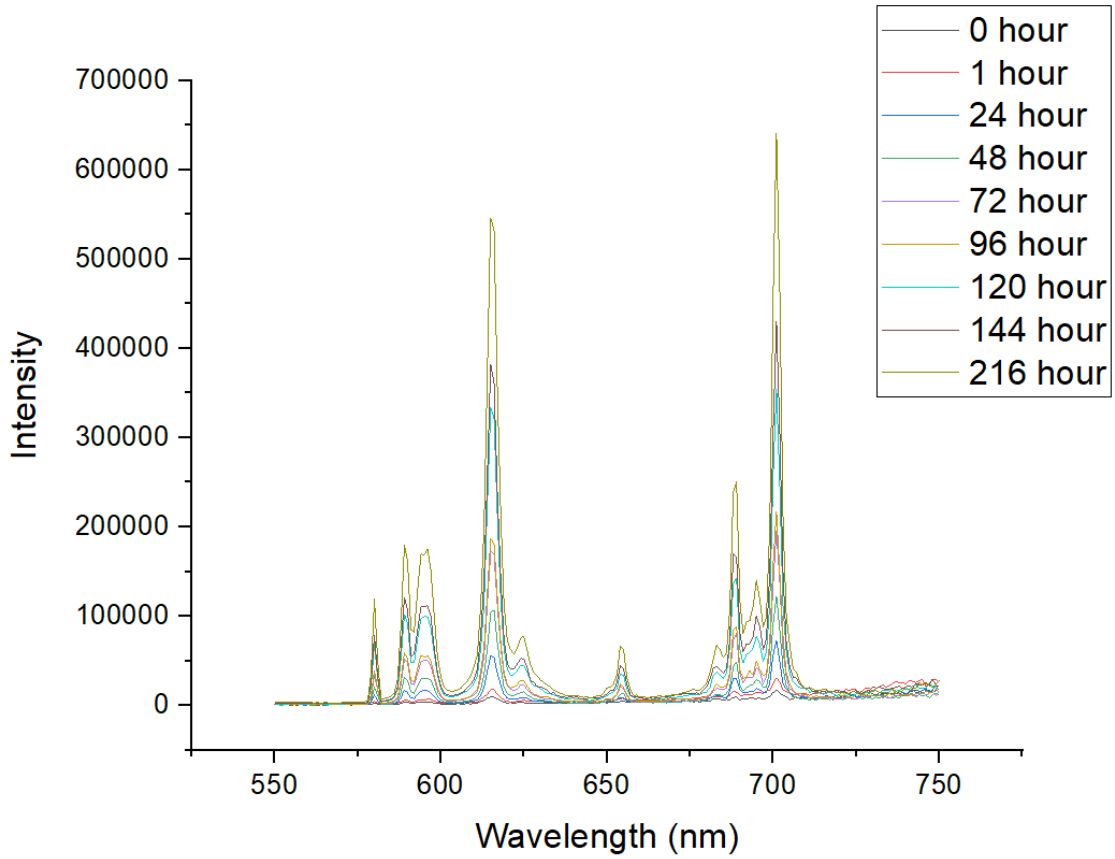

***Figure 6.1**: Luminescence spectrum of **Eu.4.7** with 20eq. AA; λ_{ex} = 330 nm, emission slit = 1 nm.*

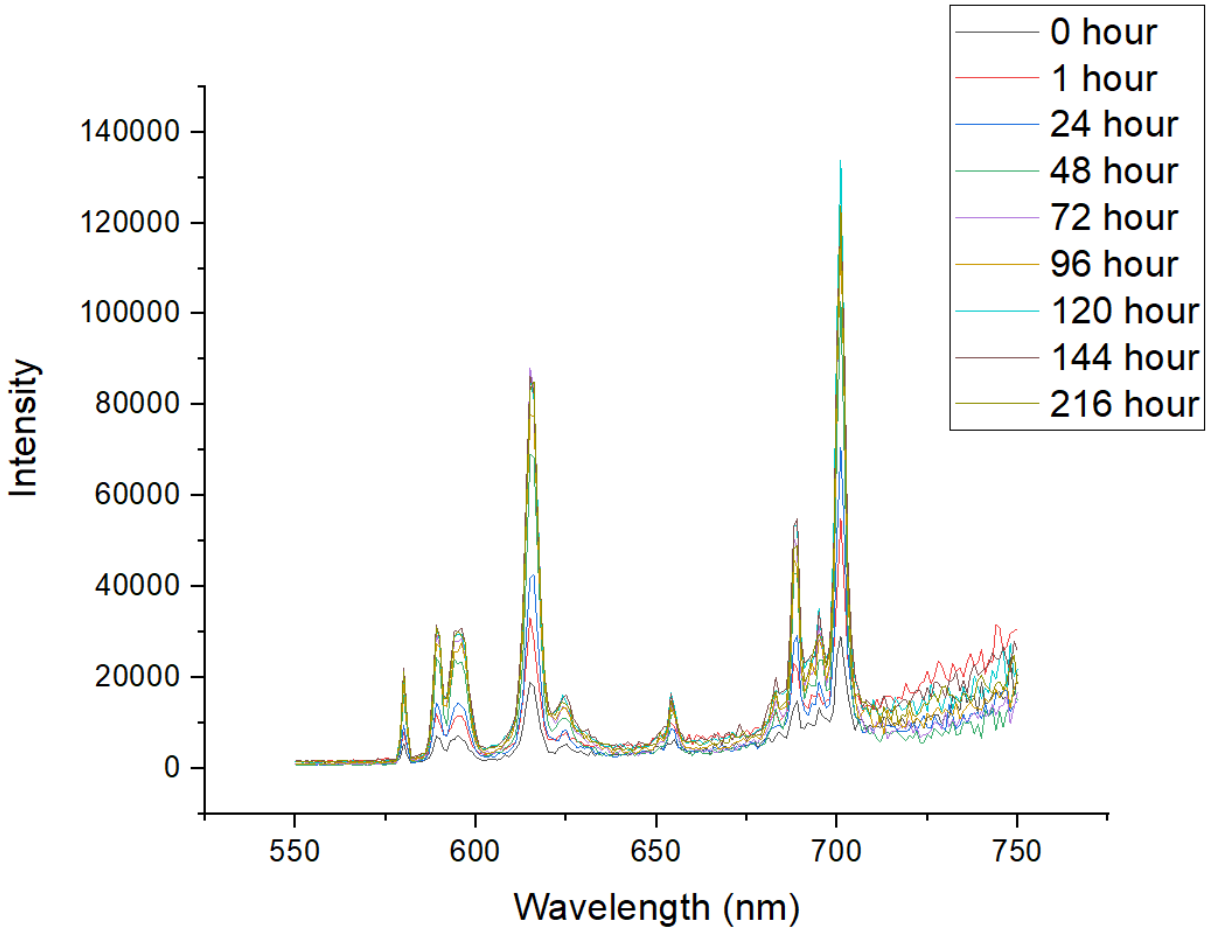

***Figure 6.2**: Luminescence spectrum of **Eu-salicylicDO3A-Pt-1OA** with 20eq. AA; λ_{ex} = 330 nm, emission slit = 1 nm.*

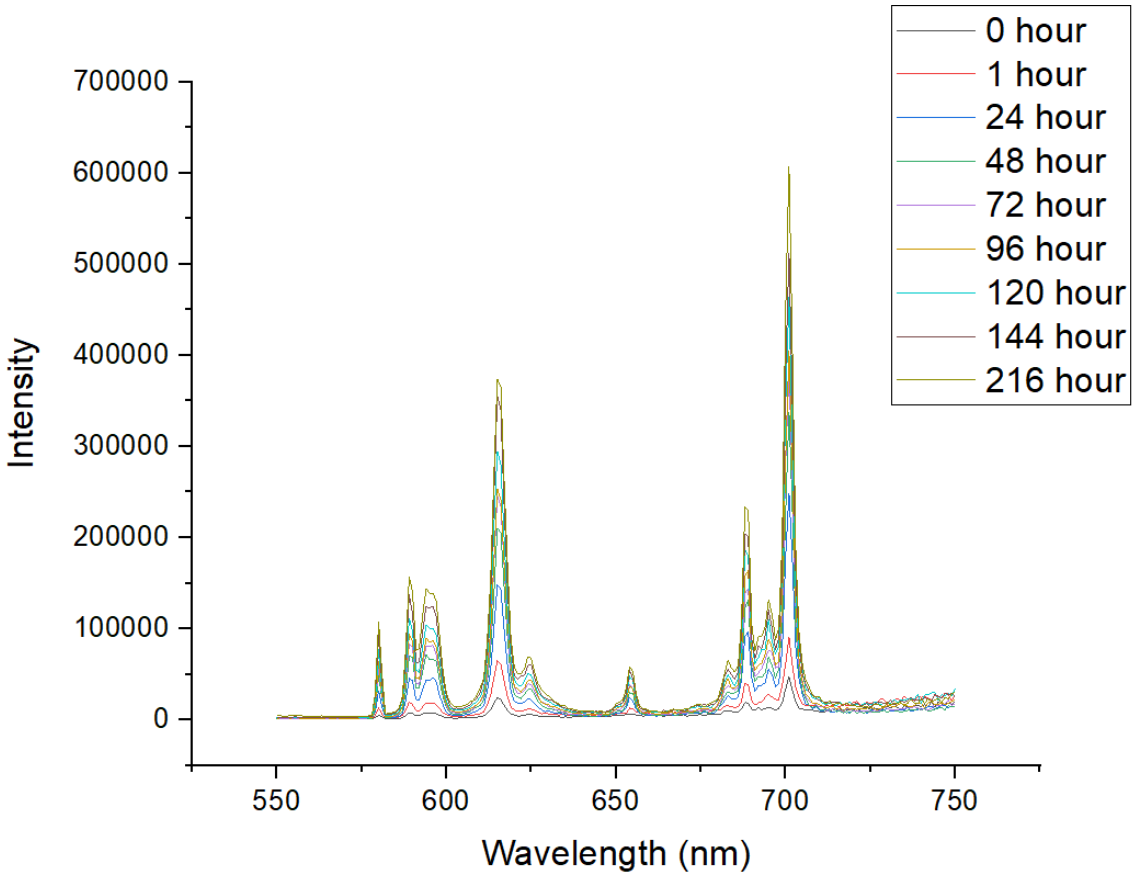

***Figure 6.3**: Luminescence spectrum of **Eu.4.8** with 20eq. AA; λ_{ex} = 330 nm, emission slit = 1 nm.*

References

1 G. Karunanithy, R. J. Wheeler, L. R. Tear, N. J. Farrer, S. Faulkner and A. J. Baldwin, *J. Magn. Reson.*, 2019, **302**, 1–13.

2 L. Palatinus and G. Chapuis, *J. Appl. Crystallogr.*, 2007, **40**, 786–790.

3 P. W. Betteridge, J. R. Carruthers, R. I. Cooper, K. Prout and D. J. Watkin, *J. Appl. Crystallogr.*, 2003, **36**, 1487–1487.

4 R. I. Cooper, A. L. Thompson and D. J. Watkin, *J. Appl. Crystallogr.*, 2010, **43**, 1100–1107.

5 P. Parois, R. I. Cooper and A. L. Thompson, *Chem. Cent. J.*, 2015, **9**, 1–14.

6 A. Dadabhoy, S. Faulkner and P. G. Sammes, *J. Chem. Soc. Perkin Trans. 2*, 2002, 348–357.

7 P. B. Sarode, S. P. Bahekar and H. S. Chandak, *Synlett*, 2016, **27**, 2681–2684.

8 G. Bottaro, F. Rizzo, M. Cavazzini, L. Armelao and S. Quici, *Chem. - A Eur. J.*, 2014, **20**, 4598–4607.

9 M. Tropiano and S. Faulkner, *Chem. Commun.*, 2014, **50**, 4696–4698.

10 B. P. Sullivan, D. J. Salmon and T. J. Meyer, *Inorg. Chem.*, 1978, **17**, 3334–3341.

11 M. Jauregui, W. S. Perry, C. Allain, L. R. Vidler, M. C. Willis, A. M. Kenwright, J. S. Snaith, G. J. Stasiuk, M. P. Lowe and S. Faulkner, *J. Chem. Soc. Dalt. Trans.*, 2009, 6283–6285.

12 M. Claros, F. Ungeheuer, F. Franco, V. Martin-Diaconescu, A. Casitas and J. Lloret-Fillol, *Angew. Chemie*, 2019, **131**, 4923–4928.

13 M. Tropiano, C. J. Record, E. Morris, H. S. Rai, C. Allain and S. Faulkner, *Organometallics*, 2012, **31**, 5673–5676.

14 N. Forte, I. Benni, K. Karu, V. Chudasama and J. R. Baker, *Chem. Sci.*, 2019, **10**, 10919–10924.

15 N. J. Farrer, J. A. Woods, L. Salassa, Y. Zhao, K. S. Robinson, G. Clarkson, F. S. MacKay and P. J. Sadler, *Angew. Chemie - Int. Ed.*, 2010, **49**, 8905–8908.

16 N. J. Farrer, G. Sharma, R. Sayers, E. Shaili and P. J. Sadler, *Dalt. Trans.*, 2018, **47**, 10553–10560.

17 I. Kii, A. Shiraishi, T. Hiramatsu, T. Matsushita, H. Uekusa, S. Yoshida, M. Yamamoto, A. Kudo, M. Hagiwara and T. Hosoya, *Org. Biomol. Chem.*, 2010, **8**, 4051–4055.

18 S. N. Senadheera, T. Zhang, C. E. Groer and M. L. Forrest, 2018, 452–456.

19 J. D. Routledge, X. Zhang, M. Connolly, M. Tropiano, O. A. Blackburn, A. M. Kenwright, P. D. Beer, S. Aldridge and S. Faulkner, *Angew. Chemie - Int. Ed.*, 2017, **56**, 7783–7786.

Appendix A: X-ray crystallographic data

A.1 Complex 3.3b

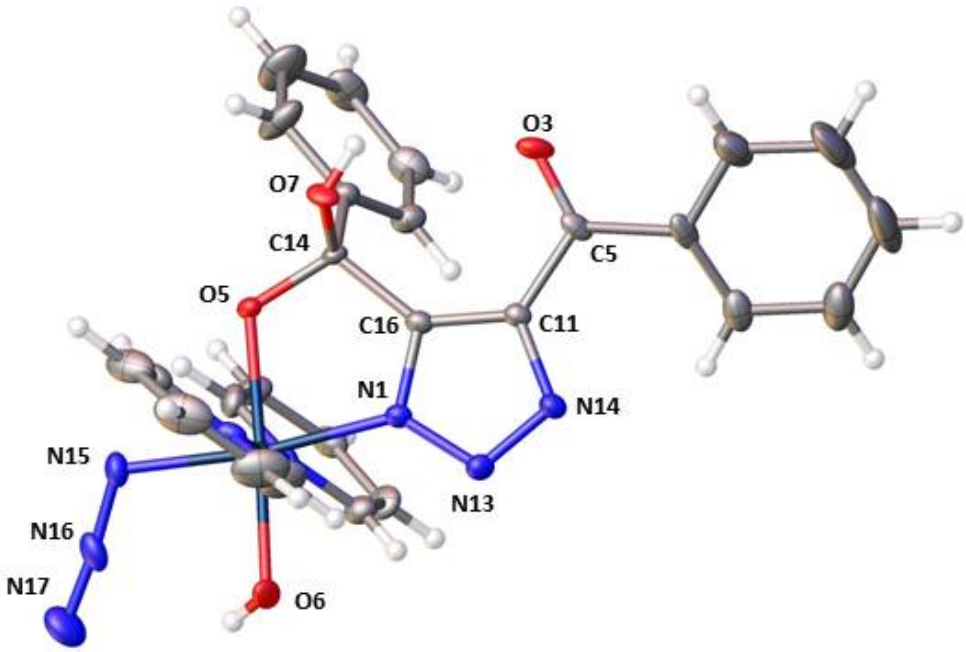

Figure A.1: *X-Ray carystallographic structure of* ***3.3b*** *with thermal ellipsoids display at 50% probability.*

Crystal data and structure refinement for complex **3.3b**	
Identification code	18KE08-1
Empirical formula	$C_{31}H_{32}N_8O_5Pt$
Formula weight	791.73
Temperature/K	100
Crystal system	orthorhombic
Space group	Pbca
a/Å	15.5699(6)
b/Å	13.6495(5)
c/Å	28.6384(12)
α/°	90

β/°	90
γ/°	90
Volume/Å^3	6086.3(4)
Z	8
ρ_{calc}g/cm^3	1.728
μ/mm^{-1}	4.666
F(000)	3136.0
Crystal size/mm^3	0.651 × 0.321 × 0.155
Radiation	MoKα (λ = 0.71073)
2Θ range for data collection/°	6.94 to 58.392
Index ranges	-19 ≤ h ≤ 19, -9 ≤ k ≤ 17, -31 ≤ l ≤ 39
Reflections collected	20849
Independent reflections	6965 [R_{int} = 0.0447, R_{sigma} = 0.0511]
Data/restraints/parameters	6965/0/408
Goodness-of-fit on F^2	1.116
Final R indexes [I>=2σ (I)]	R_1 = 0.0414, wR_2 = 0.0735
Final R indexes [all data]	R_1 = 0.0537, wR_2 = 0.0779
Largest diff. peak/hole / e Å^{-3}	1.69/-1.80

A.2 Complex 3.5

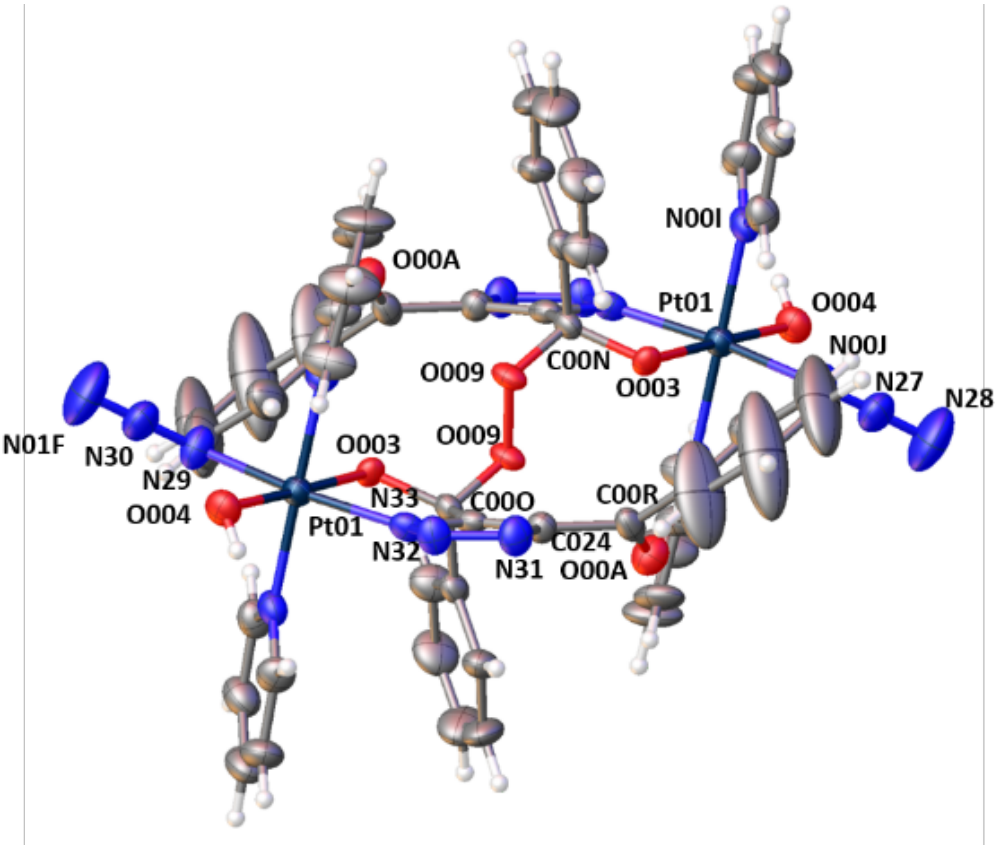

***Figure A.2**: X-Ray crystallographic OLEX2 structure of the peroxide dimer **3.5** with thermal ellipsoids displayed at 50 %.*

Crystal data and structure refinement for complex **3.5**	
Identification code	18KE09_2
Empirical formula	$C_{54.5}H_{46.5}N_{17.5}O_8Pt_2$
Formula weight	1464.77
Temperature/K	298
Crystal system	triclinic
Space group	P-1
a/Å	9.8284(3)
b/Å	14.7485(8)
c/Å	20.9424(8)
α/°	80.340(4)

β/°	83.445(3)
γ/°	84.553(4)
Volume/Å^3	2964.2(2)
Z	2
ρ_{calc}g/cm^3	1.641
μ/mm^{-1}	4.781
F(000)	1432.0
Crystal size/mm^3	0.808 × 0.1 × 0.05
Radiation	MoKα (λ = 0.71073)
2Θ range for data collection/°	6.744 to 52
Index ranges	-12 ≤ h ≤ 10, -18 ≤ k ≤ 17, -21 ≤ l ≤ 25
Reflections collected	19786
Independent reflections	11536 [R_{int} = 0.0427, R_{sigma} = 0.0866]
Data/restraints/parameters	11536/24/775
Goodness-of-fit on F^2	1.049
Final R indexes [I>=2σ (I)]	R_1 = 0.0462, wR_2 = 0.0949
Final R indexes [all data]	R_1 = 0.0749, wR_2 = 0.1098
Largest diff. peak/hole / e Å^{-3}	1.86/-1.61

A.3 Complex 3.7

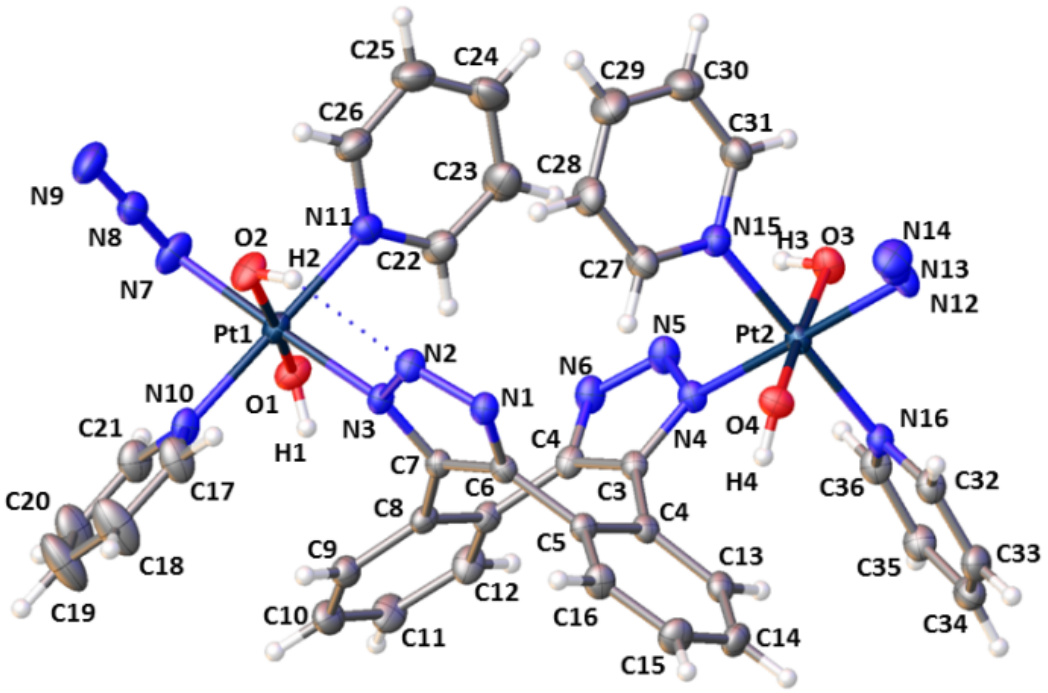

Figure A.3: *X-ray crystallographic structure of* ***3.7-[N1, N3]*** *with thermal ellipsoids displayed at 50% probability.*

Crystal data and structure refinement for complex **3.7**	
Identification code	CCDC 1885195
Empirical formula	$C_{42}H_{41}N_{19}O_4Pt_2$
Formula weight	1266.12
Temperature/K	150(2)
Crystal system	monoclinic
Space group	$P2_1/c$
a/Å	13.23900(10)
b/Å	16.72960(10)
c/Å	20.55360(10)
α/°	90
β/°	90.3440(10)
γ/°	90
Volume/Å^3	4552.20(5)
Z	4
ρ_{calc}g/cm^3	1.847
μ/mm^{-1}	11.872
F(000)	2456.0

Crystal size/mm^3	0.080 × 0.080 × 0.040
Radiation	CuKα (λ = 1.54184)
2Θ range for data collection/°	8.518 to 152.272
Index ranges	-16 ≤ h ≤ 16, -20 ≤ k ≤ 11, -25 ≤ l ≤ 25
Reflections collected	37582
Independent reflections	9459 [R_{int} = 0.0280, R_{sigma} = 0.0227]
Data/restraints/parameters	9459/9/622
Goodness-of-fit on F^2	1.130
Final R indexes [I>=2σ (I)]	R_1 = 0.0244, wR_2 = 0.0614
Final R indexes [all data]	R_1 = 0.0260, wR_2 = 0.0626
Largest diff. peak/hole / e Å^{-3}	2.08/-0.93

A.4 Complex Eu.4.6

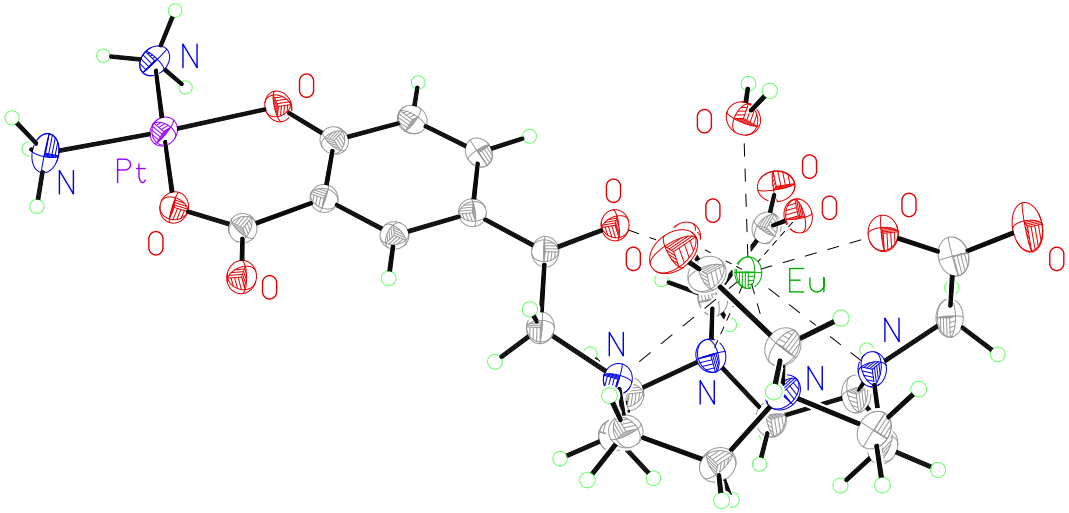

Figrue A.4: *Molecular structure of **Eu.4** from single crystal X-ray diffraction studies; thermal ellipsoids are drawn at 20% probability.*

Crystal data and structure refinement for complex **Eu.4.6**	
Empirical formula	$C_{23}H_{60}EuN_6O_{23.5}Pt$
Formula weight	1143.81
Temperature	150 K
Wavelength	1.54184 Å
Crystal system	Orthorhombic
Space group	P b c n
Unit cell dimensions	a = 22.1561(1) Å α= 90°. b = 18.9237(1) Å β= 90°. c = 19.3441(1) Å γ = 90°.

Volume	8110.50(7) $Å^3$
Z	8
Density (calculated)	1.873 Mg/m^3
Absorption coefficient	18.119 mm^{-1}
F(000)	4552
Crystal size	0.21 x 0.15 x 0.14 mm^3
Theta range for data collection	3.829 to 76.242°.
Index ranges	-27<=h<=27, -23<=k<=20, -23<=l<=23
Reflections collected	47882
Independent reflections	8432 [R(int) = 0.036]
Completeness to theta = 74.717°	99.7 %
Absorption correction	Sphere
Max. and min. transmission	0.04823 and 0.00242
Refinement method	Full-matrix least-squares on F^2
Data / restraints / parameters	8403 / 0 / 517
Goodness-of-fit on F2	0.9995
Final R indices [I>2sigma(I)]	R1 = 0.0853, wR2 = 0.2000
R indices (all data)	R1 = 0.0869, wR2 = 0.2057
Largest diff. peak and hole	4.76 and -1.11 $e.Å^{-3}$

Dalton Transactions

ROYAL SOCIETY OF CHEMISTRY

PAPER

View Article Online
View Journal | View Issue

Cite this: *Dalton Trans.*, 2021, **50**, 8761

Cell-permeable lanthanide–platinum(IV) anti-cancer prodrugs†

Kezi Yao,[a] Gogulan Karunanithy, ‡[a] Alison Howarth,§[a] Philip Holdship,[b] Amber L. Thompson,[a] Kirsten E. Christensen,[a] Andrew J. Baldwin,[a] Stephen Faulkner[a] and Nicola J. Farrer *[a]

Received 29th March 2021,
Accepted 28th May 2021

DOI: 10.1039/d1dt01688a

rsc.li/dalton

Platinum compounds are a vital part of our anti-cancer arsenal, and determining the location and speciation of platinum compounds is crucial. We have synthesised a lanthanide complex bearing a salicylic group (Ln = Gd, Eu) which demonstrates excellent cellular accumulation and minimal cytotoxicity. Derivatisation enabled access to bimetallic lanthanide–platinum(II) and lanthanide–platinum(IV) complexes. Luminescence from the europium–platinum(IV) system was quenched, and reduction to platinum(II) with ascorbic acid resulted in a "switch-on" luminescence enhancement. We used diffusion-based ^{1}H NMR spectroscopic methods to quantify cellular accumulation. The gadolinium–platinum(II) and gadolinium–platinum(IV) complexes demonstrated appreciable cytotoxicity. A longer delay following incubation before cytotoxicity was observed for the gadolinium–platinum(IV) compared to the gadolinium–platinum(II) complex. Functionalisation with octanoate ligands resulted in enhanced cellular accumulation and an even greater latency in cytotoxicity.

Introduction

Approximately 50% of chemotherapy regimens worldwide include a platinum-based drug[1] and platinum(II) complexes such as cisplatin, carboplatin and oxaliplatin are well-established, highly effective anti-cancer agents. These complexes are highly reactive *in vivo* and the side-effects of treatment caused by off-target reactivity are often debilitating.[2,3] Platinum(IV) complexes can potentially reduce the side-effects of treatment,[4] as they typically require reduction to platinum(II) species before exerting their anti-cancer effect.[5] Their cellular uptake and rate of reduction inside cells depends strongly on the coordinated ligands.[6] For example, lipophilic ligands such as octanoate (OA) enable $[Pt^{IV}(NH_3)_2(Cl_2)(OA)_2]$ to exhibit a 106-fold enhancement in cellular accumulation in ovarian (A2780) cancer cells in comparison to its synthetic precursor, *cis*,*cis*,*trans*-$[Pt^{IV}(NH_3)_2(Cl_2)(OH)_2]$.[7] The additional cellular uptake for the octanoate complex results in an increased cytotoxicity by two orders of magnitude, compared to cisplatin.[8]

Lanthanide complexes have played a central role in the development of magnetic resonance imaging (MRI) agents for over thirty years.[9–11] Gadolinium complexes with octadentate ligands have favourable relaxation properties that have enabled them to become a key tool in diagnostic imaging.[12] While initially employed for imaging vasculature,[13] through careful ligand design "smart" systems have been developed that can be targeted to particular tissue types, or that exhibit a response modulated by external biochemical stimuli.[14,15] To enable us to localise gadolinium compounds, we recently developed a diffusion-based ^{1}H NMR method that can be used to distinguish between intra- and extracellular pools of water, relying on the fact that water diffusion in intracellular fluids is defined by the boundaries of the cell.[16] Since the cell is much smaller than the voxel (volume pixel) in an MRI image, this means that intracellular fluid can be treated as a slow diffusing pool, whilst extra-cellular fluid is treated as a fast diffusing pool. The INDIANA (IN cell DIffusion Analysis) methodology allows these two pools and their properties to be quantitatively described, including relaxation rates.

Complexes which incorporate lanthanides such as europium also offer attractive luminescence properties. The general concept of generating "switch-on" luminescence following reduction of a platinum(IV) prodrug to platinum(II) is a highly promising strategy for tracking (sub)cellular distribution and reduction of platinum(IV) prodrugs. Previously

[a]*Chemistry Research Laboratory, University of Oxford, Mansfield Road, OX1 3TA, UK. E-mail: Nicola.Farrer@chem.ox.ac.uk*
[b]*Department of Earth Sciences, University of Oxford, OX1 3AN, UK*

†Electronic supplementary information (ESI) available: Experimental details, material characterisation data and crystallographic details. CCDC 1960280. For ESI and crystallographic data in CIF or other electronic format see DOI: 10.1039/d1dt01688a

‡Current address: Institute of Structural and Molecular Biology, Division of Biosciences, University College London, London, WC1E 6BT, UK.
§Current address: Centre for Medicines Discovery, Nuffield Department of Medicine, University of Oxford, Oxford OX3 7DQ, UK.

reported strategies include axial platinum(IV) coordination of quenched fluorophores such as fluorescein[17] and selective fluorescence reporting from organic probes following reaction with specific platinum(II) reduction fragments.[18] Lanthanides provide a significant advantage over purely organic fluorophores, by producing a highly distinctive emission profile when excited, from which background autofluorescence can also be effectively removed through time-gating.[19]

In order to develop redox-active platinum anti-cancer agents, whilst simultaneously providing a means to accurately track their distribution in the body, two gadolinium(III)–Pt(IV) complexes derived from carboplatin and cisplatin have been recently developed.[20] Moreover, a series of platinum(IV) prodrugs conjugated to Gd-texaphyrin have shown greater stability towards hydrolysis and nucleophilic attack compared to their platinum(II) analogues, while the Gd-texaphyrin fragment presented the ability to activate the platinum(IV) prodrug species through redox cycling.[21]

Microscopy on luminescent analogues can provide insights in isolated cells or tissue slices,[22,23] but does not translate readily to whole body imaging. Similarly, MRI resolution does not approach the diameter of a single cell, meaning that it is difficult to assess distribution of a contrast agent between intra- and extra-cellular fluid. In this manuscript, we address the issue of how MR methods can be used to define cellular uptake by exploiting the constraints on diffusion imposed by intracellular localization of a bimetallic lanthanide–platinum complex.

Drawing these concepts together, we have synthesized and characterized a dual-purpose lanthanide(III)–platinum(IV) system which includes a sensitizing salicylic group. This can enable both *in cellulo* tracking in preclinical development (Ln = Eu, Gd), and *in vivo* tracking (Ln = Gd), through simple modulation of the lanthanide, whilst retaining very similar pharmacological properties regardless of the choice of lanthanide. This first reported example of a Eu(III)–Pt(IV) complex that has the potential to provide highly diagnostic real-time.

We established the minimal cytotoxicity of the gadolinium salicylic acid precursor, and the contrasting cytotoxicity of the Gd(III)–Pt systems, and correlated accumulation with the effect that oxidation state and choice of axial ligand of the platinum group has on the cytotoxicity of these complexes. Information on the reductive activation of a Pt(IV) prodrug. Our established diffusion-based ^{1}H NMR method enabled us to determine the extent to which the new complexes **1–4** (Fig. 1) accumulated within cells.

Results and discussion

We have previously used phenacyl–DO3A derivatives to good effect, as kinetically stable building blocks for more complicated architectures.[24–26] The lanthanide complex (**1**) (Fig. 1) (where Ln = Gd, Eu) builds on this work, and was conceived as a system in which the lanthanide is bound in an octadentate binding site, while the pendent salicylic acid group can act as a ligand to a second metal centre – such as platinum – to give **2**. The synthesis of the ligands and complexes are summarized in Scheme 1. Triester (**L1**)[27] was reacted with methyl 5-bromoacetyl-2-hydroxybenzoate (**B**), to yield the protected pro-ligand, **L2**. Deprotection was accomplished by treating **L2** with TFA to give the unmasked pro-ligand, **L3**, which was reacted with the appropriate lanthanide trifluoromethane sulfonate to produce the desired Ln(III)–Pt(II) complex **1·Ln** (where Ln = Gd, Eu). Reaction of **1·Ln** with *cis*-$[Pt(NH_3)_2(OH_2)_2]^{2+}$ yielded the heterometallic complex **2·Ln**.[28] Oxidation of **2·Ln** with H_2O_2 produced the Ln(III)–Pt(IV) di-hydroxido complex **3·Ln**.[29] Reaction of **3·Ln** with octanoyl chloride afforded the Ln(III)–Pt(IV) dioctanoic acid conjugate, **4·Ln**.[8] All compounds were purified by LCMS, with characterisation data consistent with the proposed structures (see ESI†) and in accordance with previously reported Ln(III)–Pt(II) complexes.[30] The complexes were also characterized by ICP-MS to confirm the Ln : Pt ratio and ensure that complexation had occurred (Table S1†).

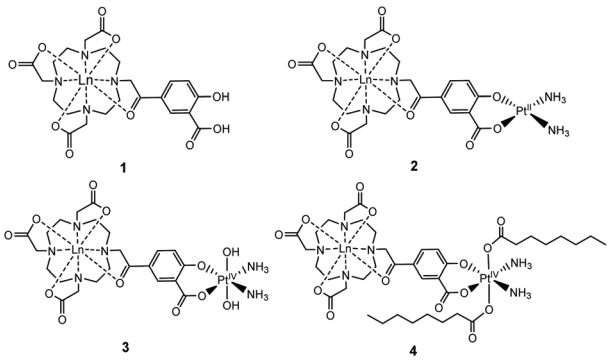

Fig. 1 Structures of the complexes **1–4** reported, where Ln = Gd, Eu.

Additionally, complex **2·Eu** was crystallised from aqueous solution at 4 °C and characterised by single crystal X-ray diffraction. The structure was solved by charge-flipping using 'Superflip',[31] and refined by full-matrix least squares on F^2 using CRYSTALS suite (Fig. 2).[32–34] The structure demonstrated a monocapped square antiprism (SAP) configuration of the Eu centre.

To the best of our knowledge, this is the first reported europium–platinum X-ray single crystal structure with a kinetically stable macrocyclic lanthanide complex; bond lengths and angles are essentially consistent with other previously reported Ln(III)–Pt(II) complexes.[35,36]

Complexes **1–4** were purified by HPLC with different retention times (see Fig. S13† for the HPLC traces of **(1–4)·Gd** complexes). The complexes were also characterised by mass spectroscopy and NMR spectroscopy. ^{195}Pt NMR spectroscopy of **2·Lu** revealed a single resonance at −1608 ppm (D_2O, Fig. S8†), while **3·Lu** gave a resonance at 1691 ppm (D_2O, Fig. S9†), which are consistent with Pt(II) and Pt(IV) oxidation states, respectively.[37] Whilst the Pt(II) species **2·Lu** was observed as a singlet, the Pt(IV) complex **3·Lu** was observed as a quintet, as a result of coupling to the two equivalent quadrupolar ($I = 1$) ^{14}N nuclei of the NH_3 ligands. The magnitude of the ^1J (^{195}Pt, ^{14}N)

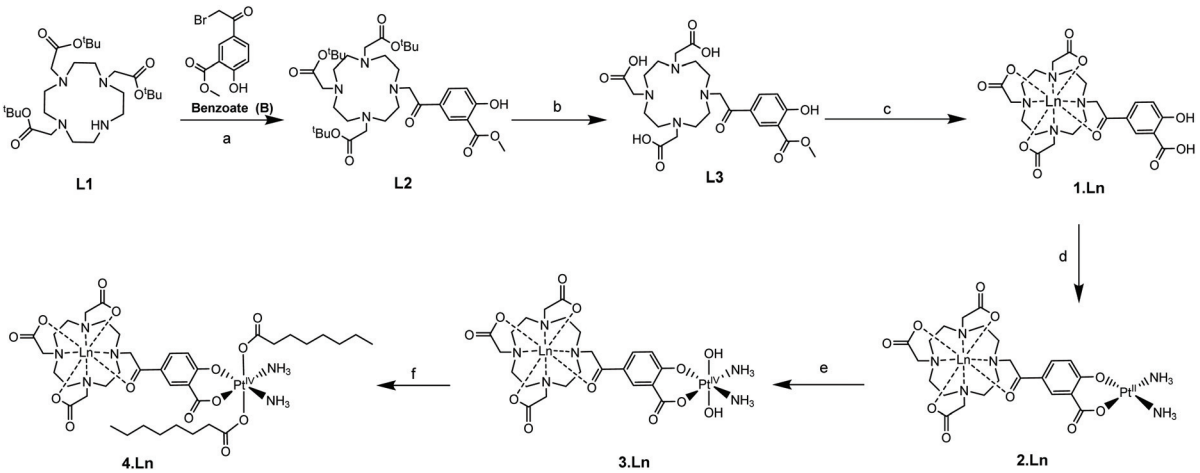

Scheme 1 Synthetic route to the complexes (Ln = Gd, Eu). Reagents and conditions: (a) K_2CO_3, MeCN, room temperature, 16 h; (b) TFA, CH_2Cl_2, 24 h; (c) $Ln(OTf)_3$, MeOH, 60 °C, 48 h; (d) $Pt(NH_3)_2I_2$, $AgNO_3$, H_2O_2, pH 10, room temperature, 24 h; (e) H_2O_2, H_2O, room temperature, 16 h; (f) octanoyl chloride, acetone, pyridine, room temperature, 16 h.

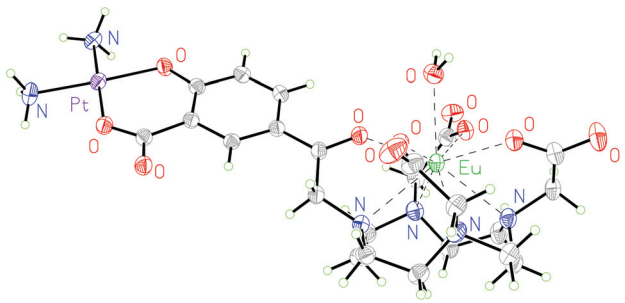

Fig. 2 Molecular structure of **2·Eu** from single crystal X-ray diffraction studies; thermal ellipsoids are drawn at 20% probability and water in the solvent sphere is omitted for clarity.

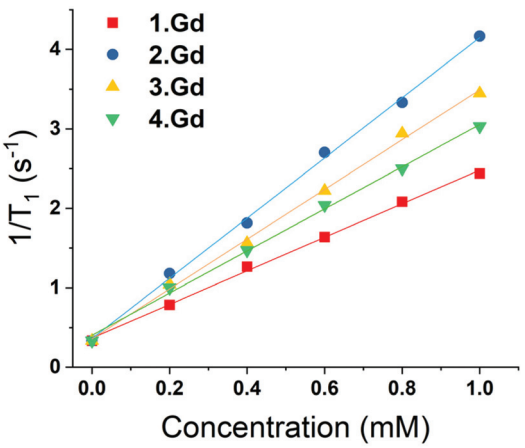

Fig. 3 Variation of $1/T_1$ with concentration of gadolinium for complexes **(1–4)·Gd** at different concentrations (at 25 °C, in DMEM, 14.1 T).

coupling constant (213 Hz) is consistent with other ^1J (^{14}N, ^{195}Pt) constants that we have previously observed, for example in the platinum(IV) species, *cis*,*cis*,*cis*-$[Pt(N_3)_2(OH)_2(NH_3)_2]$ (167 Hz).[38] The ^1H NMR spectra of the europium complexes (Fig. S10†) are consistent with those of other phenacyl–DO3A analogues, and show structures dominated by the square antiprismatic diastereoisomers of the complexes, in agreement with the molecular structure of **2·Eu** determined using single crystal X-ray diffraction. Measurement of the T_1 relaxation enhancements obtained with complexes **(1–4)·Gd** offers further insights into their solution state structure. The relaxivity of the complexes was determined by observing the variation of $1/T_1$ with complex concentration in media (DMEM) as shown in Fig. 3. In all cases, the resulting plots showed a linear response to concentration across a wide range, indicating that all complexes were essentially stable in solution, and that their properties are not changed by their local environment (since a change in speciation would be expected to result in curvature of the plots). All the complexes **(1–4)·Gd** exhibit relaxivities consistent with a single water molecule in their inner coordination sphere (Table 1).

Table 1 Relaxivities of complexes **1·Gd–4·Gd**

Compound	Relaxivity (s^{-1} mM^{-1})	(±)
1·Gd	2.21	0.04
2·Gd	3.96	0.12
3·Gd	3.21	0.1
4·Gd	2.89	0.11

This is corroborated by the molecular structure of the europium analogue, **2·Eu**, determined using single crystal X-ray diffraction. This shows a single bound water molecule in the inner coordination sphere of the lanthanide (Fig. 2). **1·Eu** displays luminescence properties in line with other phenacyl–DO3A derivatives, exhibiting intense lanthanide-centred emission. The luminescence lifetimes (τ_{H_2O} = 0.66 ms and, τ_{D_2O} = 2.13 ms, Table S3†) were used to calculate the number of inner sphere solvent molecules using established methods.[39] The

value obtained (q = 1.0) is consistent with expectations for a europium ion complexed by an octadentate ligand. **2·Eu** displays very similar luminescence properties: the observed luminescence lifetimes (τ_{H_2O} = 0.61 ms, τ_{D_2O} = 1.87 ms) are also consistent with q = 1.0 and with the structure of **2·Eu** determined from X-ray diffraction studies.

Furthermore, the steady state spectra of the two complexes show strong similarities, suggesting that the coordination environments at the europium ion are similar. In comparison, **3·Eu** and **4·Eu** exhibited only very weak luminescence, and poor signal-to-noise ratios were obtained (Fig. S15†). However, when the platinum(IV) centre in **3·Eu** was treated with ascorbic acid (AA), a dramatic enhancement in luminescence intensity was observed – resulting in a 37-fold enhancement of signal on regenerating **2·Eu** (Fig. 4). The excited-state manifold of the platinum(IV) complex acts to quench the europium emission, meaning that switching on of signal can potentially be used to observe reduction of the complex *in situ*. The bis-octanoic acid platinum(IV) complex **4·Eu** also showed a "switch-on" in luminescence when reduced with ascorbic acid (Fig. S16†).

This is consistent with other Pt(IV)/Pt(II) couples that display reductive "switch on" fluorescence; the quenching in the Pt(IV) state being thought to arise from the presence of metal-based d-orbitals energetically positioned between the HOMO and LUMO of the fluorophore.[40] Quenching of the Eu(III) emission by the Pt(IV) centre is therefore suggested to occur through energy transfer to low-lying electronic states in the platinum(IV) complex. Luminescence in the Pt(IV) oxidation state is more likely to be observed if one or more ligands are cyclometallated.[41,42] Although the mechanism of reduction *in cellulo* is likely to be complicated and involve more than one reducing species,[43] ascorbate acid-mediated reduction gives an initial insight into the potential for monitoring the reduction of these compounds through fluorescence microscopy. During cellular processing it is anticipated that the lanthanide–salicylic acid ligand will dissociate from the platinum(II) complex which is likely to further affect the lanthanide luminescence, further study is needed to investigate this modulation in detail.

As shown previously, using the INDIANA model,[16] the diffusive behaviour of water within cellular systems can be robustly described using a two-pool model with the water residing in either an intra- or extra-cellular pool. This results from the intrinsic diffusion of water being slower in the viscous intra-cellular compartment and its maximum displacement being restricted by the presence of the cell membrane. The model also explicitly accounts for exchange between the two environments. This methodology builds on previous experiments to characterise restricted diffusion in cellular systems.[44–47]

When fitting variable diffusion delay data from ^{1}H NMR spectroscopic experiments, it is possible to derive a number of system properties including intra- and extra-cellular diffusion coefficients, populations of water in the two environments, exchange rate of water over the membrane, average cell radius and, crucially for this study, intra- and extra-cellular longitudinal relaxation rates of water. Due to the relaxation enhancement caused by MRI imaging reagents, by comparing the difference in relaxation rates in the presence and absence of these agents in cellular systems we can quantitatively assess the degree to which they are localised within cells. As the relaxivities of the four complexes are different, this must be considered when using an increased intra-cellular relaxation rate as a proxy for cellular uptake of imaging agent. To address this, we used the relaxivity of the complexes measured in

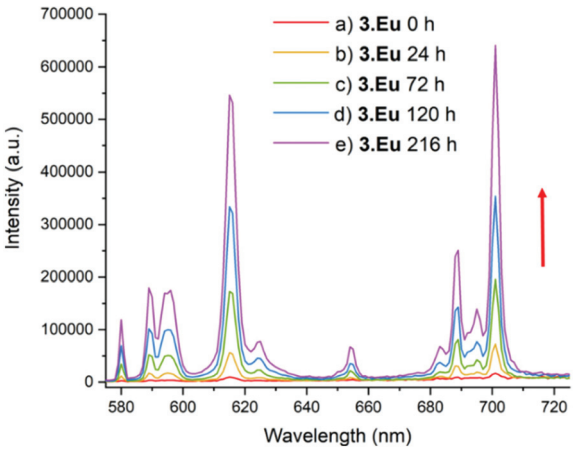

Fig. 4 Luminescence spectrum of **3·Eu**; λ_{ex} = 330 nm, emission slit = 1 nm. (a) before addition, (b) 24 h after addition of excess (20-fold) ascorbic acid (AA) and (c) 72 h after addition of AA, (d) 120 h after addition of AA, (e) 216 h after addition of AA. The red arrow shows that as time increases the intensity of emission increases.

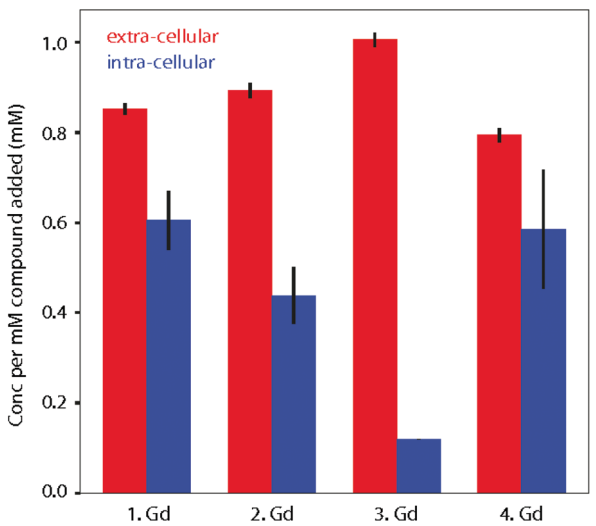

Fig. 5 Calculated partitioning of complexes **1–4·Gd** between extra- and intra-cellular environments following 1.5 h incubation with KNS42 cells. The concentration of complexes in the two environments is found by comparing longitudinal relaxation rates in the presence and absence of the compounds (ΔR_1) and then dividing by the relaxivity. The error bars are calculated by propagating the error in ΔR_1 for three independent samples and taking the standard deviation.

Table 2 Cytotoxicity (IC_{50}, μM) values of compounds **(1–4)·Gd** in KNS42 cell line. Cells were exposed to $\frac{1}{2}$ log serial dilutions of compounds for 1.5, 24, 48 and 72 h. IC_{50} values were determined using a 3 parameter log inhibitor *vs.* concentration curve fit. Two independent sets of three (6 in total) were performed for all compounds. Mean IC_{50} values and 95% confidence interval (CI) are shown below; *P* values are given in the ESI (Table S4†)

Complex	**1·Gd**		**2·Gd**		**3·Gd**		**4·Gd**	
Time/h	IC_{50}	95% CI	IC_{50}	95% CI	IC_{50}	95% CI	IC_{50}	95% CI
1.5	>1000	—	637.9	446.1–934.3	227.6	183.2–283.7	>1000	—
24	>1000	—	316.7	226.6–445.9	96.5	80.13–116.4	>1000	—
48	>1000	—	75.3	65.79–86.25	91.4	73.43–114.0	747.5	644.4–871.2
72	>1000	—	75.7	64.68–88.82	53.2	43.34–65.50	142.8	111.2–84.5

DMEM (Fig. 3). To estimate the partitioning of the four complexes between extra- and intra-cellular environments we assumed that the relaxivity of the compounds inside cells could be approximated by their relaxivity in media. Using the INDIANA method described above we found the extra- and intracellular longitudinal relaxation and compared this to the values in the absence of any complex to give ΔR_1 for each compound in the two environments. This value was then divided by the relaxivity to show how the compound was partitioned. The results of our analysis are shown in Fig. 5. The ^{1}H diffusion measurements were used to quantify the accumulation of the compounds within cells. Complex **1·Gd** accumulated relatively well in the cells, whilst there was a small drop reduction in accumulation for **2·Gd** which incorporated the Pt(II) group. Gadolinium complexes enter cells predominantly by micropinocytosis,[48,49] whereas platinum(II) complexes enter cells through a combination of copper transporters, anion/cation transporters and passive diffusion.[50] Significantly lower cellular accumulation was observed for the platinum(IV) compound, **3·Gd**, consistent with the oxidation state and ligand sphere of the Pt modulating the ability of the complex to enter cells. The copper transporter mechanism is less viable for platinum(IV) complexes, since there are no vacant positions available in the octahedral platinum(IV) coordination sphere. Cellular uptake of platinum(IV) complexes is therefore thought to occur through a combination of passive diffusion and active pathways.[51]

Finally, **4·Gd**, which incorporates OA ligands, showed a similar uptake to **1·Gd**, demonstrating the notable effect of the modified coordination sphere of the platinum(IV) on the degree of cellular accumulation. If diffusion is the predominant cellular uptake of the mechanism for **3·Gd**, increasing the lipophilicity through inclusion of octanoic acid groups as in **4·Gd** would be anticipated to significantly enhance uptake, and the data are consistent with this, although without discounting the possibility of uptake through micropinocytosis. The dominant route(s) of cellular uptake for other lanthanide–platinum conjugates are unknown, since only a handful of examples have been reported, with either labile,[52,53] or kinetically inert lanthanide chelation.[19,20,27] From these data, we suggest that the route(s) vary significantly depending on the coordination sphere platinum. These diffusion results are particularly enlightening in combination with the cytotoxicity results to give an overall picture of the cellular behaviour of the complexes.

A paediatric glioma cell line was specifically chosen for investigation, due to our interest in developing novel anticancer compounds for these malignancies.[54] Complex **1·Gd** was well-tolerated by KNS42 (paediatric glioblastoma) cells (viability <90%) across all concentrations and time-points tested. This indicated minimal cytotoxicity for **1·Gd**, with IC_{50} values exceeding 1000 μM (Table 2, Table S5, Fig. S18†). The Gd(III)–Pt(II) complex **2·Gd** demonstrated increasing cytotoxicity after 1.5 h exposure (IC_{50} = 637.9 μM at 1.5 h incubation, Fig. S18†). The Gd(III)–Pt(IV) complex **3·Gd** was significantly more cytotoxic than complex **2·Gd** after 1.5 h (P < 0.0001) and 24 h (P = 0.0031) exposure. However, no significant difference in cytotoxic effect between **2·Gd** and **3·Gd** was observed at longer (48 h and 72 h) exposure times (P values 0.0584 and 0.1482 respectively) (Fig. S18†). Complex **4·Gd** was less cytotoxic than **2·Gd** and **3·Gd** at all exposure times, with IC_{50} > 1000 μM at 1.5 h and 24 h, with increasing cytotoxicity after 48 h exposure (P = 0.0027 and <0.0001) (Fig. S18†). Whilst complex **1·Gd** showed no toxicity towards cells up to a concentration of 1000 μM, the platinum-containing bimetallic complexes **2–4·Gd** displayed varying degrees of cytotoxicity. As kinetically-inert $5d^6$ complexes, platinum(IV) complexes are suggested to reduce to platinum(II) intracellularly before ligand exchange and binding to cellular targets (*e.g.* DNA, proteins) can occur.[55] Complexes **3–4·Gd** all demonstrated increased cytotoxicity towards the cells with prolonged contact time. However, complex **4·Gd** showed a more pronounced "latent" period of initial lower cytotoxicity, compared with complexes **2·Gd** and **3·Gd**, consistent with an outer-sphere mechanism of reduction for **4·Gd** which is likely to be slower than an inner-sphere mechanism of reduction for **3·Gd**. For **3·Gd**, the reduction mechanism could involve bridging to one or both axial hydroxido groups,[5] which is not possible for **4·Gd**. An investigation into the sub-cellular location and time-resolved fluorescence reporting of complexes **1·Eu–4·Eu** using microscopy is planned.

Conclusions

Complexes **(1–4)·Gd** all show cellular accumulation in paediatric glioblastoma (KNS42) cells, as demonstrated by diffusion ^{1}H NMR spectroscopic experiments. At equimolar concentrations, the platinum(IV) complex **3·Gd** showed significantly

lower cellular accumulation than the platinum(II) complex **2·Gd** after 1.5 h. Complex **3·Gd** was derivatised through inclusion of octanoate axial ligands to produce **4·Gd** which enhanced the cellular accumulation of the complex in comparison to **3·Gd**. The lack of cellular toxicity of **1·Gd** suggests that lanthanide complexes based on **1** have significant potential for development as cell-permeant probes. The cellular accumulation, cytotoxicity and "switch-on" luminescence following reduction of prodrugs **3·Ln** and **4·Ln** makes them ideal candidates for studying the real-time accumulation and reduction of platinum(IV) prodrugs *in cellulo*, as well as making them candidates for further development as anti-cancer prodrugs. ^{1}H NMR diffusion-based models have considerable potential in establishing compound localisation and internalization and open up a new approach for using magnetic resonance imaging modalities to achieve this goal *in vivo*.

Author contributions

SF and NF and AB were responsible for conceptualization, formal analysis, funding acquisition, methodology, project administration, resources, supervision, visualization and writing. KY carried out synthesis and characterisation, GK and KY carried out diffusion NMR experiments. AH carried out the biological experiments with assistance from KY. PH conducted ICP-MS experiments. ALT and KEC solved the X-ray crystallographic structure.

Conflicts of interest

There are no conflicts to declare.

Acknowledgements

This work was supported by the Wellcome Trust (201406/Z/16/Z), Cancer Research UK (CR-UK) grant number C5255/A18085, through the Cancer Research UK Oxford Centre, L'Oréal, the John Fell Fund and the EPSRC (EP/S019901/1).

Notes and references

1 N. J. Wheate, S. Walker, G. E. Craig and R. Oun, *Dalton Trans.*, 2010, **39**, 8113.
2 S. R. McWhinney, R. M. Goldberg and H. L. McLeod, *Mol. Cancer Ther.*, 2009, **8**, 10.
3 R. J. Browning, P. J. T. Reardon, M. Parhizkar, R. B. Pedley, M. Edirisinghe, J. C. Knowles and E. Stride, *ACS Nano*, 2017, **11**, 8560.
4 H. Anderson, J. Wagstaff, D. Crowther, R. Swindell, M. J. Lind, J. McGregor, M. S. Timms, D. Brown and P. Palmer, *Eur. J. Cancer Clin. Oncol.*, 1988, **24**, 1471.
5 E. Wexselblatt and D. Gibson, *J. Inorg. Biochem.*, 2012, **117**, 220.
6 Z. Xu, Z. Wang, Z. Deng and G. Zhu, *Coord. Chem. Rev.*, 2021, **442**, 213991.
7 M. Alessio, I. Zanellato, I. Bonarrigo, E. Gabano, M. Ravera and D. Osella, *J. Inorg. Biochem.*, 2013, **129**, 52.
8 V. Novohradsky, I. Zanellato, C. Marzano, J. Pracharova, J. Kasparkova, D. Gibson, V. Gandin, D. Osella and V. Brabec, *Sci. Rep.*, 2017, **7**, 1.
9 M. C. Heffern, L. M. Matosziuk and T. J. Meade, *Chem. Rev.*, 2014, **114**, 4496.
10 J. Wahsner, E. M. Gale, A. Rodríguez-Rodríguez and P. Caravan, *Chem. Rev.*, 2019, **119**, 957.
11 G. Ferrauto, E. Di Gregorio, S. Lanzardo, L. Ciolli, M. Iezzi and S. Aime, *Sci. Rep.*, 2018, **8**, 1.
12 J. Lohrke, T. Frenzel, J. Endrikat, F. C. Alves, T. M. Grist, M. Law, J. M. Lee, T. Leiner, K. C. Li, K. Nikolaou, M. R. Prince, H. H. Schild, J. C. Weinreb, K. Yoshikawa and H. Pietsch, *Adv. Ther.*, 2016, **33**, 1.
13 K. Van Dijke, N. Van Bruggen, J. Mann and S. Ostrowitzki.
14 H. Li and T. J. Meade, *J. Am. Chem. Soc.*, 2019, **141**, 17025.
15 C. T. Yang and K. H. Chuang, *MedChemComm*, 2012, **3**, 552.
16 G. Karunanithy, R. J. Wheeler, L. R. Tear, N. J. Farrer, S. Faulkner and A. J. Baldwin, *J. Magn. Reson.*, 2019, **302**, 1.
17 Y. Song, K. Suntharalingam, J. S. Yeung, M. Royzen and S. J. Lippard, *Bioconjugate Chem.*, 2013, **24**, 1733.
18 J. X. Ong, C. S. Q. Lim, H. Van Le and W. H. Ang, *Angew. Chem., Int. Ed.*, 2019, **58**, 164.
19 S. Faulkner, S. J. A. Pope and B. P. Burton-Pye, *Appl. Spectrosc. Rev.*, 2005, **40**, 1.
20 C. J. Adams and T. J. Meade, *Chem. Sci.*, 2020, **11**, 2524.
21 G. Thiabaud, G. He, S. Sen, K. A. Shelton, W. B. Baze, L. Segura, J. Alaniz, R. M. MacIas, G. Lyness, A. B. Watts, H. M. Kim, H. Lee, M. Y. Cho, K. S. Hong, R. Finch, Z. H. Siddik, J. F. Arambula and J. L. Sessler, *Proc. Natl. Acad. Sci. U. S. A.*, 2020, **117**, 7021.
22 M. Delbianco, V. Sadovnikova, E. Bourrier, G. Mathis, L. Lamarque, J. M. Zwier and D. Parker, *Angew. Chem., Int. Ed.*, 2014, **53**, 10718.
23 C. P. Montgomery, B. S. Murray, E. J. New, R. Pal and D. Parker, *Acc. Chem. Res.*, 2009, **42**, 925.
24 J. D. Routledge, X. Zhang, M. Connolly, M. Tropiano, O. A. Blackburn, A. M. Kenwright, P. D. Beer, S. Aldridge and S. Faulkner, *Angew. Chem., Int. Ed.*, 2017, **56**, 7783.
25 M. Tropiano and S. Faulkner, *Chem. Commun.*, 2014, **50**, 4696.
26 J. Lehr, M. Tropiano, P. D. Beer, S. Faulkner and J. J. Davis, *Chem. Commun.*, 2015, **51**, 15944.
27 A. Dadabhoy, S. Faulkner and P. G. Sammes, *J. Chem. Soc., Perkin Trans. 2*, 2002, 348.
28 F. J. Dijt, G. W. Canters, J. H. J. den Hartog, A. T. M. Marcelis and J. Reedijk, *J. Am. Chem. Soc.*, 1984, **106**, 3644.
29 N. J. Farrer, J. A. Woods, L. Salassa, Y. Zhao, K. S. Robinson, G. Clarkson, F. S. Mackay and P. J. Sadler, *Angew. Chem., Int. Ed.*, 2010, **49**, 8905.

30 O. J. Stacey, A. J. Amoroso, J. A. Platts, P. N. Horton, S. J. Coles, D. Lloyd, C. F. Williams, A. J. Hayes, J. J. Dunsford and S. J. A. Pope, *Chem. Commun.*, 2015, **51**, 12305.
31 L. Palatinus and G. Chapuis, *J. Appl. Crystallogr.*, 2007, **40**, 786.
32 P. W. Betteridge, J. R. Carruthers, R. I. Cooper, K. Prout and D. J. Watkin, *J. Appl. Crystallogr.*, 2003, **36**, 1487.
33 P. Parois, R. I. Cooper and A. L. Thompson, *Chem. Cent. J.*, 2015, **9**, 1.
34 R. I. Cooper, A. L. Thompson and D. J. Watkin, *J. Appl. Crystallogr.*, 2010, **43**, 1100.
35 N. M. Shavaleev, L. P. Moorcraft, S. J. A. Pope, Z. R. Bell, S. Faulkner and M. D. Ward, *Chem. Commun.*, 2003, 1134.
36 T. K. Ronson, T. Lazarides, H. Adams, S. J. A. Pope, D. Sykes, S. Faulkner, S. J. Coles, M. B. Hursthouse, W. Clegg, R. W. Harrington and M. D. Ward, *Chem. – Eur. J.*, 2006, **12**, 9299.
37 B. M. Still, P. G. A. Kumar, J. R. Aldrich-Wright and W. S. Price, *Chem. Soc. Rev.*, 2007, **36**, 665.
38 N. J. Farrer, P. Gierth and P. J. Sadler, *Chem. – Eur. J.*, 2011, **17**, 12059.
39 A. Beeby, I. M. Clarkson, R. S. Dickins, S. Faulkner, D. Parker, L. Royle, A. S. de Sousa, J. A. G. Williams and M. Woods, *J. Chem. Soc., Perkin Trans. 2*, 1999, **2**, 493.
40 J. J. Wilson and S. J. Lippard, *Inorg. Chim. Acta*, 2012, **389**, 77.
41 J. E. Expósito, M. Álvarez-Paíno, G. Aullón, J. A. Miguel and P. Espinet, *Dalton Trans.*, 2015, **44**, 16164.
42 J. C. López-López, D. Bautista and P. González-Herrero, *Chem. – Eur. J.*, 2020, **26**, 11307.
43 E. Wexselblatt and D. Gibson, *J. Inorg. Biochem.*, 2012, **117**, 220.
44 A. Szafer, J. Zhong and J. C. Gore, *Magn. Reson. Med.*, 1995, **33**, 697.
45 C. Meier, W. Dreher and D. Leibfritz, *Magn. Reson. Med.*, 2003, **50**, 500.
46 E. Fieremans, D. S. Novikov, J. H. Jensen and J. A. Helpern, *NMR Biomed.*, 2010, **23**, 711.
47 I. Åslund, A. Nowacka, M. Nilsson and D. Topgaard, *J. Magn. Reson.*, 2009, **200**, 291.
48 E. Mathieu, A. Sipos, E. Demeyere, D. Phipps, D. Sakaveli and K. E. Borbas, *Chem. Commun.*, 2018, **54**, 10021.
49 E. J. New and D. Parker, *Org. Biomol. Chem.*, 2009, **7**, 851.
50 D. P. Gately and S. B. Howell, *Br. J. Cancer*, 1993, **67**, 1171.
51 S. B. Howell, R. Safaei, C. A. Larson and M. J. Sailor, *Mol. Pharmacol.*, 2010, **77**, 887.
52 I. M. Etchells, M. C. Pfrunder, J. A. G. Williams and E. G. Moore, *Dalton Trans.*, 2019, **48**, 2142.
53 Z. Zhu, X. Wang, T. Li, S. Aime, P. J. Sadler and Z. Guo, *Angew. Chem., Int. Ed.*, 2014, **53**, 13225.
54 M. H. C. Boulet, L. K. Marsh, A. Howarth, A. Woolman and N. J. Farrer, *Dalton Trans.*, 2020, 5703.
55 N. Graf and S. J. Lippard, *Adv. Drug Delivery Rev.*, 2012, **64**, 993.

EurJIC
European Journal of Inorganic Chemistry

Full Papers
doi.org/10.1002/ejic.202100041

Chemistry Europe
European Chemical Societies Publishing

Solvent-Dependent Reactivity and Photochemistry of Dinuclear and Mononuclear Platinum(IV) Azido Triazaolato Complexes

Kezi Yao,[a] Arnau Bertran,[b] Jacques Morgan,[a] Charlotte Greenhalgh,[a] Katharina Edkins,[c] Alice M. Bowen,[b, d] and Nicola J. Farrer*[a]

Reaction between the platinum(IV) azido complex *trans,trans,trans*-[Pt(py)$_2$(N$_3$)$_2$(OH)$_2$] (**1**) and 1,4-diphenyl-2-butyne-1,4-dione **2** in MeCN produces the intermediate peroxide-bridged dimeric platinum(IV) azido triazolato species (**5**), which has been characterised by X-ray crystallography. However, if the reaction between **1** and **2** is conducted in MeOH it results in decomposition. Over time in MeCN, dimer (**5**) converts into mononuclear complexes *trans,trans,trans*-[Pt(py)$_2$(N$_3$)(triazole)(OH)$_2$] (**3a**/**3b**), which are in dynamic exchange. If resuspended in protic solvents (MeOH,H$_2$O), **3a**/**3b** undergo a slow (22 d) irreversible rearrangement to a cyclised platinum(IV) species **4** which contains a formally N,O-chelated ligand. Conversion of **3a**/**3b** to **4** in d_4-MeOH can be accelerated (384x) by irradiation with visible light, although continued irradiation also produces $N_3^{\bullet}$ and $OH^{\bullet}$ radicals, and the [**4**-N$_3$]$^+$ species can be readily detected by ESI-MS. Solvent choice significantly effects both the cycloaddition reaction between **1** and **2**, and the stability of the resultant complexes.

Introduction

1,3-dipolar cycloaddition reactions of metal azido complexes with acetylenes to form 1,2,3-triazoles are a well-established route to novel metal complexes.[1] These reactions have been previously explored by other groups for platinum(II) complexes[2–5] and by us for platinum(IV) azido complexes.[6–8] Inorganic platinum-click reactions enable the synthesis of novel (potentially multimetallic) platinum complexes and metallopolymers.[9] They can also provide plausible routes to introduce functional groups for fluorescent monitoring[4] and to monitor Pt-azido drug localisation.[10] The cycloaddition reaction results in the formation of 1,2,3-triazoles, and these organic ligands can show promising anti-cancer activity both in their own right[11] and as components of metal complexes.[12] Triazoles are also widely employed as chemosensors.[13] Understanding the solution chemistry and photochemistry of metal triazole complexes is crucially important for further rational design.

We previously reported that the platinum(IV) azido complex **1** undergoes a spontaneous reaction with acetylene **2** in MeCN to produce complex **3**, a *mono* triazolato cycloaddition product, which exists as an equilibrium between two rapidly interconverting species; **3a** and **3b** (Scheme 1).[7] A small amount of another complex – **5** – was also detected during HPLC purification of **3a**/**3b** but we previously were unable to isolate sufficient quantities of **5** for further characterisation. We now report that compound **5** is a peroxide-bridged dimer, which slowly evolves over time in the dark in MeCN to form **3a**/**3b** (Scheme 2). We have also determined that both **5** and **3a**/**3b** respond to irradiation with blue light. Furthermore, that in protic solvents **3a**/**3b** (which exist in equilibrium) evolve into a single cyclised Pt^{IV} complex, **4** which is then stable to further rearrangement. Here we report our findings in detail.

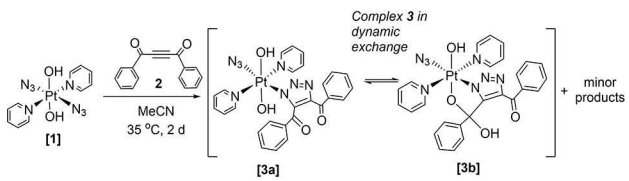

Scheme 1. Reaction of *trans,trans,trans*-[Pt(N$_3$)$_2$(OH)$_2$(py)$_2$] (**1**) with 1,4-diphenyl-2-butyne-1,4-dione (**2**) showing formation of **3** (**3a**/**3b**) as well as other minor products.

[a] K. Yao, J. Morgan, C. Greenhalgh, Dr. N. J. Farrer
Chemistry Research Laboratory, University of Oxford,
12 Mansfield Road, Oxford, OX1 3TA, United Kingdom
E-mail: Nicola.Farrer@chem.ac.uk
http://farrer.chem.ox.ac.uk
[b] A. Bertran, Dr. A. M. Bowen
Centre for Advanced Electron Spin Resonance and Inorganic Chemistry Laboratory,
Department of Chemistry, University of Oxford,
South Parks Road, Oxford OX1 3QR, United Kingdom
[c] Dr. K. Edkins
School of Health Sciences, University of Manchester,
Oxford Road, Manchester M13 9PL, United Kingdom
[d] Dr. A. M. Bowen
The Department of Chemistry, Photon Science Institute and the National EPR Research Facility,
University of Manchester,
Oxford Road, Manchester M13 9PL, United Kingdom

Supporting information for this article is available on the WWW under https://doi.org/10.1002/ejic.202100041

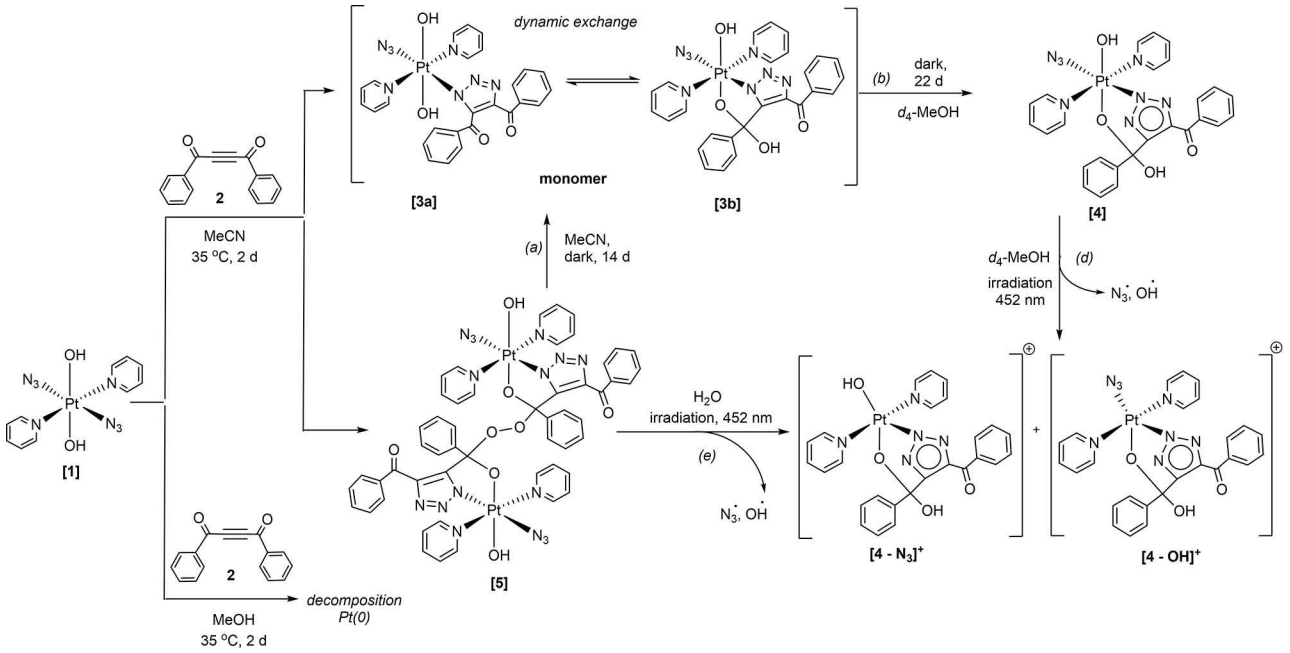

Scheme 2. Reaction of *trans,trans,trans*-$[Pt(N_3)_2(OH)_2(py)_2]$ (**1**) with 1,4-diphenyl-2-butyne-1,4-dione (**2**), showing pathways of reactivity to different products and the effect of different solvents. The presence of H_2O_2 enables greater production of **5**, and results in low-level production of OH radicals in the dark during transofrmation (a), in accordance with reports for other platinum(IV) complexes.[15]

Synthesis

Trans, trans, trans-$[Pt(N_3)_2(OH)_2(py)_2]$ (**1**) was synthesised as previously reported, the final step of the synthesis involving oxidation with H_2O_2 followed by crystallisation.[14] We previously reported that when the reaction was conducted in MeCN, both the main product **3a**/**3b**[7] and several minor species including **5** were successfully obtained, without any observed decomposition. However, here we report that when the cycloaddition reaction between **1** and 1,4-diphenyl-2-butyne-1,4-dione (**2**) is conducted in MeOH (35 °C, 2 d), it results in decomposition, with formation of a black platinum(0) precipitate (Scheme 2). The solvent choice for the cycloaddition therefore has a significant effect on the reaction. Complex **5** ($t_R = 4.01$ min) was previously challenging to isolate, since it formed as a minor product in the reaction (7%), eluting immediately before **3a**/**3b** ($t_R = 4.31$ min) during HPLC purification (Figure S1). However, we now report that if **1** is not purified by HPLC or recrystallised before use (therefore retaining residual H_2O_2 from the final synthetic step) the quantity of **5** observed significantly increases, such that it forms 31% of the total integrated HPLC trace (UV-Vis detection, Figure S2), making it considerably easier to isolate as the $5 \cdot H_2O_2$ adduct, and to fully characterise (Figure S3). Historically, platinum(IV) complexes such as *cis,cis,-trans*-$[Pt^{IV}Cl_2(NH_3)_2(OH)_2]$ have shown a propensity for co-crystallisation of H_2O_2.[15] We were initially unaware that **5** was a dinuclear species, since the molecular weight of the compound exceeded the detection limit of the HPLC mass spectrometer (1250 *m/z*), and the ESI-MS conditions did not favour the detection of multiply charged ions. Therefore, $5 \cdot H_2O_2$ was observed by HPLC via both UV-Vis absorption and the detection of the common fragmentation product $[3\text{-OH}]^+$ at 688.05 *m/z* (Figure S2, *bottom*). This rendered it indistinguishable from complex **3a**/**3b** which results in the same fragmentation species in the HPLC. Following HPLC purification, crystals of **5** were grown from MeCN, and were shown by X-ray crystallography to consist of a peroxide-bridged dimer, with no H_2O_2 observed in the crystal lattice (Figure 1).

The X-ray crystallographic structure of **5** has an O–O bond length of 1.475(8) Å, consistent with a bond order of **1**[17] and it also exhibits a C00N–O009(peroxide) bond length of 1.432(8) Å.

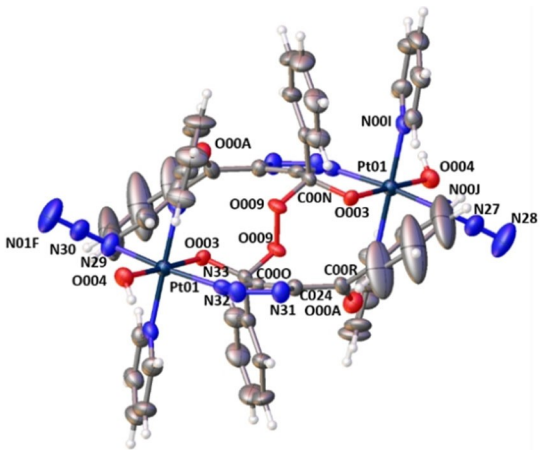

Figure 1. Single crystal X-ray structure of the peroxide dimer **5** with thermal ellipsoids displayed at 50% probability.[16] For clarity, only key atoms discussed in the text are labelled here, the fully labelled structure is given in Figure S4. Colour code: carbon (grey), nitrogen (blue), oxygen (red), hydrogen (light grey), platinum (cyan).

The Pt–N azido (Pt–N29–N30–N01F) ligand shows slightly greater linearity (176.8(9)°) than is observed in the azido ligand (s) contained in both **3b** and **1**. The bond lengths within the azido ligand are very similar to **3b** and to **1**; 1.210(9) Å (N29–N30) and 1.147(9) Å (N30–N01F). The angle subtended at Pt–N29–N30 (116.0(5)°) is intermediate between that seen for complex **3b** and complex **1**, and the Pt–N33 triazole bond length is 2.011(6) Å, slightly elongated in comparison to **3b**.[7]

IR spectroscopy of a MeOH solution of **5**·H_2O_2 showed a strong $\nu_{asym}N_3$ stretch at 2049.04 cm^{-1} (Figure S5), consistent with the presence of the azido groups.

If the cycloaddition was carried out with **1** which had residual H_2O_2 remaining from the syntheses, **5** was recovered from the HPLC and observed by ESI-MS as the H_2O_2 adduct; $[\mathbf{5}\cdot H_2O_2+Na]^+$ at 1465.2604 *m/z* (confirmed by HRMS, error 5.59 ppm, Figure S6). Collision-induced dissociation studies (MS/MS) of $[\mathbf{5a}\cdot H_2O_2+Na]^+$ at 1465.00 *m/z* revealed facile fragmentation by homolytic cleavage of the peroxide bond and retention of the sodium to give $[Pt(OH)_2(N_3)(triazole)(py)_2O+Na]^+$ as a stable species at 744.22 *m/z* as well as other minor species (Figure S7). The species at 744.03 *m/z* observed in the low-resolution ESI-MS of **5** (Figure S1) could therefore correspond to this same fragmentation product.

^{195}Pt NMR spectroscopy of **5**·H_2O_2 (in d_3-MeCN) showed a single resonance at 776 ppm (Figure S8). In the same solvent, the monomers **3a** (689 ppm) and **3b** (785 ppm) give rise to two resonances.[7] This suggests that dynamic exchange processes similar to those seen for **3a**/**3b** do not occur in **5**, consistent with the carbonyl/hydroxyl group of the triazole ligand being part of the stable peroxide bond.

The ^{1}H NMR spectrum could be assigned in agreement with the proposed structure of **5**, although determination of the py′ and py rings are tentative (Figures S9, S10, S11). A singlet was observed for **5**·H_2O_2 at 9.16 ppm, which underwent exchange with the residual water peak (^{1}H NMR NOESY, Figure S12); this may correspond to protons of the associated/coordinated H_2O_2. Assignment of the ^{13}C NMR spectra (Figure S13) was aided by HSQC and HMBC experiments (Figures S14 and S15 respectively). Many features of the ^{13}C NMR spectrum of **5**·H_2O_2 were similar to that of **3b**, including the observation of a $^2J_{CPt}$ coupling of 43.8 Hz for one of the quaternary triazole carbon resonances in **5**·H_2O_2 (151.5 ppm). The quaternary carbon connected to the Pt–O group, the Ph ring and the peroxide bridge was observed at 112.1 ppm (showing a 3-bond HMBC correlation to the Ph_{ortho} protons). This was at higher field than for complex **3b**, in which the sp^3 carbon coordinated to an OH group rather than a O–O group was observed at 103.0 ppm. The UV-Vis absorbance spectrum of **5**·H_2O_2 was broadly similar to the spectrum of **3a**/**3b** (Figure S16).

Conversion of 5·H_2O_2 to 3a/3b in d_3-MeCN

Both **5**·H_2O_2 and **3a**/**3b** were isolated as pale yellow powders, although **5**·H_2O_2 was noticeably less soluble than **3a**/**3b** in organic solvents (MeCN, MeOH). Complex **5**·H_2O_2 was unstable in MeCN solution, changing over time in the absence of light. Comparing ^{1}H NMR spectra obtained immediately following dissolution (Figure S9) with 2D ^{1}H and ^{13}C NMR spectra acquired later the same day, new resonances can already be seen appearing in the later spectra (for example * in Figure S10).

Monitoring this conversion by cw-EPR in the presence of the spin trap DMPO (Figure S17) revealed a build-up of a small amount of a nitroxide species – over several weeks – in MeCN (Figure S18), showing hyperfine coupling only to a single nitrogen. No radical species were detected in the analogous spin trapping experiment performed with **3a**/**3b** in MeCN (Figure S19). When the same experiments were carried out in water, a small amount of a DMPO$^\bullet$–OH radical adduct was observed over several days with **5**·H_2O_2, indicating the slow formation and subsequent trapping of OH$^\bullet$ (Figure S20), while no radical species were detected under the same conditions from **3a**/**3b** in H_2O (Figure S21). We suggest this is due to release of peroxide, which appears to be strongly associated with **5**. Evolution of OH$^\bullet$ from platinum(IV) prodrugs containing trace amounts of H_2O_2 has been previously reported.[15] Observation of the evolution of OH$^\bullet$ in the dark is also compatible with the slow conversion of **5** to **3a**/**3b** taking place through homolytic cleavage of the peroxide bridge. In H_2O, the resulting [**3b**-H]$^\bullet$ species would produce **3b** by hydrogen abstraction from the solvent, producing OH$^\bullet$, which would be trapped by DMPO. In MeCN, more complicated radical processes could occur, involving degradation of the spin trap by either H_β abstraction or cleavage of the $N_{nitroxidic}$–C_α bond.[18]

Conversion of 3a/3b to 4 in d_4-MeOH

When the synthesis of **3a**/**3b** was conducted in MeCN followed by solvent removal and resuspension of solid **3a**/**3b** in protic solvents, it did not result in decomposition. Instead, **3a**/**3b** underwent a conversion to a new complex (**4**) in d_4-MeOH (Scheme 1, Figure 2). By the time ^{13}C, ^{1}H-^{13}C HSQC and HMBC NMR spectral data had been acquired for a freshly prepared

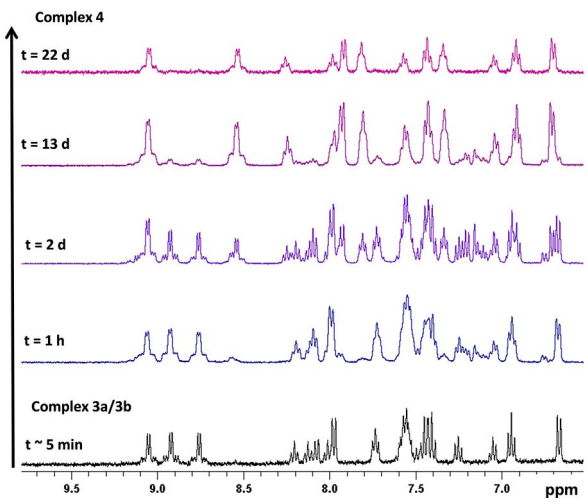

Figure 2. ^{1}H NMR spectra of **3a**/**3b** converting to **4** over 22 d (d_4-MeOH) at 20 °C.

solution of **3a**/**3b** in d_4-MeOH, partial conversion to **4** had already begun. Complete conversion of **3a**/**3b** to **4** was relatively slow, with 100% conversion after 22 d (^{1}H NMR spectroscopy, d_4-MeOH, Figure 2 and Figure S22). During this time, the ^{195}Pt NMR resonances at 832 ppm (**3a**) and 784 ppm (**3b**) converged to a single resonance at 824 ppm for **4** (d_4-MeOH). EPR experiments revealed no detectable radical production during the conversion of **3a**/**3b** to **4** in the dark (Figure S21).

Analysis of complex 4

Following completion of the conversion of **3a**/**3b** to **4** in d_4-MeOH, complex **4** (Figure 3) was isolated as a pale yellow solid by rotary evaporation of the solvent, and was fully characterised by ESI-MS, ^{1}H, ^{13}C, ^{195}Pt and ^{14}N NMR spectroscopy, IR and UV-Vis spectroscopy.

Complex **3a**/**3b** had been previously detected by ESI-MS predominantly as the [**3a**/**3b**-OH]$^+$ (688.14 *m/z*) species.[7] Conversion of **3a**/**3b** to **4** resulted in similar low-resolution ESI-MS: [**4**-OH]$^+$ was detected as the dominant species at 687.89 *m/z*, ($C_{26}H_{21}N_8O_3Pt$, calcd. 688.13 *m/z*) with [**4** + H]$^+$ observed at a significantly lower abundance, at 705.71 *m/z* ($C_{26}H_{23}N_8O_4Pt$, calcd 706.15 *m/z*). The ESI-MS were identical regardless of whether the conversion to **4** was carried out in MeOH or d_4-MeOH, effectively ruling out the possibility that the solvent had been incorporated into the observed species as part of the conversion, since a difference would have been detected due to the difference in molecular weight between the deuterated and undeuterated solvents (Figure S23).

In the ^{1}H NMR spectrum of complex **4** in d_4-MeOH (Figure S24) the resonances in **4** corresponding to Py_{para} and Py_{meta} protons were observed at higher chemical shifts than for **5**, whilst the other aromatic ^{1}H NMR resonances were very similar for the two complexes. Complex **4** has two inequivalent Ph rings and two inequivalent Py rings, and NOESY correlations were observed between one pyridyl group and one phenyl ring (Figure S25), in agreement with the proposed structure. Following conversion from **3a**/**3b**, complex **4** was stable in solution (d_4-MeOH) for over 12 months, and speciation remained essentially unchanged (judged by ^{1}H NMR spectroscopy and ESI-MS).

The rearrangement of **3a**/**3b** to **4** in MeOH followed by reconstitution of **4** in d_3-MeCN enabled a direct comparison of **3a**/**3b** and **4** in the same solvent (Figure S26). This revealed changes predominantly in the Py_{para} (shielded) Ph_{ortho} (deshielded) and Py_{meta} (shielded) protons but revealed little other structural information. ^{13}C NMR spectra were assigned through comparison with previous structures and through ^{1}H COSY, ^{1}H-^{13}C HSQC, ^{1}H-^{13}C HMBC and ^{1}H NOESY experiments (Figures S23–S29). The ^{14}N NMR spectrum of **4** showed resonances corresponding to the N_β (227.0 ppm) and N_γ/$N_{triazole}$/N_{py} environments (166.2 ppm) (Figure S31). The Pt-coordinated N_α of the azide was anticipated to come into resonance at *ca.* 57 ppm but was broadened beyond detection. As previously observed[19] and subsequently explained by DFT calculations,[20] the quadrupolar interaction of the ^{14}N nucleus with the local electric field gradient (EFG) results in significant anisotropic broadening of spectral lines for less symmetric environments, such as the azido N_α resonance. Since the ^{14}N NMR spectrum of **4** provided only limited information we felt it would be unlikely that acquisition of ^{14}N NMR of **3** or **5** would provide any additional or useful comparative information. Comparison of IR (d_4-MeOH) of **3a**/**3b** (sample made immediately prior to measurement) and of complex **4** revealed only minor changes; the $\nu_{asym}N_3$ IR stretch being observed at 2048 cm^{-1} for **4** (Figure S32). The UV-vis spectrum of **4** (Figure S33) was also consistent with **4** being a monoazido complex.

Despite repeated and ongoing attempts, it was not possible to grow crystals of **4** suitable for analysis by X-ray diffraction. However, the structure proposed for **4** (Figure 3) is consistent with the reported analytical data. We suggest that **4** forms from **3a**/**3b** in protic solvents as a result of N1–N2 rearrangement of the triazole ring.[4] An alternative structure for **4** could result from isomerisation at the platinum(IV) centre through exchange of azide and OH (resulting in *cis* OH groups); such isomerisation has been reported for other platinum(IV) complexes, however we suggest that triazole rearrangement is more likely.[21]

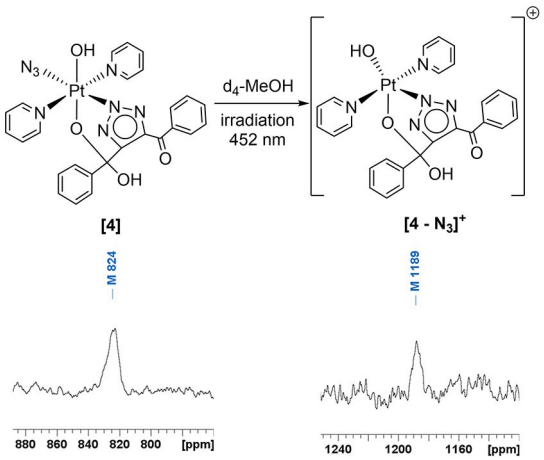

Figure 3. ^{195}Pt NMR spectra (d_4-MeOH) of complex **4** (a) before irradiation (86.1 MHz) and (b) after irradiation with blue light, forming [**4**-N_3]$^+$ (107.6 MHz).

Photochemistry of 3a/3b, 4 and 5

The slow conversion of **3a**/**3b** to **4** in d_4-MeOH could be accelerated by heat, and was also significantly accelerated (by 384x) through irradiation with light (452 nm) with 80% conversion observed in 60 min. However, small amounts (< 5%) of [**3**-N_3]$^+$ (663.1318 *m/z*) were also observed by HPLC after 60 min irradiation, in contrast to conversion in the dark. We chose the irradiation wavelength of 452 nm (blue light) since it is the longest wavelength – of a commercially available LED light source – which affords photochemical conversion of **3a**/**3b** within a reasonable length of time. Since the tissue penetration of light is wavelength-dependent, it is desirable to use the longest wavelength possible to activate these com-

pounds – towards the phototherapeutic window of 630 nm–900 nm. We do however note that successful treatment of superficial tumours has been achieved with blue light, which has the advantage of minimising damage to underlying tissue.[22] We have previously demonstrated using TD-DFT that platinum(IV) azido complexes have strongly dissociative states at longer wavelengths, which explains why they can be successfully photoactivated with visible light, despite demonstrating only modest absorption at these longer wavelengths.[14]

We previously showed that if irradiation of **3a**/**3b** is carried out in phosphate buffered saline (PBS) in the presence of 5′-GMP, no platination of 5′-GMP was observed.[7] ^{195}Pt NMR spectroscopy of **4** (d_4-MeOH) under irradiation also showed conversion from the resonance at 824 ppm (**4**) to 1189 ppm [**4**-N_3]$^+$ in the platinum(IV) region of the spectrum (Figure 3). This is consistent with our previous report of the photochemistry of **3a**/**3b** (d_3-MeCN),[7] which showed the ^{195}Pt resonances move to a more deshielded position following irradiation and release of azide.

EPR spin-trapping experiments under irradiation (440–480 nm) were also carried out with freshly prepared **3a**/**3b** and **5** in the presence of DMPO. The formation of DMPO$^•$–N_3 and DMPO$^•$–OH radical adducts indicated evolution and trapping of $N_3^•$ and OH$^•$ radicals in both cases (Figure 4a, Figure 4c, Figure S33 and Figure S34).

For **3a**/**3b**, a steady state total radical adduct concentration was reached after ~30 min of continuous irradiation and remained almost constant during the period of irradiation (~3 h) (Figure 4b). For **5**, the total radical adduct concentration peaked after ~30 min irradiation and then decayed (Figure 4d). Based on our previous work with similar platinum(IV) azido complexes, we attribute the steady radical adduct signal from **3a**/**3b** to its high concentration in solution, which saturates the light absorption of the EPR sample at the wavelengths of irradiation.[8]

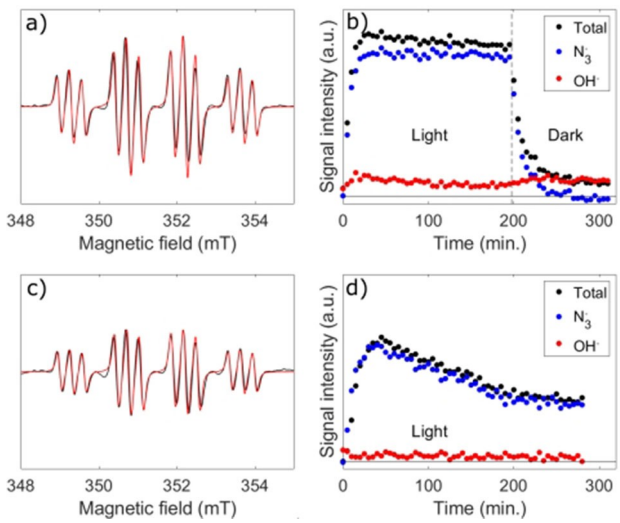

Figure 4. EPR spin trapping experiments under irradiation (440–480 nm) of compounds **3a**/**3b** at 10.5 mM in H_2O (a, b) and 5·H_2O_2 at < 1 mM (c, d) in the presence of 21 mM DMPO. (a, c) Experimental spectra averaged over 100 min of continuous illumination after reaching the maximum signal intensity (black) and simulations with a DMPO$^•$–N_3: DMPO$^•$–OH molar ratio of 90:10 (a) and 95:5 (c) (red). The average total radical adduct concentrations over the first 100 minutes determined from spectral integration are (5.5 ± 0.6) μM (a) and (3.1 ± 0.3) μM (c). (b, d) EPR peak height transients of the total radical adduct signal (black), DMPO$^•$–N_3 signal (blue) and DMPO$^•$–OH signal (red). Vertical axes have the same scale in (a, c) and (b, d), respectively, for comparison.

The comparatively low concentration of **5** in the experiment was due to its reduced solubility in H_2O. DMPO$^•$–N_3: DMPO$^•$–OH molar ratios of 90:10 and 95:5 were determined by spectral simulation for **3a**/**3b** and **5**, respectively (Figure 4a and Figure 4c). The DMPO$^•$–N_3 signals quickly disappeared after irradiation ceased, with a lifetime of ~7 min, demonstrating that radical evolution in aqueous solution can be controlled by blue light irradiation (Figure 4b and Figure S34). The persistance of the DMPO$^•$–OH signal is due to the much longer lifetime of that radical adduct in comparison to DMPO$^•$–N_3,[23] rather than due to the evolution of OH$^•$ radicals in the dark from **3a**/**3b**.

Evolution of OH$^•$ radicals from **3a**/**3b** in H_2O is induced by irradiation, evidenced by the initial rise in the DMPO$^•$–OH signal (Figure 4b, red trace), while it seems to be light-independent for 5·H_2O_2 (Figure 4d, red trace), with the same weak DMPO$^•$–OH signal under irradiation as is observed in the dark (Figure S18).

The higher radical molar fraction of DMPO$^•$–OH observed for **3a**/**3b** could be due to the coexistance of the two forms of the monomeric complex, where **3a** has two OH ligands per platinum centre that can be potentially released upon irradiation, in comparison to the one OH ligand per platinum in **5** (Scheme 2). Analogous experiments demonstrate that **4**, which is stable in aqueous solution in the absence of light, also evolves predominantly $N_3^•$ radicals under irradiation without undergoing photoreduction, with a smaller fraction of observed DMPO$^•$–OH (4%) than for **3a**/**3b** (Figure S36).

ESI-MS of **4** following 60 min irradiation (452 nmm MeOH) showed [**4**-N_3]$^+$ at 663.23 *m/z* as the most abundant species, as had been reported previously for **3a**/**3b**,[7] with no observable [**4**-N_3, OH]$^{2+}$ (anticipated at 324.07 *m/z*) or [**4**-N_3, OH]$^+$ (anticipated at 646.13 *m/z*) (Figure S37). Since [**4**-OH]$^+$ is already commonly observed as a product of electrospray ionisation both prior and post-irradiation no conclusions could be drawn as to what proportion of this was produced as a result of OH$^•$ ejection or not, but the spectrum was clearly dominated by the [**4**-N_3]$^+$ species, in agreement with the EPR experiments.

Conclusions

We have demonstrated that the choice of reaction solvent has a significant effect on the outcome of the cycloaddition reaction between *trans*,*trans*,*trans*-[Pt(py)$_2$(N_3)$_2$(OH)$_2$] (**1**) and 1,4-diphenyl-2-butyne-1,4-dione (**2**). Decomposition is observed if the reaction is carried out in MeOH, whereas triazole products **3a**/**3b** are formed if the reaction is carried out in MeCN. If residual H_2O_2 is present during the cycloaddition reaction, this favours the formation of a peroxide-bridged intermediate (**5**·H_2O_2) which slowly converts to triazole products **3a**/**3b**. If no H_2O_2 is

present then **3a**/**3b** are formed as the major reaction product, with only small amounts of **5** being observed.

The major product **3a**/**3b** is stable in MeCN indefinitely, yet suspension in protic solvents causes triazole rearrangement to a new compound **4**, which is then itself stable in solution for at least 12 months. Complex **4** also appears to remain unchanged following re-isolation and dissolution in MeCN.The rearrangement to **4** can be significantly accelerated (x384) by irradiation with 420 nm light (although slight photodecomposition is also observed), or by modest heating. We are now investigating the effect of irradiation with longer wavelength light on this rearrangement process. Irradiation of complex **4** (440–480 nm) produces predominantly $[\mathbf{4}\text{-}N_3]^+$ with concommitant azido radical production. Platinum(IV) photoproduct(s) were observed by ESI-MS and ^{195}Pt NMR spectroscopy. EPR experiments confirmed the production of predominantly azido radicals from **3a**/**3b**, **4** and **5**·H_2O_2 under blue light (440–480 nm) irradiation in H_2O, consistent with these findings.

Experimental Section

Materials and Methods. $K_2[PtCl_4]$ was purchased from Precious Metals Online. HPLC-grade solvents and Millipore-filtered H_2O were used for the preparation of compounds and purification by HPLC. DMPO (≥98%) was purchased from Cambridge Bioscience Ltd. All other reagents were purchased from Sigma-Aldrich or Alfa Aesar and used as received. (IM) indicates use of a nylon syringe filter (pore size 0.2 μM). All manipulations were carried out under reduced lighting and solutions were prepared stored and handled with minimal exposure to light.

NMR spectroscopy. Due to the potential photosensitivity of the compounds, amberised NMR spectroscopy tubes (Goss Scientific/Norrell) were used. Spectra were acquired at 298 K unless otherwise stated and processed using Topspin 4.0. All chemical shift (δ) values are given in parts per million and are referenced to residual solvent unless otherwise stated, *J* values are quoted in Hz.**^{1}H, ^{195}Pt and ^{14}N spectra**: were acquired on a Bruker AVIIIHD 500 MHz (500.13 MHz) equipped with a 5 mm z-gradient broadband X-19F/1H BBFO SMART probe, or on a Bruker AVIIIHD 400 nanobay (400.17 MHz). **^{13}C NMR spectra**: were acquired on a Bruker AVII 500 MHz spectrometer equipped with a z-gradient triple resonance inverse ^{1}H/^{19}F(^{13}C) TXI probe. **^{1}H-^{195}Pt HMBC NMR spectra**: ^{195}Pt chemical shifts were externally referenced to K_2PtCl_6 in 1.5 mM HCl in D_2O (δ 0 ppm). **^{1}H NOESY NMR spectra**: run with d8 = 0.8 (8 scans, 2 h, noesyphsw). **^{14}N NMR spectra**: were acquired with an aring pulse sequence as previously reported.[19] The prescan delay (DE) was 6.5 ms, the 908 pulse length was 17.25 ms and spectra were acquired with a relaxation delay (d1) of 0 s. Spectra were processed to remove the quadrature spike if needed (bc_mod qfil, bcfw 0.02, efp) with an exponential line broadening (lb) of 50. Spectra were externally referenced to a 5 mm tube containing NH_4Cl (1.5 M) in 1 M HCl, with a D_2O solution in an internal capillary (δ 0 ppm). **Mass Spectrometry**: low resolution ESI-MS were obtained with a Waters Micromass LCT Premier XE spectrometer. **HRMS**: obtained with a Thermofisher Exactive Plus with a Waters Acuity UPLC system. **MS/MS experiments**: were performed on an Acuity UPLC in flow injection analysis mode, equipped with a Waters Xevo G25 QTOF. All MS data were processed using MassLynx 4.0. Isotope patterns are predicted using Molecular Weight Calculator http://www.alchemistmatt.com/. **HPLC**: were performed with a Waters Autopurification system, equipped with a Waters X-Bridge OBD semi-prep column (5 μm, 19 mm × 50 mm), with an injection loop of 1 ml, eluting with H_2O + 0.1% NH_4OH (pH 9)/MeCN + 0.1% NH_4OH. The crude samples (in H_2O/MeCN) were filtered (nylon, 0.2 μm) and injected in 750 μL aliquots, with mass-directed purification with an ACQUITY QDa performance mass spectrometer. Analytical HPLC used the same solvents and system, with a Waters X-Bridge OBD column (5 μm, 4.6 mm × 50 mm) and an injection loop of 0.02 ml. Retention times (t_R) are quoted for the solvent gradient: 0 min (95% A: 5% B); 1 min (95:5), 7.5 min (5:95) on the analytical column. **UV-visible absorption spectra** were acquired with the Waters HPLC or a UV-Vis spectrometer (Cary 60 UV-Vis, Agilent Technologies, Figure S12). **Photochemistry**: samples were irradiated with stirring at a distance of 50 mm from a MiniSun GU10 27 SMD LED bulb with an output centred at 452 nm (see Figure S37) or with a MiniSun UVA bulb. **EPR spectroscopy**: Aqueous samples were prepared as follows. Freshly-prepared solutions of the complexes, all containing 21 mM DMPO, were loaded into bottom-sealed quartz capillaries (1.2 mm exterior diameter) using metal needles and plastic syringes. MeCN samples were prepared as follows. DMPO was dissolved in MeCN at a concentration of 21 mM and was degassed in a Schlenk tube by freeze-pump-thaw cycles until no further bubbling was observed. The solution was then transferred to a N_2 glove-box and used to dissolve complex (previously freeze-dried) to a Pt concentration of 10.5 mM. This solution was pipetted into a 25 μL glass microcapillary (IntraMark, Blaubrand), and both ends were sealed with *cristaseal* sealing wax (Hawksley). The capillaries were placed in a larger (4 mm external diameter) EPR quartz tubes and inserted into the resonator. Sample volume and position were adjusted so that the length of the sample matched the optical window of the resonator, for an optimal illumination. The EPR experimental setup consisted of a Xe arc lamp (operated at 700 W) coupled to the resonator (Bruker X-band Super High Sensitivity Probehead) of the EPR spectrometer (X-band EMXmicro, Brucker) through a liquid waveguide. The light was filtered before entering the waveguide, using a 410 nm long-pass filter followed by a 440–480 nm band pass filter. Measurements were carried out in continuous-wave mode, at X-band frequency (ca. 9.5 GHz) and room temperature, using the following parameters: field sweep of 8 mT, receiver gain of 30 dB, modulation amplitude of 0.1 mT and microwave attenuation of 23.0 dB. Quantification was done using the second integral of the spectra averaged over 100 min of continuous illumination after reaching the steady state, by interpolation of a calibration curve of TEMPO solutions of known concentrations measured in the same conditions as the sample, in the dark. The uncertainty in the radical adduct concentrations was estimated by measuring a TEMPO standard. Simulations were carried out in Matlab®, using a modified EasySpin[24] *garlic* function to allow two species to be fitted simultaneously. For the DMPO$^•$–N_3 adduct, isotropic hyperfine couplings to the nitroxidic nitrogen (a_{NO}^N = 1.450 mT), the β-proton of DMPO (a_β^H = 1.475 mT) and the α-nitrogen of the trapped azidyl radical (a_α^N = 0.314 mT) were considered. For the DMPO$^•$–OH adduct, only the first two previous hyperfine couplings were included. An isotropic g-tensor (g = 2.0005) was used in both cases. Radical adduct transients were produced from the spectral peak heights. The DMPO$^•$–N_3 transient was obtained using the two side peaks of each of the four triplets and estimating the height of the central peak as the average of the two side peaks. The DMPO$^•$–OH transient was obtained by subtraction of the DMPO$^•$–N_3 transient from the total radical adduct transient.

Synthetic procedures

Caution! ***No problems were encountered during this work, however heavy metal azides are known to be shock sensitive detonators, therefore it is essential that platinum azides compound are handled with care***

Trans, trans, trans-$[Pt(N_3)_2(OH)_2(py)_2]$ (**1**) was synthesised as previously reported. For increased production of **5**, complex **1** was isolated by crystallisation directly from the reaction solution and was not recrystallised before use, retaining residual H_2O_2 content.

Reaction of 1 with 1,4-diphenyl-2-butyne-1,4-dione (2) in MeCN to give complex 5·H_2O_2 and 3a/3b

As previously reported,[7] 1,4-diphenyl-2-butyne-1,4-dione (70 mg, 0.299 mmol) and *trans,trans,trans*-$[Pt(N_3)_2(OH)_2(py)_2]$ (150 mg, 0.318 mmol) dissolved in MeCN (22 ml) and stirred at 35 °C (48 h) produced complex **3a**/**3b** as the major product, and as well as other minor species. These products included dimer **5**, which had not been previously characterised or identified as a dimer, since the mass exceeded the detection limit of the HPLC machine. The solvent volume was reduced to 5 ml *in vacuo*, syringe filtered and purified by HPLC. Complexes **5**·H_2O_2 (t_R = 4.83 min (**31%**) and **3a**/**3b** (t_R = 5.13 min, **13%**) were isolated and the solvent removed by freeze-drying to give both as pale yellow solids (see *Figure S2*).

^{1}H NMR (**5**·H_2O_2, 500 MHz, d_3-MeCN) δ: 9.16 (s, br, 1H, H_2O_2, OH), 9.14 (dd, $^3J_{HPt}$ = 26.7, $^3J_{HH}$ = 6.7, 4H, $H_{Pyortho'}$), 8.51 (dd, $^3J_{HPt}$ = 26.7, $^3J_{HH}$ = 6.6, 4H, $H_{Pyortho}$), 8.11 (t, $^3J_{HH}$ = 7.6, 2H, $H_{Pypara'}$), 8.06 (d, $^3J_{HH}$ = 8.3, 4H, $H_{Phortho'}$), 7.85 (t, $^3J_{HH}$ = 7.8, 2H, H_{Pypara}), 7.68 (t, $^3J_{HH}$ = 7.8, 4H, $H_{Pymeta'}$), 7.59 (t, $^3J_{HH}$ = 7.5, 2H, $_{Phpara'}$), 7.46 (t, $^3J_{HH}$ = 7.8, 4H, $_{Phmeta'}$), 7.22 (t, $^3J_{HH}$ = 6.6, 4H, H_{Pymeta}), 7.09 (t, $^3J_{HH}$ = 7.4, 2H, H_{Phpara}), 6.95 (t, $^3J_{HH}$ = 7.8, 4H, H_{Phmeta}), 6.75 (d,$^3J_{HH}$ = 8.3, 4H, $H_{Phortho}$). **^{13}C NMR** (**5**·H_2O_2, 151 MHz, d_3.MeCN) δ: 187.9 (q, CO), 153.3 (q, triazole), 151.6 (q, triazole, $^2J_{CPt}$ 43.8 Hz), 150.42 (Py_{ortho}), 150.37 ($Py_{ortho'}$), 143.1 (q, Ph_{ipso}), 143.0 ($Py_{para'}$), 142.8 (Py_{para}), 138.6 (q, Ph'_{ipso}), 133.8 ($Ph_{para'}$), 131.3 ($Ph_{ortho'}$), 129.1 ($Ph_{meta'}$), 127.2 (t, $^3J_{CPt}$ = 27.2, $Py_{meta'}$), 127.0 (t, $^3J_{CPt}$ = 26.2, Py_{meta}), 128.8 (Ph_{para}), 128.6 (Ph_{meta}), 126.4 (Ph_{ortho}), 112.1 (q, C–OH).

Characterisation of 3a/3b in d_4-MeOH (freshly prepared) before rearrangement

^{195}Pt NMR (107 MHz, d_4-MeOH) δ: 832 and 784.

IR ν cm^{-1} (d_4-MeOH): 3418.25(br), 2505.31(br), 2360.65, 2342.09, 2047.76 (sharp, $\nu_{asym}N_3$), 1652.13, 1613.86, 1596.93, 1576.75, 1458.93, 1400.85, 1258.62, 1213.35, 1077.10, 1022.18, 946.22, 898.43, 768.63, 690.11. Additional characterisation of **3a**/**3b** is as previously described.[7]

Characterisation of complex 4 following rearrangement in d_4-MeOH

^{1}H NMR (**4**, 400 MHz, d_4-MeOH) δ: 9.05 (d, $^3J_{HPt}$ = 25, $^3J_{HH}$ = 6, 2H, $H_{Pyortho'}$), 8.54 (d, $^3J_{HPt}$ = 25, $^3J_{HH}$ = 6, 2H, $H_{Pyortho}$), 8.26 (dd, $^3J_{HH}$ = 6, 1H, $H_{Pypara'}$), 7.97 (dd,$^3J_{HH}$ = 6, 1H, H_{Pypara}), 7.93 (d, $^3J_{HH}$ = 6, 2H, $H_{Phortho'}$), 7.81 (dd, $^3J_{HH}$ = 7, 2H, $H_{Pymeta'}$), 7.57 (t, $^3J_{HH}$ = 7, 1H, $H_{Phpara'}$), 7.43 (dd, 2H, $^3J_{HH}$ = 7, $H_{Phmeta'}$), 7.33 (dd, 2H, H_{Pymeta}), 7.04 (dd, 1H, $^3J_{HH}$ = 7, H_{Phpara}), 6.91 (t, 2H, $^3J_{HH}$ = 7, H_{Phmeta}), 6.71 (d, 2H, $^3J_{HH}$ = 6, $H_{Phortho}$).

^{13}C NMR (**4**, 126 MHz, d_4-MeOH) δ: 188.0 (q, C_{PhCO}), 152.0 (q, $C_{triazole}$), 151.3 ($C_{Pyortho'}$), 150.7 ($C_{Pyortho}$), 145.3 (q, C_{ipsoPh}), 143.8 ($C_{Pypara'}$), 143.6 (q, $C_{triazole}$), 143.4 (C_{Pypara}), 138.8 (q, $C_{ipsoPh'}$), 134.1 ($C_{Phpara'}$), 131.2 ($C_{Phortho'}$), 129.9 ($*_{impurity}$), 129.2 ($C_{Phmeta'}$), 128.8 (C_{Phmeta}), 128.6 (C_{Phpara}), 128.1 ($^3J_{13C195Pt}$ = 26, $C_{Pymeta'}$), 127.6 ($^3J_{13C195Pt}$ = 26, C_{Pymeta}), 126.3 ($C_{Phortho}$), 108.4 (q, $C_{PhC\text{-}OX}$).

^{195}Pt NMR (**4**, 107 MHz, d_4-MeOH) δ: 824.

IR ν cm^{-1} (**4**, d_4-MeOH): 3391.11 (br), 2508.44 (br), 2048.63 (sharp, $\nu_{asym}N_3$), 1654.70, 1613.38, 1597.02, 1460.08, 1405.16, 1254.93, 1213.32, 1106.53, 1013.34, 934.54, 894.13, 768.44, 691.38.

ESI-MS (**4**, MeOH) *m/z*: (M = *trans,trans,trans*-[Pt-$(N_3)(C_{16}H_{10}N_3O_2)(OH)_2(py)_2$]): 705.71 ($[M+H]^+$ $C_{26}H_{23}N_8O_4Pt$, calcd 706.15), 687.83 ($[M–OH]^+$ $C_{26}H_{21}N_8O_3Pt$, calcd 688.13).

Deposition Number 2008628 (for **5**) contains the supplementary crystallographic data for this paper. These data are provided free of charge by the joint Cambridge Crystallographic Data Centre and Fachinformationszentrum Karlsruhe Access Structures service www.ccdc.cam.ac.uk/structures.

Acknowledgements

This work was supported by the Wellcome Trust (201406/Z/16/Z), Cancer Research UK (CR-UK) grant number C5255/A18085, through the Cancer Research UK Oxford Centre and the John Fell Fund. NF thanks Dr. Alan Kenwright and Profs. Stephen Faulkner and Andrew Weller for helpful discussions. EPR measurements were performed in the Centre for Advanced Electron Spin Resonance at the University of Oxford supported by the EPSRC (EP/L011972/1). A.M.B. gratefully acknowledges her fellowship support from the Royal Society and EPSRC for a Dorothy Hodgkin Fellowship (DH160004), and A.M.B and A.B acknowledge the support from the Royal Society Grant for Research Fellows (RGF \R1\180099).

Conflict of Interest

The authors declare no conflict of interest.

Keywords: Azides · Photoactivity · Platinum · Radicals · Structure elucidation

[1] W. P. Fehlhammer, W. Beck, *Z. anorg. allg. Chem.* **2015**, *641*, 1599–1678.
[2] P. Kreutzer, C. Weis, H. Boehme, T. Kemmerich, W. Beck, C. Spencer, R. Mason, *Z. Naturforsch* **1972**, *27b*, 745–747.
[3] K. Peng, V. Mawamba, E. Schulz, M. Löhr, C. Hagemann, U. Schatzschneider, *Inorg. Chem.* **2019**, *58*, 11508–11521.
[4] K. Peng, R. Einsele, P. Irmler, R. F. Winter, U. Schatzschneider, *Organometallics* **2020**, *39*, 1423–1430.
[5] A. R. Powers, X. Yang, T. J. Del Castillo, I. Ghiviriga, K. A. Abboud, A. S. Veige, *Dalton Trans.* **2013**, 14963–14966.
[6] N. J. Farrer, G. Sharma, R. Sayers, E. Shaili, P. J. Sadler, *Dalton Trans.* **2018**, *47*, 10553–10560.
[7] K. Yao, A. Bertran, J. Morgan, S. M. Hare, N. H. Rees, A. M. Kenwright, K. Edkins, A. M. Bowen, N. J. Farrer, *Dalton Trans.* **2019**, *48*, 6416–6420.
[8] K. Yao, A. Bertran, A. Howarth, J. M. Goicoechea, S. M. Hare, N. H. Rees, M. Foroozandeh, A. M. Bowen, N. J. Farrer, *Chem. Commun.* **2019**, 11287–11290.
[9] C. C. Beto, E. D. Holt, Y. Yang, I. Ghiviriga, K. S. Schanze, A. S. Veige, *Chem. Commun.* **2017**, *53*, 9934–9937.
[10] N. J. Farrer, D. M. Griffith, *Curr. Opin. Chem. Biol.* **2020**, *55*, 59–68.
[11] U. F. Röhrig, S. R. Majjigapu, A. Grosdidier, S. Bron, V. Stroobant, L. Pilotte, D. Colau, P. Vogel, B. J. Van Den Eynde, V. Zoete, et al., *J. Med. Chem.* **2012**, *55*, 5270–5290.

[12] H. Song, N. J. Rogers, V. Brabec, G. J. Clarkson, J. Coverdale, H. Kostrhunova, R. M. Phillips, M. L. Postings, S. Shepherd, P. Scott, *Chem. Commun.* **2020**, *56*, 6392–6395.
[13] F. Ahmed, H. Xiong, *Dyes Pigm.* **2021**, *185*, 108905.
[14] N. J. Farrer, J. A. Woods, L. Salassa, Y. Zhao, K. S. Robinson, G. Clarkson, F. S. Mackay, P. J. Sadler, *Angew. Chem. Int. Ed.* **2010**, *49*, 8905–8908; *Angew. Chem.* **2010**, *122*, 9089–9092.
[15] J. F. Vollano, E. E. Blatter, J. C. Dabrowiak, *J. Am. Chem. Soc.* **1984**, *106*, 2732–2733.
[16] O. V. Dolomanov, L. J. Bourhis, R. J. Gildea, J. A. K. Howard, H. Puschmann, *J. Appl. Crystallogr.* **2009**, *42*, 339–341.
[17] P. L. Holland, *Dalton Trans.* **2010**, *39*, 5415–5425.
[18] J. M. Fontmorin, R. C. Burgos Castillo, W. Z. Tang, M. Sillanpää, *Water Res.* **2016**, *99*, 24–32.
[19] N. J. Farrer, P. Gierth, P. J. Sadler, *Chem. Eur. J.* **2011**, *17*, 12059–12066.
[20] K. Sutter, J. Autschbach, *J. Am. Chem. Soc.* **2012**, *134*, 13374–13385.
[21] A. Yahav, I. Goldberg, A. Vigalok, *Organometallics* **2005**, *24*, 5654–5659.
[22] A. Radu, R. Conde, C. Fontolliet, G. Wagnieres, H. Van den Bergh, P. Monnier, *Gastrointest. Endosc.* **2003**, *57*, 897–905.
[23] F. A. Villamena, C. M. Hadad, J. L. Zweier, *J. Phys. Chem. A* **2003**, *107*, 4407–4414.
[24] S. Stoll, A. Schweiger, *J. Magn. Reson.* **2006**, *178*, 42–55.

Manuscript received: January 18, 2021
Revised manuscript received: February 23, 2021
Accepted manuscript online: March 1, 2021

ChemComm

COMMUNICATION

View Article Online
View Journal | View Issue

Cite this: *Chem. Commun.*, 2019, 55, 11287

Received 10th July 2019,
Accepted 30th July 2019

DOI: 10.1039/c9cc05310g

rsc.li/chemcomm

A visible-light photoactivatable di-nuclear Pt^{IV} triazolato azido complex†

Kezi Yao, Arnau Bertran, Alison Howarth, Jose M. Goicoechea, Samuel M. Hare, Nicholas H. Rees, Mohammadali Foroozandeh, Alice M. Bowen and Nicola J. Farrer *

A novel Pt^{IV} triazolato azido complex [3]-[N1,N3] has been synthesised *via* a strain-promoted double-click reaction (SPDC) between a Pt^{IV} azido complex (1) and the Sondheimer diyne (2). Photoactivation of [3]-[N1,N3] with visible light (452 nm) in the presence of 5′-guanosine monophosphate (5′-GMP) produced both Pt^{IV} and Pt^{II} 5′-GMP species; EPR spectroscopy confirmed the production of both azidyl and hydroxyl radicals. Spin-trapping of photogenerated radicals – particularly hydroxyl radicals – was significantly reduced in the presence of 5′-GMP.

Of the cancer patients who are treated with chemotherapy, approximately 50% receive a Pt^{II} drug such as cisplatin, carboplatin or oxaliplatin.[1] However, the side-effects of treatment with Pt^{II} drugs can be severe, and the development of resistance can also be a serious problem.[2] Octahedral low-spin $5d^6$ Pt^{IV} prodrugs are more kinetically inert than their Pt^{II} counterparts, and have the potential to address these issues.[3–6] Both redox-activatable[7,8] and photoactivatable[9–12] Pt^{IV} prodrugs can exhibit promising pharmacological properties and can also incorporate ligands which - when released upon reduction of Pt^{IV} to Pt^{II} – exert an anti-cancer effect through mechanisms of action which are different from those of established Pt^{II}-based drugs.[5,13]

Whilst the photochemistry of Pt^{IV} diazido complexes has been extensively investigated, Pt^{IV} monoazido complexes are less well explored. It was not known if two azido groups are necessary for photoreduction to Pt^{II}, and what products were likely to be formed under irradiation. Direct derivation of a Pt^{IV} diazido complex was anticipated to be an effective way to answer these questions. Cycloaddition (click) reactions of metal azido complexes are well-established[14] – although mostly for Pt^{II} rather than Pt^{IV}. We recently reported the first Pt^{IV} triazolato monoazido complexes; synthesised *via* click reactions of Pt^{IV} azido complexes with both electron-deficient (*e.g.* 1,4-diphenyl-2-butyne-1,4-dione)[15] and strained alkynes (*e.g.* DBCO; dibenzocyclooctyne-amine).[16] Due to the popularity of click chemistry, a range of 1,2,3-triazoles with potential biomedical applications have been reported;[17–19] 1,2,3-triazoles have the potential to participate in C–H hydrogen bonding; behave as hydrogen bond donors through both non-coordinated N-atoms; act as intercalating agents *via* π–π stacking and substitute for amides; making them attractive ligands.[20] Pt^{II} triazole complexes[21] and triazolato-bridged Pt^{II} complexes have been shown to demonstrate promising anti-cancer activity.[22]

Strain-promoted azide–alkyne [3+2] cycloaddition (SPAAC) exploits the spontaneous reactivity of cyclooctynes and azides due to inherent ring strain in the cyclooctyne.[23] It can be used to assemble constructs under mild conditions for both biological (*e.g.* vascularly-targeted radiolabelled liposomes,[24] glycan imaging[25] and glycocalyx selective editing[26]) and chemical (*e.g.* Ru azido DBCO[27] and Pt^{II}-DBCO fluorophore[28]) applications.

The Sondheimer diyne (5,6,11,12-tetradehydrodibenzo[*a*,*e*]-cyclooctene) (2) (Scheme 1) is a strained diyne which is straightforward to synthesise. It has been used as a monomer in Mo-catalysed ring-opening alkyne metathesis polymerization reactions[29] and to couple together Ag(I) species[30] and biomolecules.[31] For our purposes, it enables the union of two – potentially different – Pt^{IV} azido complexes under catalyst-free conditions, without interaction of either Pt^{IV} centre with any other functional groups on the newly formed 1,2,3-triazole

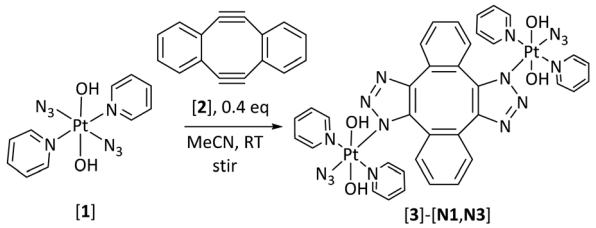

Scheme 1 Synthesis of Pt^{IV} triazolato azido complex **(3)-[N1,N3]**.

Chemistry Research Laboratory, University of Oxford, 12 Mansfield Road, Oxford, OX1 3TA, UK. E-mail: Nicola.Farrer@chem.ox.ac.uk; Tel: +44 (0)1865 285131

† Electronic supplementary information (ESI) available: Synthetic details and characterisation data including X-ray crystallographic tables. CCDC 1885195 contains the supplementary crystallographic data for this paper. For ESI and crystallographic data in CIF or other electronic format see DOI: 10.1039/c9cc05310g

ligands – something which has complicated our earlier studies.[15,16] Di-nuclear Pt^{IV} complexes are promising since they can be used to deliver multiple different biologically active agents to cancer cells.[8] Here we report the facile, catalyst-free assembly of the water-soluble, water-stable, di-nuclear Pt^{IV} 1,2,3-triazolato azido complex **3-[N1,N3]** and our investigations into its photochemical properties (Scheme 1).

Diyne (**2**) was synthesised according to literature reports and purified by column chromatography (ESI†).[32,33] *trans*,*trans*,*trans*-$[Pt(N_3)_2(OH)_2(py)_2]$ (**1**) was synthesised and purified by HPLC.[34] The reaction between **1** (200 mg, 0.42 mmol) and **2** (30 mg, 0.15 mmol, 0.4 eq.) in MeCN (150 ml) at room temperature was monitored by LCMS and was judged to be complete after 2d. No mono-Pt^{IV} cycloaddition intermediates were detected by ESI-MS during the course of the reaction. This is consistent with DFT calculations of the reactivity profile of **2**, which indicate that the activation energy for the second cycloaddition is lower than for the first, due to the highly distorted alkyne bond in the mono-substituted intermediate, arising from steric repulsion between the substituent on the triazole ring and the hydrogen atom on the benzene ring.[31] The reaction solution was dilute, minimising the formation of Pt^{IV} oligomers (see Fig. S1, ESI†) due to potential reactivity of the second Pt^{IV}-azido ligand.

The major product (**3**) was detected by LCMS, as both $[\mathbf{3} + H]^+$ (1143.20 *m*/*z*) and $[\mathbf{3} + Na]^+$ (1165.36 *m*/*z*) adducts. Complex **3** was isolated by mass-directed LCMS as a mixture of two regioisomers: **3-[N1,N3]** and **3-[N3,N3]** (Fig. S2, ESI†). HPLC re-injection confirmed the isomers co-eluted with a purity of 95% (Fig. S3, ESI†). Following solvent removal and reconstitution of the pale yellow solid in d_3-MeCN, ^{1}H NMR spectroscopy indicated that **3-[N1,N3]** – which has two-fold symmetry – was the major isomer present. This is consistent with the previously reported reaction of **2** with excess benzyl azide which resulted in a 60% [N1,N3]: 38% [N1,N1] product distribution.[31] Yellow crystals of **3-[N1,N3]** rapidly formed from the solution of regioisomers in d_3-MeCN, on standing for 24 h.

Recrystallisation from MeCN afforded X-ray crystallographic quality crystals of **3-[N1,N3]** (Fig. 1), confirming [N1,N3] Pt^{IV}-triazole coordination and revealing the ligand interactions around the puckered chair of the cyclooctene ligand. Distances between pyridine, triazole and benzene groups are shown in Fig. S4–S6 (ESI†); the pyridine ligands undergo π–π interactions with the cyclooctene ring ranging from 3.527–4.509 Å in length. A hydrogen-bond interaction of 2.178(3) Å was observed between Pt(1)–OH(2) and triazole N(2); the corresponding hydrogen-bond interaction on the other side of the molecule measured 2.242 Å (Pt–OH(3) to triazole N(5)). The identity of **3** was also confirmed by HRMS $[\mathbf{3} + H]^+$ ($C_{36}H_{32}N_{16}O_4Pt_2H$): 1143.2123 *m*/*z* found; 1143.2069 *m*/*z* calcd (Fig. S7, ESI†).

Collision-induced dissociation (MS/MS) experiments of $[$**3-[N1,N3]** $+ H]^+$ demonstrated that at low collision energies the complex readily fragmented through loss of OH and N_3 ligands, to give stable species $[$**3-[N1,N3]**$–N_3OH + H]^+$ (1083.32 *m*/*z*) and $[$**3-[N1,N3]**$–2(N_3OH)]^+$, (1023.30 *m*/*z*), consistent with our previous observations of azido ligand loss during MS/MS fragmentation of **1**.[34] Stable mono-Pt fragments were also

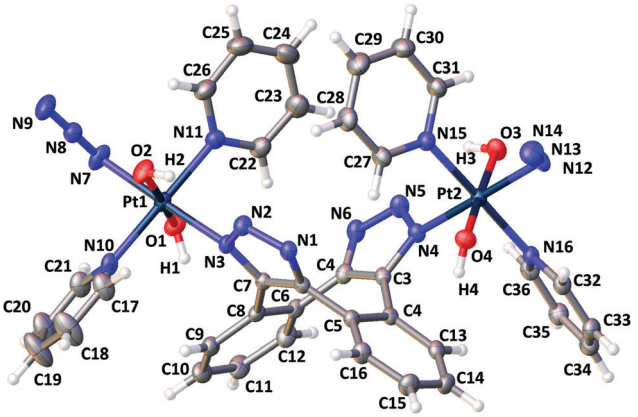

Fig. 1 X-ray crystallographic structure of **3-[N1,N3]** with thermal ellipsoids displayed at 50% probability.[35] Selected bond lengths (Å): Pt1–N3: 2.060(2), Pt1–N7: 2.041(3), N7–N8: 1.219(4), N8–N9: 1.151(5). Pt1–O2: 2.002(2). Selected angles (°): Pt1–N7–N8: 114.1(2); N7–N8–N9: 174.5(4). (See Tables S1–S3, ESI†).

observed, including $[Pt(C_{16}N_6H_7)N_3]^+$ (520.15 *m*/*z*) resulting from ejection of several small ligands and one Pt fragment from the central cyclooctene ligand, as well as smaller fragments including $([Pt(py)_2(OH)_2]^+$ (387.12 *m*/*z*)) $([Pt(py)_2(OH)]^+$ (370.11 *m*/*z*)) and $([Pt(Py)_2]^+$ (352.10 *m*/*z*)) demonstrating cleavage of the Pt–triazole bond (Fig. S7, ESI†).

Complex **3-[N1,N3]** was fully characterised by ^{195}Pt, ^{1}H and ^{13}C NMR spectroscopic methods. ^{1}H NMR spectroscopy revealed four different phenyl environments; a 2D ^{1}H TOCSY experiment was used to determine the complete spin systems and to obtain coupling constants for overlapping signals (Fig. S9, ESI†) and 1D NOESY experiments revealed nOe interactions between pyridine (H_o) and phenyl ring (H_A) protons, confirming the regiochemistry of the product (Fig. S10, ESI†). ^{13}C NMR spectral assignment (Fig. S11, ESI†) was aided by ^{1}H–^{13}C HSQC and HMBC experiments. Complex **3-[N1,N3]** gave rise to a single ^{195}Pt NMR spectral resonance at 723 ppm (d_3-MeCN, Fig. S12-top, ESI†).

Whilst **3-[N1,N3]** is stable in both d_3-MeCN and D_2O for a period of at least 5 weeks as judged by ^{1}H NMR spectroscopy, the resonances change position markedly in the different solvents. Solvent removal from a sample of **3-[N1,N3]** in d_3-MeCN followed by reconstitution in D_2O resulted in an overall 163 ppm upfield shift in ^{195}Pt NMR resonance from 723 ppm (d_3-MeCN) to 857 ppm (1 : 1 d_3-MeCN : D_2O) to 886 ppm (D_2O, Fig. S12-bottom, ESI†). In the ^{1}H NMR spectrum (D_2O), the $H_{A'}$ and $H_{B'}$ protons of the benzene rings no longer superimposed on the pyridyl H_m resonances (Fig. S13 and S14, ESI†). Consistent with this, the ^{195}Pt NMR resonance of **1** also changes by 164 ppm on changing solvent from d_3-MeCN (778 ppm, this work) to D_2O (942 ppm).[34] Selective ^{1}H NOESY NMR experiments on **3-[N1,N3]** (D_2O) revealed the same nOe correlations which were observed in d_3-MeCN, with dissolution in 1 : 1 MeCN/D_2O showing ^{1}H NMR resonances at intermediate chemical shifts (Fig. S14-middle, ESI†), indicating that the change is unlikely to be due to a formal N1–N2 Pt–triazole rearrangement in D_2O – a

possibility for metal triazole complexes which we wanted to rule out.[27,36,37]

IR spectroscopy of a d_3-MeCN sample of **3-[N1,N3]** (Fig. S15, ESI†) showed a strong $\nu_{asym}N_3$ stretch at 2043 cm^{-1}; slightly lower than observed for **1** (2051 cm^{-1}, solid).[38] The UV-Vis spectrum of **3-[N1,N3]** showed a long shoulder with λ_{max} *ca.* 254 nm tailing into the visible region corresponding to the N_3 → Pt LMCT transition band, with increased intensity at shorter wavelengths compared to **1** due to the additional aromatic groups (Fig. S16, ESI†).

A D_2O (1 ml) solution of complex **(3)-[N1,N3]** (5.6 mg) and the DNA model 5′-GMP (2 eq. 4.8 mg) was irradiated (λ_{irr} 452 nm) with regular monitoring by LCMS and ^{1}H NMR spectroscopy. Both Pt^{IV} and Pt^{II} photoproducts were detected by LCMS including non-5′-GMP bound species (where M = **3-[N1,N3]**): $[M–N_3]^+$ at 1100.12 *m/z*; $[M–H_2O_2 + H]^+$ at 1109.12 *m/z*; $[$**3-[N1,N3]**$–N_3OH + H^+]^+$ 1084.05 *m/z*. The cyclic-5′-GMP species $[Pt^{II}(OH)(py)_2(N_5C_{10}O_7H_{12}P)]^+$ was observed at 715.14 *m/z*, although – unlike for similar investigations with complex **1** – no evidence of $[Pt(OH)(py)_2(5′\text{-GMP})]^+$ was observed (predicted 733.1097 *m/z*). The LCMS *m/z* range is limited to 1250 *m/z* and a different ESI-MS instrument was therefore used to detect the presence of higher mass species, including the Pt^{II}*bis*-GMP adduct: $[M–2(H_2O_2)–2N_3 + 2(5′\text{-GMP}) + Na]^+$ at 1739.85 *m/z*. (Fig. S17, ESI†).

The photochemistry was also monitored by ^{1}H–^{195}Pt HMBC and 1D ^{195}Pt NMR spectroscopy (**(3)-[N1,N3]** 22 mM; 5′-GMP 46 mM, 1 : 1 D_2O : d_3-MeCN, λ_{irr} 452 nm, 180 min). During irradiation, the intensity of the ^{195}Pt NMR spectroscopic resonance corresponding to **(3)-[N1,N3]** (854 ppm) decreased, with small amounts of new Pt^{IV} species (1267, 1350 ppm) and two more intense Pt^{II} signals appearing (−2224 ppm and −2369 ppm; Fig. S18 and S19, ESI†). These spectra were consistent with the formation of multiple Pt^{II} and Pt^{IV} photoproducts, as observed by LCMS (for discussion see end of ESI†).

Irradiation of a solution of **3-[N1,N3]** (1.15 mM) and 5,5-dimethyl-1-pyrroline *N*-oxide (DMPO, 20 mM) monitored by EPR spectroscopy in either water or cell-free lysate (KNS42) generated azidyl ($N_3^•$) and hydroxyl ($OH^•$) radical species, trapped in a 85 : 15 and 90 : 10 molar ratio, respectively (Fig. S20(a), ESI† and Fig. 2(a)), with a maximum trapped radical concentration of 7 μM. The signals started to decay after ∼30 min irradiation (Fig. S23(a), ESI† and Fig. 2(b)). The inclusion of 5′-GMP in the solution of **3-[N1,N3]** in lysate had a significant effect; the maximum trapped radical concentration reduced to 3 μM with a 95 : 5 $N_3^•$: $OH^•$ molar ratio (Fig. S22(a), ESI†) and radical trapping slowed down (Fig. S25(a), ESI†). These experiments were repeated with complex **1** (Fig. S20(b), S21(b) and S22(b), ESI†) which released almost no hydroxyl radicals, reaching a much higher trapped radical maximum concentration of 32 μM in water and lysate. The rise and decay of the signal was faster (Fig. S23(b) and S24(b), ESI†) in comparison to **3-[N1,N3]**, consistent with **1** having a greater absorbance at the wavelength of irradiation. The effect of including 5′-GMP in the lysate solution of complex **1** was less pronounced (Fig. S22(b) and S25(b), ESI†) than for **3-[N1,N3]**, with only a slightly lower maximum trapped radical concentration (28 μM) and slower

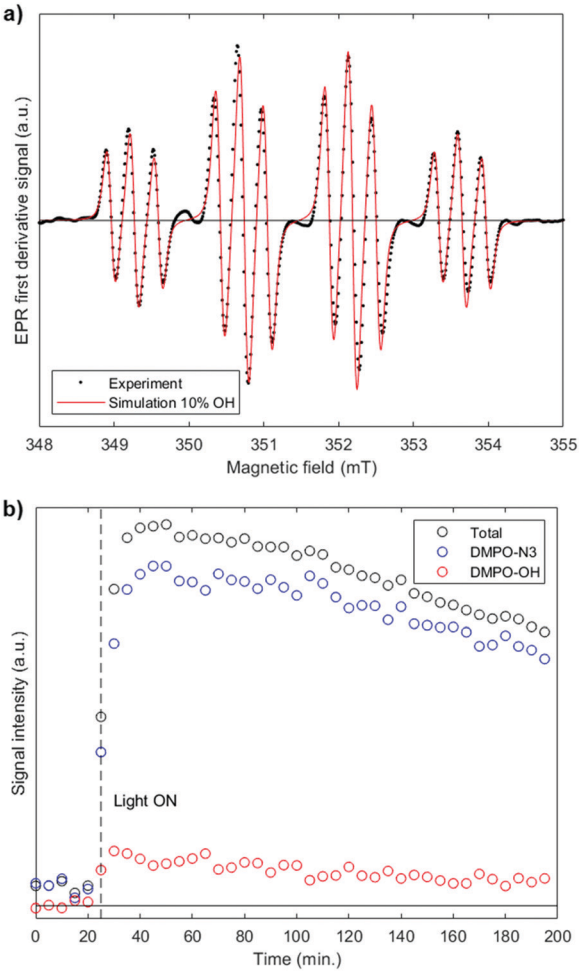

Fig. 2 X-band cw-EPR spectrum (a) showing trapping of azidyl ($N_3^•$) and hydroxyl ($OH^•$) radicals (1.15 mM **(3)-[N1,N3]** + 20 mM DMPO spin-trap) in freshly prepared KNS42 lysate (λ_{irr} 440–480 nm; spectra averaged over 1 h of maximum signal intensity); (b) fitted spectrum with 90% DMPO-N_3 and 10% DMPO-OH (red line). The kinetic profile (b) for the total radical adduct signal (black) has been deconvoluted into the DMPO-N_3 (blue) and DMPO-OH (red) contributions.

kinetics in the presence of 5′-GMP. Minimal radical release was observed in the absence of irradiation in aqueous solution, consistent with the observed stability of **3-[N1,N3]** and **1** (Fig. S26, ESI†). Irradiation of controls (DMPO, and 5′-GMP + DMPO) in lysate did not result in any trapped radicals (Fig. S27, ESI†).

To conclude, we have demonstrated an effective method for joining together two Pt^{IV} azido complexes to give the di-nuclear Pt^{IV} triazolato azido complex **3-[N1,N3]** which is soluble and stable in aqueous solution for at least 5 weeks. Irradiation of **3-[N1,N3]** with visible light (λ_{irr} 452 nm) in the presence of 5′-GMP results in the formation of new Pt^{IV} and Pt^{II} species as well as radical species ($N_3^•$, $OH^•$) in both H_2O and cell-free lysate. Whilst the presence of two Pt-azido groups in complex **1** predominantly favours photochemical release of azido radicals, **3-[N1,N3]** undergoes photoreduction to Pt^{II} with the production of a greater proportion of hydroxyl radicals, consistent with the Pt^{IV} monoazido structure. Radical – particularly $OH^•$ – trapping

from **3-[N1,N3]** was affected to a greater extent by the presence of 5′-GMP, in contrast to irradiation of **1**. It has previously been shown that $N_3^\bullet$ produced by irradiation of **1** can be quenched by L-tryptophan (Trp),[39] forming Trp radicals;[40] our future work will investigate the interaction of hydroxyl radicals with 5′-GMP and the possible photocytotoxicity of **3-[N1,N3]**.

We thank the Wellcome Trust (201406/Z/16/Z), Cancer Research UK (C5255/A18085) through the Cancer Research UK Oxford Centre, the John Fell Fund and L'Oréal (Women in Science Fellowship). NF thanks Prof. Stephen Faulkner and Prof. Andy Weller for helpful discussions and Dr Richard Hill and Prof. Chris Jones for the KNS42 cell line. EPR measurements were performed in the Centre for Advanced Electron Spin Resonance at the University of Oxford EPSRC (EPL011972/1). AMB thanks the Royal Society and EPSRC for a Dorothy Hodgkin Fellowship (DH160004); AMB and AB thank the Royal Society for a Grant for Research Fellows (RGF\R1\180099). MF thanks the Royal Society for a University Research Fellowship and an Enhancement Award (grant numbers URF\R1\180233 and RGF\EA\181018).

Conflicts of interest

There are no conflicts to declare.

Notes and references

1 M. Galanski, M. A. Jakupec and B. K. Keppler, *Curr. Med. Chem.*, 2005, **12**, 2075.
2 R. Oun, Y. E. Moussa and N. J. Wheate, *Dalton Trans.*, 2018, **47**, 6645.
3 D. Gibson, *J. Inorg. Biochem.*, 2019, **191**, 77.
4 M. Ravera, E. Gabano, M. J. McGlinchey and D. Osella, *Inorg. Chim. Acta*, 2019, **492**, 32.
5 R. G. Kenny, S. W. Chuah, A. Crawford and C. J. Marmion, *Eur. J. Inorg. Chem.*, 2017, 1596.
6 T. C. Johnstone, K. Suntharalingam and S. J. Lippard, *Chem. Rev.*, 2016, **116**, 3436.
7 K. G. Z. Lee, M. V. Babak, A. Weiss, P. J. Dyson, P. Nowak-Sliwinska, D. Montagner and W. H. Ang, *ChemMedChem*, 2018, **13**, 1210.
8 E. Petruzzella, J. P. Braude, J. R. Aldrich-Wright, V. Gandin and D. Gibson, *Angew. Chem., Int. Ed.*, 2017, **56**, 11539.
9 S. Perfahl, M. M. Natile, H. S. Mohamad, C. A. Helm, C. Schulzke, G. Natile and P. J. Bednarski, *Mol. Pharmaceutics*, 2016, **13**, 2346.
10 H. C. Tai, Y. Zhao, N. J. Farrer, A. E. Anastasi, G. Clarkson, P. J. Sadler and R. J. Deeth, *Chem. – Eur. J.*, 2012, **18**, 10630.
11 I. Infante, J. M. Azpiroz, N. G. Blanco, E. Ruggiero, J. M. Ugalde, J. C. Mareque-Rivas and L. Salassa, *J. Phys. Chem. C*, 2014, **118**, 8712.
12 G. J. Clarkson, J. Song, V. Venkatesh, I. Romero-Canelón, H. Shi, V. Brabec, O. Novakova, P. J. Sadler, M. Hreusova and A. Habtemariam, *Inorg. Chem.*, 2018, **57**, 14409.
13 J. J. Wilson and S. J. Lippard, *Chem. Rev.*, 2014, **114**, 4470.
14 W. P. Fehlhammer and W. Beck, *Z. Anorg. Allg. Chem.*, 2015, **641**, 1599.
15 K. Yao, A. Bertran, J. Morgan, S. M. Hare, N. H. Rees, A. M. Kenwright, K. Edkins, A. M. Bowen and N. J. Farrer, *Dalton Trans.*, 2019, **48**, 6416.
16 N. J. Farrer, G. Sharma, R. Sayers, E. Shaili and P. J. Sadler, *Dalton Trans.*, 2018, **47**, 10553.
17 D. Dheer, V. Singh and R. Shankar, *Bioorg. Chem.*, 2017, **71**, 30.
18 E. Bonandi, M. S. Christodoulou, G. Fumagalli, D. Perdicchia, G. Rastelli and D. Passarella, *Drug Discovery Today*, 2017, **22**, 1572.
19 B. Schulze and U. S. Schubert, *Chem. Soc. Rev.*, 2014, **43**, 2522.
20 A. Massarotti, S. Aprile, V. Mercalli, E. Del Grosso, G. Grosa, G. Sorba and G. C. Tron, *ChemMedChem*, 2014, **9**, 2497.
21 A. Maisonial, P. Serafin, M. Traïkia, E. Debiton, V. Théry, D. J. Aitken, P. Lemoine, B. Viossat and A. Gautier, *Eur. J. Inorg. Chem.*, 2008, 298.
22 S. Komeda, M. Lutz, A. L. Speck, M. Chikuma and J. Reedijk, *Inorg. Chem.*, 2000, **39**, 4230.
23 J. C. Jewett and C. R. Bertozzi, *Chem. Soc. Rev.*, 2010, **39**, 1272.
24 E. D. Hood, C. F. Greineder, T. Shuvaeva, L. Walsh, C. H. Villa and V. R. Muzykantov, *Bioconjugate Chem.*, 2018, **29**, 3626.
25 H. Stöckmann, A. A. Neves, S. Stairs, H. Ireland-Zecchini, K. M. Brindle and F. J. Leeper, *Chem. Sci.*, 2011, **2**, 932.
26 H. Xiao, E. C. Woods, P. Vukojicic and C. R. Bertozzi, *Proc. Natl. Acad. Sci. U. S. A.*, 2016, **113**, 10304.
27 T. Cruchter, K. Harms and E. Meggers, *Chem. – Eur. J.*, 2013, **19**, 16682.
28 E. Kitteringham, D. Wu, S. Cheung, B. Twamley, D. F. O'Shea and D. M. Griffith, *J. Inorg. Biochem.*, 2018, **182**, 150.
29 W. S. Perkins, S. von Kugelgen, F. R. Fischer, R. R. Cloke and D. E. Bellone, *J. Am. Chem. Soc.*, 2016, **138**, 6234.
30 B. Hellbach, F. Rominger and R. Gleiter, *J. Organomet. Chem.*, 2006, **691**, 1814.
31 I. Kii, A. Shiraishi, T. Hiramatsu, T. Matsushita, H. Uekusa, S. Yoshida, M. Yamamoto, A. Kudo, H. Masatoshi and T. Hosoya, *Org. Biomol. Chem.*, 2010, **8**, 4051.
32 H. N. C. Wong, P. Garratt and F. Sondheimer, *J. Am. Chem. Soc.*, 1974, **96**, 5604.
33 A. Orita, D. Hasegawa, T. Nakano and J. Otera, *Chem. – Eur. J.*, 2002, **8**, 2000.
34 N. J. Farrer, J. A. Woods, L. Salassa, Y. Zhao, K. S. Robinson, G. Clarkson, F. S. Mackay and P. J. Sadler, *Angew. Chem., Int. Ed.*, 2010, **49**, 8905.
35 O. V. Dolomanov, L. J. Bourhis, R. J. Gildea, J. A. K. Howard and H. Puschmann, *J. Appl. Crystallogr.*, 2009, **42**, 339.
36 P. Schmid, M. Maier, H. Pfeiffer, A. Belz, L. Henry, A. Friedrich, F. Schönfeld, K. Edkins and U. Schatzschneider, *Dalton Trans.*, 2017, **46**, 13386.
37 K. S. Singh, K. A. Kreisel, G. P. A. Yap and M. R. Kollipara, *J. Organomet. Chem.*, 2006, **691**, 3509.
38 R. R. Vernooij, T. Joshi, E. Shaili, M. Kubeil, D. R. T. Appadoo, E. I. Izgorodina, B. Graham, P. J. Sadler, B. R. Wood and L. Spiccia, *Inorg. Chem.*, 2016, **55**, 5983.
39 J. S. Butler, J. a Woods, N. J. Farrer, M. E. Newton and P. J. Sadler, *J. Am. Chem. Soc.*, 2012, **134**, 16508.
40 C. Vallotto, E. Shaili, H. Shi, J. S. Butler, C. J. Wedge, M. E. Newton and P. J. Sadler, *Chem. Commun.*, 2018, **54**, 13845.

Dalton Transactions

PAPER

View Article Online
View Journal | View Issue

Cite this: *Dalton Trans.*, 2019, **48**, 6416

A novel Pt(IV) mono azido mono triazolato complex evolves azidyl radicals following irradiation with visible light†

Kezi Yao,[a] Arnau Bertran,[a] Jacques Morgan,[a] Samuel M. Hare,[a] Nicholas H. Rees,[a] Alan M. Kenwright,[b] Katharina Edkins,[c] Alice M. Bowen[a] and Nicola J. Farrer*[a]

The platinum(IV) azido complex *trans,trans,trans*-[$Pt^{IV}(N_3)_2(OH)_2(py)_2$] (**1**) undergoes cycloaddition with 1,4-diphenyl-2-butyne-1,4-dione (**2**) under mild, catalyst-free conditions, affording a number of mono and bis click products. The major mono click product (**3**) exists in MeCN as an equilibrium mixture between two species; **3a** and **3b** rapidly interconvert through nucleophilic attack of the axial Pt–OH group at the adjacent Ph–CO group. The kinetic and thermodynamic parameters for this interconversion have been measured by selective saturation-transfer NMR spectroscopic experiments and are consistent with cyclisation at the Pt centre. Complex **3b** was also characterised by X-ray crystallography. Visible light irradiation (440–480 nm) of **3** in d_3-MeCN produces azidyl radicals ($N_3^{\bullet}$), as demonstrated by EPR spin-trapping with DMPO; no generation of hydroxyl radicals was observed. $^{1}H-^{195}Pt$ HMBC NMR confirmed that the photoproducts were Pt^{IV} rather than Pt^{II} species, and HPLC was consistent with these being [**3**–N_3]$^+$ species; no facile photoejection of the triazolato ligand was observed, consistent with MS/MS fragmentation of **3**. When **3** was irradiated in the presence of 5′-GMP, no 5′-GMP photoproducts were observed, suggesting that complex **3** is likely to exhibit significantly simplified biological activity (release of azidyl radicals but not DNA binding) compared with complex **1**.

Received 18th March 2019,
Accepted 29th March 2019

DOI: 10.1039/c9dt01156k

rsc.li/dalton

Introduction

Reactivity of metal azides towards acetylenes in a [3 + 2] 1,3-dipolar cycloaddition (or "click" reaction) to form triazoles is a well-established route to form new metal complexes and new ligands which are not readily accessible by other routes.[1] Although [3 + 2] cycloadditions have been extensively investigated in organic synthesis, the potential of cycloaddition reactions of metal-coordinated ligands is less well-explored. To date, click reactions between metal azides and alkynes (or masked alkynes)[2] have been used in a range of synthetic investigations; forming Pt(II)–Au(I) heterometallic arrays,[3] tri-Au(I) triazoles,[4] Ru-based catalysts[5] and metalloenzyme inhibitors.[6] They have also been used to synthesise Au(I) triazole peptide conjugates targeted to mitochondria, which showed promising anti-cancer activity.[7] The new triazole ligands formed in these cycloaddition reactions themselves have a wide-range of chemistries and potential applications.[8] Whilst copper(I)-catalysed (CuAAC) reactions dominate the literature,[9] our focus is on copper-free cycloadditions, since the cytotoxicity of copper salts is undesirable for biological applications.[10] We recently reported that *trans,trans,trans*-[$Pt(N_3)_2(OH)_2(py)_2$] **1** is reactive towards a number of strained cyclooctynes and highly electron-deficient acetylenes including DMAD, but does not react with other acetylenes including phenylpropiolic acid, 1-phenyl-2-propyn-1-ol and 3-butyn-2-one.[11]

We focused on internal alkynes, because terminal alkynes (HC≡CR) often undergo azide-acetylene ligand exchange with metal azides, rather than 1,3-dipolar cycloaddition; for example, *cis*-[$Pt(N_3)_2(PPh_3)_2$] reacts with acetylenylbenzene to give *trans*-[$Pt(C{\equiv}CPh)_2(PPh_3)_2$].[12] Consequently, we investigated the reactivity of the azido complex **1** towards the acetylene 1,4-diphenyl-2-butyne-1,4-dione (**2**) and here we report our findings.

Although no Pt(II) or Pt(IV) examples have been previously reported, acetylene **2** (Scheme 1) undergoes cycloadditions

[a]*Chemistry Research Laboratory, University of Oxford, 12 Mansfield Road, Oxford, OX1 3TA, UK. E-mail: Nicola.Farrer@chem.ox.ac.uk; Tel: +44 (0)1865 285131*
[b]*School of Pharmacy, Queen's University Belfast, 97 Lisburn Road, Belfast BT9 7BL, UK*
[c]*Department of Chemistry, University of Durham, South Road, Durham DH1 3LE, UK*

†Electronic supplementary information (ESI) available: Synthetic details and characterisation data including X-ray crystallographic tables. CCDC 1883808. For ESI and crystallographic data in CIF or other electronic format see DOI: 10.1039/c9dt01156k

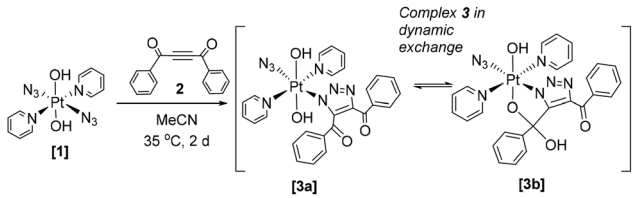

Scheme 1 Reaction of *trans,trans,trans*-$[Pt(N_3)_2(OH)_2(py)_2]$ (**1**) with 1,4-diphenyl-2-butyne-1,4-dione (**2**) showing formation of the major product **3** (**3a**/**3b**).

with both Pd(II)[13] and Ni(II)[14] mono azido complexes. For Pd(II), the coordinated triazole ligand is not constrained through additional cyclisation, and equivalent ^{1}H NMR spectral resonances for the Ph groups were observed, consistent with rearrangement to N2 triazole coordination. For Ni(II), in addition to triazole formation, one of the PhCO groups of the triazole condensed with a ligand-based NH_2 group, forming a 5-membered ring containing the Ni; the IR and ^{1}H NMR spectra indicated triazole formation and retention of N1-coordination. It is generally accepted that the N1-bound triazole isomer forms as the kinetic product of the cycloaddition reaction. For metal-based cycloadditions – in contrast to purely organic cycloadditions – this isomer may often then undergo rearrangement to the more thermodynamically stable N2-bound isomer.[15] The N1/N2 coordination preference appears to be a balance of sterics, electronics and any potential ligand cyclisation which could "lock" the triazole in N1 coordination. Small modifications in the ligands may alter the N1/N2 preference; for the reaction of Ru-azido complexes with DMAD and diethylacetylenedicarboxylate (DEACD), X-ray crystallography confirmed a change in preference from N1 (ethyl) to N2 (methyl) triazole coordination depending on the ligand substituents for a number of Ru azido complexes.[16,17]

Since Pt(IV) azido groups are considerably less electron-rich than Pt(II) azides they are anticipated to be even less amenable to cycloaddition with electron-deficient acetylenes. We were therefore surprised to observe the reaction of **2** with the Pt^{IV} diazido complex **1** under mild conditions.

Results and discussion

After stirring a solution of **1** and **2** (1.1 eq.) in MeCN (35 °C, 2 d) the reaction solution was concentrated under vacuum and filtered. RP-HPLC (MeCN + 0.1% NH_4OH/H_2O + 0.1% NH_4OH, pH 9) purification of the filtrate revealed four new cycloaddition products, three mono-substituted species; (t_R = 4.01 min, 8%); complex **3** (t_R = 4.31 min, 73%); (t_R = 5.44 min, 2%) and one bis-substituted species (t_R = 5.94 min, 7%) (Fig. S1†).

Complex 3 consists of interconverting isomers 3a and 3b

HPLC solvent was removed from the main product **3** (t_R 4.3 min, 73%) by freeze-drying; yellow crystals were grown by vapour diffusion of tetrahydropyran into a concentrated MeCN solution of **3**. Single crystal X-ray crystallography revealed the structure of the mono-click product (**3b**) which had cyclised *via* attack of the Pt–OH ligand at the PhCO group to form a 5-membered ring (Fig. 1).

Both the azido ($Pt–N_\alpha–\mathbf{N_\beta}–N_\gamma$) ligand angle and bond lengths are very similar to those seen in the diazido precursor complex; (174.8(6)° in **3b** *vs.* 174.4(4)/175.3(4)° in **1**);[19] and 1.218(6)/1.215(4), 1.218(5), Å ($N_\alpha–N_\beta$) and 1.142(6)/1.139(4), 1.146(5) Å ($N_\beta–N_\gamma$) in **3b** and **1** respectively. The angle subtended at $Pt–\mathbf{N_\alpha}–N_\beta$ is more acute for complex **3b** (114.2(3)°) compared to complex **1** (118.0(3)°, 120.3(2)°). The Pt–N1 triazole bond length is 1.998(4) Å, which compared to reported Pt^{II} N1-coordinated 1,4-disubstituted triazole complexes with lengths of 2.149(2) Å–2.139(2) Å, is indicative of relatively strong bonding.[8,20]

Although on re-injection for analytical HPLC, **3** eluted as a single peak (t_R = 4.40 min) (Fig. S2†), in d_3-MeCN solution at 25 °C, **3** existed in dynamic equilibrium between two isomers – **3a** and **3b** – in a 1 : 1 ratio. ^{1}H and ^{13}C NMR spectral resonances of complexes **3a** and **3b** were fully characterised by 1D and 2D (COSY/ROESY/HSQC/HMBC) spectroscopic techniques (Fig. S3†).

^{1}H–^{195}Pt HMBC NMR spectroscopy revealed two distinct ^{195}Pt environments, for **3a** (689 ppm) and **3b** (785 ppm) respectively (Fig. 2). Addition of D_2O to the d_3-MeCN NMR sample resulted in the loss of the **3b** C-OH ^{1}H NMR spectral resonance at 4.93 ppm, as a result of proton/deuterium exchange. The equilibrium species **3a**/**3b** were stable in d_3-MeCN (in the dark), for a period of at least 6 months.

Depending on the mass spectrometer, either Na^+ or H^+ adducts of **3** were also observed by ESI-MS; $[(\mathbf{3})_2 + Na]^+$ was detected at 1433.29 *m*/*z* and $[\mathbf{3} + Na]^+$ at 728.14 *m*/*z*; and under some conditions $[\mathbf{3} + H]^+$ was detected at 706.15 *m*/*z*. The $[\mathbf{3}–OH]^+$ adduct at 688.15 *m*/*z* was consistently observed on all instruments (Fig. S4†). HRMS of **3** supported the identity of both $[\mathbf{3} + H]^+$ (706.1438 *m*/*z*) (Fig. S5†) and $[\mathbf{3}–OH]^+$ (688.1379 *m*/*z*) (Fig. S6†) species. MS/MS fragmentation of the $[\mathbf{3} + H]^+$ species (706.15 *m*/*z*) revealed that it very readily fragmented to give $[\mathbf{3}–OH]^+$ (688.14 *m*/*z*, $C_{26}H_{21}N_8O_3Pt$ calc. 688.14 *m*/*z*) and

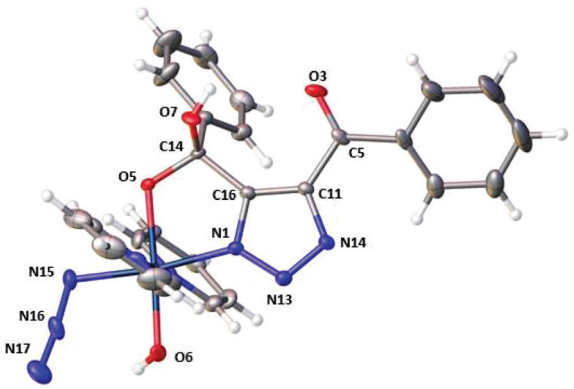

Fig. 1 X-Ray crystallographic structure of **3b** with thermal ellipsoids displayed at 50% probability.[18] Pt-Azido group naming convention; N15 = N_α, N16 = N_β and N17 = N_γ.

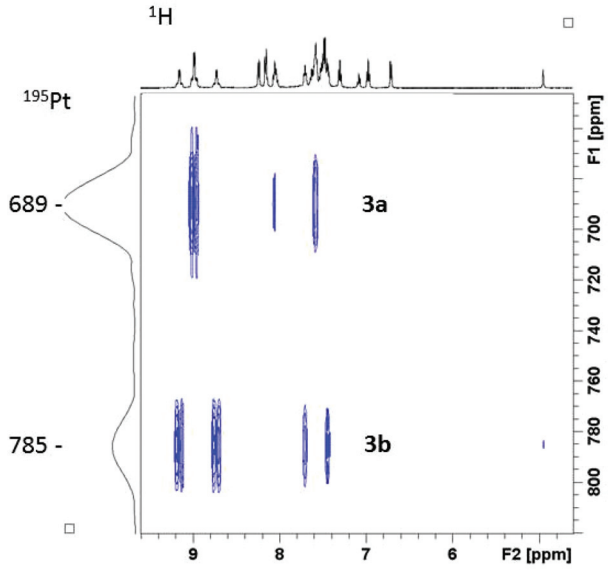

Fig. 2 ^{1}H–^{195}Pt HMBC NMR (proton at 500 MHz) spectrum of complex **3** in d_3-MeCN, showing the presence of two isomers **3a** and **3b**.

also the $[Pt(triazole)(py)(OH)]^+$ species (567.09 *m/z*, $C_{21}H_{16}N_4O_3Pt$ calc. 567.09 *m/z*) through loss of pyridine and azide (where triazole = $C_{16}H_{10}N_3O_2$) (Fig. S4†).

The $[3–triazole]^+$ fragment ($[Pt(OH)_2Py_2(N_3)]^+$ *ca.* 429.06 *m/z*) was not observed, indicating that the triazole ligand does not preferentially dissociate to give a stable charged species without other ligands also being lost; however, smaller fragments such as $[Pt(OH)(py)_2]^+$ (370.0546 *m/z*, $C_{10}H_{11}N_2OPt$, calc. 370.0519 *m/z*) and $[Pt(N_3)(triazole)]^+$ (513.0912 *m/z*, $C_{16}H_{10}N_6O_2Pt$, calc. 513.0513 *m/z*) were detected. MS/MS of the $[3–OH]^+$ 688.14 *m/z* ion gave identical daughter ions and fragmentation behaviour to MS/MS of the $[3 + H]^+$ (706.15 *m/z*) species.

UV-Vis spectroscopy of **3** was consistent with partial loss of a $N_3 \rightarrow Pt$ LMCT band, with λ_{max} moving to shorter wavelengths, from 299.5 nm (**1**) to 261.5 nm (**3**) (Fig. S7†). IR spectroscopy of a freshly prepared d_4-MeOH sample of **3** (Fig. S8†) showed the strong $\nu_{asym}N_3$ stretch at 2048 cm^{-1} was slightly weaker compared to the starting diazido complex **1** (2051 cm^{-1}, solid)[21] but similar to the value we reported for the cyclometallated mono triazole DMAD complex *trans*,*trans*,*trans*-$[Pt(N_3)(C_5H_3N_3O_4)(OH)(py)_2]$ at 2046 cm^{-1} (solid).[11]

Interconversion kinetics of 3a/3b

The kinetics of the **3a**/**3b** equilibrium were investigated *via* selective saturation-transfer experiments on interconverting ^{1}H NMR spectroscopic signals at 6.94 ppm ($\mathbf{3b}_{Phmeta}$) and 7.28 ppm ($\mathbf{3a}_{Phmeta}$) in d_3-MeCN.[22] Data was acquired at 9 temperature points; the final values for the thermodynamic parameters were calculated using an Eyring plot (Fig. S9†): $\Delta G^{\ddagger}$ = 76 (1) kJ mol^{-1} (at 298 K); $\Delta S^{\ddagger}$ = −173 (4) J mol^{-1} K^{-1}, and $\Delta H^{\ddagger}$ = 25 (1) kJ mol^{-1} (error in brackets). The exchange rate constant *k* was determined as 0.28 s^{-1} (298 K), consistent with similar processes.[23] The negative entropic change is consistent with cyclisation of **3a** to **3b**. We were unable to find reports of any directly comparable systems involving cyclisation of a ligand which is attached to a Pt centre, rather than bond breaking/formation at the metal centre itself. However, the activation barrier appears to be in the appropriate range for a reversible transformation at a metal centre on the NMR timescale, and values reported for reversible bond formation and breakage at a Pt^{IV} centre[24] and rotation of a Pt^{II}–allene complex[25] are consistent with our findings.

Photochemistry of 3

A solution of **3** and 5′-GMP (5 equiv.) in phosphate-buffered saline (PBS) solution was irradiated with UVA light and the reaction monitored by LCMS (Fig. 3). Photochemically-induced azide release was observed, through detection of the $[3–N_3]^+$ fragment (663.16 *m/z*) in the mass spectrometer. The identity of this main photoproduct was confirmed by HRMS (663.1318 *m/z* measured, $C_{26}H_{22}N_5O_4Pt$, calc. 663.1325 *m/z*, Fig. S11†).

The photochemistry of **3** was also investigated by ^{195}Pt NMR spectroscopy in d_3-MeCN. Following irradiation (452 nm, 1 h), new Pt^{IV} signals were observed, but no new ^{195}Pt signals were observed in the Pt^{II} region of the spectrum. This supports the hypothesis that upon irradiation, **3** does not form Pt^{II} photoproducts, unlike for the precursor diazido complex **1** which forms a variety of photoproducts, including Pt^{II} species. We previously reported a range of adducts formed when **1** is irradiated in the presence of 5′-GMP.[19] In contrast, when complex **3** was irradiated in the presence of 5′-GMP, no adducts were detected by ESI-MS. Pt^{IV} diazido complexes have demonstrated evolution of azidyl and hydroxyl radicals under irradiation, which is thought to contribute to their potent photocytotoxic effects.[26–28] EPR experiments in nitrogen-saturated MeCN solutions confirmed production of azidyl radicals under blue light irradiation (440–480 nm) by trapping with DMPO to form the DMPO–$N_3^{\bullet}$ adduct, which quickly built up a steady-state

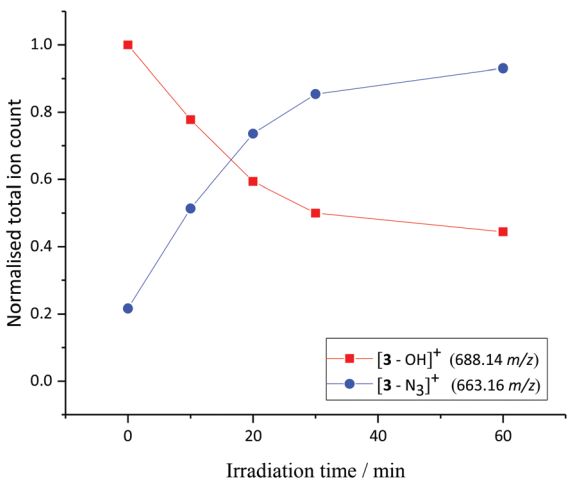

Fig. 3 Irradiation of **3** (detected by ESI-MS predominantly as $[3–OH]^+$) in the presence of 5′-GMP with UVA irradiation in PBS solution; resulted in photorelease of N_3 and formation of $[3–N_3]^+$, as monitored by HPLC.

concentration of 18 μM, and then decayed on further illumination. This is consistent with our previous results from irradiation of Pt^{IV} azido complexes.[27] Although no hydroxyl radicals were detected through trapping with DMPO to form DMPO–$OH^{\bullet}$, small quantities (4 μM) of a stable non-coupled nitroxide species was formed on a timescale significantly slower than the formation of DMPO–$N_3^{\bullet}$. It was not detected when DMPO alone was irradiated in nitrogen-saturated MeCN. It is known that azide spin-adducts can themselves be transformed *via* S_N1 chemistry into other secondary species;[29] further investigation is ongoing (Fig. S12–S14†).

Experimental

For materials, methods and procedures see ESI.†

Conclusions

The Pt^{IV} mono azido mono triazolato complex product (complex **3**) of the reaction between **1** and **2**, has been fully characterised. To the best of our knowledge, the isomer **3b** is the first reported X-ray crystal structure of a Pt(IV) mono azido complex. In MeCN, complex **3** exists as an equilibrium mixture of open **3a** and cyclised **3b** isomers in 50 : 50 ratio; the thermodynamics of this interconversion are consistent with ring-opening and closing. Complex **3** can be photoactivated with UVA (365 nm) and visible (452 nm) light in solution to give $[Pt^{IV}–N_3]^+$ as the main photoproduct, as determined by ESI-MS. EPR experiments of an MeCN solution of **3** under irradiation (440–480 nm) confirmed production of azidyl radicals through spin-trapping with DMPO, as seen previously for the precursor diazido species **1**. No OH radicals were trapped when **3** was irradiated, consistent with a $[\mathbf{3}–N_3]^+$ species being the major photoproduct.

We did not detect photoejection of the triazole ligand from the Pt centre of **3** in any of our irradiation experiments, possibly due to the additional stability afforded by cyclisation of the biphenyl ligand, resulting in bidentate coordination. MS/MS studies of **3** also confirmed the strong binding of the triazole ligand. Irradiation of **3** in the presence of the DNA model 5′-GMP with either UVA or 452 nm light did not produce any detectable 5′-GMP-Pt products.

The photocytotoxic mechanisms of diazido complexes such as **1** are complicated, since azidyl radicals, hydroxyl radicals, $^1O_2$, various DNA-binding Pt^{IV} and Pt^{II} fragments can be produced upon irradiation.[28] The relatively simple photochemistry observed for complex **3** may enable us to better understand the photocytotoxic role and relative importance of the azidyl radical when released *in cellulo* – these photobiological experiments are ongoing. Such azidyl-releasing complexes in the same line as photoCORMS (CO-releasing)[30] and NORMS (NO releasing)[31] complexes may find application as phototherapeutics since azidyl radicals and azide anions are cytotoxic; one pathway by which azidyl radicals may exert their cytotoxic activity is *via* oxidative attack of tryptophan residues in proteins;[28] and sodium azide inhibits cytochrome oxidase in the mitochondrial electron transport chain causing cell death.[32]

Conflicts of interest

There are no conflicts to declare.

Acknowledgements

This work was supported by the Wellcome Trust (201406/Z/16/Z), Cancer Research UK (CR-UK) grant number C5255/A18085, through the Cancer Research UK Oxford Centre; and the John Fell Fund. NF thanks Prof. Guy Clarkson and Dr Zoe Turner for helpful discussions, Dr James Wickens for obtaining some of the MS/MS data and Profs. Stephen Faulkner and Andrew Weller for support. The EPR measurements were performed in the Centre for Advanced Electron Spin Resonance at the University of Oxford supported by the EPSRC (EPL011972/1). A. M. B. gratefully acknowledges her fellowship support from the Royal Society and EPSRC for a Dorothy Hodgkin Fellowship (DH160004), and A. M. B and A. B acknowledge the support from the Royal Society Grant for Research Fellows (RGF\R1\180099). AMK gratefully acknowledges Keble College for a Visiting Research Fellowship.

References

1 W. P. Fehlhammer and W. Beck, *Z. Anorg. Allg. Chem.*, 2015, **641**, 1599.
2 L. Henry, C. Schneider, B. Mützel, P. V. Simpson, C. Nagel, K. Fucke and U. Schatzschneider, *Chem. Commun.*, 2014, **50**, 15692.
3 A. R. Powers, X. Yang, T. J. Del Castillo, I. Ghiviriga, K. A. Abboud and A. S. Veige, *Dalton Trans.*, 2013, 14963.
4 J. E. Heckler, B. L. Anderson and T. G. Gray, *J. Organomet. Chem.*, 2016, **818**, 68.
5 C. K. Chen, H. C. Tong, C. Y. C. Hsu, C. Y. Lee, Y. H. Fong, Y. S. Chuang, Y. H. Lo, Y. C. Lin and Y. Wang, *Organometallics*, 2009, **28**, 3358.
6 E. Evangelio, N. P. Rath and L. M. Mirica, *Dalton Trans.*, 2012, **41**, 7782.
7 S. D. Köster, H. Alborzinia, S. Can, I. Kitanovic, S. Wölfl, R. Rubbiani, I. Ott, P. Riesterer, A. Prokop, K. Merz and N. Metzler-Nolte, *Chem. Sci.*, 2012, **3**, 2062.
8 B. Schulze and U. S. Schubert, *Chem. Soc. Rev.*, 2014, **43**, 2522.
9 L. Casarrubios, M. C. de la Torre and M. A. Sierra, *Chem. – Eur. J.*, 2013, **19**, 3534.
10 S. Shaligram and A. Campbell, *Toxicol. In Vitro*, 2013, **27**, 844.

11 N. J. Farrer, G. Sharma, R. Sayers, E. Shaili and P. J. Sadler, *Dalton Trans.*, 2018, **47**, 10553.
12 S. Mukhopadhyay, J. Lasri, M. F. C. Guedes da Silva, M. A. Januário Charmier and A. J. L. Pombeiro, *Polyhedron*, 2008, **27**, 2883.
13 P. Paul, S. Chakladar and K. Nag, *Inorg. Chim. Acta*, 1990, **70**, 27.
14 P. Paul and K. Nag, *Inorg. Chem.*, 1987, **26**, 2969.
15 P. Schmid, M. Maier, H. Pfeiffer, A. Belz, L. Henry, A. Friedrich, F. Schönfeld, K. Edkins and U. Schatzschneider, *Dalton Trans.*, 2017, **46**, 13386.
16 K. S. Singh, K. A. Kreisel, G. P. A. Yap and M. R. Kollipara, *J. Organomet. Chem.*, 2006, **691**, 3509.
17 T. Cruchter, K. Harms and E. Meggers, *Chem. – Eur. J.*, 2013, **19**, 16682.
18 O. V. Dolomanov, L. J. Bourhis, R. J. Gildea, J. A. K. Howard and H. Puschmann, *J. Appl. Crystallogr.*, 2009, **42**, 339.
19 N. J. Farrer, J. A. Woods, L. Salassa, Y. Zhao, K. S. Robinson, G. Clarkson, F. S. Mackay and P. J. Sadler, *Angew. Chem., Int. Ed.*, 2010, **49**, 8905.
20 B. M. J. M. Suijkerbuijk, B. N. H. Aerts, H. P. Dijkstra, M. Lutz, A. L. Spek, G. van Koten and R. J. M. Klein Gebbink, *Dalton Trans.*, 2007, **1**, 1273.
21 R. R. Vernooij, T. Joshi, E. Shaili, M. Kubeil, D. R. T. Appadoo, E. I. Izgorodina, B. Graham, P. J. Sadler, B. R. Wood and L. Spiccia, *Inorg. Chem.*, 2016, **55**, 5983.
22 A. D. Bain and J. A. Cramer, *J. Magn. Reson., Ser. A*, 1996, **118**, 21.
23 R. L. Jarek, R. J. Flesher and S. K. Shin, *J. Chem. Educ.*, 1997, **74**, 978.
24 P. A. Shaw, G. J. Clarkson and J. P. Rourke, *Chem. Sci.*, 2017, **8**, 5547.
25 M. T. Quirós, J. Angulo and M. P. Muñoz, *Chem. Commun.*, 2015, **51**, 10222.
26 J. S. Butler, J. A. Woods, N. J. Farrer, M. E. Newton and P. J. Sadler, *J. Am. Chem. Soc.*, 2012, **134**, 16508.
27 Y. Zhao, N. J. Farrer, H. Li, J. S. Butler, R. J. McQuitty, A. Habtemariam, F. Wang and P. J. Sadler, *Angew. Chem., Int. Ed.*, 2013, **52**, 13633.
28 C. Vallotto, E. Shaili, H. Shi, J. S. Butler, C. J. Wedge, M. E. Newton and P. J. Sadler, *Chem. Commun.*, 2018, **54**, 13845.
29 P. Ionita, B. C. Gilbert and A. C. Whitwood, *J. Chem. Soc., Perkin Trans. 2*, 2002, 2436.
30 U. Schatzschneider, *Inorg. Chim. Acta*, 2011, **374**, 19.
31 E. Orlowska, M. V. Babak, O. Dömötör, E. A. Enyedy, P. Rapta, M. Zalibera, L. Bučinský, M. Malček, C. Govind, V. Karunakaran, Y. C. S. Farid, T. E. McDonnell, D. Luneau, D. Schaniel, W. H. Ang and V. B. Arion, *Inorg. Chem.*, 2018, **57**, 10702.
32 D. Ji, T. A. Kamalden, S. Del Olmo-Aguado and N. N. Osborne, *Apoptosis*, 2011, **16**, 425.

Dalton Transactions

ROYAL SOCIETY OF CHEMISTRY

PAPER

View Article Online
View Journal | View Issue

Cite this: *Dalton Trans.*, 2020, **49**, 2989

Enhancing ^{31}P NMR relaxation rates with a kinetically inert gadolinium complex†

Louise R. Tear,[a,b] Mahon L. Maguire,[b,c] Manuel Tropiano,[a] Kezi Yao,[a] Nicola J. Farrer, [a] Stephen Faulkner *[a] and Jurgen E. Schneider [b,d]

Received 22nd September 2019,
Accepted 22nd January 2020

DOI: 10.1039/c9dt03761f

rsc.li/dalton

The kinetically stable heptadentate gadolinium complex Gd.pDO3A (**1.Gd**) demonstrates significant ^{31}P nuclear magnetic resonance (NMR) relaxation enhancement of biologically relevant phosphate species; adenosine triphosphate (ATP), phosphocreatine (PCr) and inorganic phosphate. Gd.pDO3A (**1.Gd**) binds these species in fast exchange, enabling the relaxation of the bulk phosphate species in solution. This gives rise to ^{31}P relaxation enhancements up to 250-fold higher than those observed for ^{31}P relaxation enhancements with the commercial MRI contrast agent Gd.DOTA (DOTAREM), **2**. Gd.pDO3A-like complexes may have potential applications as ^{31}P magnetic resonance contrast agents, since shortening the T_1 relaxation time of phosphate species would reduce the time needed to acquire ^{31}P-MR spectra.

Introduction

Lanthanide complexes are powerful tools for imaging and assay, and have played key roles in a variety of applications from contrast enhanced MRI[1–4] to time-gated optical imaging and bioassay.[5–7]

While the physical properties of open-shell lanthanide ions lend themselves to such applications – since the 4f electrons have little role in bonding – their chemical properties present a challenge when using lanthanides for biological applications. Lanthanide ions are too toxic to administer as free ions, form labile complexes with simple ligands, and tend to form insoluble salts with a variety of common ions. This challenge can be addressed through coordination chemistry.[8–10] Multidentate ligands derived from macrocycles can offer high kinetic and thermodynamic stability, removing free lanthanide ions from solution, and eliminating lanthanide toxicity. Kinetic control is particularly important in this context, since precipitation of lanthanide species can act as a kinetic trap. Kinetically labile complexes can give rise to hazards in biology: for instance nephrogenic systemic fibrosis (NSF) has been correlated with the use of labile gadolinium complexes in clinical imaging.[11–14]

More than thirty years after the clinical approval of the first generation of MRI contrast agents, the clinical use of MRI contrast media remains broadly focused on the use of blood pool contrast agents.[15] These operate as T_1-shortening magnetic resonance contrast agents by using the paramagnetism of gadolinium to cause rapid relaxation of water protons in bulk solution, through fast exchange between lanthanide-bound solvent and bulk solvent.[1,16]

A variety of reports detail the preparation and use of gadolinium complexes as responsive contrast agents, where the relaxation enhancement varies depending on the interaction of the complex with an analyte of interest.[6] However, these have found little traction in clinical applications due to difficulties in quantifying the observed response: since the contrast agent changes the behaviour of bulk water, it is very difficult to distinguish between a small quantity of complex in its "on" state (where relaxation is enhanced greatly) and a large quantity of complex in the "off" state. This dichotomy has been successfully addressed in the case of luminescent complexes, where ratiometric imaging methods can be used to quantify behaviour on the basis of taking the ratio between two different emission wavelengths.[7,17] However, such an approach is very challenging in the context of MRI, though Caravan and coworkers have had some success in quantitative imaging using the DREMR protocol, which measures relaxation at two different fields and relies on differences in field dependence of relaxivity between the "off" and "on" forms of a complex.[18]

In this manuscript, we describe how ^{31}P NMR methods can be used to probe the interaction of a lanthanide complex with some ionic phosphate species.[6,19–21] Relatively weak and

[a]*Chemistry Research Laboratory, University of Oxford, Mansfield Road, OX1 3TA, UK. E-mail: stephen.faulkner@chem.ox.ac.uk; Tel: +44 (0)1865 272640*
[b]*British Heart Foundation Experimental MR Unit (BMRU), University of Oxford, Roosevelt Drive, Oxford, OX3 7BN, UK*
[c]*Centre for Preclinical Imaging, University of Liverpool, Nuffield Wing, Sherrington Building, Crown Street, Liverpool, L69 3BX, UK*
[d]*Leeds Institute of Cardiovascular and Metabolic Medicine, Biomedical Imaging Science Department, University of Leeds, Clarendon Way, Leeds, LS2 9JT, UK*

†Electronic supplementary information (ESI) available: Materials and methods including spectroscopy, determination of binding constants and isotherms. See DOI: 10.1039/c9dt03761f

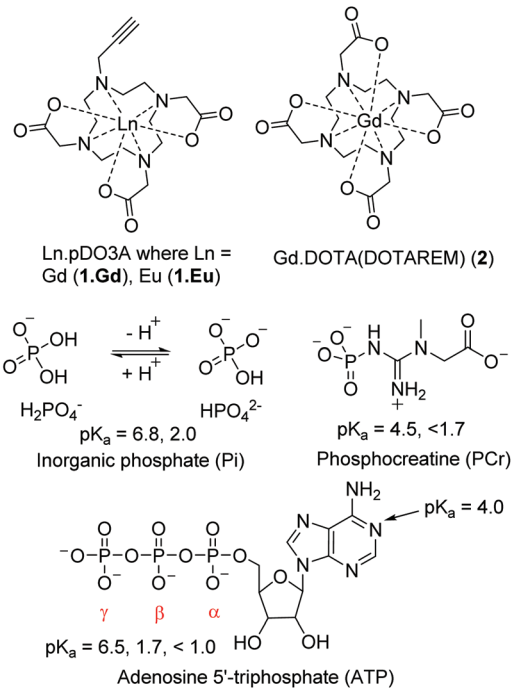

Fig. 1 Structures of complexes discussed in this study; commercial contrast agent Gd.DOTA; complexes of p.DO3A complexes of Gd (**1.Gd**) and Eu (**1.Eu**) which are investigated in this study; relevant phosphate species with reported pK_a values (H_2O) of the phosphate groups.[27–29]

rapidly reversible phosphate binding gives rise to ^{31}P relaxation enhancement for bulk phosphate species, while different species respond to the complex to different degrees. Such results potentially open up a new strategy for imaging.

Here we report our investigation into using the kinetically inert lanthanide complex (Gd.pDO3A (**1.Gd**) Fig. 1)[22–26] as a ^{31}P contrast agent for enhancing phosphorus relaxation. **1.Gd** comes from a family of pDO3A complexes which we have previously used as building blocks for more complex architectures: it combines high kinetic stability with charge neutrality: we reasoned that this combination would reduce the affinity for phosphate, permitting us to anticipate relatively rapid exchange of bound phosphate with bulk. As such we chose this system to test the hypothesis of using **1.Gd** as a contrast medium for ^{31}P relaxation enhancement.

Results and discussion

Both gadolinium (**1.Gd**) and europium (**1.Eu**) pDO3A complexes were synthesized and characterised using established procedures.[22] Given the importance of maintaining the integrity of these complexes and the issues associated with the formation of phosphate colloids with free lanthanide ions,[11–14] we resolved to explore their stability before embarking on a more detailed study. In such a system, precipitation constitutes a kinetic trap, and absolute measurements of thermodynamic stability can be misleading as they do not guarantee safety of complexes where the system is under thermodynamic control.[11] Under such circumstances, kinetic stability is essential, and our previous studies on heterometallic systems[26] led us to believe that these systems would be kinetically inert. The method of Tóth[30] was used to explore the stability of the complexes by challenging the europium complex with an excess of free gadolinium ions in aqueous solution. No change in the form of the observed spectrum was observed over a period of five days, indicating that the complex is kinetically inert (since the luminescence spectra of free and complexed europium are very different, as can be seen in the ESI† to this paper).

The interaction of **1.Eu** with three phosphate metabolites – inorganic phosphate (P_i), PCr and ATP – was assessed by luminescence spectroscopy. Titration of each metabolite with **1.Eu** in HEPES buffer at pH 7.4 resulted in modulation of the Eu emission intensity. Changes to the emission spectra clearly reveal a change to the local coordination environment at the metal centre (Fig. 2, and Fig. S1 and S2†), from which it is possible to infer phosphate displacing water at the metal centre. In the case of inorganic phosphate (Fig. 2), the consequences of binding are clear, with significant changes to the local ligand field being evident from changes to the fine structure of the $^5D_0$–$^7F_1$ transition (around 595 nm) and to the relative intensity of the $^5D_0$–$^7F_2$ transition, which is hypersensitive to local symmetry.

The integrated intensity of the $^5D_0$–$^7F_2$ transition (λ_{em} = 617 nm) was plotted against the phosphate species concentration to determine the strength of the binding interaction (the inset to Fig. 2 shows a binding isotherm for inorganic phosphate: the others are recorded in Fig. S1 and S2†).

These were fitted using Dynafit®[31] and modelled to a 1 : 1 binding equilibrium (ESI, eqn (S1)†) to determine the association constants K_a listed in Table 1. Since the values calculated were measured in the presence of HEPES, which has limited

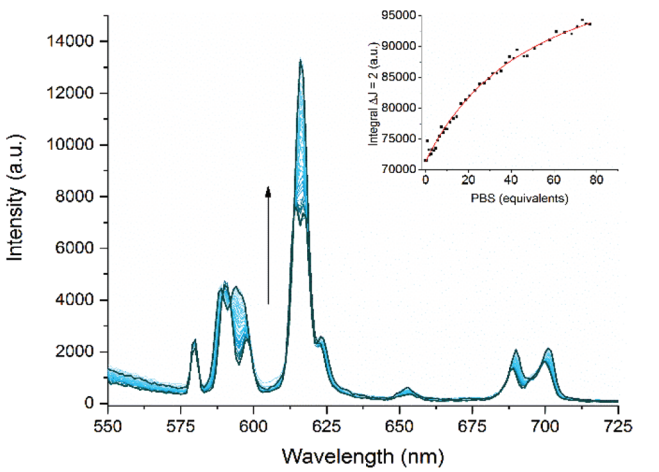

Fig. 2 Main figure: changes to the total emission spectrum (λ_{ex} = 394 nm) of a solution of **1.Eu** in HEPES buffer with increasing concentration of inorganic phosphate. Inset: the binding isotherm obtained from changes in the intensity of the $^5D_0$–$^7F_2$ emission band centred on 617 nm and fitted using Dynafit®.[31]

Table 1 Association constants (K_a) for **1.Eu** with each phosphate species, pH 7.4, λ_{ex} = 394 nm

Phosphate species[a]	K_a [b] (M^{-1})	95% confidence interval
P_i [c]	194 ± 12	[172–218]
ATP	200 ± 8	[185–216]
PCr	120 ± 8	[104–138]

[a] All samples in 10 mM HEPES, with 0.1 mM **1.Eu**. [b] ± standard deviation. [c] In the absence of HEPES an apparent K_a of 261 ± 15 [232–292] was determined.

ionic strength and can potentially interact with lanthanide complexes, these values represent effective binding constants, but clearly reveal consistent binding of a variety of phosphate species, with slightly weaker binding of PCr as a result of its zwitterionic nature.

The observed values of K_a are fully consistent with fast exchange between bulk phosphate and phosphate bound to **1.Eu**. The three phosphate species all exhibit very similar affinity constants. Binding of phosphate was further demonstrated by measuring the luminescence lifetimes in H_2O and D_2O, and determining the number of inner-sphere water molecules using the modified Horrocks equation.[32] This revealed that q = 2 for **1.Eu** in the absence of phosphate, but q = 0.9 in the presence of phosphate – consistent with monodentate coordination of phosphate in line with literature precedent.[6]

To further explore exchange, we used **1.Gd** to explore the possibility of observing changes to the bulk relaxation rates of phosphate species in the presence of increasing concentrations of **1.Gd**, reasoning that fast exchange would lead to clear concentration dependent enhancement of the ^{31}P longitudinal relaxation rates, in the same way that conventional MRI contrast agents enhance the relaxation of bulk water. ^{31}P relaxation rates ($R_1 = 1/T_1$) were measured for ATP, PCr and P_i with increasing concentrations of **1.Gd** (Fig. 3).

1.Gd showed a significant linear relaxation enhancement of all phosphate species (Fig. 3), suggesting that fast exchange is indeed occurring. This linear enhancement also confirms that the gadolinium complex is kinetically stable under the conditions of the experiment, since exchange of gadolinium and formation of a new gadolinium bound species results in significant curvature to the plot, as previously observed by Muller and co-workers (who observed significant competition between ATP and gadolinium complexes of DTPA bis amide ligands).[33]

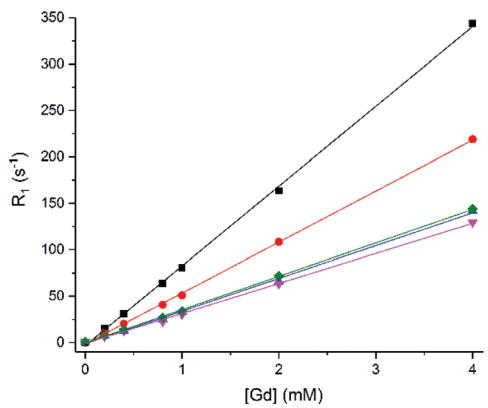

Fig. 3 ^{31}P Relaxation rate (R_1) of P_i (■), PCr (●) and α-(▼), β-(◆), γ-(▲) ATP (8.7, 5.5 and 7.9 mM) *versus* concentration of **1.Gd**, pH 7.2, 162 MHz, 298 K.

The relaxivities obtained (r_1 = 1/([Gd]T_1)) are displayed in Table 2 for **1.Gd**. The table also shows the ^{31}P relaxivity properties for **2** (Gd.DOTA-, Dotarem®) for comparison. These values for **1.Gd** are all greater than 30 mM^{-1} s^{-1}, with the most significant effect observed for P_i followed by PCr and then ATP. This is most likely to be a result of the size of the phosphate molecule and the consequently easy access to the Gd binding site.

Increasing concentrations of contrast agent **2** resulted in a much smaller, though still linear, relaxation enhancement across all five phosphate resonances (P_i, PCr, α-ATP, β-ATP, γ-ATP) (Table 2 and Fig S4†). The ^{31}P relaxivity values (r_1 = 1/([Gd]T_1) of all phosphate species were below 0.5 mM^{-1} s^{-1}. These relaxivity values for **2** are more than 60 times smaller than the relaxivity values measured for **1.Gd**.

Taking the observations on **1.Gd** together with those on **2**, it is clear that phosphate affinity is playing an important role in relaxation rate enhancement. For **2**, which displays negligible affinity for phosphate, the small enhancements observed are likely to be the consequence of an outer sphere interaction.

Outer-sphere relaxation is defined by diffusion, the distance of closest approach and the electronic relaxation time of the metal ion.[34] For complexes of a similar size and molecular weight, the outer-sphere contribution to longitudinal relaxation rate is considered to be comparable and independent of differences in functional groups on the ligand. On this basis, we can use the relaxivity measurements obtained using **2** to estimate the inner sphere contribution to ^{31}P relaxivity with **1.Gd**, using eqn (1).

$$r_1 = r_1^{IS} + r_1^{OS} \quad (1)$$

From this equation the inner-sphere contribution to the overall observed ^{31}P relaxivity for **1.Gd** is estimated to be ≥99% and is clearly the dominant effect. This is much greater than is

Table 2 ^{31}P relaxivity (r_1) of phosphate species with **1.Gd** and **2**, 162 MHz, pH 7.2, 298 K

	r_1 [b] (mM Gd^{-1} s^{-1})	
Phosphate species[a]	**1.Gd**	**2**
P_i	85.96 ± 1.00	0.35 ± 0.01
PCr	54.97 ± 0.48	0.24 ± 0.01
α-ATP	32.35 ± 0.46	0.39 ± 0.03
β-ATP	35.97 ± 0.35	0.27 ± 0.01
γ-ATP	35.30 ± 0.64	0.25 ± 0.01

[a] Solution contains [PBS] = 8.7 mM, [PCr] = 5.5 mM, [ATP] = 7.9 mM. [b] ± Standard error of linear fit, R^2 values >0.99 for all fits.

commonly observed for ^{1}H relaxivity, where the outer sphere contribution for a q = 1 complex can be around 40% (at imaging field strengths).[35,36] The much lower outer-sphere contribution for phosphates undoubtedly reflects that there are invariably many water molecules in the outer coordination sphere of a complex. Since the total concentration of phosphate nuclei will be around three orders of magnitude lower than that of water protons (25 mM total phosphate species *versus* ~55 M water) the contribution of second-sphere phosphate molecules is always likely to be relatively small.

Since phosphate binds to **1.Gd**, it was anticipated that phosphate binding would exclude water from the inner coordination sphere. To confirm this, the ^{1}H water relaxation rate was measured with increasing concentrations of **1.Gd** in distilled water and in phosphate solution (Fig. 4, values in Table 3). The relaxivity in water is very similar to that for DO3A[37] and greater than that for Dotarem, as would be expected for a complex with q = 2.[1]

The ^{1}H relaxivity was found to be about 16% lower in phosphate solution than in distilled water. This is due to the competition between water and phosphate species for the gadolinium centre, which reduces the concentration of bound water molecules relative to bulk. This suggests that a combination of the decrease in ^{1}H signal and increase in ^{31}P signal may allow the possibility for ratiometric determination of phosphate from multinuclear relaxometric measurements – though it is clear that current instrumentation would make such simultaneous dual measurements extremely challenging.

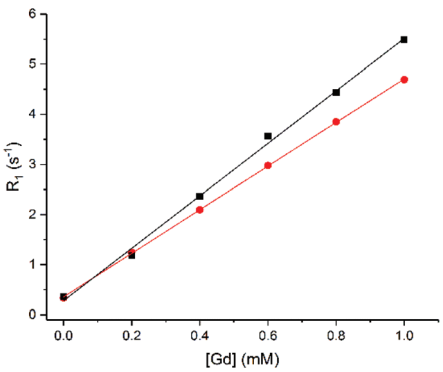

Fig. 4 ^{1}H water relaxation rate (R_1) in DI water (■) or phosphate solution (●) (8.7 mM PBS, 5.5 mM PCr and 7.9 mM ATP) *versus* concentration of **1.Gd**, pH 7.2, 400 MHz, 298 K. Error bars are within the size of the data points.

Table 3 H_2O ^{1}H relaxivity (r_1) with **1.Gd** at 400 MHz, pH 7.2, 298 K

	r_1 [b] (mM Gd^{-1} s^{-1})	
Complex	Water	Phosphate solution[a]
1.Gd	5.24 ± 0.13	4.36 ± 0.02

[a] Phosphate solution = [PBS] = 8.7 mM, [PCr] = 5.5 mM, [ATP] = 7.9 mM. [b] ± Standard error of linear fit, R^2 values >0.99 for all fits.

Experimental

For materials, methods and procedures see ESI.†

Conclusions

In this study, we have shown how binding and fast exchange between a gadolinium complex and anionic phosphate species can be exploited to enhance relaxation of bulk phosphate anions in solution. We have demonstrated significant ^{31}P relaxation enhancement using a kinetically inert heptadentate lanthanide complex **1.Gd**. We observe dramatic enhancements in relaxation for a variety of phosphorus containing species (particularly phosphate itself, ATP and phosphocreatine). Preliminary studies suggest that this **1.Gd** is not internalised by cells to any significant extent,[38] limiting the biological application of this complex to extracellular investigation without further derivation. The use of phosphate contrast media may prove a profitable avenue for investigation if these issues of cellular uptake can be addressed.

Conflicts of interest

There are no conflicts to declare.

Acknowledgements

This work was supported by funding from the Engineering and Physical Sciences Research Council (EPSRC), the Medical Research Council (MRC) [grant number EP/L016052/1] and the British Heart Foundation (FS/11/50/29038). NF thanks the Wellcome Trust (201406/Z/16/Z), Cancer Research UK (C5255/A18085) through the Cancer Research UK Oxford Centre, L'Oréal (Women in Science Fellowship) and Singapore Chemical Group (Innovation Fund Young Researcher Award) for funding.

Notes and references

1 P. Caravan, J. J. Ellison, T. J. McMurry and R. B. Lauffer, *Chem. Rev.*, 1999, **99**, 2293.
2 J. Lohrke, T. Frenzel, J. Endrikat, F. C. Alves, T. M. Grist, M. Law, J. M. Lee, T. Leiner, K. C. Li, K. Nikolaou, M. R. Prince, H. H. Schild, J. C. Weinreb, K. Yoshikawa and H. Pietsch, *Adv. Ther.*, 2016, **33**, 1.
3 L. M. De León-Rodríguez, A. F. Martins, M. C. Pinho, N. M. Rofsky and A. D. Sherry, *J. Magn. Reson. Imaging*, 2015, **42**, 545.
4 G.-P. Yan, L. Robinson and P. Hogg, *Radiography*, 2007, **13**, e5.
5 K. Y. Zhang, Q. Yu, H. Wei, S. Liu, Q. Zhao and W. Huang, *Chem. Rev.*, 2018, **118**, 1770.
6 S. J. Butler and D. Parker, *Chem. Soc. Rev.*, 2013, **42**, 1652.
7 S. H. Hewitt and S. J. Butler, *Chem. Commun.*, 2018, **54**, 6635.

8 T. J. Sørensen and S. Faulkner, *Acc. Chem. Res.*, 2018, **51**, 2493.
9 D. Messeri, M. P. Lowe, D. Parker and M. Botta, *Chem. Commun.*, 2001, **1**, 2742.
10 M. Tropiano, O. A. Blackburn, J. A. Tilney, L. R. Hill, M. P. Placidi, R. J. Aarons, D. Sykes, M. W. Jones, A. M. Kenwright, J. S. Snaith, T. J. Sørensen and S. Faulkner, *Chem. – Eur. J.*, 2013, **19**, 16566.
11 M. Le Fur and P. Caravan, *Metallomics*, 2019, **11**, 240.
12 W. A. High, R. A. Ayers, J. Chandler, G. Zito and S. E. Cowper, *J. Am. Acad. Dermatol.*, 2007, **56**, 21.
13 P. Marckmann, L. Skov, K. Rossen, A. Dupont, M. B. Damholt, J. G. Heaf and H. S. Thomsen, *J. Am. Soc. Nephrol.*, 2006, **17**, 2359.
14 T. Grobner, *Nephrol., Dial., Transplant.*, 2006, **21**, 1104.
15 J. Wahsner, E. M. Gale, A. Rodríguez-Rodríguez and P. Caravan, *Chem. Rev.*, 2019, **119**, 957.
16 V. C. Pierre, M. J. Allen and P. Caravan, *J. Biol. Inorg. Chem.*, 2014, **19**, 127–131.
17 T. J. Sørensen, A. M. Kenwright and S. Faulkner, *Chem. Sci.*, 2015, **6**, 2054.
18 J. K. Alford, A. G. Sorensen, T. Benner, B. A. Chronik, W. B. Handler, T. J. Scholl, G. Madan and P. Caravan, *Proc. Int. Soc. Magn. Reson. Med.*, 2011, **19**, 452.
19 P. Atkinson, Y. Bretonnière, D. Parker and G. Muller, *Helv. Chim. Acta*, 2005, **88**, 391.
20 J. I. Bruce, R. S. Dickins, L. J. Govenlock, T. Gunnlaugsson, S. Lopinski, M. P. Lowe, D. Parker, R. D. Peacock, J. J. B. Perry, S. Aime and M. Botta, *J. Am. Chem. Soc.*, 2000, **122**, 9674.
21 R. N. Muller, B. Radüchel, S. Laurent, J. Platzek, C. Piérart, P. Mareski and L. Vander Elst, *Eur. J. Inorg. Chem.*, 1999, 1949.
22 M. Jauregui, W. S. Perry, C. Allain, L. R. Vidler, M. C. Willis, A. M. Kenwright, J. S. Snaith, G. J. Stasiuk, M. P. Lowe and S. Faulkner, *Dalton Trans.*, 2009, 6283.
23 A. K. R. Junker, M. Tropiano, S. Faulkner, T. J. Sørensen, A. Kathrine, R. Junker, M. Tropiano, S. Faulkner and T. Just Sørensen, *Inorg. Chem.*, 2016, **55**, 12299.
24 M. Tropiano, N. L. Kilah, M. Morten, H. Rahman, J. J. Davis, P. D. Beer and S. Faulkner, *J. Am. Chem. Soc.*, 2011, **133**, 11847.
25 C. Allain, P. D. Beer, S. Faulkner, M. W. Jones, A. M. Kenwright, N. L. Kilah, R. C. Knighton, T. J. Sørensen and M. Tropiano, *Chem. Sci.*, 2013, **4**, 489.
26 M. Tropiano, A. M. Kenwright and S. Faulkner, *Chem. – Eur. J.*, 2015, **21**, 5697.
27 P. Oesper, in *Phosphorus Metabolism*, ed. W. D. McElroy and B. Glass, John Hopkins University Press, Baltimore, 1951, vol. I, pp. 523–536.
28 L. Chen, *Biomed. Res.*, 2017, **28**, 8195.
29 P. Kaczmarek, W. Szczepanik and M. Jezowska-Bojczuk, *Dalton Trans.*, 2005, 3653.
30 É. Tóth, R. Király, J. Platzek, B. Radüchel and E. Brücher, *Inorg. Chim. Acta*, 1996, **249**, 191.
31 P. Kuzmič, *Methods Enzymol.*, 2009, **467**, 247.
32 A. Beeby, I. M. Clarkson, R. S. Dickins, S. Faulkner, D. Parker, L. Royle, A. S. de Sousa, J. A. G. Williams and M. Woods, *J. Chem. Soc., Perkin Trans. 2*, 1999, 493.
33 L. Vander Elst, Y. Van Haverbeke, J. F. Goudemant and R. N. Muller, *Magn. Reson. Med.*, 1994, **31**, 437.
34 S. Aime, M. Botta, M. Fasano and E. Terreno, *Chem. Soc. Rev.*, 1998, **27**, 19.
35 S. Aime, A. S. Batsanov, M. Botta, J. A. K. Howard, D. Parker, K. Senanayake and G. Williams, *Inorg. Chem.*, 1994, **33**, 4696.
36 M. Botta, *Eur. J. Inorg. Chem.*, 2000, 399.
37 P. Placidi, L. S. Natrajan, D. Sykes, A. M. Kenwright and S. Faulkner, *Helv. Chim. Acta*, 2009, **92**, 2427.
38 L. R. Tear, *Molecular Imaging Probes for 31P Contrast*, DPhil Thesis, University of Oxford, Oxford, UK, 2018.